SAPIENZA
UNIVERSITÀ DI ROMA

Doctoral School "Vito Volterra" in Astronomical, Chemical, Earth, Mathematical and Physical Sciences

Doctor of Philosophy in Earth Sciences
XXXV cycle

Definition of a genetic model for the dark-colored overgrowths in pegmatitic gem tourmaline crystals

SSD GEO/06

Ph.D. Candidate:
Alessandra Altieri

Supervisor
Prof. Ferdinando Bosi

Co-Supervisor
Dr. Federico Pezzotta

2019-2022

"Somewhere,
something incredible is waiting to be known"

Carl Sagan

Structure of the Ph.D thesis

SUMMARY

Elba gem tourmalines are renowned for the delicate pastel colors and the perfection of their crystal shapes in small size. Characteristic for these tourmalines is the presence of color anomalies that occur as dark-colored terminations, frequently at the analogous pole that typically are rich in Fe and/or Mn.

The formation of such dark-colored overgrowths is related to sudden physicochemical changes in the crystallization environment during the latest-stages of tourmaline crystal growth. However, the detailed events that led to the availability of Fe and/or Mn in the pocket environment, resulting in the growth of late-stage tourmalines, remained unclear.

The goal of this Ph.D project is the definition of a genetic model for the dark-colored overgrowths in pegmatitic gem tourmaline crystals. Since tourmaline is an excellent petrogenetic indicator, the origin and chemical composition of fluids involved in tourmaline crystallization, responsible for such color anomalies, have also been investigated. To achieve this goal, selected gem tourmaline crystals with dark overgrowths of different colors and textural features from several miarolitic Li-bearing aplite-pegmatite veins, located in the eastern border of Monte Capanne monzogranite pluton (Elba Island, Italy), were studied.

Chemical and spectroscopic investigations were applied as experimental approach in order to describe the crystal-chemical characteristics of the zones characterized by such color anomalies. This information, along with microstructural and paragenetic observations of the cavities in which the studied tourmaline samples were collected, were used to determine and propose a general genetic model for the color anomalies observed at the termination of Elba gem tourmaline crystals.

This study was further extended to tourmaline samples collected from the Alto Ligonha pegmatite district (Nampula Province, NE Mozambique). Gem-quality tourmalines from the Alto Ligonha pegmatite district are among the most renowned for the combination of color and rarity. These features make them unique from a gemological viewpoint and therefore with a high commercial value,

limiting the information regarding their crystal-chemical characteristics. To fill this gap, several tourmaline samples from the secondary deposit of Mavuco, in the eastern portion of the Alto Ligonha pegmatite district, were studied. These tourmaline samples were provided by ongoing mining projects, and were subjected to an in-depth analysis. Specifically, a detailed chemical characterization as well as a correlation study between compositional data and color displayed by the tourmaline crystals, were conducted. In addition, on selected samples with particular chromatic features, optical absorption spectroscopy analyses were performed. For all the tourmaline samples analyzed, the gemological variety, according to the color displayed, was identified and the relative color mechanisms were investigated.

Tourmaline grains from the secondary deposit of Mavuco are also characterized by a dark-colored prismatic overgrowth. The genetic mechanisms responsible for these prismatic overgrowths have not been defined so far, as the pegmatitic source from which these tourmalines originated was still uncertain. This uncertainty was essentially due to the strong NYF (Niobium-Yttrium-Fluorine) geochemical affinity (Li- and B-poor composition) of the Alto Ligonha pegmatites located quite close the secondary deposit of Mavuco, as well as the rudimentary excavation techniques, which did not allow the exploration of new pegmatitic deposits in the Alto Ligonha district.

To gain information about the processes that led to the formation of the prismatic dark-colored overgrowths, selected tourmaline crystals from a recently discovered pegmatitic field, the so-called "Marina" pegmatite (Mavuco area), were analyzed. The "Marina" pegmatite was hypothesized to be a source of the detrital tourmaline grains of the Mavuco area, given its proximity to the secondary deposit, and its LCT geochemical signature. Studies on tourmaline crystals from the "Marina" pegmatite were carried out to confirm the above hypothesis, through the comparison of the compositional data obtained from such tourmaline crystals with those obtained from the detrital tourmalines of the secondary deposit of

Mavuco. The same studies allowed obtain detailed information on the genesis of the dark-colored prismatic overgrowths, which also characterize some of the detrital tourmalines.

During the chemical characterization activity, two new mineral species of the tourmaline supergroup were discovered. Both of them were approved by the IMA-CNMNC (International Mineralogical Association-Commission on New Minerals, Nomenclature and Classification) and named celleriite, ideally $\square(Mn^{2+}_2Al)Al_6(Si_6O_{18})(BO_3)_3(OH)_3(OH)$, and ferro-bosiite, ideally $NaFe^{3+}_3(Al_4Fe^{2+}_2)(Si_6O_{18})(BO_3)_3(OH)_3O$.

The results obtained in this PhD research improved the knowledge on the opening of geochemical systems in which tourmaline crystallized, and allowed the definition of a genetic model for the formation of the dark-colored overgrowths in tourmaline crystals. This model can be exported to explain late-stage color and composition anomalies of gem tourmaline crystals of many other gem-pegmatite deposits in the world.

1. INTRODUCTION

1.1 Tourmaline constituents and species

Tourmaline is the dominant host for boron (B) in most rocks of the Earth's crust, occurring in granites and granite pegmatites but also in low-grade to ultrahigh-pressure metamorphic rocks and as detrital grain in sandstones and conglomerates (e.g., van Hinsberg at al., 2011a,b; Dutrow and Henry, 2018; Henry and Dutrow, 2018).

Tourmalines are a supergroup of chemically complex minerals with a significant compositional variability due to the occurrence of, at least, 27 relevant constituents different in charge and size, which accommodate into 7 crystallographic sites (*X*, *Y*, *Z*, *T*, *B*, O1, and O3). These constituents include both light and heavy elements, from H to Pb, some of them characterized by more than one oxidation state (e.g., Fe^{2+}-Fe^{3+} and Mn^{2+}-Mn^{3+}) (Table 1.1).

Table 1.1. The 27 relevant constituents occurring in tourmaline.

Valence	0	1	2	3	4
	$^{[9]\text{-}[6]}\square$	$^{[9]}\mathbf{Na^{+}}$	$^{[9]}\mathbf{Ca^{2+}}$	$^{[6]\text{-}[4]}\mathbf{Al^{3+}}$	$^{[6]}\mathbf{Si^{4+}}$
		$^{[9]}\mathbf{K^{+}}$	$^{[6]}\mathbf{Mg^{2+}}$	$^{[6]}\mathbf{Cr^{3+}}$	$^{[4]}\mathbf{Ti^{4+}}$
		$^{[6]}\mathbf{Li^{+}}$	$^{[6]}\mathbf{Fe^{2+}}$	$^{[6]}\mathbf{V^{3+}}$	
		$^{[9]}Ag^{+}$	$^{[6]}\mathbf{Mn^{2+}}$	$^{[6]}\mathbf{Fe^{3+}}$	
		$\mathbf{H^{+}}$	$^{[6]}Ni^{2+}$	$^{[6]}Ga^{3+}$	
		$^{[3]}\mathbf{F^{-}}$	$^{[6]}Co^{2+}$	$^{[3]\text{-}[4]}\mathbf{B^{3+}}$	
			$^{[6]}Zn^{2+}$	$^{[6]}Mn^{3+}$	
			$^{[6]}Pb^{2+}$		
			$^{[3]\text{-}[4]}\mathbf{O^{2-}}$		

Notes: Vacancy (□) is considered as a constituent in accord with the IMA-CNMNC rules. Brackets indicate coordination numbers. Bold indicates constituents characterizing the 38 species of the tourmaline-supergroup minerals.

In accordance with Henry et al. (2011), the general formula of tourmaline may be written as $XY_3Z_6T_6O_{18}(BO_3)_3V_3W$, where X = Na^{+}, K^{+}, Ca^{2+}, Pb^{2+}, □ (□ = vacancy); Y = Mg^{2+}, Fe^{2+}, Mn^{2+}, Li^{+}, Al^{3+}, Fe^{3+}, Cr^{3+}, V^{3+}, Ti^{4+}; Z = Al^{3+}, Fe^{3+}, Cr^{3+}, V^{3+}, Mg^{2+}, Fe^{2+}, Ti^{4+}; T = Si^{4+}, Al^{3+}, B^{3+}; B = B^{3+}; V = OH^{1-}, O^{2-} and W = OH^{1-}, F^{1-}, O^{2-}. The non-italicized letters X, Y, Z, T and B represent groups of cations accommodated at the $^{[9]}X$, $^{[6]}Y$,

$^{[6]}Z$, $^{[4]}T$ and $^{[3]}B$ crystallographic sites (italicized letters). The letters V and W represent groups of anions accommodated at the $^{[3]}$O3 and $^{[3]}$O1 crystallographic sites, respectively. The H atoms occupy the H3 and H1 sites, which are related to O3 and O1, respectively.

Given the relatively large number of constituent-coordination environments ([3], [4], [6], and [9] coordination) compared to most other minerals, tourmaline violates the Pauling's parsimony rule, which emphasizes that the number of topochemically different environments in a structure tends to be small (Hawthorne, 2006). In theory, this relatively large number of substantially different sites would decrease the stability, but tourmaline exists over environments that extend from the surface of the crust to the upper mantle (e.g., Marschall et al., 2009; Lussier et al., 2016) in the presence of H_2O, B-, and F-bearing fluids.

The dominance of specific ions at one or more sites of the structure gives rise to a range of distinct mineral species. At present, the tourmaline supergroup consists of 38 mineral species approved by the International Mineralogical Association's Commission on New Minerals, Nomenclature and Classification (IMA-CNMNC) (Table 1.2).

1.2 Tourmaline crystal structure

The tourmaline structure is typically rhombohedral, space group *R3m* with Z = 3, although some studies report lower symmetry such as orthorhombic, monoclinic, or triclinic (e.g., Akizuki et al., 2001; Shtukenberg et al., 2007; Hughes et al., 2011).

Tourmaline has an intermediate structural complexity of about 200 bits per unit cell (Krivovichev, 2013), which is larger than that of amphibole (about 150 bits per unit cell), but smaller than that of some other minerals such as analcime (usually much over 200 bits per unit cell).

The structure of tourmaline belongs to the subclass of cyclosilicate as it consists of rings of six TO_4 tetrahedra, lying in a plane parallel to (0001). Because all tetrahedra point in the same direction, tourmaline lacks center of symmetry,

giving the crystal a strongly polar character. Thus tourmaline is both pyroelectric and piezoelectric.

Table 1.2. The 38 mineral species of tourmaline recognized by the IMA-CNMNC.

Species name	Ideal end-member formula
Adachiite	$CaFe^{2+}_3Al_6(Si_5AlO_{18})(BO_3)_3(OH)_3OH$
Alumino-oxy-rossmanite	$\square Al_3Al_6(Si_5AlO_{18})(BO_3)_3(OH)_3O$
Bosiite	$NaFe^{3+}_3(Al_4Mg_2)Si_6O_{18})(BO_3)_3(OH)_3O$
Celleriite	$\square(Mn^{2+}_2Al)Al_6(Si_6O_{18})\ )(BO_3)_3(OH)_3(OH)$
Chromium-dravite	$NaMg_3Cr_6Si_6O_{18})(BO_3)_3(OH)_3OH$
Chromo-alumino-povondraite	$NaCr_3(Al_4Mg_2)Si_6O_{18})(BO_3)_3(OH)_3O$
Darrellhenryite	$NaLiAl_2Al_6Si_6O_{18}(BO_3)_3(OH)_3O$
Dravite	$NaMg_3Al_6Si_6O_{18}(BO_3)_3(OH)_3OH$
Dutrowite	$Na(Fe_{2.5}Ti_{0.5})Al_6Si_6O_{18}(BO_3)_3(OH)_3O$
Elbaite	$Na(Li_{1.5}Al_{1.5})Al_6Si_6O_{18}(BO_3)_3(OH)_3OH$
Ferro-bosiite	$NaFe^{3+}_3(Al_4Fe^{2+}_2)(Si_6O_{18})(BO_3)_3(OH)_3O$
Feruvite	$CaFe^{2+}_3(MgAl_5)Si_6O_{18}(BO_3)_3(OH)_3OH$
Fluor-buergerite	$NaFe^{3+}_3Al_6\ Si_6O_{18}(BO_3)_3O_3F$
Fluor-dravite	$NaMg_3Al_6Si_6O_{18}(BO_3)_3(OH)_3F$
Fluor-elbaite	$Na(Li_{1.5}Al_{1.5})Al_6Si_6O_{18}(BO_3)_3(OH)_3F$
Fluor-liddicoatite	$Ca(Li_2Al)Al_6Si_6O_{18}(BO_3)_3(OH)_3F$
Fluor-schorl	$NaFe^{2+}_3Al_6Si_6O_{18}(BO_3)_3(OH)_3F$
Fluor-tsilaisite	$NaMn^{2+}_3Al_6Si_6O_{18}(BO_3)_3(OH)_3F$
Fluor-uvite	$CaMg_3(Al_5Mg)\ Si_6O_{18}(BO_3)_3(OH)_3F$
Foitite	$\square(Fe^{2+}_2Al)Al_6Si_6O_{18}(BO_3)_3(OH)_3OH$
Lucchesiite	$Ca(Fe^{2+})_3Al_6Si_6O_{18}(BO_3)_3(OH)_3O$
Magnesio-foitite	$\square(Mg_2Al)Al_6Si_6O_{18}(BO_3)_3(OH)_3OH$
Magnesio-lucchesiite	$CaMg_3Al_6Si_6O_{18}(BO_3)_3(OH)_3O$
Maruyamaite	$K(MgAl_2)(Al_5Mg)Si_6O_{18}(BO_3)_3(OH)_3O$
Olenite	$NaAl_3Al_6Si_6O_{18}(BO_3)_3O_3OH$
Oxy-chromium-dravite	$NaCr_3(Mg_2Cr_4)Si_6O_{18}(BO_3)_3(OH)_3O$
Oxy-dravite	$Na(Al_2Mg)(Al_5Mg)Si_6O_{18}(BO_3)_3(OH)_3O$
Oxy-foitite	$\square(Fe^{2+}Al_2)Al_6Si_6O_{18}(BO_3)_3(OH)_3O$
Oxy-schorl	$Na(Fe^{2+}_2Al)Al_6Si_6O_{18}(BO_3)_3(OH)_3O$
Oxy-vanadium-dravite	$NaV_3(V_4Mg_2)Si_6O_{18}(BO_3)_3(OH)_3O$
Povondraite	$NaFe^{3+}_3(Fe^{3+}_4Mg_2)Si_6O_{18}(BO_3)_3(OH)_3O$
Princivalleite	$Na(Mn^{2+}_2Al)Al_6Si_6O_{18}(BO_3)_3(OH)_3O$
Rossmanite	$\square(LiAl_2)Al_6Si_6O_{18}(BO_3)_3(OH)_3OH$
Schorl	$NaFe^{2+}_3Al_6Si_6O_{18}(BO_3)_3(OH)_3OH$
Tsilaisite	$NaMn^{2+}_3Al_6Si_6O_{18}(BO_3)_3(OH)_3OH$
Uvite	$CaMg_3(Al_5Mg)\ Si_6O_{18}(BO_3)_3(OH)_3OH$
Vanadio-oxy-chromium-dravite	$NaV_3(Cr_4Mg_2)Si_6O_{18}(BO_3)_3(OH)_3O$
Vanadio-oxy-dravite	$NaV_3(Al_4Mg_2)Si_6O_{18}(BO_3)_3(OH)_3O$

Each tetrahedron shares one edge with the trigonal antiprism XO_9, which is located along the threefold axis passing through the center of each six-membered ring [T_6O_{18}]. The nine-coordinated *X* site is the largest site, thus able to accommodate large cations (commonly Na^+ and Ca^{2+}, with some minor K^+ or remain vacant (Henry and Dutrow, 1996,2011; Henry et al., 2011). The occupant of the *X* site forms the basis for the initial discrimination between primary groups of tourmaline (*X*-site vacant, alkali and calcic), and thus the root name of the tourmaline species (Henry et al., 2011). The antiprism XO_9 and the ring [T_6O_{18}] combine with two sets of three octahedra YO_6: an [Y_3O_{15}] triplet of octahedra caps the XO_9 polyhedron toward the +**c** axis and the other [Y_3O_{13}] caps the [T_6O_{18}] ring of tetrahedra toward the –**c** axis. The most extensive compositional variation occurs at the *Y* site, which is able to incorporate constituents of different sizes and charges (Mg^{2+}, Fe^{2+}, Mn^{2+}, Li^+, Al^{3+}, Fe^{3+}, Cr^{3+}, V^{3+} and Ti^{4+} as well as other elements at trace amounts). The partitioning of the *X* and *Y*-site constituents between +**c** and -**c** poles was calibrated and is useful to reconstruct the chemical history of the fluids involved in tourmaline crystallization (van Hinsberg et al., 2011a,b; Dutrow and Henry, 2018; Bosi et al., 2022a; Altieri et al., 2022,b). The BO_3 groups oriented sub-parallel to (0001) lie between the tetrahedral rings and are fully occupied by B, which makes tourmaline one of the most important B-bearing minerals in the Earth (Grew et al., 2016). The structural arrangement of [T_6O_{18}], XO_9, [Y_6O_{18}], and $(BO_3)_3$ form "islands" that are stacked in columns along the **c** axis. These islands are attached to one another along the **a** and **b** crystallographic axes by spiral chains of ZO_6 octahedra (Fig. 1.1A), which also extend along to the **c** axis according to a 3_1 triad screw axis. The three-dimensional framework of the tourmaline structure is therefore given by the screw-like arrangement of ZO_6 (Fig. 1.1B).

This framework is characterized by similar strong Z-O bonds (~0.5 valence units), which would explain some physical properties, such as hardness (~7–7½ Mohs), lack of cleavage, resistance to weathering in clastic sediments, and extensive

pressure-temperature stability up to about 7 GPa and 950 °C (van Hinsberg et al., 2011b). Another important feature of the tourmaline structure is provided by the orientation of the hydrogen atoms, which are sub-parallel to the **c** axis: H1-hydrogen point down **–c** toward the oxygen at O1, and H3-hydrogen points up **+c** toward the oxygen at O3. Thanks to this orientation of (OH) dipoles, the fundamental (OH)-stretching bands in infrared spectra of tourmalines display a very strong pleochroism, with $\varepsilon >> \omega$ (e.g., Skogby et al., 2012).

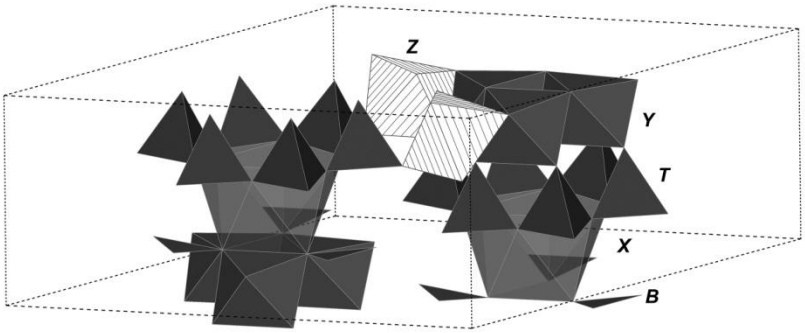

Figure 1.1A. Polyhedral arrangements in the tourmaline crystal structure. Dark-gray polyhedra coordinate the *Y*, *T*, *X*, and *B* sites. Stripefilled octahedra coordinate the *Z* site. Dashed-line represents the unit cell (from Bosi 2018).

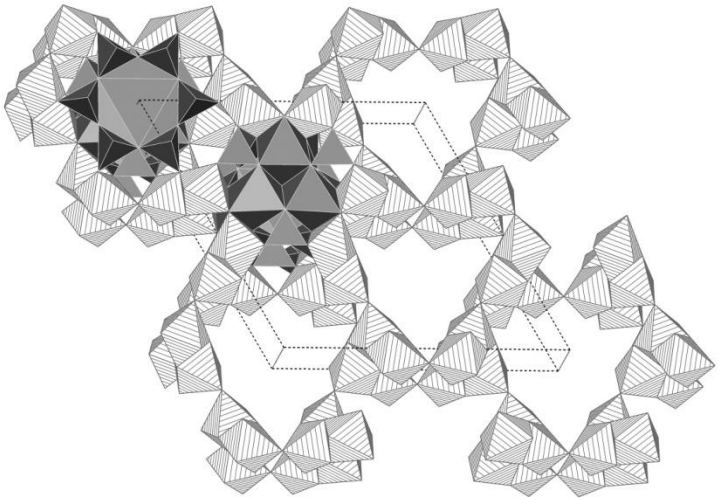

Figure 1.1B. The crystal structure of a rhombohedral R3m tourmaline projected onto (001). Dark-gray polyhedra represent structural islands. Stripe-filled octahedra coordinate the *Z* site. Dashed-line represents the unit cell (from Bosi 2018).

1.3 Morphological crystallography and habits

Tourmaline is typically euhedral and shows a variety of forms (Goldschmidt, 1922). Crystals are predominantly prismatic, varying from tabular to elongated in the fastest growth direction (**c**-axis) (Fig. 1.2), but in some cases, they can show a fibrous/acicular texture at the crystal termination, which can be particularly spectacular when accompanied by a color change (Lussier et al., 2008) (Fig. 1.3). A characteristic feature for the tourmaline identification in hand specimen is the presence of striation parallel to [0001] along the prismatic faces (Hawthorne and Dirlam, 2011).

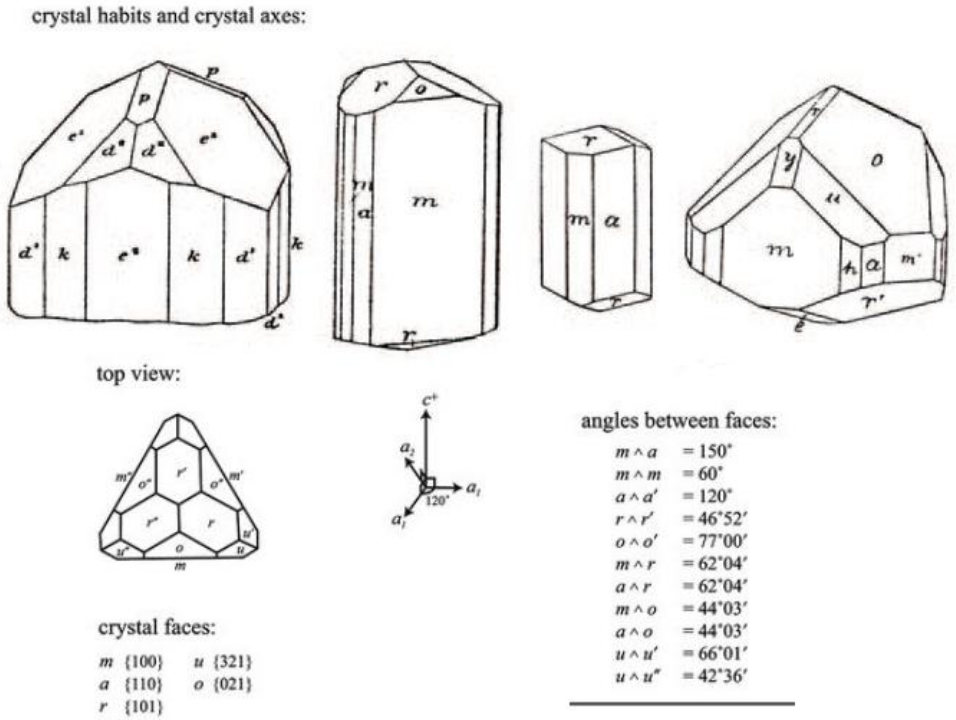

Figure 1.2. Typical morphological forms of tourmaline (modified from Goldschmidt 1922).

Figure 1.3. Tourmaline crystal with a thick black overgrowth composed by an arrangements of needles. Crystal size 15 mm (from F. Pezzotta collection).

When doubly terminated, tourmaline crystals usually exhibit a hemimorphic character. This means that they show different pyramidal faces and forms at the opposite ends along the **c**-axis. These morphological differences are very useful in the identification of the +**c** and –**c** poles. The antilogous pole of the crystal (the end that occurs along the +**c** axis), exhibits steeper pyramidal faces and a lustrous pedion face (0001), whereas the analogous pole (the end that occurs along the -**c** axis), is characterized by less steep pyramidal faces and the pedion has a rather matt luster (Henry and Dutrow, 1996). The hemimorphic feature of the tourmaline crystal, is the result of its asymmetric nature, due to the fact that all apices of the TO_4 tetrahedra point toward the analogous (-**c**-end) pole. A further consequence of its non-centrosimmetric nature is that tourmaline is strongly polar. Such asymmetric polar character results in pyroelectric and piezoelectric responses to changing in temperature and pressure. When heated, the antilogous (+**c**) pole of the crystal develops a negative charge and the analogous (-**c**) pole a positive one. Application of pressure to the crystal along the **c**-axis will cause the antilogous pole (+**c**) to develop a positive charge and the analogous (-**c**) pole to develop a negative charge (Barton, 1969; Dietrich, 1985).

1.4 Tourmaline as a petrogenetic indicator

The importance of tourmaline as an efficient geological tool for investigating *P*–*T*–*X* conditions in all crustal settings within the Earth was recognized in the early- and mid-20th century. This is the consequence of new and improved instrumentation available for tourmaline investigation and the understanding on tourmaline's nature and its utility as an excellent petrogenetic indicator (Henry and Dutrow, 1996; Dutrow and Henry, 2018). In fact, due to its complex crystal structure, which allows incorporate several major as well as trace elements (Bosi, 2018), tourmaline is extremely able to register any chemical-physical variation of the crystallization environment during its growth. This is evidenced by the presence of typical color zoning along the crystal, which testifies a variation in the

chemical composition of fluids involved in tourmaline crystallization (Fig. 1.4).

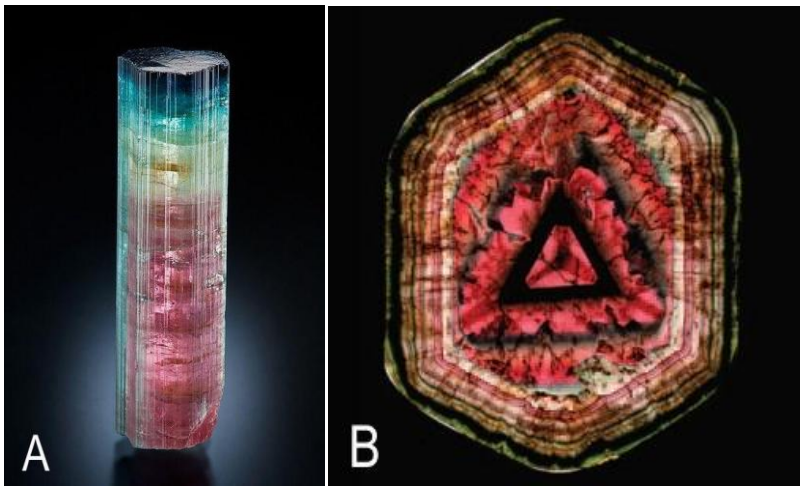

Figure 1.4. A) Tourmaline crystal with a bluish overgrowth at the analogous pole (Sapo Mine, Ferruginha, Conselheiro Pena, Doce valley, Minas Gerais, Brasile). Crystal size: 5 cm x 1.5 cm x 1.4 cm. B) A complexly zoned slice of fluor-liddicoatite cut parallel to (001), from Anjanabonoina, Madagascar. This slice measures approximately 10 cm in its longest dimension, and displays a trigonal star pattern and "aggregate-type" zoning. The outer region consists of fine-scale color zoning roughly parallel to the prism faces (from Dirlam et al. 2002).

This record can be preserved within the tourmaline crystal because of its extensive *P*–*T* stability range field, and the occurrence of an extensive short-range order, which may impose extremely slow diffusion rates of the chemical constituents in the structure (van Hinsberg et al., 2011a). As a result of the broad range in composition and the refractory behaviour, tourmaline is a very useful indicator of petrological and geochemical conditions in igneous, sedimentary, hydrothermal and metamorphosed systems, which can provide provide information about the formation and evolution of its complex crystals over time, acting like a "geologic DVD" (e.g., Dutrow and Henry, 2011, van Hinsberg et al., 2011a,b; Henry and Dutrow, 2012; Dutrow and Henry 2016).

1.5 Tourmaline: a kaleidoscopic gemstone

Owing to its compositional sensitivity to the environment in which it grows, tourmaline can display a wide range of appealing colors, from red-pink, through yellow, orange, green, blue, and violet, to brown and black, which in combination to durability and rarity, make it recognizable as one of the most important

gemstone on the market (e.g., Pezzotta and Laurs, 2011).

Colors in tourmaline are essentially related to transitions elements (Ti, V, Cr, Fe, Mn and Cu), acting as color-causing agents through several mechanisms at structural levels, with the most common ones being crystal field transitions (CFT), intervalence charge transfer interactions (IVCT), and color centres (e.g., Fritsch and Rossman,1987; Pezzotta and Laurs, 2011; Rossman, 2014). Most transition elements occupy the *Y* and *Z* edge-sharing octahedral sites (Hawthorne and Dirlam, 2011), and they influence color and color intensity typically through both CFT and IVCT. In absence of compositional data, tourmalines are generally distinguished by the use of a series of color-based trade names that are common in the marketplace (Table 1.3). The varietal names are *rubellite* (rose, dark pink, to red), *indicolite* (blue-green to blue), *canary tourmaline* (yellow, orange, to brown), *verdelite* (yellow-green to green), *chrome tourmaline* (vivid green), and *achroite* (colorless) (Zang and da Fonseca-Zang 2002). However, these trade names do not correlate to a specific tourmaline species. In fact, tourmaline crystals with a given color can develop in several species, and some individual species can develop many colors. For example, elbaite and fluor-elbaite, which represent most of the tourmaline gemstones, can display a nearly complete color spectrum (Table 1.3). Among the tourmaline varieties, the most desirable and precious colored gemstones in the market are those with bright blue to-green to-purplish hues, termed "*Paraiba-type*" (Fig. 1.5).

Figure 1.5. Cu-bearing gem tourmalines from Mozambique (1.28-3.03 ct) (from Laurs et al. 2008).

Table 1.3. List of tourmaline colors, varieties, causes of color and species[(a)].

Color	Varietal name	Cause of color	Tourmaline species
Colorless	*Achroite*	No or minor chromophores	Elbaite, fluor-elbaite, rossmanite, fluor-liddicoatite.
Pink and red	*Rubellite*	Mn^{3+} [(b)], Mn^{3+} + Fe or Mn^{2+}-Mn^{3+} IVCT Natural radiation	Elbaite, fluor-elbaite, rossmanite, fluor-liddicoatite, darrellhenryite.
Yellow, yellow-green, orange	*"Canary tourmaline"*	Mn^{2+} , Mn^{2+}-Ti^{4+} IVCT	Elbaite, fluor-elbaite, fluor-liddicoatite, tsilaisite, fluor-tsilaisite, dravite.
Green	*Verdelite*	Fe^{2+}, Fe^{3+}, Fe^{2+}-Ti^{4+} IVCT	Elbaite, fluor-elbaite, fluor-liddicoatite.
Green (deep)	*"Chrome tourmaline"*	V^{3+}, Cr^{3+}	Dravite–uvite.
Blue	*Indicolite*	Fe^{2+} or Fe^{2+}-Fe^{3+} IVCT, Fe^{2+}-Ti^{4+} IVCT	Elbaite, fluor-elbaite, fluor-liddicoatite, dravite, princivalleite.
Blue (neon)	*"Paraíba-type"*	Cu^{2+}	Elbaite, fluor-elbaite.
Brown	--	Fe^{2+}-Ti^{4+} IVCT, Mn^{2+}-Ti^{4+} IVCT	Elbaite, fluor-elbaite, dravite, oxy-dravite, fluor-dravite, celleriite, dutrowite, bosiite.
Black	--	High concentrations of Fe^{2+}, Mn^{2+} and/or Ti^{4+}	Schorl, oxy-schorl, fluor-schorl, foitite, dravite, fluor-dravite, bosiite, lucchesiite, magnesio-lucchesiite.

(a) Compiled after Rossman and Mattson (1986), Mattson and Rossman (1987), Reinitz and Rossman (1988), Rossman (1997, 2014) and Pezzotta and Laurs (2011), Altieri et al. (2022a,b);

(b) Commonly associated with ionizing radiation.

The name 'Paraíba' derived from the Brazilian locality where this gemstone was first mined in the late 1980s (Koivula and Kammerling, 1989), becoming notorious for its highly saturated "neon" colors. Additional deposits to the Paraiba State were found in the neighbouring Rio Grande do Norte State during the 1990s (Shigley et al., 2001), and more were discovered in Nigeria from 2001 (Smith et al., 2001; Furuya and Furuya, 2007; Breeding et al., 2007). At present, the newest source of *Paraiba-type* tourmalines is the Mavuco area in the Alto Ligonha pegmatite district of Mozambique, which was first described in 2004 (e.g., Wentzell, 2004; Laurs et al., 2008). Although the blue to-green to-purplish colors of the Mozambique material are typically less saturated than those of its Brazilian counterpart, the lower price and greater availability have further enhanced this tourmaline's popularity.

The coloration of "*Paraíba-type*" tourmaline is mainly controlled by a combination of cationic concentrations and oxidation states of Cu and Mn (Fritsch et al., 1990; Rossman et al., 1991; Laurs et al. 2008). In particular, its blue (electric blue, neon blue, violet blue), bluish green to greenish blue color is mainly caused by the influence of Cu^{2+} in the crystal structure.

In general, gem tourmalines are found in a number of geologic settings, and their origin is mostly related to miarolitic cavities occurring in moderately to highly differentiated granitic pegmatites (e.g., Pezzotta, 2000,2021; Pezzotta and Laurs, 2011). Such miarolitic pegmatites are typically emplaced in the continental crust at moderate to shallow depth in a pressure range of 0.1–0.3 MPa. The ages of these gem tourmaline–bearing pegmatites are variable. Many of the largest and important commercial pegmatitic fields, including those in Brazil, Namibia, Afghanistan, Mozambique and Madagascar, are about 500–550 Ma and were formed during the latest stages of the tectonometamorphic Pan-African event involving the Gondwana supercontinent (e.g., Fritsch et al., 1990; De Vito et al., 2002; Laurs et al., 2008). However, some gem tourmaline–bearing pegmatites were formed more recently. For example, the tourmaline-bearing pegmatites of Elba

Island, Italy, were formed about 6.2 Ma ago (Dini et al. 2002).

Because of their high resistance to mechanical and chemical weathering, gem tourmaline can also accumulate in eluvial and alluvial deposits, such as those formed in Madagascar and Mozambique (Dirlam, et al., 2002; Laurs et al., 2008).

2. AIM OF THE PROJECT

The goal of this Ph.D project is the definition of a model aimed at reconstructs the genesis of gem-quality tourmalines characterized by dark-colored overgrowths, which occur as color anomalies at the termination of the crystals and/or along the prism faces. Since tourmaline is an excellent petrogenetic indicator, the origin and chemical composition of fluids involved in tourmaline crystallization, responsible for the color anomalies, have also been investigated. To achieve this goal, selected gem tourmaline crystals with dark overgrowths of different colors and textural features from miarolitic cavities occurring in Elba Island pegmatitic veins (San Piero and Sant'Ilario in Campo locality, eastern border of Monte Capanne pluton, Italy) were used as a case study. Microchemical, structural and spectroscopic investigations were applied as experimental approach. This study was further extended to tourmaline samples collected from the Alto Ligonha pegmatite district (Nampula Province, NE Mozambique).

Among the most renowned gem-quality tourmalines for the combination of color and rarity, are those from the secondary deposit of Mavuco in the Alto Ligonha pegmatite district. These features make them unique from a gemological viewpoint and therefore with a high commercial value, limiting the information regarding their crystal-chemical characteristics. Moreover, although such tourmalines contain Cu, the source of these minerals is not yet attributable to known pegmatites nearby the Mavuco alluvial deposit as they resulted Cu-free, also with a Li- and B-poor composition. To solve the issue about their potential origin, in this research project a comparison study between data obtained from selected tourmaline crystals from a recently discovered primary deposit, the so-called "Marina" pegmatite, and those from Cu-bearing tourmalines occurring in the secondary deposit of Mavuco, was conducted. This will allow establishing whether the exploitation of this new mining field might be economically advantageous.

3. ELBA ISLAND – Crystal-chemical study of pegmatitic gem tourmaline crystals from Elba Island (Tyrrhenian Sea, Italy) characterized by dark-colored overgrowths at the termination

3.1 Introduction

Elba gem tourmalines are renowned by mineral connoisseurs from all world localities for the delicate pastel colors and the perfection of their crystal shapes in small size. Characteristic for these tourmalines is their dark-colored termination frequently occurring at the analogous pole that is typically rich in Fe and/or Mn. Such unusual termination, which is made up by multiple thin growth sectors of blackish, brownish, purplish-to-reddish, or even bluish colors, can be defined color anomaly as it occurs darker on pale crystals.

Tourmaline crystals are excellent petrogenetic indicators due to the ability to register chemical-physical variations of the crystallization environment during their growth. Consequently, dark-colored terminations likely reflect processes that occurred in tourmaline-rich pegmatites during the latest stages of crystallization. However, the detailed events that led to the availability of Fe and/or Mn in the pocket environment resulting in the growth of late-stage tourmalines remained unclear. For this purpose, selected gem tourmaline crystals from different miarolitic Li-bearing aplite-pegmatite veins located in the eastern border of Monte Capanne monzogranite pluton were studied. All the selected tourmalines are characterized by a dark-colored overgrowth at the termination with different colorations and textures. Chemical and spectroscopic investigations were applied as experimental approach in order to describe the crystal-chemical characteristics of the zones characterized by such color anomalies. This information, along with microstructural and paragenetic observations of the cavities in which the studied tourmaline samples were collected, were used to propose a general genetic model for the color anomalies observed at the termination of Elba gem tourmaline crystals.

3.2 Geological setting

3.2.1 Stratigraphical and structural frame of Elba Island

Elba Island is located in the Northern Tyrrhenian Sea at midway between Tuscany (Northern Apennines Chain) and Corsica (Alpine Corsica structural pile). Due to its structural complexity, Elba Island was studied by many researchers who have provided different interpretations of its geology (Bortolotti et al., 2001). The starting point for all the geological studies on the central and eastern part of Elba Island is represented by the subdivision into five tectono-stratigraphic units, named "Complexes", proposed by Trevisan (1950) (Fig. 3.1).

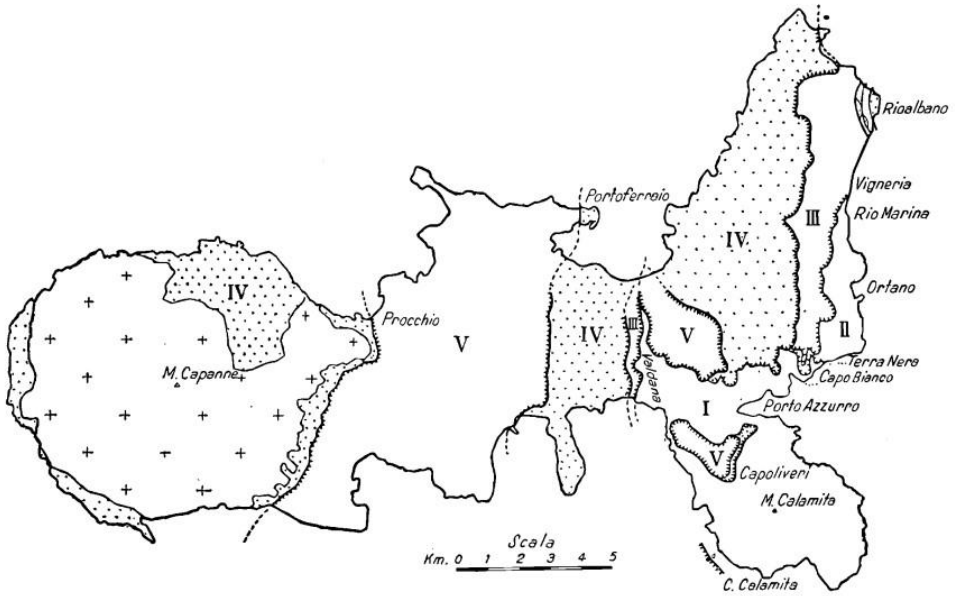

Figure 3.1. Geological sketch of Elba Island with the distribution of the five complexes. I. Calamita gneiss; II. Schists; III. La Spezia Nappe; IV. Radiolarites and ophiolite Nappe; V. Marls and porphyritic tertiary granites (from Trevisan 1950).

During the last twenty years, the tectono-stratigraphic frame of Elba Island was significantly improved. Bortolotti et al. (2001) elaborated a more complex tectono-stratigraphical model in which the five Complexes of Trevisan (1950) were re-interpreted and re-named. Specifically, Bortolotti et al. (2001) recognized nine tectonic units from the base upward: 1- Porto Azzurro Unit (PU); 2- Ortano Unit (UO); 3- Acquadolce Unit (AU); 4- Monticiano-Roccastrada Unit (MU); 5- Tuscan Nappe Unit (TN); 6- Gràssera Unit (GU); 7- Ophiolitic Unit (OU); 8- Paleogene Flysch Unit (EU); 9- Cretaceous Flysch Unit (CU) (Fig. 3.2 A,B).

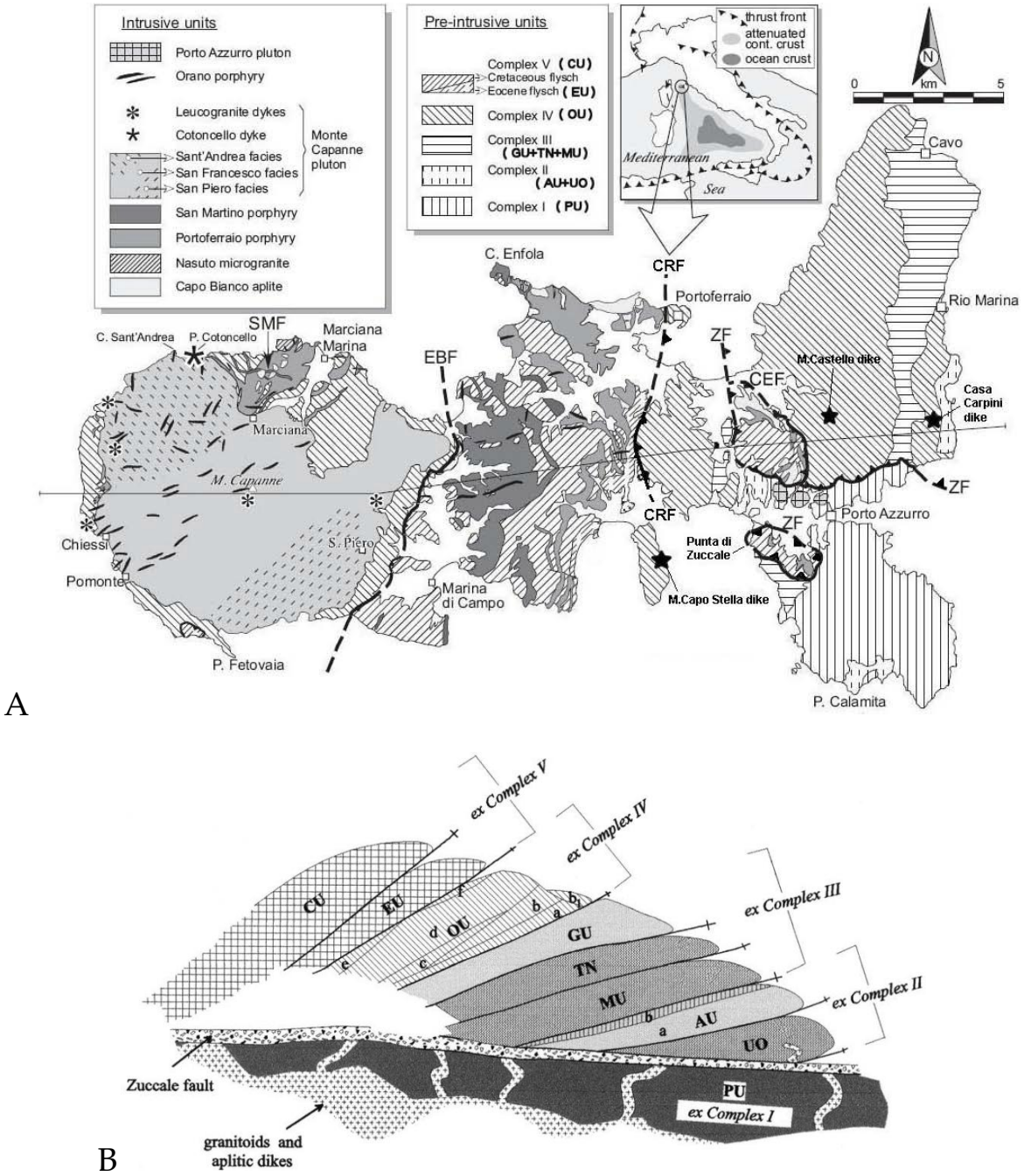

Figure 3.2. A) Schematic structural and magmatic map of the Elba Island with the Trevisan's Complexes and the corresponding Units of Bortolotti et al., 2001 (Dini et al., 2002); EBF, Eastern Border fault; CEF, Central Elba fault; ZF, Zuccale fault; CRF, Colle Reciso fault. B) The central and eastern Elba tectonic pile. **PU**- Porto Azzurro Unit; **UO**- Ortano Unit; **AU**- Acquadolce Unit (a. Porticciolo Subunit, b- Santa Filomena S.); **MU**- Monticiano-Roccastrada Unit; **TN**- Tuscan Nappe; **GU**- Gràssera Unit; **OU**- Ophiolitic Unit (a- Acquaviva Subunit; b- Mt. Serra S.; b1- Capo Vita S.; c- Sassi Turchini S.; d- Volterraio S.; e- Magazzini S.; f- Bagnaia S.); **EU**- Paleogene Flysch Unit; **CU**- Cretaceous Flysch Unit (from Bortolotti et al. 2001).

The units 1, 2, 4 and 5 belong to the Tuscan Domain, the others belong to the Ligurian Domain (3 and 6 are Ligurian-Piedmontese units). Before their final emplacement in the tectonic pile of Elba during the 8.5 to 5.4 Ma time interval, some of these units were intruded by two acidic plutons (Monte Capanne and La Serra-Porto Azzurro monzogranites), and by dikes of variable composition.

A brief description of the nine tectonic units, from bottom upward, which characterize the structural setting of central and eastern Elba Island, is reported below:

1- Porto Azzurro Unit (PU) – Complex I. It is made up of phyllites, quartzites and micaschists of the Monte Calamita Fm., likely of Paleozoic age. This unit represents the Tuscan basement, and probably includes Cambro-Ordovician and Carboniferous-Permian formations (Puxeddu et al., 1984; Garfagnoli et al., 2005). It shows a strong static recrystallization due to the La Serra-Porto Azzurro intrusion and the related aplitic dike network (6.0-5.4 Ma). On top of the Monte Calamita Fm., crystalline dolostones and dolomitic marbles were recognized and were attributed to its Mesozoic cover. A low-angle fault associated with 10 m thick cataclastic horizon (Zuccale Detachment Fault) constitutes the contact with all the overlying tectonic units described below (e.g. Bortolotti et al., 2001).

2- Ortano Unit (UO) – Complex II *pro parte*. It is composed of thermally metamorphosed rocks, such as metavolcanites and quartzitic-phyllites metasediments (Capo d'Arco schists), which can be correlated to the Early Paleozoic basement of the Apuan Alps and Central Sardinia (Pandeli and Puxeddu, 1990). In details, the top of the Unit consists of porphyroids and porphyritic schists, which grade upward to phyllites and quartzitic metasandstones and metaconglomerates. A few and thin aplitic dykes were recognized in this Unit, and most of them occur along the coast between Capo d'Arco and Ortano Valley.

3- Acquadolce Unit (AU) – Complex II *pro parte*. It includes massive marbles (partly dolomitic), grading upwards into calcschists and, finally, into phyllites,

metasiltstones and metasandstones with intercalations of calcschists which contain fossils of Early Cretaceous age. At its top, a serpentinite sheet crops. Locally, the carbonate lithotypes are transformed into Fe-skarn bodies (e.g. Torre di Rio skarn). The Unit was attributed to the Ligurian Domain (Ligurian-Piedmontese Units).

4- Monticiano-Roccastrada Unit (MU) – Complex III *pro parte*. This Tuscan Unit largely consists of Upper Carboniferous-Triassic metasiliciclastic rocks (the Permian-Carboniferous Rio Marina Fm. and the Triassic "Verrucano" Group). It also includes a Jurassic to Oligocene epimetamorphic succession (from the Capo Castello Calcschists to the Pseudomacigno), which crops out along the coast between Capo Pero and Capo Castello, and in the Valle Giove mining area (e.g. Bortolotti et al., 2001).

5- Tuscan Nappe Unit (TN) – Complex III *pro parte*. This Unit outocrops in the Porto Azzurro-Rio Marina, and Norsi-La Valdana areas. It is composed only of calcareous-dolomitic, at times vacuolar, breccias (the so-called "Calcare Cavernoso"), while northwards these rocks are overlain by Upper Triassic to Hettangian shallow marine carbonates (Rhaetavicula Limestone and Calcare Massiccio Fm), and Middle-Late Lias to Dogger carbonatic-cherty (Limano and "Rosso Ammonitico" Fm) and Posidonia pelagic sediments.

6- Gràssera Unit (GU) – Complex III *pro parte*. It mostly consists of varicolored slates and siltstones with rare manganiferous, recrystallized siliceous and calcareous beds (e.g. Bortolotti et al., 2001). Its lithofacies are different from those of all the formations of both Tuscan and Ligurian Domains. Moreover, they show a slight metamorphism, completely lacking in the Tuscan Nappe and in Ligurian formations at its base and the top, respectively. This Unit lies in tectonic unconformity on different terrains of the Tuscan Nappe. Because of its peculiar lithologic association and metamorphic overprint, it is considered a Ligurian-Piedmontese Unit (Bortolotti et al. 2001) as the "**AU"**.

7- Ophiolitic Unit (OU) – Complex IV. This Ligurian Unit is composed of seven tectonic subunits (Acquaviva "**ASU**", Monte Serra "**SSU**", Capo Vita "**CSU**", Sassi

Turchini "**TSU**", Volterraio "**VSU**", Magazzini "**MSU**" and Bagnaia "**BSU**"), which are characterized by ophiolites of the oceanic basement of the Western Tethys (serpentinites and Mg-gabbros) on which a Jurassic to Lower Cretaceous volcanic (basalts) and sedimentary (Monte Alpe cherts, Nisportino Fm., Calpionella limestones and Palombini shales) cover is generally present. In details, the "**ASU**" is mainly composed of serpentinites (or ophicalcites) with rare, thin, cherty levels at their base; the "**SSU**" is made up of an ophicalcitised serpentinite level, whose contact with the volcanic cover is almost tectonised; the "**TSU**", "**VSU**", "**MSU**" and "**BSU**" are exclusively composed by serpentinised lherzolites and harzburgites (Bortolotti et al., 2001).

A shoshonitic dike (Monte Castello Dike: 5.8 Ma) fills two ENE-WSW-trending normal faults cutting **VSU** in the Porto Azzurro area. Some calc-alkaline dikes (Monte Capo Stella Dikes) were also identified in the Ligurian basalts along the western coast of Golfo Stella.

This Unit can be interpreted as a relic of a trapped oceanic crust originally near the Corsica European margin (Bortolotti et al., 2001).

8- Paleogene Flysch Unit (EU) – Complex V *pro parte*. it is represented by a shale to calcareous-marly succession wuth turbiditic calcilutites, sandstones and ophiolitic breccias of Eocenic age.

9- Cretaceous Flysch Unit (CU) – Complex V *pro parte*. It is a Ligurian oceanic succession. This second turbiditic Unit consists of a basal tectonised complex similar to "**OU**" (ophiolites, basalts and Jurassic-Cretaceous sedimentary cover sheets), and a sedimentary succession formed by Cretaceous Palombini shales and varicolored shales, which grade upwards into an arenaceous-conglomeratic (Ghiaieto Sandstones) and then to a calcareous-marly-arenaceous (Marina di Campo Fm.) flysch of Late Cretaceous Age (probably Campanian-Maastrictian). Similar to the "**EU"**, this unit is frequently intruded by locally thick Tortonian to Messinian aplitic and porphyritic dikes, sills and laccoliths, such as the 8.4 Ma Capo Bianco aplite, the 8 Ma Portoferraio porphyry, the 7.4 Ma San Martino

porphyry (e.g. Dini et al., 2002) that pre- date the ~ 6.9 Ma Monte Capanne monzogranite intrusion (e.g. Ferrara and Tonarini 1993; Dini et al. 2002). All the pre- Monte Capanne magmatic bodies are cut along the tectonic contact with the underlying "**OU**".

The structural setting of Elba is characterized, especially in the central and eastern part of the Island, by the presence of several low-angle tectonic surfaces (thrusts and detachments), which put in contact the different Units each other (Fig. 3.2 A). Most of them are low-angle normal faults linked to extensional tectonics (e.g. the Zuccale fault and the related cataclastite put in contact the Units 2-9 with the Porto Azzurro Unit "PU"; other minor low-angle detachments are represented by "**TN**"/"**MU**": Tuscan Nappe Unit on Monticiano-Roccastrada Unit; "**CU**"/"**OU**": Cretaceous Flysch Unit on Ophiolitic Unit; "**UO**"/"**PU**": Ortano Unit on Porto Azzurro Unit). The extensional tectonics probably began during Burdigalian-Langhian, and continued during Messinian-Pliocene times, accompanied by magmatic intrusions.

Other tectonic surfaces are thrusts ("**GU**"/"**TN**": Gràssera Unit on Tuscan Nappe Unit; "**CU**"/"**EU**": Cretaceous Flysch Unit on Paleogene Flysch Unit) of Late Eocene-Early Miocene age. Low angle tectonic surfaces are of complex interpretation because they derived from the superposition of tectonic events which occurred in different times and/or in different tectonic regimes.

The western part of Elba Island is dominated by the Monte Capanne monzogranite pluton and its thermometamorphic aureole (Fig. 3.2 A). The thermometamoprhic aureole of Monte Capanne, which is tectonically separated from the flysh units (Complex V) of central Elba by the Eastern Border fault, is made up by a recrystallized ophiolitic sequences (ophiolites and volcano-sedimentary cover) intruded by the pre- Monte Capanne dykes and laccoliths (e.g. Capo Bianco aplite and Portoferraio porphyry). This meta-ophiolitic succession was related to the Ophiolitic Unit (Complex IV).

3.2.2 Tectonic evolution of Elba Island

The complex tectonic frame of Elba Island is the result of three main Alpine stages related to the collision of the Adria margin (Tosco-Umbria Domain) with Europe (Corsica). The study of the tectonic relationship between the nine tectonic units and between such tectonic units and the Messinian-Pliocene magmatic events, suggests the following geological scenario for the evolution of Elba Island (e.g. Bortolotti et al. 2001):

1) **Pre-intrusion extensional stages (> 8.5 Ma)**

The five tectono-metamorphic complexes of Elba Island suffered deformations as a result of the westward subduction of the Adria plate underneath the Corsica-Sardinia block of the Europe plate, leading to the formation of an accrectionary wedge where the deformation events piled up the Ligurian and Ligurian-Piedmont units on the Tuscan units. Such event of deformation and horizontal displacements began in the Late Cretaceous-Eocene (Fig. 3.3 A,B) and went on during the Late Eocene, Oligocene and Early-Middle Miocene (Fig. 3.3 C) (e.g., Carmignani and Kligfield, 1990). The beginning of the extensional phenomena in the Tyrrhenian area corresponds to the opening of the Corsica Basin during the Late Burdigalian-Langhian (e.g. Bartole, 1995). This led to the exhumation of Elba tectonic building through low angle normal faults, which dismembered and juxtaposed the central and Eastern units of different structural levels, with the consequent collapse of the accretionary wedge in the Early Messinian (Fig. 3.3 D). Such stages are recorded by: a) relics of the pre-Alpine schistosity within "**PU**" and "**UO**" , which can be attributed to the Sudetic phase of the Variscan orogeny; b) folding and thrusting of "**OU**", "**EU**" and "**CU**", with production of ophiolitic-carbonate breccias within "**PU**", and the tectono-metamorphic folding in "**AU**", related to Eocene intra-oceanic deformation events; c) main deformation and metamorphic events of Tuscan ("**PU**", "**UO**", "**MU**") and Ligurian-Piedmontese Units, overthrusting of the oceanic units ("**AU**", "**OU**", "**GU**", "**EU**"+"**CU**") onto the Tuscan ones, and a later refolding of the tectonic units, probably related to the

Oligocene-Early Miocene collisional events; d) emplacement of "**AU**" between "**OU**" and "**MU**", and of "**TN**" onto "**MU**". The superposition of "**TN**" onto "**MU**" can be considered the older extensional event by low-angle detachments (Middle Miocene).

A

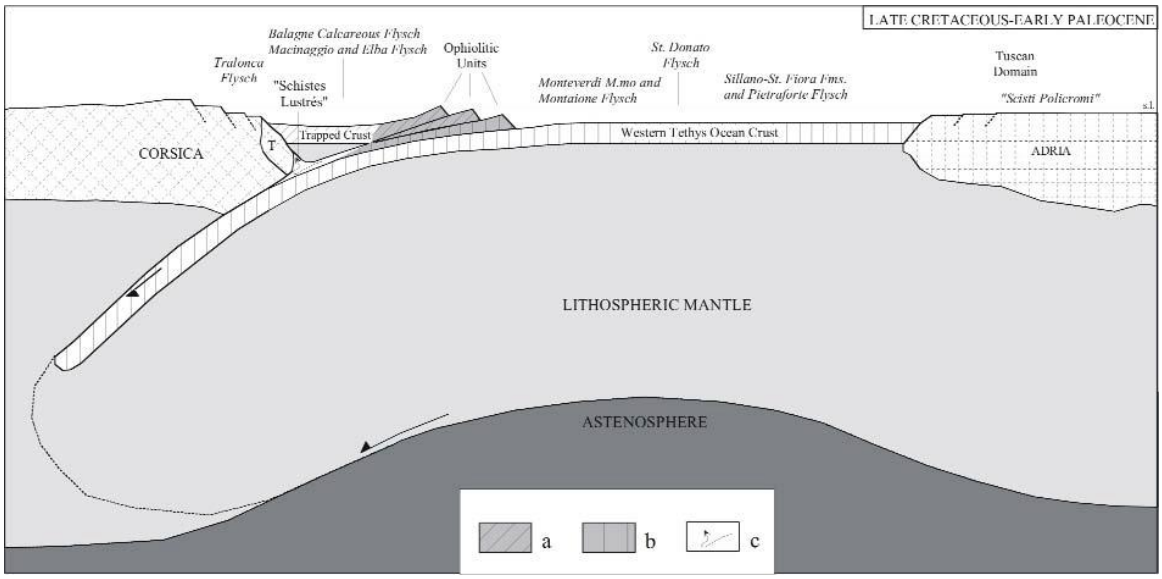

B

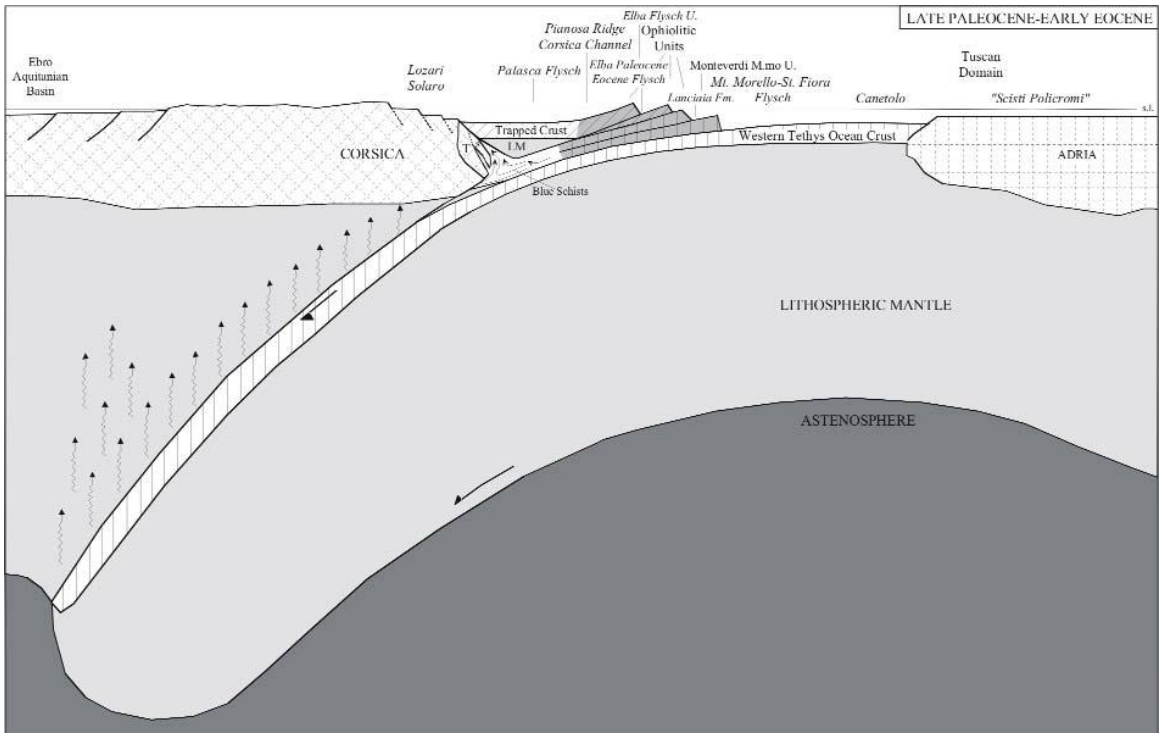

C

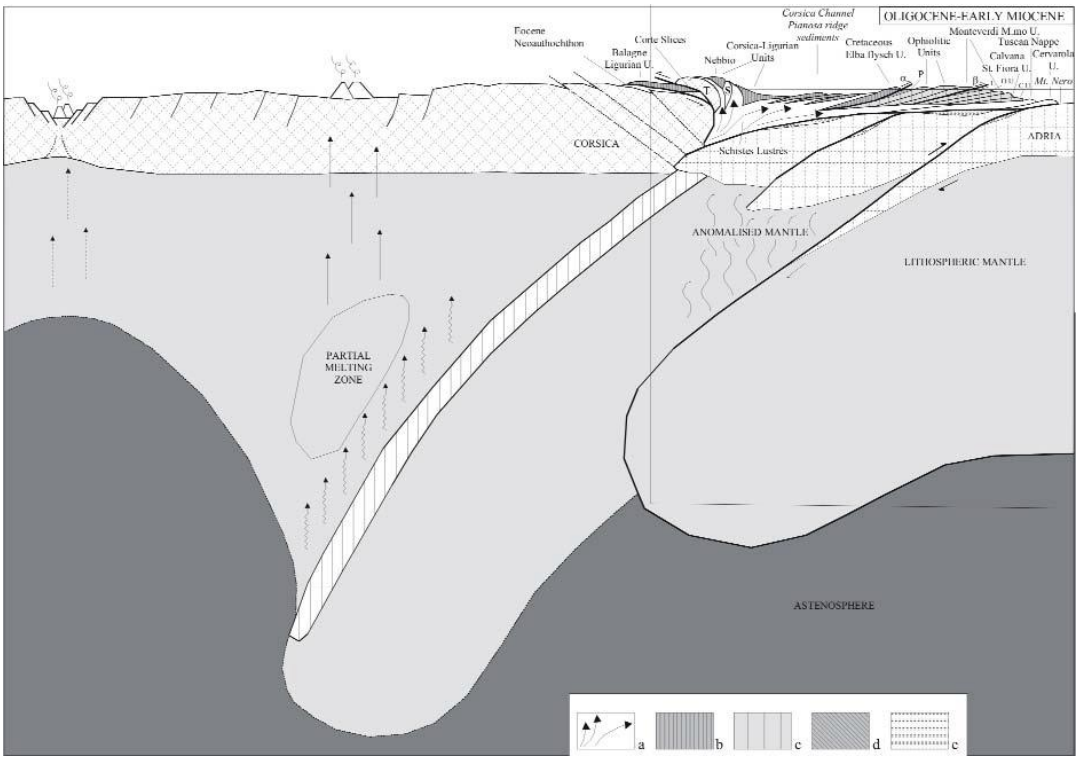
OLIGOCENE-EARLY MIOCENE
Corsica Channel
Pianosa ridge
sediments
Eocene
Neoauthochthon
Corte Slices
Balagne
Ligurian U.
Nebbio
Corsica-Ligurian
Units
Cretaceous
Elba flysch U.
Ophiolitic
Units
Monteverdi M.mo U.
Tuscan Nappe
Calvana
Cervarola
St. Fiora U.
U.
Mt. Nero
CORSICA
ADRIA
Schistes Lustrés
ANOMALISED MANTLE
LITHOSPHERIC MANTLE
PARTIAL
MELTING
ZONE
ASTENOSPHERE
a
b
c
d
e

D

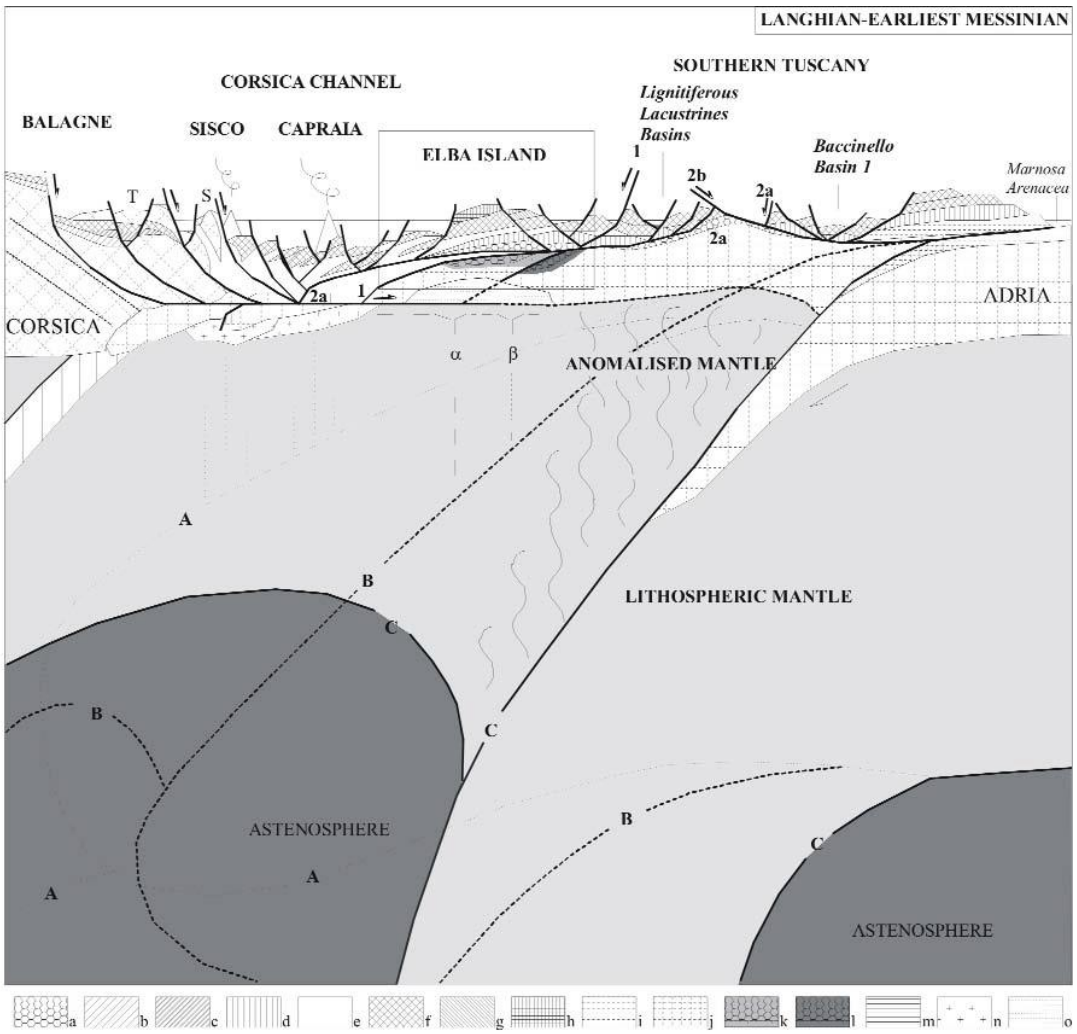
LANGHIAN-EARLIEST MESSINIAN
CORSICA CHANNEL
SOUTHERN TUSCANY
Lignitiferous
Lacustrines
Basins
BALAGNE
SISCO
CAPRAIA
ELBA ISLAND
Baccinello
Basin 1
Marnosa
Arenacea
T
S
1
2b
2a
CORSICA
ADRIA
α
β
ANOMALISED MANTLE
A
B
C
LITHOSPHERIC MANTLE
ASTENOSPHERE
a
b
c
d
e
f
g
h
i
j
k
l
m
n
o

Figure 3.3 A) Schematic cross-section of theorogenic system Corsica-Northern Apennines during Late Cretaceous-Early Paleocene times. **T**- Tenda Massif; **a**- Upper portion of the accretionary wedge (AW) formed by trapper crust material; **b**- Lower portion of AW formed by ocean crust; **c**- Upwards flow of the deepest portions of AW. For explanation, see text. Italic types are used for the formations during their deposition, normal types for the accreted units; the thickness of sediments and tectonic units is exaggerated.
B) Schematic cross-section of the orogenic system Corsica-Northern Apennines during Late Paleocene-Early Eocene times. **T**- Tenda Massif; **S**- Serra di Pigno slice; **zigzag arrows**- Path of the hydrating fluids rising from the subducting slab.
C) Schematic section of the orogenic system Corsica-Northern Apennines during Oligocene-Early Miocene times. **a**- "Schistes Lustrés" and calcschists with ophiolites (ductile metamorphic rocks of the deep portion of AW: AU and GU in Central and Eastern Elba) and their exhumation (upwards and eastwards) trajectories; **b**- Corsica Ligurides and Internal Ligurides; **c**- External Ligurides and epi-Ligurides; **d**- metamorphic Tuscan unit. **Vertical arrows**- feeders of the calc-alkaline offshore magmatism of Sardinia and Western Corsica. Vertical hatched arrows-feeders of the tholeiitic magmatism linked to the opening of the Ligurian-Balearic basin. Probable out-of-sequence thrusts: a- Cretaceous Elba flysch onto Paleogene Elba flysch; b- Monteverdi Marittimo unit (internal portion) onto the Lanciaia fm. The area outlined is shown in D.
D) Schematic section of the orogenic system Corsica-Elba-Northern Apennines during Langhian-earliest Messinian times. **a**- Tuscan metamorphic units; **b**- Corsica Middle Eocene neoautochthon; **c**- Corte slices; **d**- Tuscan Nappe; **e**- "Schistes Lustrés" and calcschists with ophiolites; **f**- Ligurids; **g**- Elba Paleogene flysch unit; **h**- Elba Cretaceous flysch unit; **i**- non metamorphic Cervarola and Umbria units; **j**- Adriatic metamorphic basement s.l.; **k**- internal Tuscan metamorphic basement (Ortano unit –UO- in the Elba Island); **l**- external Tuscan metamorphic basement (Porto Azzurro unit –PU- in the Elba Island); **m**- Neogene lacustrine deposits; nunderplating magmatic bodies; **o**- anatectic zone beneath Elba Island. **1** and **2a**- progressive west-vergent master detachment faults; **2b**- east-vergent master detachment fault. **A, B, C**- successive boundaries between the subducting slab and the lithospheric and asthenospheric mantle, due to the eastwards shifting of the subduction zone. Hatched linesfeeders of the supra-subduction magmatism (a- of the Monte Capanne and b- of the La Serra-Porto Azzurro plutons). **T**- Tenda Massif. **S**- Serra di Pigno slice. (from Pandeli et al. 2013).

2) Syn- intrusion stages

This stage begins with the genesis and rise of anatectic melts due to the uplift of the asthenospheric mantle, within the stretched inner part of the Apenninic orogenic belt. The normal faulting allowed the emplacement and uplift of the Messinian main intrusive bodies, such as the Monte Capanne and La Serra-Porto Azzurro monzogranites.

During the uprise of the Monte Capanne granitoid (6.8 Ma), most of its cover that was constituted by "**EU**" and "**CU**" (already injected by acidic dikes), was

thermometamorposed, and then detached and shifted eastwards along a low-angle fault, the Central Elba Fault "CEF", which was formed almost simultaneously the uplift of the Monte Capanne pluton (e.g., Westerman et al., 2004). During this event, the acidic dikes of the basal part of the flysch were sericitised (6.7 Ma). Farther east, a shoshonitic dike intruded "**OU**" at 5.8 Ma and, possibly, lamprophyric dikes were emplaced within "**AU**".

A new uplift of the Monte Capanne caused a further glide eastwards of "**EU**"+"**CU**" onto "**OU**" in the central Elba, and the development of transfer faults (as lateral ramps of detachments) within the Ligurian Units and, probably, the onset of the Zuccale Fault.

At 6.0-5.4 Ma the emplacement of the La Serra-Porto Azzurro granitoid produced a wide thermometamorphic aureola and local skarn bodies within the host "**PU**", "**UO**", "**AU**" and "**MU**". The uplift of this granitoid caused, or completed, the separation of the eastern and central Elba tectonic pile through the Zuccale detachment Fault. During this stage, the back-gliding of "**OU**" onto "**EU**"+"**CU**" in the Colle Reciso area, and the north- or north-eastwards gliding of "CSU", completed the present tectonic pile of central and eastern Elba.

3) **Post-intrusion stages (< 5.4 Ma)**

High-angle, N-S trending normal faults dismembered the orogenic pile and allowed the final circulation of idrothermal-mineralising fluids, with the formation of the hematite-rich ores of eastern Elba (~5.3 Ma) (Bortolotti et al. 2001) (Fig. 3.4).

The reconstruction of the tectonic evolution of Elba Island fits in the geodynamic context of the orogenic system Corsica-Northern Apennines, as shown by a series of tectonic sketches starting from the Late Cretaceous.

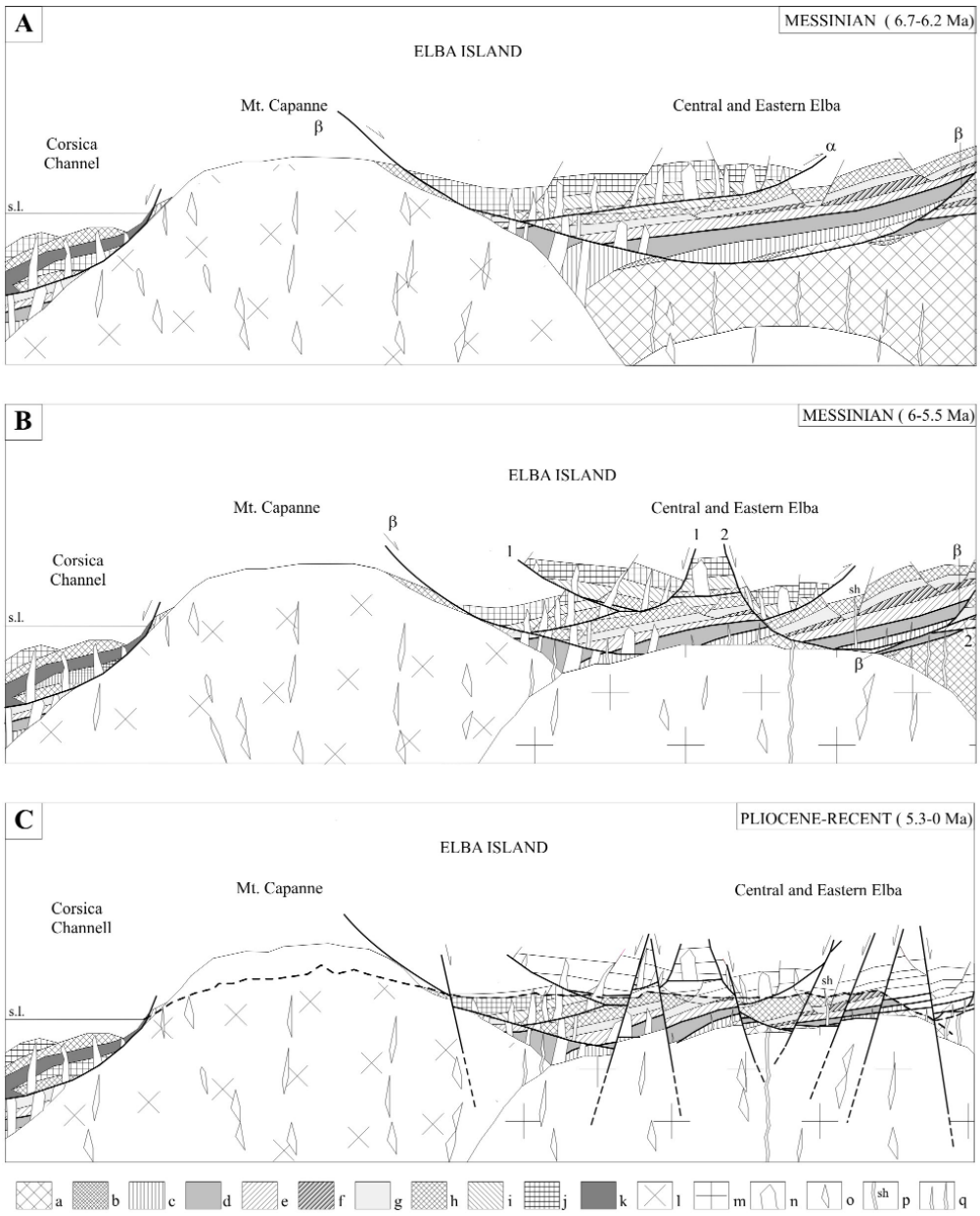

Figure 3.4 Schematic sections of the Elba Island from 6.7 to 0 Ma (uppermost Messinian to Present). **A-** Early Messinian (6.7-6.2 Ma). Early Messinian final uplift of the Monte Capanne pluton and the quasi-contemporaneous development of detachment faults (a-CEF 1 and b-CEF 2), producing westwards and eastwards delamination of the tectonic pile; **B-** Messinian (6-5.5 Ma). Final uplift of the La Serra - Porto Azzurro pluton and development of ZDFZuccale (2) and RDF- Colle Reciso (1) divergent delaminations; **C-** Late Messinian high angle normal faulting and the contemporaneous formation of the ore mineralisations. The sketched line represents the present W-E Monte Capanne-Monte Arco topographic section. **a**- Paleozoic successions of the Porto Azzurro unit; **b**- Mesozoic cover of the Porto Azzurro unit; **c**- Ortano unit; **d**- Acquadolce unit; **e**- Monticiano Roccastrada unit; **f**- Tuscan Nappe; **g**- Grassera unit; **h**- Ophiolitic unit; **i**- Paleogene flysch unit; **j**- Cretaceous flysch unit; **k**- "Schistes Lustrés" and calcschists with ophiolites; l- Monte Capanne pluton; **m**- La Serra-Porto Azzurro pluton; **n**- aplitic and porphyritic dykes within the Ligurids; **o**- acidic and basic dykes and enclaves in the plutonic bodies; **p**- shoshonitic dykes; **q**-aplitic and microgranitic dykes in the Porto Azzurro unit (from Pandeli et al. 2013).

3.2.3 The Mio-Pliocene magmatism in Elba Island

Elba Island is characterized by two monzogranitic plutons, along with their microgranites, aplite and pegmatite dyke swarms. Such intrusive bodies are the Monte Capanne (6.9 Ma) and La Serra- Porto Azzurro plutons (5.9 Ma), cropping out respectively in the western and eastern part of Elba (Fig. 3.2 A). Between the two, the Monte Capanne intrusion represents the main plutonic mass of Elba and post-dates the emplacement of a subvulcanic multilayer "Christmas-tree" laccolithic complex including three intrusive units that were emplaced between 8 and 7.4 Ma into the ophiolitic successions (Complex IV) and in the Cretaceous an Paleogene flysh units (Complex V) of central Elba (Fig. 3.5) (e.g., Dini et al., 2002).

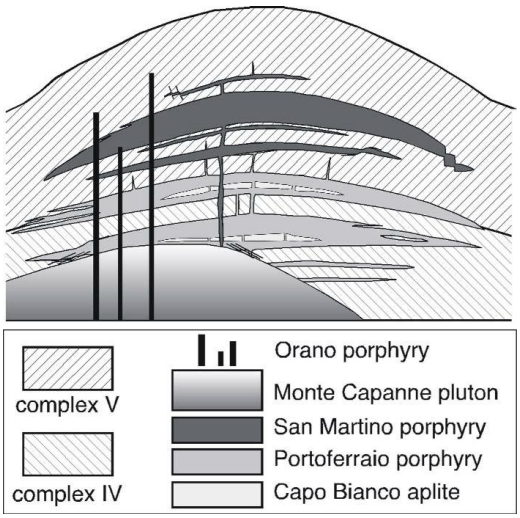

Figure 3.5. Sketch of the geometrical relationships between the magmatic bodies of central and western Elba Island at 6.8 Ma (after Dini et al. 2002).

The oldest intrusive units of such subvulcanic complex are represented by two sills of the Capo Bianco aplite and Nasuno microgranite (8-8.5 Ma). These rocks, are very-fine grained alkali feldspar granites with tiny phenocrysts of quartz, feldspars and muscovite locally showing concentrations of tourmaline in orbicules. The slightly younger intrusive unit is represented by the monzogranitic-syenogranitic Portoferraio porphyry (ca. 8 Ma), which consists of four main layers characterized by small phenocrysts of quartz, feldspars and biotite. Successively,

the monzogranitic San Martino porphyry (7.4 Ma) was emplaced as a multi-layer laccolith, which is characterized by a different mineralization consisting of abundant sanidine megacrysts and quartz, plagioclase, biotite phenocrysts.

After the emplacement of the San Martino porphyry layers, the multiple laccolith complex was then intruded at the base by the Monte Capanne monzogranite pluton (6.9 Ma) and its associated leucogranites. This pluton is a slightly peraluminous biotite monzogranite intrusion (Dini et al., 2002) formed by the downward stacking of multiple magma pulses that coalesced into a single intrusion (Farina et al., 2010). Three main facies characterize this pluton, where the first and the second are the most important. The first is represented by the Sant'Andrea facies, which is characterized by abundant large K-feldspar megacrysts and mafic enclaves. The second is the granodioritic-monzogranitic San Piero facies, typically quarried for its homogeneous texture almost free of large megacrysts and mafic enclaves. The third is represented by the San Francesco facies, which shows intermediate feature between the Sant'Andrea and the San Piero facies (e.g., Dini et al., 2002). The patchy distribution of the Sant'Andrea facies, mainly around the margin of the pluton, suggests that was emplaced first and was then disturbed by the arrival of the San Piero facies, which dominate the eastern border of the Monte Capanne pluton.

The acidic dykes of Monte Capanne occur mainly close to the pulton's contact, within both the pluton and its thermometamorphic aureole. These intrusions are essentially composed of leucogranites dykes/sills and aplite-pegmatite veins strike N-S and dip 30°-75° E. The leucogranites are interpreted as a series of fractionation products from a magma having similar characteristics to those of the San Piero facies. These rocks have a width ranging from few centimeters to up 20 meters and a medium grain size, containing quartz, K-feldspar, plagioclase, subordinate biotite and white mica, and locally abundant cordierite. Tourmaline, zircon, apatite, titanite, andalusite, sulphides and other opaque minerals, are accessory phases. A late circulation of magmatic fluids is responsible for the local alteration

of feldspars and Fe-Mg minerals.

The aplites occur commonly as thin (0.1 to 2 m) and short (up to a few meters) veins and dykes, cross-cutting the pluton, its thermometamorphic rocks and, in some places, the leucogranite dykes. They show a variable grain size, with rare patches of quartz-rich massive pegmatite. Their composition is characterized by quartz, K-feldspar, plagioclase, scarce biotite and/or white micas. Zircon, apatite and andalusite are rare accessory phases. A tourmaline-rich facies, with abundant subhedral to anhedral tourmaline crystals, is widespread. Such tourmaline-rich facies locally displays a strong alteration, with almost complete discoloration and/or chloritization of biotite, formation of iron hydroxides and kaolinization and sericitization of feldspars.

3.2.4 The miarolitic Li-bearing aplite-pegmatite dikes

The aplite-pegmatite dikes are distributed along the eastern contact of the Monte Capanne monzogranite pluton, in its peripheral parts and in the surrounding thermometamorphic rocks (Marinelli, 1959). In the eastern border of the pluton, they share the same NNE-SSW strike of the leucogranite sills, but unlike the sills, dip to the west at high angles (Pezzotta, 2000).

The best known occurrences are located near the villages of San Piero in Campo and Sant'Ilario in Campo (Fig. 3.6). The size of these dikes ranges from few centimeters up to 2 meters in width, and up to 20 meters along strike. Such aplite-pegmatite dikes are characterized by a lithium-cesium-tantalum (LCT) geochemical signature and, on a small scale, they share many major features with other important gem-bearing pegmatite districts around the world, such as the Pala and the Ramona districts in California, as well as in the Nuristan province of Afghanistan. Their age is estimated at 6.9 Ma (Dini et al., 2002), making them among the youngest known gem-bearing pegmatites in the world.

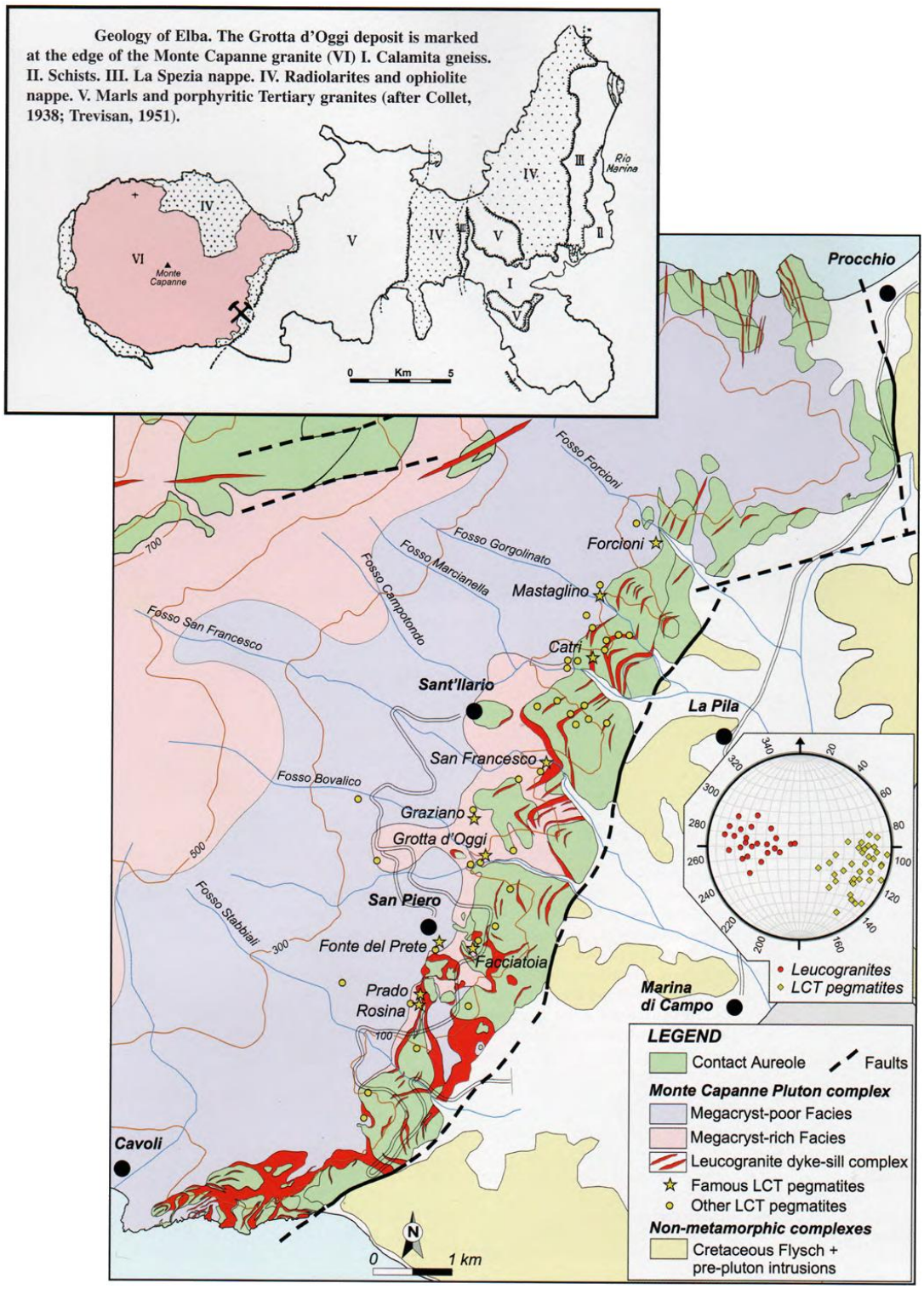

Figure 3.6. Geologic map of the eastern border on the Monte Capanne monzogranite pluton, showing the areas of occurrence of gem-bearing pegmatites (from Pezzotta 2021).

All of the productive tourmaline-bearing veins crop out in an area of less than 4 km^2, and are hosted in both the megacryst-rich and the megacryst-poor monzogranite facies as well as within the contact metamorphic rocks of the Monte Capanne pluton. Moreover, most of them contain miarolitic cavities lined with

quartz, feldspars and lepidolite, along with multicolored tourmaline crystals and several accessory minerals. In general, the mineralogy of the largest miarolitic cavities reflects the textural and mineralogical structure of the dikes. The footwall is mostly composed of albite and quartz of medium grain size, with abundant tourmaline and petalite. On the contrary, the hanging wall is mostly composed of perthitic K-feldspar, albite and quarz with a much coarser grain size, and scarce tourmaline and petalite (Pezzotta, 2021). In such pockets, two main stages of the paragenetic sequence were recognized: an "aplitic-pegmatitic" stage, consisting of K- feldspar, albite, quartz, tourmaline, beryl, lepidolite, petalite, pollucite and garnet, and a "hydrothermal stage" responsible for the crystallization of pink elbaite and calcite, and the alteration of K-feldspar into kaolinite.

Elba pegmatites were classified in four distinct groups by Pezzotta (2000) based on internal structures, textural patterns, rock-forming mineralogy, pocket paragenesis and degree of geochemical evolution: I) Dikes without Li minerals; II) Li-bearing dykes with complex asymmetric zoning; III) Li-bearing dykes with simple asymmetric zoning; IV) Irregularly zoned to unzoned Li-bearing dikes. The degree of geochemical fractionation increases from I to IV group. The less geochemically evolved dikes of the I group are mostly emplaced inside the granitoids of the pluton, and the most evolved ones of the IV group are all emplaced in the thermometamorphic rocks (metasediments and metaserpentinites) of the contact aureole.

The miarolic dikes of the group I are characterized by a lack of Li- and Cs-minerals and the presence of tourmaline crystals exclusively black in color. These intrusions are hosted in the monzogranite, are a few centimeters to 1 meter thick and 2 to 20 m long. They do not display significant textural or mineralogical zoning. In fact, they are mainly aplitic, with the pegmatitic portions dispersed as irregular veins. The main components of the aplitic rock are quartz, K-feldspar, plagioclase and biotite. Tourmaline occurs as primary, zoned, prismatic, euhedral crystals in aplite and pegmatite, and as radiating crystal groups and graphic intergrowths with

quartz, albitic plagioclase, and perthitic-graphic K-feldspar in pegmatite. A second generation of intergranular tourmaline is common. The mineralogy of the miarolitic cavities reflects the primitive nature of these pegmatites. Only tourmaline and, exceptionally, spessartine garnet are locally abundant. No significant hydrothermal process of mineral alteration is evidenced.

The miarolitic dikes belonging to the group II are characterized by Li-bearing minerals, and a complex three-dimensional asymmetric zonation. They are hosted in the pophyritic portion of the Monte Capanne monzogranite pluton, a few meters apart from the contact with the thermometamorphic rocks. Most of them are 6−10 m long showing a thickness of 1−2 m. The dip can range from 25° to 75°. The contacts along strike are generally sharp, and the termination consists of a fingering-out network of small veins. In some cases, thin anastomising aplitic apophyses can run continuously for several tens of meters.

This group concerns the famous pegmatitic veins of Rosina, San Silvestro, Grotta d'Oggi quarry, Fonte del Prete and La Speranza, located in the eastern border of Monte Capanne, near the village of San Piero in Campo. These pegmatitic veins display a marked variation in abundance, texture of the rock-forming minerals, distribution as well as composition of accessory minerals. The pocket paragenensis of the dikes ranges from primitive to highly evolved, hosting black to polychromatic tourmaline crystals. Moreover, thin radial fractures and phenomena of cavity collapse are evident around the larger pockets. The presence of altered cavity-lining and -coating minerals such as biotite, spessartine garnet and K-feldspar, suggests that some leaching processes occurred in the enclosing pegmatite.

The miarolitic dikes of the group III are characterized by the presence of Li-bearing minerals, but show a simple asymmetric zoning. These dikes are hosted in the porphyritic part of the Monte Capanne monzogranite pluton, close to the contact with the country-rocks, in the leucogranite dikes, as well as in the thermometamorphic mafic rock of the contact aureole. The dikes belonging to this

group, unlike those of group I and II, are small with a length of 6−8 m and rarely exceed the thickness of 25 cm. The pegmatitic dikes from the locality of Catri, Facciatoia, Masso Foresi, Fosso Gorgolinato and Fosso dei Forcioni, near the village of Sant'Ilario in Campo, belong to the group III. Miarolitic cavities are locally abundant, and the largest one (up to 120 x 80 x 25 cm) was observed at the dike intersections. Mineral assemblages and pocket paragenesis are comparable with that of the highly evolved pockets of the group II dykes above described. A remarkable mineral segregation is present in the cavities of the group III dykes, with most of the K-feldspar crystals confined to the roof, and most of the albite and of the tourmaline, the petalite and the pollucite confined at the base. Two fracturing events can be distinguished in such veins and cavities: a first one which is very limited and it is associated with the formation of a dark overgrowth at the termination of the tourmaline crystals; and a local, second, more dramatic one which is associated with a deep late-stage corrosion of feldspars and tourmaline, and occasionally even quartz (Orlandi and Pezzotta, 1996; Pezzotta, 2000).

The group IV miarolitic dikes contain Li-bearing minerals, are irregularly zoned to unzoned, and are characterized by a random distribution of accessory minerals. Such dikes are hosted in the hydrothermally altered mafic rocks and in the metasedimentary hornfels of the thermometamorphic aureole of the Monte Capanne pluton. Their thickness ranges from a few centimeters up to 2 meters and the length can attain 6-7 meters. The internal structure of these dikes vary from irregularly distributed masses of aplitic and pegmatitic rocks, with local concentrations of tourmalines and white to pink micas, to medium-grained rock with minerals homogeneously distributed. In the pegmatitic masses, tourmalines occur locally as radiating groups, as well as randomly oriented prismatic crystals. Tourmaline crystals are typically black in color, but occasionally are also present as polychromatic crystals with black to green and pink colors. White to pink micas are locally abundant, along with albite in aggregate crystals. Miarolitic cavities are rare, and absent in some dikes. The mineral paragenensis of such pockets is

simple: only small crystals of polychromatic tourmaline, white to pink micas, and occasionally pink apatite were found.

The pocket evolution is complex, especially in the large cavities of dikes of the II group, and includes pocket ruptures and hydrothermal stages. The structural, mineralogical, and paragenetic characteristics of the dikes of the III group and the central portion of those belonging to the II group, share many similarities with those reported in the literature for miarolitic, gem-bearing dikes from California and Afghanistan (Pezzotta, 2000; 2021).

3.3 CASE STUDY 1 - First crystal-chemical characterization and insights into the genesis of gem tourmaline crystals with blue-growth zones from the San Piero in Campo pegmatites, Elba Island (Tyrrhenian Sea, Italy)

3.3.1 Introduction

Gem-quality tourmalines from Elba Island are easily recognizable and distinguishable from those of all other world localities for the delicate pastel colors and the perfection of their crystal shape, even in small size. Specifically, the main features which make them unique are the pastel colors of the crystal prismatic section and an unusual dark colored termination at the analogous pole (the so-called "Moor's head" textural type), which is frequently black (Pezzotta, 2021). However, in some cases, the terminations of the tourmaline crystals are not black, but they are composed of multiple thin growth zones of greenish, brownish, purplish or even bluish colors (Pezzotta, 2021). The blue hues are the rarest and thus, the most scientifically fascinating colors among Elba Island tourmalines. During the last decades, the only Elba pegmatitic veins in which some tourmaline crystals with a blue growth zone at the termination were sampled, are those named San Silvestro and Fucili (Grotta d'Oggi quarry), located respectively a few hundred meters south and north of the San Piero in Campo village (Pezzotta, 2021) (Fig. 3.7).

Figure 3.7. Tourmaline crystal with a blue-growth zone on quartz, 18 mm in length. An historic specimen from the San Silvestro pegmatite (San Piero in Campo, Elba Island, Italy). Federico Pezzotta collection. Antonio Miglioli photo.

Tourmaline crystals with blue growth zones from Elba have always been sought after and appreciated by collectors from all over the world. Although their morphology was described in detail since the 19th century by mineralogists such as Giovanni D'Achiardi (D'Achiardi, 1894, 1897), their rarity and collectability have hindered studies concerning their crystal-chemical characteristics. In fact, few data are currently available on a detailed compositional or spectroscopic analysis. Moreover, a correlation study between ultraviolet-visible-near-infrared optical absorption spectra (UV-NIR) and local structural information obtained by Fourier-transform infrared spectroscopy (FTIR) as well as an in-depth study of the atomic mechanisms that regulate cause of color has never been done.

Elbaite crystals with a blue coloration were found in other locations. These include copper-bearing crystals from Paraiba State (Brazil), iron-bearing crystals from Pakistan and Usakos (Namibia), and blue cap tourmalines from the Tourmaline Queen Mine (Pala, San Diego County, California). OAS data of most of these samples can be found on the Caltech website (http://minerals.caltech.edu/files/visible/tourmaline).

This study characterizes two tourmaline crystals with a blue-growth zone at the analogous pole, respectively from the San Silvestro and the Fucili pegmatites, located in the eastern border of Monte Capanne monzogranite pluton (Fig. 3.8 A). San Silvestro and Fucili are LCT-type granitic pegmatites belonging to the II group of the Monte Capanne aplitic-pegmatitic veins classification system according to Pezzotta (2000) criteria. The San Silvestro pegmatite shows a complex and well-structured internal asymmetric zoning, which includes a well-defined aplitic-layered unit at the footwall. Fucili is composed by a swarm of narrow pegmatitic and aplitic veins, sub-parallel or locally intersecting each other at low angles, hosted in monzogranite. These pegmatites are frequently miarolitic, with cavities containing euhedral crystals of quartz, feldspar, lepidolite, gem tourmaline and several accessory minerals (Pezzotta, 2021).

This work represents the first detailed chemical and spectroscopic study on

tourmaline crystals with a blue-growth zone from Elba Island. Furthermore, because tourmaline is an excellent petrogenetic indicator, able to register the chemical-physical variations of the crystallization environment during its growth (e.g., Hawthorne and Dirlam, 2011), this study contributes to the understanding on the origin and chemical composition of fluids involved in tourmaline crystallization, which are responsible for the color changes at the analogous termination observed in Elba tourmaline crystals.

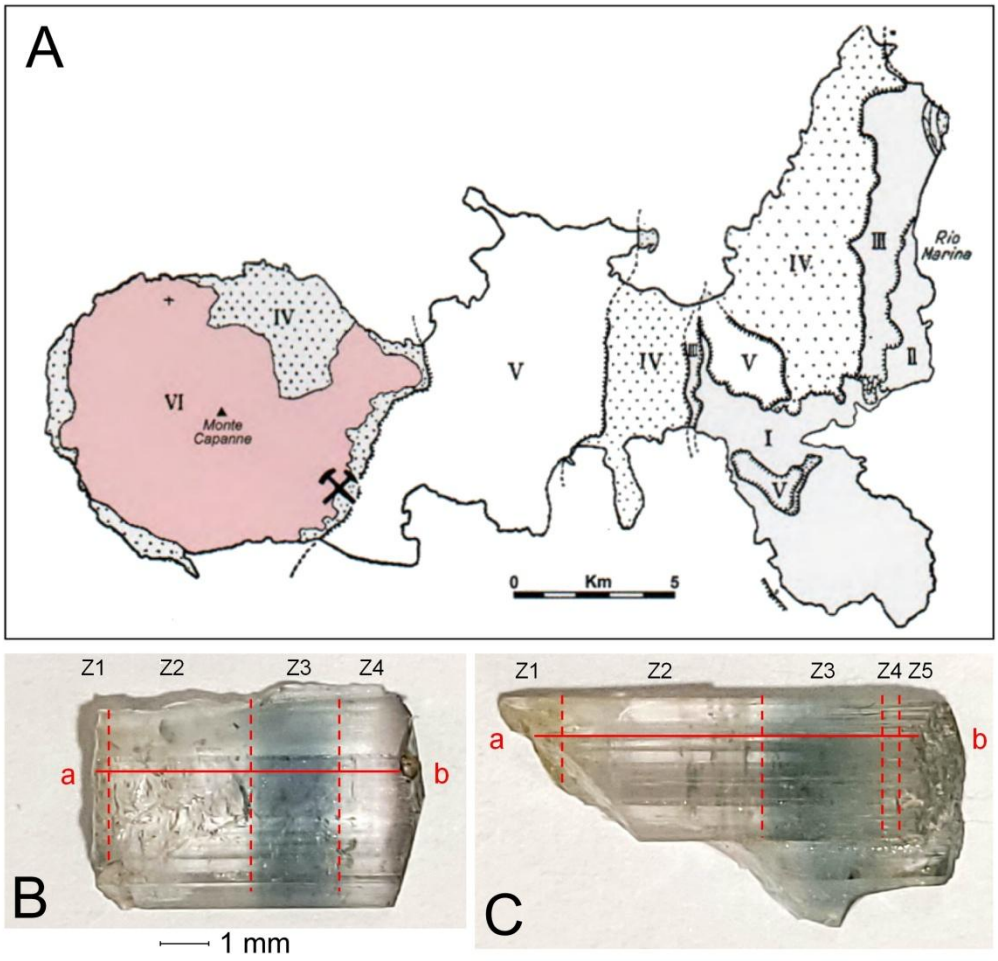

Figure 3.8. A) Geologic map of Elba Island. The occurrence area of the tourmaline samples investigated in this study is marked at the edge of the Monte Capanne granite (VI). B) Crystal from the Fucili pegmatite (Grotta d'Oggi quarry, north of San Piero in Campo, Elba Island, Italy), 9 mm in length. C) Crystal from the San Silvestro pegmatite (south of San Piero in Campo, Elba Island, Italy), 12 mm in length. Scale bar = 1 mm. The analyzed traverses (a-b) are represented by solid red lines, while the dashed red lines divide the crystal in the different zones labelled as Z1—Z4/Z5 based on colour/chemistry.

The results obtained from this study were published in *Mineralogical Magazine* (Altieri et al., 2022). In this paper, the candidate is the first author and the main responsible for the analytical work, data interpretation, figures and tables production and the manuscript draft.

3.3.2 Analytical Methods

Samples description and preparation

The two tourmaline samples, Fucili and San Silvestro (Fig. 3.8 B,C), are characterized by a blue-growth zone at the analogous pole, with a more intense greenish hue in the Fucili sample. An additional yellow-green colored zone is observable close to the base of both crystals; this zone is better defined in the San Silvestro crystal.

The samples were glued to a glass-slide using epoxy resin, with their length parallel to the surface of the slide. A slice of each crystal was cut along the fastest growth direction (crystallographic **c**-axis) and subsequently ground and polished to produce a flat surface with a uniform thickness of 500 μm for electron microprobe analysis (EMPA).

A section of the blue zone showing significant Fe contents by EMPA was cut from the Fucili sample using a thin-blade diamond wheel saw. Small amounts (1–2 mg) of the material were finely ground under acetone in an agate mortar, mixed with thermoplastic resin and then shaped to a millimetre-sized cylindrical absorber under mild heating for Mössbauer spectroscopy analysis.

For infrared and optical absorption spectroscopy analyses, samples were glued to a glass-slide using a thermoplastic resin and cut along the **c**-axis, as above described. Before analyses, tourmaline slices were further thinned to appropriate thickness and doubly polished (Fucili sample: 45 μm and 364 μm for infrared and optical absorption spectroscopy analyses, respectively; San Silvestro sample: 74 μm and 865 μm for infrared and optical absorption spectroscopy analyses, respectively).

Electron-microprobe analysis (EMPA)

Compositional data were collected along a straight traverse parallel to the **c**-axis from the base to the termination of each crystal with an average step size of 300 μm using a CAMECA SX50 electron-microprobe at the Istituto di Geologia Ambientale e Geoingegneria (CNR of Rome, Italy). A total of 24 and 37 spot analyses for Fucili and San Silvestro samples were obtained, respectively. EMP analyses were done operating in wavelength-dispersion mode with an accelerating potential of 15 kV, a sample current of 15 nA and a beam diameter of 10 μm. Minerals and synthetic compounds were used as primary standards: wollastonite (Si, Ca), magnetite (Fe), rutile (Ti), corundum (Al), karelianite (V), fluorphlogopite (F), periclase (Mg), jadeite (Na), orthoclase (K), rhodonite (Mn), metallic Cr, Cu and Zn. The PAP correction procedure for quantitative electron probe micro analysis was applied (Pouchou and Pichoir, 1991). Relative error on data was < 5% and detection limits < 0.03 wt%.

Mössbauer spectroscopy (MS)

The ^{57}Fe Mössbauer spectrum of the blue zone of the Fucili sample was acquired using a conventional spectrometer system equipped with a 10 mCi point source and operated in constant acceleration mode. The absorber was mounted on strip tape and positioned close (<1 mm) to the tip of the point source. Data were collected at room temperature over the velocity range ±4.2 mm/s and recorded in a multichannel analyzer with 1024 channels. The velocity was calibrated with an α-Fe foil. The obtained spectrum was fitted to Lorentzian line-shapes using the *MossA* fitting program (Prescher et al., 2012).

Optical absorption spectroscopy (OAS)

Polarised, room temperature optical absorption spectra of Fucili and San Silvestro yellow-green and blue zones in the range of 30000–11500 cm^{-1} were obtained at a spectral resolution of 1 nm on doubly polished sections, using an AVASPEC-ULS2048 × 16 spectrometer attached via a 400 μm ultraviolet (UV) optical fibre

cable to a Zeiss Axiotron UV-microscope. A 75 W Xenon arc lamp was used as light source and Zeiss Ultrafluar 10× lenses served as objective and condenser. An UV-quality Glan-Thompson prism, with a working range from 40000 to 3704 cm^{-1} was used as a polariser. Spectra data in the range 11500-5000 cm^{-1} were taken from the FTIR measurements. The colorless central region for both samples was also measured as reference spectra.

Fourier-transform infrared (FTIR) spectroscopy

Polarised Fourier-transform infrared spectra of Fucili and San Silvestro blue zones in the range 2000–13000 cm^{-1} were collected at a resolution of 4 cm^{-1} from the same sections studied by OAS spectroscopy but with a reduced thickness. Analyses were performed using a Bruker Vertex 70 spectrometer attached to a Hyperion 2000 microscope and equipped with a halogen-lamp source, a CaF_2 beam-splitter, a ZnSe wire-grid polariser and an InSb detector.

Determination of atomic fractions

The wt% of element oxides determined by EMPA was used to calculate the atomic fractions (apfu). The B^{3+} content was assumed to be stoichiometric (B = 3.00 atoms per formula unit, apfu). Lithium was calculated in accord with Pesquera et al. (2016). The (OH) content was calculated by charge balance with the assumption (T + Y + Z) = 15.00 apfu and 31 anions.

According to the MS results (see below), all Fe in the blue zone of Fucili sample is in the reduced state +2, within an estimated detection limit of 3%. Based on this result, all Mn was considered as Mn^{2+}. Concerning the San Silvestro sample, given the comparable chemical composition, the oxidation state of Fe and Mn were also assumed to be +2.

3.3.3 Results

Chemical composition

Chemical data along the **c**-axis in the direction of the analogous termination showed an heterogeneity in composition for selected elements (Fe and Mn) that can be correlated with color displayed. Other elements did not show appreciable variation along the **c**-axis, with the exception of fluorine and calcium. Vanadium, Cr, Cu and Mg were below detection limits. On the basis of the variation in chemical homogeneity and color displayed, each sample was divided in different zones: four for the Fucili and five for the San Silvestro sample. Figure 3.9 and Figure 3.10 display the pattern of selected elements (as wt% oxides) determined along the considered traverse. Tables 1 and 2 summarize the chemical compositions in wt% and apfu for each selected zone of Fucili and San Silvestro samples, respectively.

In both samples, the blue colored zone located at the upper part of the crystals is characterized by the highest amount of Fe (Z3, Fig. 3.9 and Fig. 3.10). In Fucili, FeO increases up to 1 wt% and then decreases to below detection at the colorless termination of the crystal (Z4, Fig. 3.9). In San Silvestro, the blue zone is characterized by a lower FeO concentration, which increases up to 0.7 wt%, and slowly decreases to below detection approaching the termination of the crystal, with a concomitant fading of color (Z4, Fig. 3.10). FeO concentration abruptly increases to 0.6 wt% at the rim of the crystal, where an additional thin bluish overgrowth occurs (Z5, Fig. 3.10). In all blue colored zones TiO_2 content was below detection limits (Tables 3.1 and 3.2).

The prismatic initial part of the two crystals exhibits a yellow-green color and contains the highest amount of Mn. This zone appears more extended and darker in the San Silvestro sample and is characterized by MnO up to ~ 4.5 wt%, which decreases to values below detection in the remaining part of the crystal (Fig. 3.10). This zone is also enriched in TiO_2 (up 0.11 wt%) (Table 3.2). Similarly, the Fucili yellow-green zone shows MnO up to ~ 1.5 wt%, which sharply decreases to values

0.1-0.3 wt% in the remaining part of the crystal (Fig. 3.9).

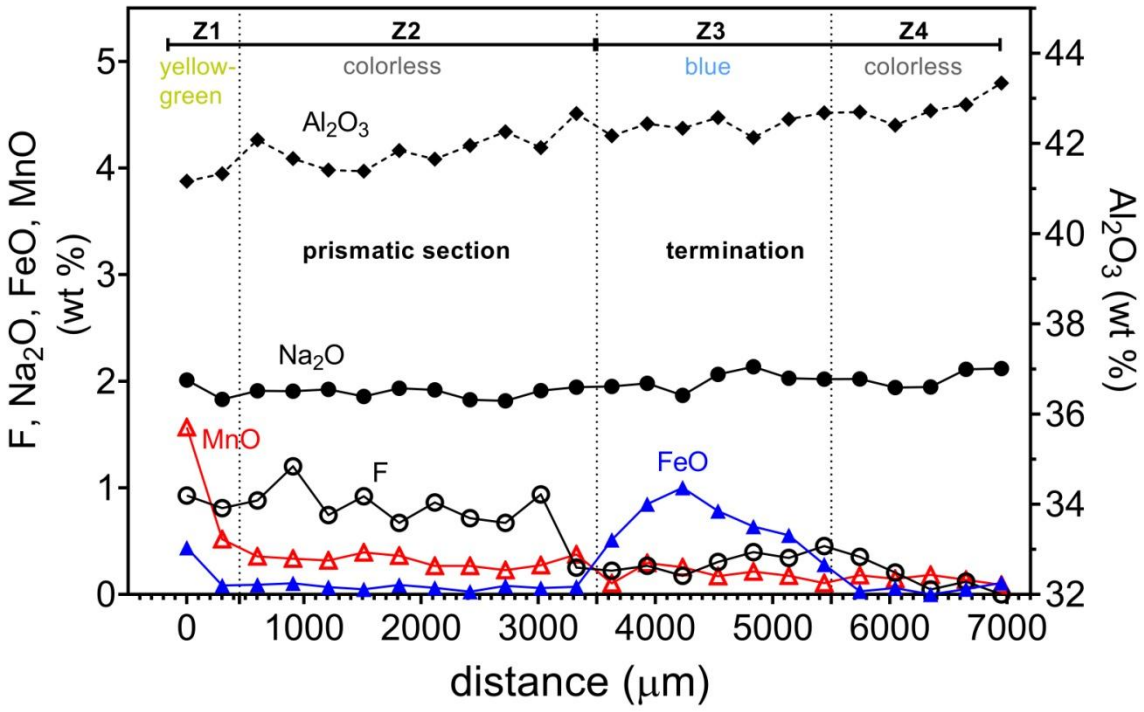

Figure 3.9. EMP analysis of Fucili sample along a straight traverse parallel to the **c**-axis (only selected oxides are reported). See Table 3.1 for complete chemistry.

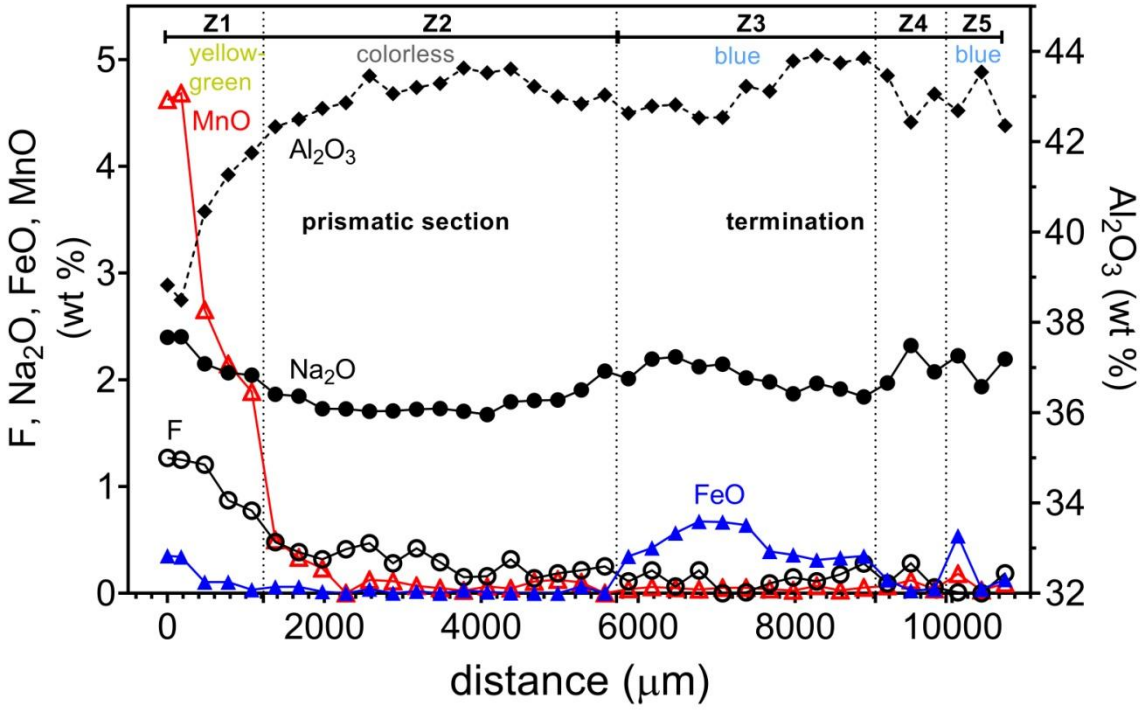

Figure 3.10. EMP analysis of San Silvestro sample along a straight traverse parallel to the **c**-axis (only selected oxides are reported). See Table 3.2 for complete chemistry.

Table 3.1. Average chemical composition and atoms per formula unit (a.p.f.u) for each zone of the Fucili sample (San Piero in Campo, Elba Island, Italy)

	Z1	**Z2**	**Z3**	**Z4**
	$n = 2$	$n = 10$	$n = 7$	$n = 5$
SiO_2 (wt%)	38.90(25)	38.39(61)	38.52(92)	38.08(81)
TiO_2	0.03(1)	0.03(2)	0.01(1)	0.02(1)
B_2O_3[a]	11.19	11.13	11.21	11.15
Al_2O_3	41.25(12)	41.88(39)	42.41(21)	42.81(34)
FeO	0.26(25)	0.07(2)	0.66[b](24)	0.05(4)
MnO	1.04(74)	0.32(6)	0.19(7)	0.15(4)
CaO	0.38(1)	0.37(14)	0.04(3)	0.03(2)
Na_2O	1.92(13)	1.90(5)	2.01(9)	2.03(9)
Li_2O[c]	1.97	1.98	1.85	1.87
K_2O	0.03(1)	0.01(1)	0.01(1)	0.01(1)
F	0.87(8)	0.79(25)	0.31(10)	0.15(14)
H_2O[a]	3.32	3.31	3.55	3.58
$-O \equiv F$	−0.37	−0.33	−0.13	−0.06
Total	100.82	99.91	100.74	99.90
Atoms normalized to 31 anions				
Si (a.p.f.u)	6.043	5.992	5.973	5.936
Ti^{4+}	0.003	0.003	0.001	0.002
B	3.000	3.000	3.000	3.000
Al	7.562	7.715	7.751	7.864
Fe^{2+}	0.034	0.009	0.086	0.007
Mn^{2+}	0.137	0.042	0.025	0.019
Ca	0.062	0.061	0.007	0.005
Na	0.579	0.574	0.603	0.613
Li	1.231	1.243	1.154	1.172
K	0.006	0.003	0.001	0.002
F	0.427	0.388	0.152	0.072
OH	3.440	3.450	3.676	3.723

[a] Calculated by stoichiometry (see text)

[b] Determined by Mössbauer spectroscopy

[c] Estimated with the procedure of Pesquera et al. (2016)

Errors for oxides and fluorine are standard deviations (in brackets)

Table 3.2. Average chemical composition and atoms per formula unit (a.p.f.u) for each zone of the San Silvestro sample (San Piero in Campo, Elba Island, Italy)

	Z1	**Z2**	**Z3**	**Z4**	**Z5**
	n = 5	*n* = 15	*n* = 11	*n* = 3	*n* = 3
SiO_2 (wt%)	38.51(23)	39.57(28)	38.16(99)	38.88(68)	38.29(63)
TiO_2	0.11(7)	0.02(2)	0.02(2)	0.02(2)	0.03(1)
B_2O_3[a]	11.10	11.43	11.20	11.30	11.20
Al_2O_3	40.15(99)	43.09(39)	43.18(56)	42.98(52)	42.86(61)
FeO	0.18(15)	0.02(2)	0.46(15)	0.06(5)	0.24(27)
MnO	3.19(99)	0.13(14)	0.02(1)	0.08(4)	0.10(8)
ZnO	0.03(4)	0.02(2)	0.03(3)	0.04(3)	0.04(1)
CaO	0.14(11)	0.02(1)	0.07(9)	0.06(8)	0.02(2)
Na_2O	2.21(18)	1.79(11)	2.03(13)	2.12(18)	2.12(16)
Li_2O[b]	1.72	2.02	1.78	1.95	1.86
K_2O	0.03(1)	0.01(1)	0.01(1)	0.02	0.01(1)
F	1.07	0.30	0.13	0.14	0.07
H_2O[a]	3.17	3.73	3.52	3.63	3.61
$-O \equiv F$	−0.45	−0.13	−0.05	−0.06	−0.03
Total	101.23	102.05	100.59	101.24	100.50
	Atoms normalized to 31 anions				
Si (a.p.f.u)	6.033	6.018	5.934	5.979	5.952
Ti^{4+}	0.013	0.003	0.003	0.002	0.003
B	3.000	3.000	3.000	3.000	3.000
Al	7.414	7.723	7.899	7.791	7.850
Fe^{2+}	0.025	0.003	0.060	0.008	0.030
Mn^{2+}	0.424	0.016	0.003	0.010	0.013
Zn	0.004	0.002	0.003	0.004	0.004
Ca	0.024	0.003	0.012	0.009	0.003
Na	0.672	0.527	0.610	0.633	0.637
Li	1.084	1.236	1.111	1.206	1.161
K	0.005	0.003	0.001	0.004	0.001
F	0.532	0.144	0.064	0.070	0.032
OH	3.308	3.781	3.644	3.722	3.735

[a] Calculated by stoichiometry (see text)

[b] Estimated with the procedure of Pesquera et al. (2016)

Errors for oxides and fluorine are standard deviations (in brackets)

The yellow-green zones of the Fucili and the San Silvestro samples (Z1) are enriched in F, compared to other parts of the crystals. In the Fucili sample, the F content remains higher throughout the entire length of the prismatic colorless section (Z2), with an average value of 0.7 wt%, decreasing to lower values at the terminal part of the crystal (Fig. 3.9). In contrast, the San Silvestro sample contains the highest concentration in F (~1.2 wt%) close to the base of the crystal. Fluorine content slowly decreases within the yellow-green zone to reach very low values in the remaining part of the crystal (Fig. 3.10).

Iron speciation

To evaluate the Fe redox state, the blue zone of Fucili sample, characterized by the highest Fe content, was subjected to MS analysis. The spectrum could be accurately fitted with three Lorentzian doublets with centre shift (δ) values around 1.09 mm/s, consistent with $^{[6]}Fe^{2+}$ (Fig. 3.11).

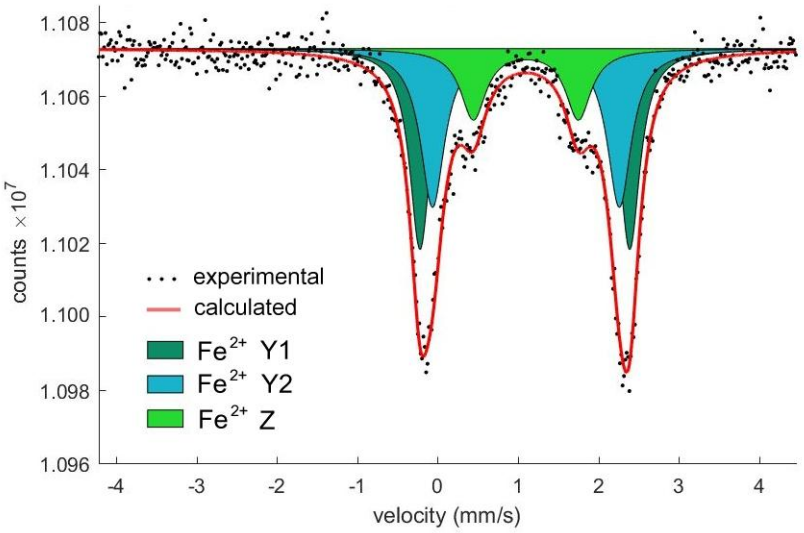

Figure 3.11. Room temperature 57Fe Mössbauer spectrum for the blue zone of the Fucili sample. Experimental spectrum (exp) is represented by dots, calculated spectrum (calc) by thick red curve. Lorentzian absorption doublets assigned to Fe2+ are represented by coloured areas. The different color of the areas refers to the assignment of Fe2+ between Y and Z sites.

The doublets are distinguished by their quadrupole splitting (ΔE_Q) values: the first two doublets with ΔE_Q equal to 2.61 mm/s and 2.33 mm/s, were interpreted as Fe^{2+} at the *Y* site (*Y1* and *Y2*), whereas the third Fe^{2+} doublet, which has ΔE_Q = 1.31

mm/s, was interpreted as $^{[6]}Fe^{2+}$ at the *Z* site according to the model described in Andreozzi et al. (2008). No indication of the presence of Fe^{3+}, within the experimental error, was observed by MS analysis, consistent with the absence of Fe^{3+}-related signals in OAS spectra (see below). The hyperfine parameters of the MS doublets and the relative Fe oxidation state and site assignment for the blue zone of Fucili sample are summarized in Table 3.3.

Table 3.3 Room temperature ^{57}Fe Mössbauer parameters for the blue zone of the Fucili sample
(San Piero in Campo, Elba Island, Italy)

δ mm/s	ΔE_Q mm/s	Γ mm/s	Assignment	%Area
1.09	2.61	0.31	Fe^{2+} (*Y*1)	43
1.10	2.33	0.37	Fe^{2+} (*Y*2)	39
1.10	1.31	0.38	Fe^{2+} (*Z*)	18

Centroid shift (δ) in mm/s relative to α-Fe foil; errors are estimated no less than ±0.02 mm/s for δ, quadrupole splitting (ΔE_Q), and peak width (Γ), and no less than ±3% for doublets areas.

Determination of site population and mineral formula

The site populations for each zone of Fucili and San Silvestro samples were calculated following Henry et al. (2011). The resulting empirical formulae are reported in Table 3.4. All the compositions are consistent with a tourmaline belonging to the alkali-group, subgroup 2 (Henry et al., 2011): they are Na-dominant at the *X* position of the tourmaline general formula and hydroxy-dominant at *W* with $(OH+F)^- > O^{2-}$ and (OH) >> F, with the exception of Z1 yellow-green zone of San Silvestro which is fluor-dominant. All studied tourmalines are ^{Z}Al- and $^{Y}(Al_{1.5}Li_{1.5})$-dominant, thus they are elbaitic from a nomenclature viewpoint (Henry et al., 2011). In detail, all the zones of Fucili and San Silvestro can be classified as elbaite, ideally $Na(Li_{1.5}Al_{1.5})Al_6Si_6O_{18}(BO_3)_3(OH)_3OH$, except for Z1 of San Silvestro that is fluor-elbaite, ideally $Na(Li_{1.5}Al_{1.5})Al_6Si_6O_{18}(BO_3)_3(OH)_3F$. The Z1 zone of both samples is a Mn-bearing tourmaline (MnO > 1 wt%), whereas the Z3 zone of the two samples and Z5 of San Silvestro are Fe-bearing tourmalines (FeO > 0.2 wt%).

Table 3.4. Empirical chemical formulae of the different zones of the Fucili and San Silvestro samples.

Fucili	
Z1 yellow-green sector	$^{X}(Na_{0.58}K_{0.01}\square_{0.35}Ca_{0.06})_{\Sigma 1.00}{}^{Y}(Al_{1.56}Li_{1.23}Fe^{2+}_{0.03}Mn^{2+}_{0.14}Ti_{0.003})_{\Sigma 2.96}{}^{Z}Al_6(^{T}Si_{6.04}O_{18})(BO_3)_3{}^{V}(OH)_3{}^{W}[(OH)_{0.44}F_{0.43}O_{0.13}]_{\Sigma 1.00}$
Z2	$^{X}(Na_{0.58}\square_{0.36}Ca_{0.06})_{\Sigma 1.00}{}^{Y}(Al_{1.71}Li_{1.24}Fe^{2+}_{0.01}Mn^{2+}_{0.04}Ti_{0.003})_{\Sigma 3.00}{}^{Z}Al_6[^{T}(Si_{5.99}Al_{0.01})_{\Sigma 6.00}O_{18}](BO_3)_3{}^{V}(OH)_3{}^{W}[(OH)_{0.45}F_{0.39}O_{0.16}]_{\Sigma 1.00}$
Z3[a] blue sector	$^{X}(Na_{0.60}\square_{0.39}Ca_{0.01})_{\Sigma 1.00}{}^{Y}(Al_{1.74}Li_{1.15}Fe^{2+}_{0.08}Mn^{2+}_{0.03}Ti_{0.001})_{\Sigma 3.00}{}^{Z}(Al_{5.99}Fe^{2+}_{0.01})_{\Sigma 6.00}$ $[^{T}(Si_{5.98}Al_{0.02})_{\Sigma 6.00}O_{18}](BO_3)_3{}^{V}(OH)_3{}^{W}[(OH)_{0.68}F_{0.15}O_{0.17}]_{\Sigma 1.00}$
Z4	$^{X}(Na_{0.61}\square_{0.38}Ca_{0.01})_{\Sigma 1.00}{}^{Y}(Al_{1.80}Li_{1.17}Fe^{2+}_{0.01}Mn^{2+}_{0.02}Ti_{0.002})_{\Sigma 3.00}{}^{Z}Al_6[^{T}(Si_{5.94}Al_{0.06})_{\Sigma 6.00}O_{18}](BO_3)_3{}^{V}(OH)_3{}^{W}[(OH)_{0.72}F_{0.07}O_{0.21}]_{\Sigma 1.00}$
San Silvestro	
Z1 yellow-green sector	$^{X}(Na_{0.67}K_{0.01}\square_{0.30}Ca_{0.02})_{\Sigma 1.00}{}^{Y}(Al_{1.41}Li_{1.08}Fe^{2+}_{0.03}Mn^{2+}_{0.42}Ti_{0.01})_{\Sigma 2.97}{}^{Z}Al_6(^{T}Si_{6.03}O_{18})(BO_3)_3{}^{V}(OH)_3{}^{W}[(OH)_{0.31}F_{0.53}O_{0.16}]_{\Sigma 1.00}$
Z2	$^{X}(Na_{0.53}\square_{0.47})_{\Sigma 1.00}{}^{Y}(Al_{1.72}Li_{1.24}Fe^{2+}_{0.003}Mn^{2+}_{0.02}Ti_{0.003})_{\Sigma 2.98}{}^{Z}Al_6(^{T}Si_{6.02}O_{18})(BO_3)_3{}^{V}(OH)_3{}^{W}[(OH)_{0.78}F_{0.14}O_{0.16}]_{\Sigma 1.00}$
Z3 blue sector	$^{X}(Na_{0.61}\square_{0.38}Ca_{0.01})_{\Sigma 1.00}{}^{Y}(Al_{1.83}Li_{1.11}Fe^{2+}_{0.06}Mn^{2+}_{0.003}Ti_{0.003})_{\Sigma 3.00}{}^{Z}Al_6[^{T}(Si_{5.93}Al_{0.07})_{\Sigma 6.00}O_{18}](BO_3)_3{}^{V}(OH)_3{}^{W}[(OH)_{0.64}F_{0.06}O_{0.30}]_{\Sigma 1.00}$
Z4	$^{X}(Na_{0.63}\square_{0.36}Ca_{0.01})_{\Sigma 1.00}{}^{Y}(Al_{1.77}Li_{1.21}Fe^{2+}_{0.01}Mn^{2+}_{0.01}Ti_{0.002})_{\Sigma 3.00}{}^{Z}Al_6[^{T}(Si_{5.98}Al_{0.02})\Sigma_{6.00}O_{18}](BO_3)_3{}^{V}(OH)_3{}^{W}[(OH)_{0.72}F_{0.07}O_{0.21}]_{\Sigma 1.00}$
Z5 blue sector	$^{X}(Na_{0.64}\square_{0.36})_{\Sigma 1.00}{}^{Y}(Al_{1.80}Li_{1.16}Fe^{2+}_{0.03}Mn^{2+}_{0.01}Ti_{0.003})_{\Sigma 3.00}{}^{Z}Al_6[^{T}(Si_{5.95}Al_{0.05})_{\Sigma 6.00}O_{18}](BO_3)_3{}^{V}(OH)_3{}^{W}[(OH)_{0.74}F_{0.03}O_{0.13}]_{\Sigma 1.00}$

[a] Iron site distribution has been calculated on the basis of Mössbauer data

Optical spectra

The optical absorption spectra (**E⊥c** and **E||c**) in the UV-Vis-NIR region of San Silvestro and Fucili blue zone highlight the cause of color (shown in Figure 3.12). The spectrum of the San Silvestro sample recorded in polarized mode perpendicular to the **c**-axis direction displays two absorption bands centred at 13800 and 9200 cm^{-1} and two very weak absorption bands at ~19000 and ~23000 cm^{-1}. The same bands, with higher intensities, are also observed in the **E⊥c**-spectrum of the Fucili sample (Fig. 3.12). In light polarized parallel to the crystallographic **c**-axis, the recorded spectra are characterized by the same absorption bands observed in **E⊥c**-spectra, but with a lower intensity.

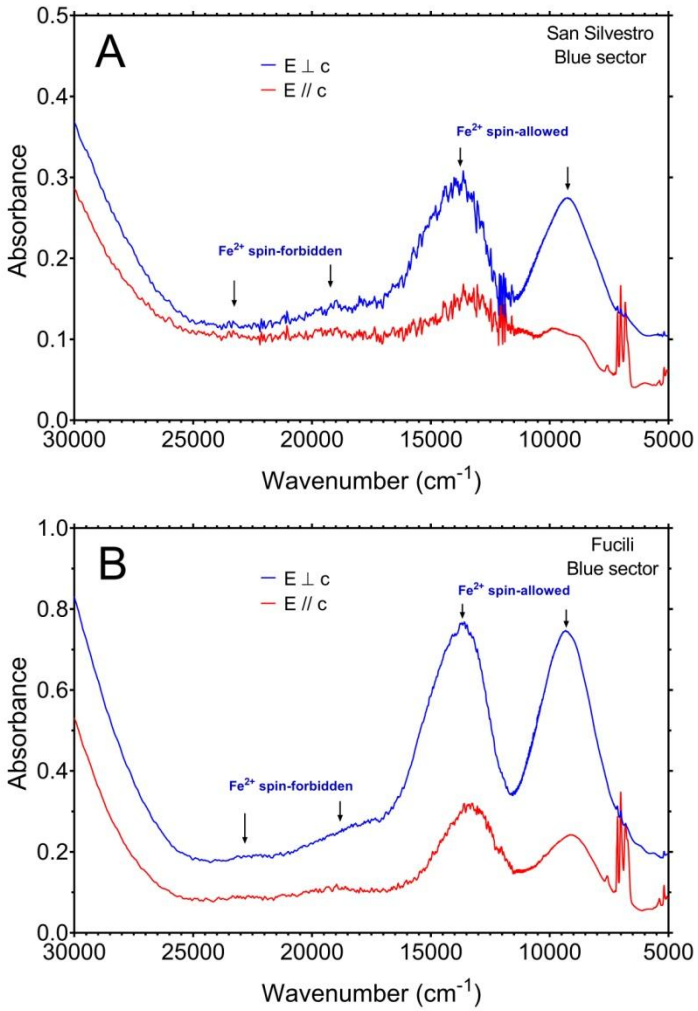

Figure 3.12. OAS spectra polarised perpendicular (E⊥c, blue line) and parallel (E||c, red line) to the c-axis direction of the blue zone of the San Silvestro (A) and Fucili (B) samples. Sample thickness: San Silvestro = 364 μm; Fucili = 865 μm. Peak positions are indicated.

The set of strongly **E**||**c**-polarised sharp bands in the NIR region of spectra of the blue zones of the San Silvestro and Fucili samples between 6700–7200 cm^{-1} are due to overtones of the fundamental (OH)-stretching modes (Fig. 3.12).

FTIR spectra in the (OH)-stretching region

FTIR spectra recorded in polarized mode perpendicular and parallel to the **c**-axis for the blue zones of San Silvestro and Fucili samples, display a set of absorption bands with different intensities in the (OH)-stretching region (3300–3800 cm^{-1}) (Fig. 3.13). As observed in previous polarized-FTIR studies on tourmalines (e.g., Gebert and Zemann, 1965), the absorption bands are strongly polarized in the **c**-axis direction, and the main bands suffer from truncation problems due to excessive absorption.

Infrared spectra of the blue zone in the San Silvestro sample display the presence of several bands where intensity is strongly dependent on the polarisation direction (Fig. 3.13 A). Four main intense bands are observable in **E**⊥**c** polarization at 3465, 3489, 3563 and 3587 cm^{-1}, and two weaker bands occur at 3653 and 3663 cm^{-1}. In the **E**||**c** direction the band at 3653 cm^{-1} shows a much stronger intensity, and an additional weak band occurs at 3705 cm^{-1}, whereas the bands below 3600 cm^{-1} are off-scale.

The FTIR spectra of the blue zone of Fucili sample (Fig. 3.13 B) display very similar features to those observed in the spectra of San Silvestro sample, with four main intense bands at 3465, 3488, 3561 and 3585 cm^{-1} (**E**⊥**c**), two relatively weak bands at 3654 (**E**||**c**) and 3663 cm^{-1} (**E**⊥**c**), and a very weak band at 3705 cm^{-1}, only present in the **E**||**c** direction.

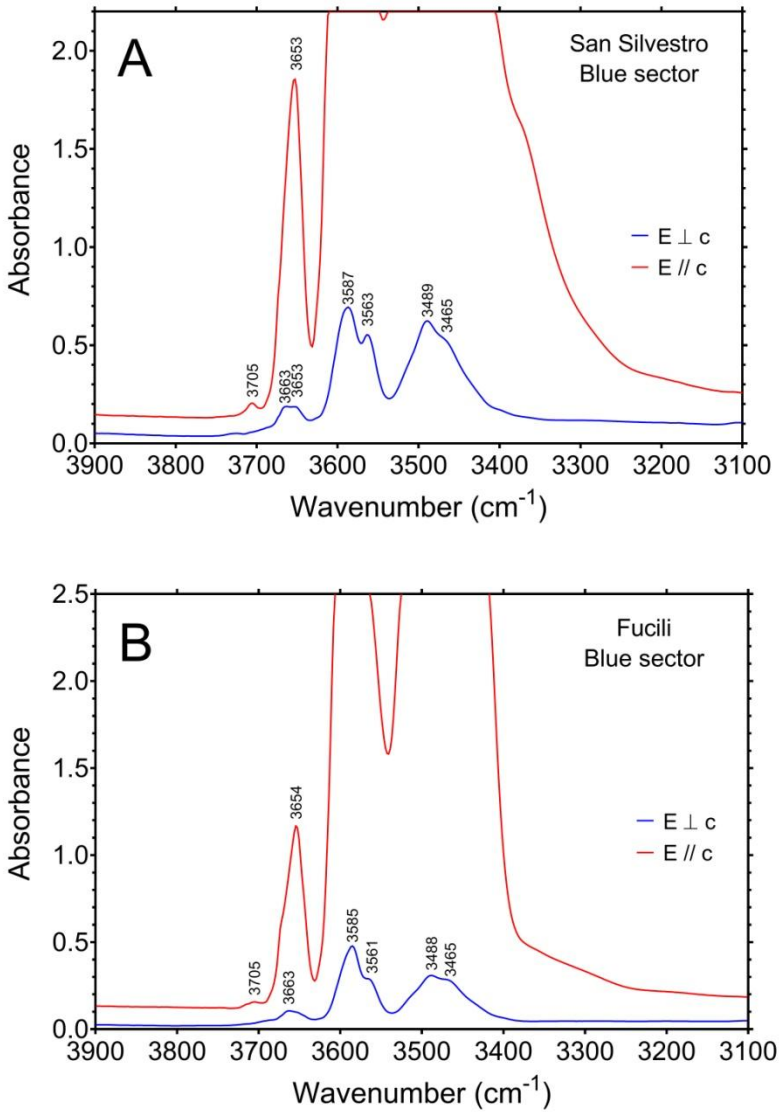

Figure 3.13. Polarised FTIR spectra (E⊥c, blue line, and E||c, red line) of the blue zone of the San Silvestro (A) and Fucili (B) samples. Peak positions are indicated. Sample thickness: San Silvestro = 74 μm; Fucili = 45 μm.

3.3.4 Discussion

Cause of color

Colors in tourmaline are essentially related to transitions elements (Ti, V, Cr, Fe, Mn and Cu), acting as color-causing agents through several mechanisms at structural levels, with the most common ones being crystal field transitions (CFT), intervalence charge transfer interactions (IVCT), and color centres (e.g., Fritsch and Rossman,1987; Pezzotta and Laurs, 2011; Rossman, 2014). Because chemical analyses of the San Silvestro and Fucili samples revealed contents of V_2O_3, Cr_2O_3

and CuO below the detection limit (≤ 0.03 wt%), the main transition metals that could contribute to the color of the blue zone of these tourmaline crystals are Fe, Mn and Ti.

Polarized spectra (**E⊥c** and **E||c)** recorded on the blue zone (Z3) of San Silvestro sample (Fig. 3.12 A) show two absorption bands centred at 13800 and 9200 cm^{-1}, which are caused by electronic transitions in Fe^{2+} (e.g., Mattson and Rossman, 1987). EMPA results confirmed the presence of Fe as only color-causing agent (FeO up to 0.7 wt%), because Mn and Ti are barely detectable (below detection) in the blue zone of this sample (Fig. 3.10). Moreover, the weak polarization of 13800 and 9200 cm^{-1} bands is attributable to the absence of Fe^{3+} in the sample. Consequently, these bands are assigned to pure spin-allowed *d-d* transitions in [6]-coordinated Fe^{2+} (e.g., Mattson and Rossman, 1987). In addition, weak absorption bands at ~19000 and 23000 cm^{-1} are tentatively assigned to spin-forbidden electronic transitions in [6]-coordinated Fe^{2+}.

As observed for San Silvestro, spectra of the blue zone (Z3) of the Fucili sample are characterized by two strong absorption bands at 13800 and 9200 cm^{-1} (Fig. 3.12 B), which are attributable to pure spin-allowed *d-d* transitions in [6]-coordinated Fe^{2+}. This assignment agrees with the Fe valency and site distribution observed from Mössbauer spectra of the blue zone of this sample (Fig. 3.11 and Table 3.3). The stronger intensity of the bands at 13800 and 9200 cm^{-1} relate to the higher concentration of Fe (FeO up to ~ 1 wt%) compared to the blue zone of the San Silvestro sample. Similarly, the weaker absorption bands due to spin-forbidden transitions in [6]-coordinated Fe^{2+} also display increased intensities.

The blue color of elbaite crystals is predominantly due to Fe^{2+}, which causes absorption in the red range of the visible spectrum, and in rare cases by Cu^{2+}. Blue hue can be amplified significantly by very low amounts of Ti^{4+} and Fe^{3+}, through Fe^{2+}-Ti^{4+} and Fe^{3+}-Fe^{2+} IVCT interactions. These latter interactions were reported in the OAS data of the "blue capped" tourmalines from the Tourmaline Queen Mine (Pala, California) (http://minerals.caltech.edu/files/visible/tourmaline). Although the

similarity with the Queen Mine tourmalines, sharing a blue zone at the analogous pole, the samples here analyzed show in the OAS spectra only absorption bands related to Fe^{2+}. Thus, the blue color for these samples is due to Fe^{2+} alone, without the influence of Ti or Fe^{3+}.

Chemical analyses of the yellow-green zones (Z1) identify Ti, Mn and Fe as potential color-causing agents (Tables 3.1 and 3.2). In the spectra of the San Silvestro sample, the broad and strongly polarized (**E⊥c**) absorption in the near UV-region extending from 19000 to 32000 cm^{-1} can be tentatively assigned to a Mn^{2+}-Ti^{4+} IVCT-band at ~30100 cm^{-1} (Rossman and Mattson, 1986) and to a Fe^{2+}-Ti^{4+} IVCT-band at ~23900 cm^{-1} (data not shown). A slightly higher energy of 23900 cm^{-1} for the Fe^{2+}-Ti^{4+} IVCT-band as compared to a previously reported energy range of 22000-22900 cm^{-1} (e.g., Smith, 1978; Taran et al., 1993; Bosi et al., 2022c) may possibly be explained by differences in local cation ordering. This suggests that Ti^{4+} acts as color-causing agent in combination with Mn^{2+} and Fe^{2+} in the yellow-green zone of San Silvestro sample, consistent with the Ti enrichment of this zone (TiO_2 up to 0.11 wt%). Concerning the **E⊥c**-spectrum of the Fucili sample, the weak band at ~24500 cm^{-1} in is caused by spin-forbidden electronic transitions in [6]-coordinated Mn^{2+} (Rossman and Mattson, 1986). Overall, these data are in agreement with the paleness of the yellow-green zone of Fucili sample, which is also much thinner than that of the San Silvestro sample (Fig. 3.8 B,C).

(OH) band assignment

In the structure of tourmaline, the O1 site (≡ *W*) is surrounded by three *Y* cations, whereas the O3 site (≡ *V*) is surrounded by one *Y* and two *Z* cations. The highest energy bands above 3600 cm^{-1} correspond to O–H stretching vibrations at the O1 site, whereas bands in the range 3600-3400 cm^{-1} are associated with OH vibrations at the O3 site (e.g., Gonzalez-Carreño et al., 1988; Bosi et al., 2015). The ^{O1}(OH) stretching modes are affected by the *X*-site constituents, with the bands between ~3600–3700 cm^{-1} normally assigned to $^{X}\square$, whereas bands above 3700 cm^{-1} are

considered associated with $^{X}Na^{+}$ for electrostatic repulsion reasons between cations at *X*-site and H^{+} of the ^{O1}(OH) group (e.g., Gonzalez-Carreño et al., 1988; Berryman et al., 2016).

Based on the studies of Bosi et al. (2012, 2016, 2021) and Watenphul et al. (2016), the four main FTIR bands between 3465 and 3587 cm^{-1} are likely caused by the occurrence of the atomic arrangements $3[^{Y}(Li,Fe^{2+},Mn^{2+},Al)^{Z}Al^{Z}Al]-^{O3}(OH)_{3}$. The bands between 3600−3700 cm^{-1} may be caused by the arrangements $^{Y}[(Li,Fe^{2+},Mn^{2+})(Mn^{2+},Al)Al]-^{O1}(OH)-^{X}(\square)$, whereas the weak band above 3700 cm^{-1} may be ascribed to $^{Y}[(Li,Fe^{2+},Mn^{2+})(Mn^{2+},Al)Al]-^{O1}(OH)-^{X}(Na)$. These possible short-arrangements are consistent with the chemical characteristics of both blue zones, specifically Fe-bearing tourmalines, ^{Z}Al- and $^{Y}(Al_{1.5}Li_{1.5})$-dominant.

Petrogenesis and evolution of the blue-growth zones in tourmaline crystals from Elba Island

The rarity of the blue growth zone in tourmaline crystals from Elba Island could be linked to unusual environmental conditions which are responsible for the chemical variation and, thus, the color variation observed along the crystals. Data obtained indicate that the blue color of San Silvestro and Fucili samples is related to a slight enrichment in Fe^{2+} in the crystallization environment.

The formation of yellow-green coloration at the base of the tourmaline crystals from Fucili and San Silvestro pegmatites, required specific geochemical conditions: the original pegmatite-forming melt, a B-rich peraluminous melt, must be enriched in Mn and relatively low in Fe (Bosi et al., 2022a). Moreover, during the early stages of tourmaline crystallization, Fe must be removed. The most likely mechanism for depleting Fe from the pegmatitic melt is early crystallization of an Fe-rich mineral, such as biotite (or garnet or Fe-sulfides). Biotite is a typical paragenetic mineral in the Fucili and San Silvestro pegmatites. Additional removal of Fe during the evolution of pegmatite crystallization is guaranteed by the development of schorl. Furthermore, Mn must be preserved when highly evolved

Li-rich tourmaline starts to crystallize; this can be achieved when spessartine garnet (the main competitor for Mn in Elba pegmatites) is absent or crystallized only during the very early stages of the pegmatite evolution. Spessartine crystallization is recognized as an important mechanism for regulating the Mn content during the evolution of the pegmatite systems (Novak et al., 2000; Laurs et al., 2007). In the studied Elba tourmalines, Mn incorporation during the early stage of tourmaline crystallization occurred when spessartine was not crystallizing. This led to the Mn-rich yellow-green zone in the initial part of both crystals, followed by a decrease in Mn content in the remaining part as a consequence of Mn depletion in the system by tourmaline crystallization.

During the latest stages of the Fucili and the San Silvestro miarolitic cavities growth, a further change in the fluid compositions occurred. This change is recorded by the presence of blue growth zones at the analogous pole of tourmaline crystals in some cavities from both pegmatites, corresponding to an increased Fe content. We interpret the formation of such blue growth zones in the studied tourmalines as the evidence of a phenomenon of partial opening of the geochemical system at the scale of the cavities, which allowed some minor addition of Fe to the crystallizing fluids. Dutrow and Henry (2000) also invoked cavity opening for stabilizing/destabilizing different tourmaline compositions. Indeed, textural and paragenetic observations of the cavities in which tourmaline samples were collected reveal that such pockets are associated with a series of micro-fractures, which crosscut some early-formed tapering biotite crystals hosted in the surrounding solid pegmatitic rock. Such crystals appear also partially altered (bleached) along the fractures and at their rims.

In our model, the late-stage minor fracturing phenomenon, possibly related to thermal contraction during the cooling of the rock, allowed the cavity fluids to infiltrate the surrounding solid pegmatite and locally react with the crosscut tapering biotite crystals. This led to the formation of a new generation of “white mica” and the release of Fe that diffuse within the cavity fluids. The crystallising

tourmaline registered this event with a bluish growth zone slightly richer in Fe^{2+}, which ceased to grow when no more Fe was available in the system. This partial opening of the geochemical system is probably similar, but much less developed than the one associated with the formation of the well-known black-cap tourmaline crystals from Elba pegmatites (Bosi et al., 2022a). This system is likely related to more or less extensive fracturing and even pocket collapse before the end of the cavity crystallization, when abundant and reactive fluids were still present. This scenario could be similar to the one that led to the formation of the "blue capped" tourmalines from Queen Mine (Pala, California) (http://minerals.caltech.edu/files/visible/tourmaline). However, because the blue color of these tourmalines is also influenced by Ti and Fe^{3+}, this required the availability of a low amount of Ti in the environment and mild oxidizing conditions.

3.3.5 Conclusions

The comparison between the chemical composition of the San Silvestro and the Fucili samples, characterized by a blue growth zone in the upper part of the crystal, suggests a common crystallization environment. Originally, the environment was rich in Mn and poor in Fe, to account for the Mn-enrichment at the base of the crystals. Here, a yellow-green coloration is related to Mn^{2+} and, for the San Silvestro sample, to Ti^{4+} in combination with Mn^{2+} and Fe^{2+}, as color-causing agents. Fluorine content in pegmatitic melts was correlated to Mn (e.g., Selway et al., 1999). This is valid for the San Silvestro sample, where the higher availability of Mn, and consequently F, in the early-stage of crystallization, led to the formation of fluor-elbaite at the base of the crystal. Subsequently, in both cases, a late-stage minor fracturing phenomenon led to a partial opening of the geochemical system at the scale of the cavities. This allowed cavity fluids to infiltrate the surrounding pegmatite and locally react with early-formed biotite crystals. As a result, the corrosion and alteration of such Fe-rich crystals due to leaching processes (i.e. mineral dissolution, hydrothermal reactions) were

responsible for the availability of Fe in the crystallization environment and thus the formation of the blue-growth zone in the upper part of the crystals. The blue color is exclusively caused by pure spin-allowed *d-d* transitions in [6]-coordinated Fe^{2+} without influence of Ti or Fe^{3+}. The presence of Fe only in the divalent state suggests that all the above described events occurred during the latest stages of crystallization did not change the redox state of the environment, which remained as reducing. This interpretation is consistent with a partial opening of the cavity system associated with minor fracturing phenomena.

3.4 CASE STUDY 2 - Dark-colored overgrowths in an elbaitic tourmaline crystal from the Rosina pegmatite, San Piero in Campo, Elba Island (Tyrrhenian Sea, Italy): evidence of late-stage opening of the geochemical system

3.4.1 Introduction

Multicolored tourmalines of pastel or light colors with dark crystal terminations at the analogous pole (the -**c** side of the crystal) are quite characteristics of Elba Island pegmatites, Italy. These terminations are usually black, though can appear in different colors such as brown, green, red-violet, and blue. Such more-or-less dark-colored terminations may occur as narrow overgrowths, but can also compose a significant zone of the crystals, such as in the case of some elbaite crystals which are overgrown by aggregates of long parallel needles (Pezzotta, 2021).

The formation of the dark-colored overgrowths in Elba tourmalines are related to physicochemical variations in the crystallization environment during the latest-stages of tourmaline crystal growth. Such changes are consequent to the partial destabilization of the pocket environment in which tourmalines grew. The opening of the geochemical system due to pocket rupture was suggested by several authors. However, the detailed events that led to chemical changes in the pocket environment, resulting in the growth of late-stage tourmalines, remain unclear. Some authors propose that fracturing of the pocket allowed the introduction of external fluids coming from other regions of consolidated pegmatite that infiltrated the host rock and modified the chemical environment (e.g., Foord 1976; Aurisicchio et al., 1999; Selway et al., 1999; London, 2006). In accord with this view, Dutrow and Henry (2000; 2016; 2018) proposed that external fluids reacted with the host-rock and, in these conditions, tourmaline crystals dissolved to alter their composition with the generation of a late-stage fibrous Fe-rich tourmaline, characterized by an external fluid signature. On the

contrary, Novák and Taylor (2000) suggested that an internal source of Fe must be sought for the origin of Fe-rich late-stage tourmalines. In agreement with this latter consideration, Černý (2000) assessed that extensive leaching and corrosion of the cavity-lining and cavity-coating minerals of the pegmatite, could led to variations in the composition of the cavity fluid. Buŕival and Novák (2015) suggested that the chemical change in the cavity system is the result of hydrothermal alteration of the cavity-lining minerals by late-stage fluids, which developed in the final stages of pegmatite crystallization. Additionally, Felch et al. (2016) inferred that the observed corrosion and leaching of cavity-lining spessartine garnet crystals, was the result of reactions with late-stage hydrothermal fluids that originated and migrated from adjacent highly evolved miarolitic cavities. More recently, Bosi et al. (2022a) and Altieri et al. (2022) proposed that the pocket rupture event, possibly related to thermal contraction during the cooling of the rock, led to some mechanical brittle deformations of the enclosing pegmatite through the formation of late-stage fractures. This allowed the highly-reactive late-stage cavity fluids to permeate the fractures surrounding the cavity where the early-crystallized cavity-lining and cavity-coating Fe- and Mn-rich minerals were hosted. Leaching and corrosion processes ascribed to the late-stage cavity fluids led to the hydrothermal alteration of such minerals, with the subsequent release of Fe, and occasionally Mn, in the pocket environment.

The relatively recent discovery of some cavities in the Rosina Pegmatite in San Piero in Campo allowed careful collecting of many, mostly elbaitic, tourmaline crystals characterized by a variety of dark-colored overgrowths. Paragenetic and structural information of the pegmatite were also recorded (Pezzotta, 2021). This study is focused on the crystal-chemical characterization of an elbaitic multicolored tourmaline crystal found in the cavity naturally broken into two fragments in a miarolitic cavity of the Rosina pegmatite (Fig. 3.14 A), and characterized by dark-colored overgrowths, respectively purplish-red at the analogous pole, and yellow-orange at the antilogous pole (Fig. 3.14 B).

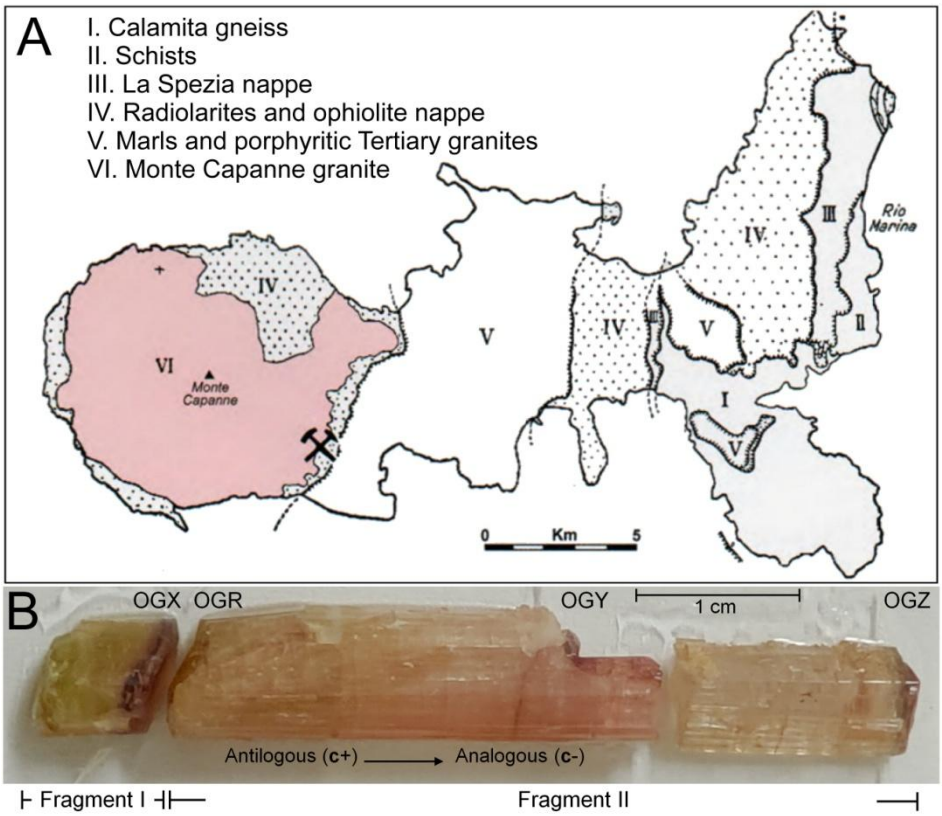

Figure 3.14. A) Geologic map of Elba Island. The occurrence area of the analysed tourmaline samples (San Piero in Campo, Elba Island, Italy) is marked at the edge of the Monte Capanne granite (after Trevisan, 1951 and modified by Pezzotta, 2021). B) The analysed tourmaline crystal fragments. The first fragment (7 mm in length) was collected as it is (fragment I), wherease the other two parts (30 and 15 mm in length, respectively) were originally connected as a single fragment (fragment II) that broke during collecting from the pocket. OGX, OGY, OGZ and OGR indicate the dark-coloured overgrowths. Scale bar = 1 cm.

This crystal was selected because it is representative of the texture of the tourmaline crystals occurring in cavities of many other Elba pegmatites that underwent a similar chemical-physical evolution (Pezzotta, 2021).

The Rosina pegmatite is located a few hundred meters south of the San Piero in Campo village, Elba Island, Italy, and since its discovery in early 1990 it has been mined for both collectibles and specimens suitable for scientific research (Pezzotta, 2021). Rosina is an LCT-type granitic pegmatite belonging to the group II of the Monte Capanne aplitic-pegmatitic veins classification system according to Pezzotta (2000) criteria. This pegmatite is frequently miarolitic, with abundant small to medium size pockets and a series of medium to large pockets (up to ~ 80

dm^3 in volume), and is significantly asymmetric in terms of its textures, mineralogy, and geochemistry. The axial core-miarolitic zone, which is rich in lepidolite, petalite and pollucite, divides the body into a medium-grained lower section enriched in albite with minor K-feldspar, quartz, spessartine, patches of sekaninaite and comb-texture tourmaline, and an upper coarse-grained section enriched in feldspar with minor albite, quartz, and tourmaline. Cavities found at shallower levels contain dark-colored tourmalines, together with pale-blue aquamarine and spessartine. In contrast, cavities found at deeper levels contain abundant polychrome and rose tourmalines with variable Mn and Fe content, morganite, petalite, pollucite and spessartine (Orlandi and Pezzotta, 1996; Pezzotta, 2000; Bosi et al., 2022a).

The tourmaline crystal samples investigated were found, together with several other crystals, in a relatively large, flat, oblate pocket of ~ 80 dm^3 in volume (90 x 65 cm, up to 25 cm high), not affected by any weathering alteration, and in the core zone of the pegmatite body. The distribution of the minerals and the rock structures of this pocket reflect the typical asymmetric compositional and textural zoning of this dike. The roof of the cavity was mostly composed of coarse-grained K-feldspar crystals, with quartz, minor albite, petalite and a few multicolored tourmaline and pink beryl crystals. The floor of the cavity was mostly composed by medium-grained albite, with quartz, petalite, numerous multicolored tourmaline crystals, and minor K feldspar crystals and pollucite. Thin radial fractures penetrating from the miarolitic cavity into the surrounding pegmatite are evident in the Rosina pegmatite (Fig. 3.15), suggesting some phenomena of partial cavity collapse. As a result, we propose that the highly-reactive cavity fluids locally infiltrate these fractures, leading to late-stage corrosion and alteration of the previously-crystallized cavity-lining minerals. These processes are supported by the occurrence of fractured and decolored biotite crystals, as well as altered spessartine garnet and petalite in the intermediate and lower border zone of the pegmatite (Fig. 3.15).

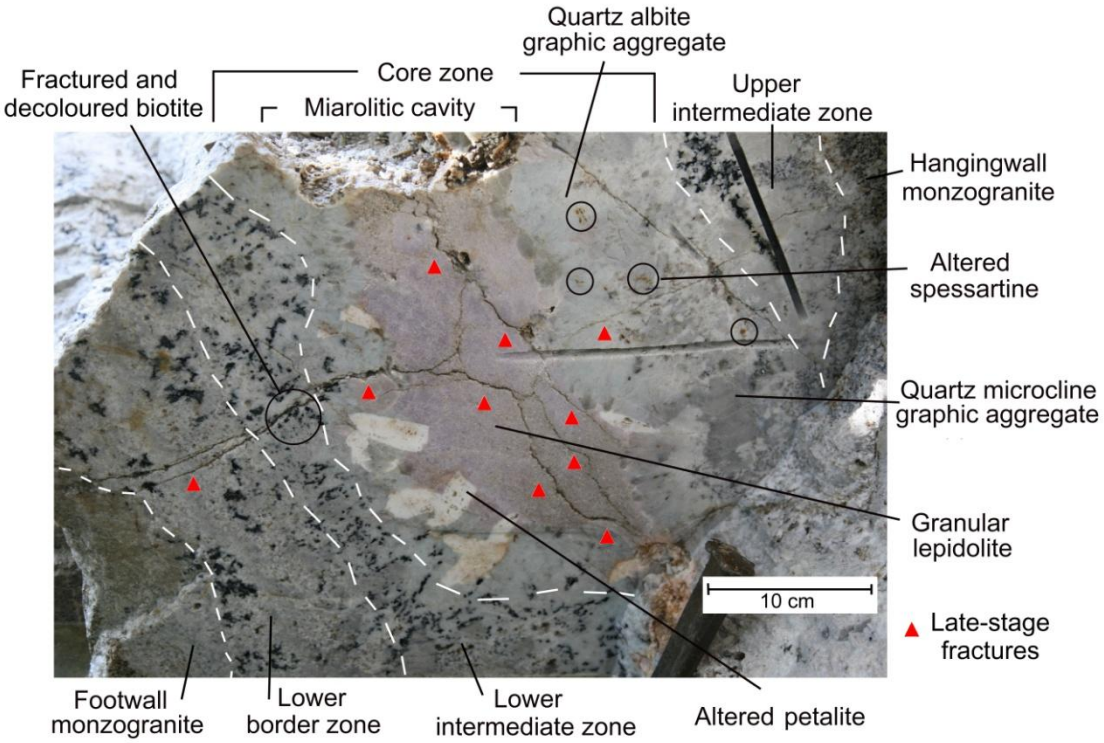

Figure 3.15. E–W section of the Rosina pegmatite (~ 60 cm in thickness), with the different textures and mineralogical zonation labelled. The altered cavity-lining minerals as well as late-stage fractures (red arrows) are also marked. Scale bar = 10 cm.

In this investigation we correlated structural evidences (fracturing of the pocket producing breakage of tourmaline crystals) to the late-stage tourmaline generation. Additionally, a comparison of the dark-colored overgrowths formed at the antilogous and analogous poles, provides information on tourmaline crystallization at the two different poles.

The results obtained from this study have been published in *Mineralogical Magazine* (Altieri et al., 2023). In this paper, the candidate is the first author and the main responsible for the analytical work, data interpretation, figures and tables production and the manuscript draft.

3.4.2 Experimental Methods

Sample preparation

The crystal fragments (Fig. 3.14 B) were glued to a glass slide using epoxy resin, with their length parallel to the surface of the slide. Then, a slice of each fragment was cut along the growth direction (crystallographic **c**-axis) and subsequently

ground and polished to produce a flat surface with a uniform thickness of 500 μm for electron microprobe analysis (EMPA).

For spectroscopic analyses, fragments were glued to a glass slide using a thermoplastic resin and cut along the c-axis, as described above, with a thickness of ~ 1100 μm. Before analyses, slices were further thinned to a suitable thickness and doubly polished.

Electron microprobe analysis (EMPA)

Compositional data were collected along two traverses (A-B and C-D) parallel to the **c**-axis (Fig. 3.16).

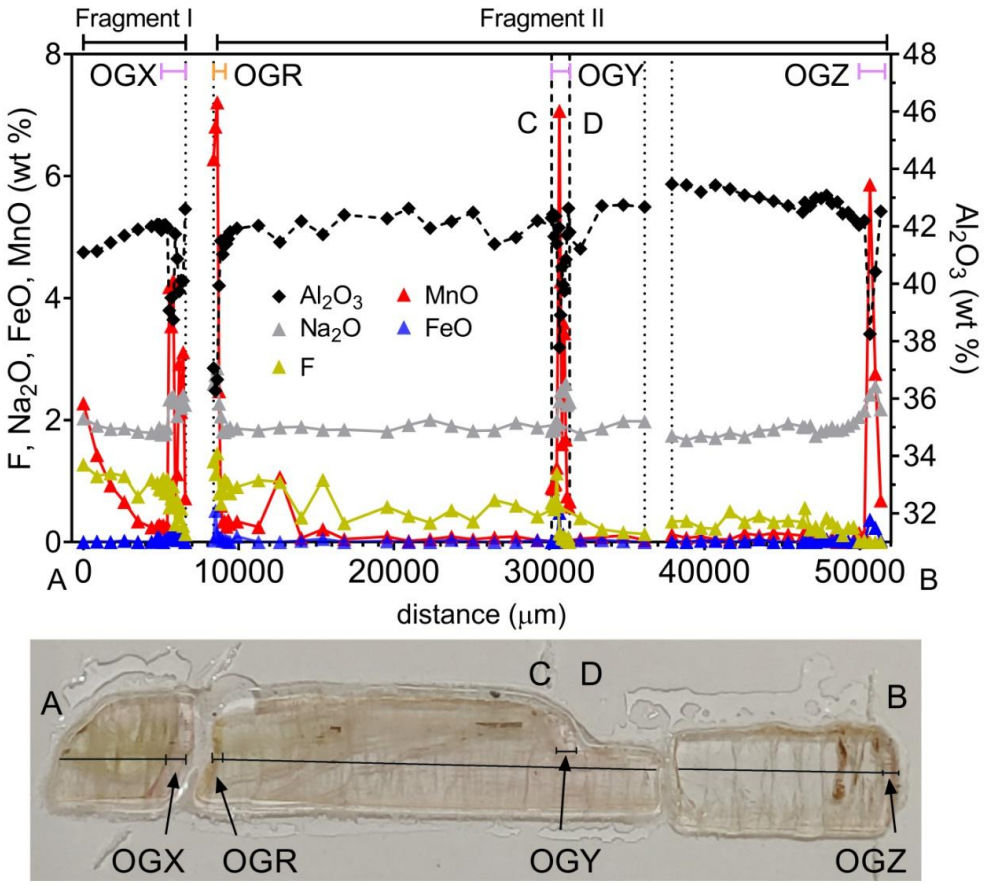

Figure 3.16. Upper panel: results of compositional analysis of the tourmaline crystal fragments along the two traverses (A–B and C–D). Lower panel: thin section of the analysed tourmaline fragments, with the traverses parallel to the **c**-axis represented by solid lines. OGX, OGR, OGY and OGZ are used for the different overgrowths.

The first one (A–B) was conducted from the base to the termination of each crystal fragment, with an average step size of 800 μm, except for where it passed through

the overgrowths, labelled as OGX, OGR and OGZ, where the step size was reduced to 130, 120 and 350 μm, respectively, to capture more fine-scale detail. A second short traverse (C–D), with a step size of 80 μm, was conducted to analyse a lateral overgrowth, labelled as OGY, and located on the prismatic section of the crystal. Electron microprobe analysis was done using a CAMECA SX50 at the Istituto di Geologia Ambientale e Geoingegneria (CNR of Rome, Italy) operating in wavelength-dispersion mode with an accelerating potential of 15 kV, a sample current of 15 nA and a beam diameter of 10 μm. Eighty-seven spot analyses were collected. Minerals and synthetic compounds were used as reference materials as follows: wollastonite (Si, Ca); magnetite (Fe); rutile (Ti); corundum (Al); karelianite (V); fluorophlogopite (F); periclase (Mg); jadeite (Na); orthoclase (K); rhodonite (Mn); and metallic Cr. The PAP correction procedure for quantitative electron probe micro analysis was applied (Pouchou and Pichoir, 1991). Relative error on data was <5% and detection limits <0.03 wt%.

Optical absorption spectroscopy (OAS)

Polarised room-temperature optical absorption spectra of the overgrowths (OGX, OGR, OGY and OGZ) were obtained in the range of 35000–11000 cm (286–909 nm) at a spectral resolution of 1 nm on doubly polished sections, using an AVASPEC-ULS2048×16 spectrometer attached via a 400 μm ultraviolet (UV) optical fibre cable to a Zeiss Axiotron UV-microscope. The diameter of the circular measure aperture was 50 μm. A 75 W xenon arc lamp was used as light source and Zeiss Ultrafluar 10× lenses served as objective and condenser. A UV-quality Glan-Thompson prism, with a working range from 40000 to 3704 cm was used as a polariser. Data in the near infrared (NIR) range (11000–5000 cm) were obtained at a spectral resolution of 4 cm using a Bruker Vertex 70 spectrometer equipped with a halogen-lamp source and CaF beam-splitter, coupled to a Hyperion 2000 IR-microscope equipped with a ZnSe wire-grid polariser and an InSb detector. The beam was collimated using an adjustable rectangular aperture with edges varying

from 50–80 μm.

Determination of site populations

The wt% of element oxides determined by EMPA were used to calculate the atomic fractions (atoms per formula unit, apfu). The B content was assumed to be stoichiometric (B = 3.00 apfu). Lithium was estimated using the procedure of Pesquera et al. (2016). The (OH) content was calculated by charge balance with the assumption (T + Y + Z) = 15.00 apfu and 31 anions. On the basis of the apfu, the site populations (see 'Mineral formulae' below) for each overgrowth and prismatic section of the two tourmaline crystal fragments were calculated following the site allocation of ions recommended by Henry et al. (2011).

3.4.3 Results

Composition

Variations in composition for selected elements (in wt%) along crystal traverses are shown in Figure 3.16. Results reveal that each fragment is characterised by low Mn and Fe contents, except for the dark-coloured overgrowths (OGX, OGY, OGZ and OGR) where the MnO and FeO content increase sharply up to ~ 7 wt% and 1 wt%, respectively. The initial part of fragment I contains a slight enrichment in MnO, starting from a value of ~ 2 wt% that progressively decreases below 0.3 wt%, and then abruptly increases at beginning of the OGX overgrowth. The variation in content of selected elements (in wt%) along the overgrowths are given in Figure 3.17. Vanadium, Cr and Mg were always below detection limits (< 0.03 wt%) in the samples investigated.

Compositions for selected representative spots analysed as well as the average values of each overgrowth (Tables 3.5 and 3.6) and prismatic section (Tables 3.7 and 3.8) of the two tourmaline crystal fragments are given in Tables 3.5-3.8.

Table 3.5. Representative compositions and atoms per formula unit (a.p.f.u) for the overgrowths OGX and OGR of the studied tourmaline crystals from San Piero in Campo, Elba Island, Italy. Average values and data for selected representative analyzed spots are reported.

	OGX			OGR	
	spot #13	spot #20	Average $n = 9$	spot #23	Average $n = 5$
Length (μm)		~1000		~500	
SiO_2 (wt%)	37.29	38.04	37.88(30)	37.39	37.05(31)
TiO_2	0.20	0.02	0.10(7)	0.39	0.25(10)
B_2O_3[a]	10.82	10.99	10.94	10.70	10.69
Al_2O_3	39.07	40.10	39.55(55)	36.27	37.48(39)
FeO_{tot}	0.10	0.10	0.10(5)	0.51	0.19(25)
MnO_{tot}	4.18	3.11	3.36(82)	6.81	5.69(47)
CaO	0.02	0.06	0.07(3)	0.34	0.20(10)
Na_2O	2.34	2.41	2.34(8)	2.74	2.61(13)
Li_2O[c]	1.56	1.70	1.71	1.41	1.46
K_2O	0.01	0.01	0.01(1)	0.02	0.02(1)
F	0.57	0.27	0.57(23)	1.12	1.17(17)
H_2O[a]	3.30	3.49	3.21	2.85	2.89
$-O \equiv F$	−0.24	−0.11	−0.24	−0.47	−0.49
MnO[d]	2.68	2.00	2.16	6.18	5.69
Mn_2O_3[d]	1.67	1.24	1.34	-	-
Total	99.27	100.20	99.62	100.16	99.25
Atoms normalized to 31 anions					
Si (a.p.f.u)	5.990	6.015	6.021	6.073	6.023
Ti^{4+}	0.024	0.003	0.012	0.048	0.030
B	3.000	3.000	3.000	3.000	3.000
Al	7.396	7.472	7.418	6.943	7.182
Fe^{3+}[b]	0.013	0.013	0.013	-	-
Fe^{2+}[b]	-	-	-	0.077	0.026
Mn^{3+}	0.204	0.149	0.162	-	-
Mn^{2+}	0.365	0.268	0.290	0.937	0.784
Ca	0.004	0.010	0.011	0.059	0.035
Na	0.728	0.740	0.720	0.863	0.824
Li	1.008	1.081	1.093	0.921	0.955
K	0.002	0.003	0.003	0.004	0.003
F	0.289	0.134	0.287	0.573	0.603
OH	3.537	3.676	3.404	3.171	3.131

[a] Calculated by stoichiometry (see text)

[b] All Fe was considered to be Fe^{3+}, with the exception of the OGR overgrowth, based on the OAS results

[c] Estimated with the procedure of Pesquera et al. (2016)

[d] Determined by OAS

Errors for oxides and fluorine are standard deviations (in brackets)

Table 3.6. Representative compositions and atoms per formula unit (a.p.f.u) for the overgrowths OGY and OGZ of the studied tourmaline crystals from San Piero in Campo, Elba Island, Italy. Average values and data for selected representative analyzed spots are reported.

	OGY			OGZ	
	spot #81	spot #84	Average $n = 8$	spot #73	Average $n = 4$
Length (μm)		~700		~1000	
SiO_2 (wt%)	37.32	38.18	37.78(34)	37.29	37.48(27)
TiO_2	0.07	0.02	0.04(4)	0.12	0.07(7)
B_2O_3[a]	10.78	11.02	10.90	10.79	10.87
Al_2O_3	37.78	39.96	39.10(99)	38.25	39.33(93)
FeO_{tot}	0.48	0.12	0.20(19)	0.37	0.30(9)
MnO_{tot}	7.07	3.60	4.59(98)	5.86	4.31(95)
CaO	0.05	0.01	0.02(2)	0.02	0.01
Na_2O	2.31	2.49	2.44(9)	2.42	2.49(10)
Li_2O[c]	1.18	1.65	1.53	1.34	1.49
K_2O	0.01	-	0.01(1)	0.03	0.04(1)
F	0.15	0.06	0.11(4)	-	-
H_2O[a]	3.18	3.44	3.35	3.29	3.33
$-O \equiv F$	−0.06	−0.02	−0.05	-	0.00
MnO[d]	5.27	2.68	3.42	4.27	3.14
Mn_2O_3[d]	2.00	1.02	1.30	1.77	1.30
Total	100.37	100.56	100.09	99.82	99.76
Atoms normalized to 31 anions					
Si (a.p.f.u)	5.997	6.024	6.023	6.004	5.995
Ti^{4+}	0.008	0.002	0.005	0.015	0.009
B	3.000	3.000	3.000	3.000	3.000
Al	7.180	7.430	7.345	7.260	7.414
Fe^{3+}[b]	0.065	0.016	0.027	0.049	0.040
Fe^{2+}[b]	-	-	-	-	-
Mn^{3+}	0.245	0.122	0.158	0.217	0.158
Mn^{2+}	0.720	0.358	0.462	0.583	0.426
Ca	0.008	0.002	0.004	0.003	0.002
Na	0.721	0.761	0.753	0.755	0.771
Li	0.765	1.047	0.981	0.868	0.958
K	0.002	-	0.002	0.006	0.008
F	0.076	0.029	0.055	-	-
OH	3.435	3.619	3.564	3.534	3.556

[a] Calculated by stoichiometry (see text)

[b] All Fe was considered to be Fe^{3+}, with the exception of the OGR overgrowth, based on the OAS results

[c] Estimated with the procedure of Pesquera et al. (2016)

[d] Determined by OAS

Errors for oxides and fluorine are standard deviations (in brackets)

Table 3.7. Representative compositions and atoms per formula unit (a.p.f.u) for the fragment I, prismatic section of the studied tourmaline crystals from San Piero in Campo, Elba Island, Italy. Average values and data for selected representative analyzed spots are reported.

	Prismatic section I		
	spot #2	spot #10	Average $n = 12$
SiO_2 (wt%)	37.14	38.05	37.95(48)
TiO_2	0.09	0.04	0.05(3)
B_2O_3[a]	10.89	11.08	11.06
Al_2O_3	41.14	42.03	41.77(36)
FeO	0.01	-	0.03(3)
MnO	1.43	0.28	0.62(64)
CaO	0.47	0.27	0.34(8)
Na_2O	1.91	1.83	1.85(7)
Li_2O[b]	1.91	1.94	1.90
F	1.08	1.04	0.99(15)
H_2O[a]	3.00	3.20	3.18
$-O \equiv F$	–0.45	–0.44	–0.42
Total	98.49	99.33	99.35
	Atoms normalized to 31 anions		
Si (a.p.f.u)	5.930	5.968	5.967
Ti^{4+}	0.011	0.004	0.006
B	3.000	3.000	3.000
Al	7.740	7.768	7.740
Fe^{2+}	0.001	-	0.003
Mn^{2+}	0.193	0.037	0.083
Ca	0.080	0.046	0.057
Na	0.591	0.556	0.563
Li	1.124	1.224	1.201
F	0.545	0.516	0.494
OH	3.193	3.344	3.334

[a] Calculated by stoichiometry (see text)

[b] Estimated with the procedure of Pesquera et al. (2016)

Errors for oxides and fluorine are standard deviations (in brackets)

Table 3.8. Representative compositions and atoms per formula unit (a.p.f.u) for the fragment II, prismatic section of the studied tourmaline crystals from San Piero in Campo, Elba Island, Italy. Average values and data for selected representative analyzed spots are reported.

	Prismatic section II					
	spot #28	spot #38	spot #40	spot # 58	spot #68	Average $n = 49$
SiO_2 (wt%)	36.55	36.06	37.23	38.84	38.37	37.74(99)
TiO_2	0.01	-	0.04	-	0.01	0.02(2)
B_2O_3[a]	10.79	10.75	10.93	11.28	11.17	11.05
Al_2O_3	41.56	42.27	41.94	42.88	42.44	42.37(64)
FeO	0.04	0.01	-	-	0.01	0.02(2)
MnO	0.34	0.09	0.05	0.15	0.06	0.14(18)
CaO	0.31	0.01	0.02	0.01	-	0.07(11)
Na_2O	1.80	1.81	2.01	1.84	1.85	1.87(9)
Li_2O[b]	1.80	1.69	1.89	1.96	1.97	1.88
F	1.02	0.58	0.32	0.33	0.11	0.46(29)
H_2O[a]	3.08	3.25	3.50	3.64	3.75	3.46
$-O \equiv F$	–0.43	–0.24	–0.13	–0.14	–0.05	–0.19
Total	96.89	96.30	97.80	100.82	99.73	98.92
Atoms normalized to 31 anions						
Si (a.p.f.u)	5.889	5.830	5.919	5.983	5.970	5.935
Ti^{4+}	0.001	-	0.004	-	0.001	0.002
B	3.000	3.000	3.000	3.000	3.000	3.000
Al	7.890	8.057	7.860	7.784	7.782	7.852
Fe^{2+}	0.005	0.002	-	-	0.001	0.002
Mn^{2+}	0.047	0.012	0.006	0.019	0.008	0.019
Ca	0.053	0.002	0.004	0.001	-	0.012
Na	0.563	0.568	0.618	0.560	0.558	0.569
Li	1.166	1.099	1.209	1.214	1.233	1.189
F	0.521	0.295	0.160	0.160	0.056	0.227
OH	3.304	3.509	3.713	3.744	3.888	3.633

[a] Calculated by stoichiometry (see text)

[b] Estimated with the procedure of Pesquera et al. (2016)

Errors for oxides and fluorine are standard deviations (in brackets)

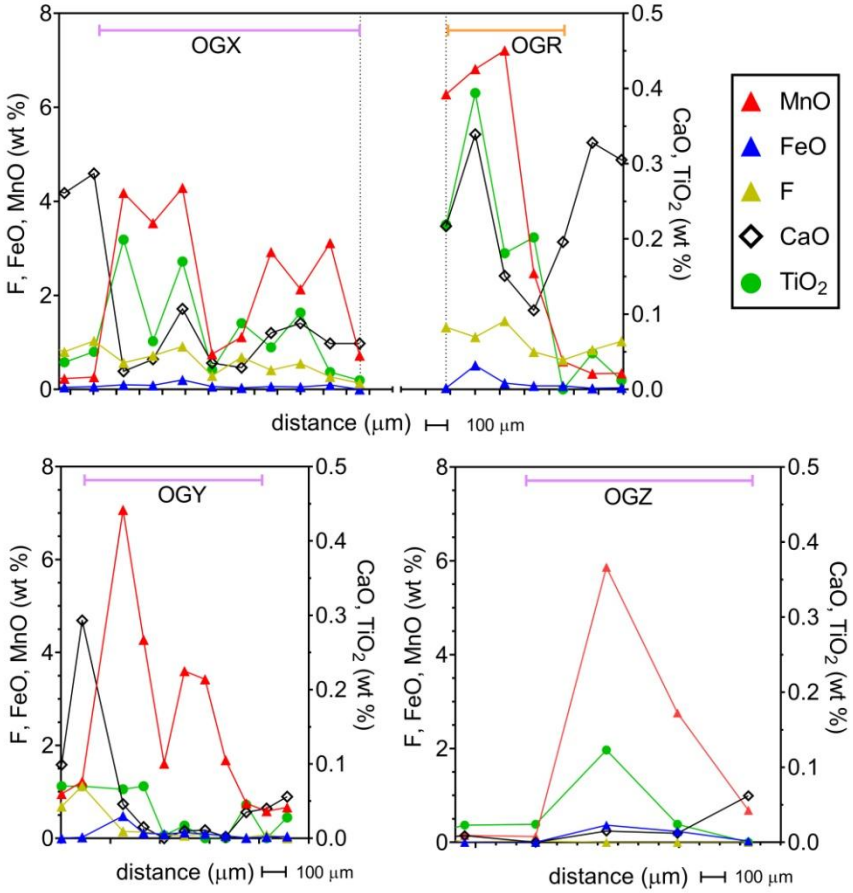

Figure 3.17. Compositional analysis of all the overgrowths (OGX, OGR, OGY and OGZ) observable in the tourmaline crystal fragments. Scale bar = 100 μm.

Note that in the overgrowths the oxidation state of Fe was assumed to be +3 as indicated by the presence of Mn revealed by optical absorption spectroscopy (OAS), except for the OGR overgrowth, which contains Fe (see below).

Compositional diagrams showing data from spot analysis relative to the prismatic section of fragment I and II, and the four different overgrowths are given in Figure 3.18.

Mineral formulae

The resulting empirical formulae written in their ordered form, relative to average compositions of each overgrowth and prismatic section of the two fragments, as well as to selected representative spots, are reported in Table 3.9.

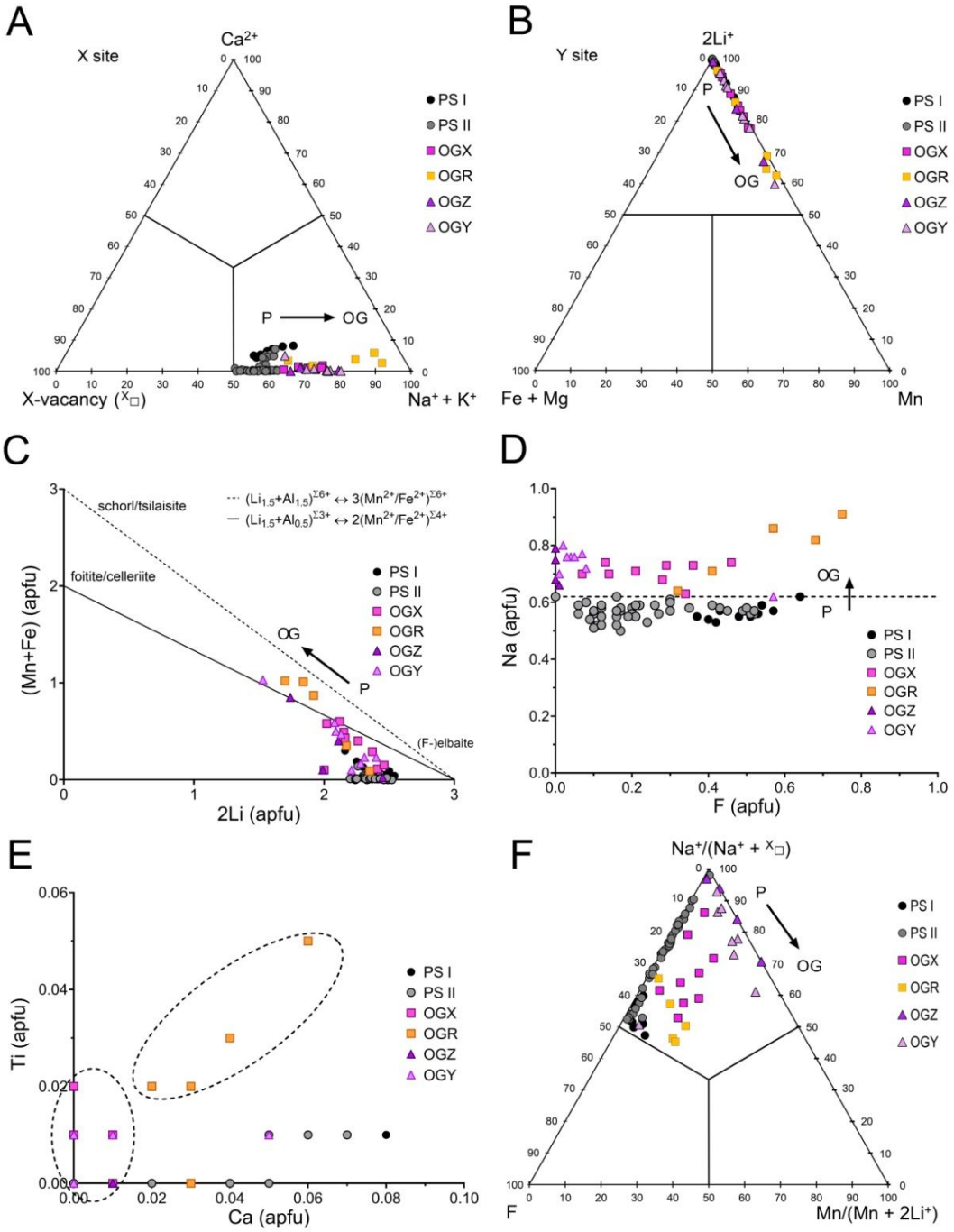

Figure 3.18. Compositional diagrams based on EMPA data. Each point represents the result in apfu of a single spot analysis. The spot data for the different overgrowths (OGX, OGR, OGY and OGZ) and the prismatic sections of the two fragments (PS I and PS II) are distinguished by colred labels. A) X-site occupancy; B) Y-site occupancy; C) Plot of 2Li vs. (Fe+Mn); D) Plot of F vs. Na; E) Plot of Ca vs. Ti; F) Ternary plot of Na/(Na + $^{X}\square$) vs. Mn/(Mn + 2Li) vs. F. Arrows highlight the compositional evolution trend from the prismatic section to the overgrowth. Dashed circles highlight the different distribution of the points relating to the overgrowth at the antilogous pole (OGR) compared to the other overgrowths (OGX, OGY and OGZ).

Table 3.9. Empirical formulae for the different overgrowths and prismatic sections of the tourmaline crystals investigated from San Piero Campo, Elba Island, Italy. Formulae relative to average compositions and for selected representative spots are reported.

Spots	Empirical chemical formulae
	OGX (analogous pole of fragment I)[a]
spot #13	$^{X}(Na_{0.73}\square_{0.27})_{\Sigma 1.00}{}^{Y}(Al_{1.39}Li_{1.01}Fe^{3+}_{0.01}Mn^{2+}_{0.37}Mn^{3+}_{0.20}Ti_{0.02})_{\Sigma 3.00}{}^{Z}Al_6[^{T}(Si_{5.99}Al_{0.01})O_{18}](BO_3)_3{}^{V}(OH)_3{}^{W}[(OH)_{0.54}F_{0.29}O_{0.17}]_{\Sigma 1.00}$
spot #20	$^{X}(Na_{0.74}\square_{0.25}Ca_{0.01})_{\Sigma 1.00}{}^{Y}(Al_{1.47}Li_{1.08}Fe^{3+}_{0.01}Mn^{2+}_{0.27}Mn^{3+}_{0.15}Ti_{0.003})_{\Sigma 2.98}{}^{Z}Al_6(^{T}Si_{6.02}O_{18})(BO_3)_3{}^{V}(OH)_3{}^{W}[(OH)_{0.68}F_{0.13}O_{0.19}]_{\Sigma 1.00}$
average (9 spots)	$^{X}(Na_{0.72}\square_{0.27}Ca_{0.01})_{\Sigma 1.00}{}^{Y}(Al_{1.42}Li_{1.09}Fe^{3+}_{0.01}Mn^{2+}_{0.29}Mn^{3+}_{0.16}Ti_{0.01})_{\Sigma 2.98}{}^{Z}Al_6(^{T}Si_{6.02}O_{18})(BO_3)_3{}^{V}(OH)_3{}^{W}[(OH)_{0.40}F_{0.29}O_{0.31}]_{\Sigma 1.00}$
	OGR (antilogous pole of fragment II)[a]
spot #23	$^{X}(Na_{0.86}\square_{0.08}Ca_{0.06})_{\Sigma 1.00}{}^{Y}(Al_{0.94}Li_{0.92}Fe^{2+}_{0.08}Mn^{2+}_{0.94}Ti_{0.05})_{\Sigma 2.93}{}^{Z}Al_6{}^{T}(Si_{6.07}O_{18})(BO_3)_3{}^{V}(OH)_3{}^{W}[(OH)_{0.17}F_{0.57}O_{0.26}]_{\Sigma 1.00}$
average (5 spots)	$^{X}(Na_{0.82}\square_{0.14}Ca_{0.04})_{\Sigma 1.00}{}^{Y}(Al_{1.18}Li_{0.96}Fe^{2+}_{0.03}Mn^{2+}_{0.78}Ti_{0.03})_{\Sigma 2.98}{}^{Z}Al_6{}^{T}(Si_{6.02}O_{18})(BO_3)_3{}^{V}(OH)_3{}^{W}[(OH)_{0.13}F_{0.60}O_{0.27}]_{\Sigma 1.00}$
	OGY (lateral overgrowth of fragment II)[a]
spot #81	$^{X}(Na_{0.72}\square_{0.27}Ca_{0.01})_{\Sigma 1.00}{}^{Y}(Al_{1.18}Li_{0.77}Fe^{3+}_{0.07}Mn^{2+}_{0.72}Mn^{3+}_{0.25}Ti_{0.01})_{\Sigma 3.00}{}^{Z}Al_6{}^{T}(Si_6O_{18})(BO_3)_3{}^{V}(OH)_3{}^{W}[(OH)_{0.44}F_{0.08}O_{0.48}]_{\Sigma 1.00}$
spot #84	$^{X}(Na_{0.76}\square_{0.24})_{\Sigma 1.00}{}^{Y}(Al_{1.43}Li_{1.05}Fe^{3+}_{0.02}Mn^{2+}_{0.36}Mn^{3+}_{0.12}Ti_{0.002})_{\Sigma 2.98}{}^{Z}Al_6{}^{T}(Si_{6.02}O_{18})(BO_3)_3{}^{V}(OH)_3{}^{W}[(OH)_{0.62}F_{0.03}O_{0.35}]_{\Sigma 1.00}$
average (8 spots)	$^{X}(Na_{0.76}\square_{0.24})_{\Sigma 1.00}{}^{Y}(Al_{1.35}Li_{0.98}Fe^{3+}_{0.03}Mn^{2+}_{0.46}Mn^{3+}_{0.16}Ti_{0.01})_{\Sigma 2.99}{}^{Z}Al_6{}^{T}(Si_{6.01}O_{18})(BO_3)_3{}^{V}(OH)_3{}^{W}[(OH)_{0.56}F_{0.06}O_{0.38}]_{\Sigma 1.00}$
	OGZ (analogous pole of fragment II)[a]
spot #73	$^{X}(Na_{0.76}K_{0.01}\square_{0.23})_{\Sigma 1.00}{}^{Y}(Al_{1.26}Li_{0.87}Fe^{3+}_{0.05}Mn^{2+}_{0.58}Mn^{3+}_{0.22}Ti_{0.02})_{\Sigma 3.00}{}^{Z}Al_6{}^{T}(Si_{6.00}O_{18})(BO_3)_3{}^{V}(OH)_3{}^{W}[(OH)_{0.53}O_{0.47}]_{\Sigma 1.00}$
average (4 spots)	$^{X}(Na_{0.77}K_{0.01}\square_{0.22})_{\Sigma 1.00}{}^{Y}(Al_{1.41}Li_{0.96}Fe^{3+}_{0.03}Mn^{2+}_{0.43}Mn^{3+}_{0.16}Ti_{0.01})_{\Sigma 3.00}{}^{Z}Al_6{}^{T}(Si_6O_{18})(BO_3)_3{}^{V}(OH)_3{}^{W}[(OH)_{0.56}O_{0.44}]_{\Sigma 1.00}$
	Prismatic section of fragment I
spot #2	$^{X}(Na_{0.59}\square_{0.33}Ca_{0.08})_{\Sigma 1.00}{}^{Y}(Al_{1.67}Li_{1.12}Mn^{2+}_{0.19}Ti_{0.01})_{\Sigma 2.99}{}^{Z}Al_6[^{T}(Si_{5.93}Al_{0.07})_{\Sigma 6.00}O_{18}](BO_3)_3{}^{V}(OH)_3{}^{W}[(OH)_{0.19}F_{0.54}O_{0.27}]_{\Sigma 1.00}$
spot #10	$^{X}(Na_{0.56}\square_{0.39}Ca_{0.05})_{\Sigma 1.00}{}^{Y}(Al_{1.74}Li_{1.22}Mn^{2+}_{0.04}Ti_{0.004})_{\Sigma 3.00}{}^{Z}Al_6[^{T}(Si_{5.97}Al_{0.03})_{\Sigma 6.00}O_{18}](BO_3)_3{}^{V}(OH)_3{}^{W}[(OH)_{0.34}F_{0.52}O_{0.14}]_{\Sigma 1.00}$
average (12 spots)	$^{X}(Na_{0.56}\square_{0.38}Ca_{0.06})_{\Sigma 1.00}{}^{Y}(Al_{1.71}Li_{1.20}Mn^{2+}_{0.08}Ti_{0.01})_{\Sigma 3.00}{}^{Z}Al_6[^{T}(Si_{5.97}Al_{0.03})_{\Sigma 6.00}O_{18}](BO_3)_3{}^{V}(OH)_3{}^{W}[(OH)_{0.33}F_{0.49}O_{0.18}]_{\Sigma 1.00}$
	Prismatic section of fragment II
spot #28	$^{X}(Na_{0.56}\square_{0.39}Ca_{0.05})_{\Sigma 1.00}{}^{Y}(Al_{1.78}Li_{1.17}Mn^{2+}_{0.05})_{\Sigma 3.00}{}^{Z}Al_6[^{T}(Si_{5.89}Al_{0.11})_{\Sigma 6.00}O_{18}](BO_3)_3{}^{V}(OH)_3{}^{W}[(OH)_{0.30}F_{0.52}O_{0.18}]_{\Sigma 1.00}$
spot #38	$^{X}(Na_{0.57}\square_{0.43})_{\Sigma 1.00}{}^{Y}(Al_{1.89}Li_{1.10}Mn^{2+}_{0.01})_{\Sigma 3.00}{}^{Z}Al_6[^{T}(Si_{5.83}Al_{0.17})_{\Sigma 6.00}O_{18}](BO_3)_3{}^{V}(OH)_3{}^{W}[(OH)_{0.51}F_{0.30}O_{0.19}]_{\Sigma 1.00}$
spot #40	$^{X}(Na_{0.62}\square_{0.38})_{\Sigma 1.00}{}^{Y}(Al_{1.78}Li_{1.21}Mn^{2+}_{0.01})_{\Sigma 3.00}{}^{Z}Al_6[^{T}(Si_{5.92}Al_{0.08})_{\Sigma 6.00}O_{18}](BO_3)_3{}^{V}(OH)_3{}^{W}[(OH)_{0.71}F_{0.16}O_{0.13}]_{\Sigma 1.00}$
spot #58	$^{X}(Na_{0.56}\square_{0.44})_{\Sigma 1.00}{}^{Y}(Al_{1.76}Li_{1.21}Mn^{2+}_{0.02})_{\Sigma 3.00}{}^{Z}Al_6[^{T}(Si_{5.98}Al_{0.02})_{\Sigma 6.00}O_{18}](BO_3)_3{}^{V}(OH)_3{}^{W}[(OH)_{0.74}F_{0.16}O_{0.10}]_{\Sigma 1.00}$
spot #68	$^{X}(Na_{0.56}\square_{0.44})_{\Sigma 1.00}{}^{Y}(Al_{1.75}Li_{1.23}Mn^{2+}_{0.01})_{\Sigma 2.98}{}^{Z}Al_6[^{T}(Si_{5.97}Al_{0.03})_{\Sigma 6.00}O_{18}](BO_3)_3{}^{V}(OH)_3{}^{W}[(OH)_{0.89}F_{0.06}O_{0.05}]_{\Sigma 1.00}$
average (49 spots)	$^{X}(Na_{0.57}\square_{0.42}Ca_{0.01})_{\Sigma 1.00}{}^{Y}(Al_{1.79}Li_{1.19}Mn^{2+}_{0.02})_{\Sigma 3.00}{}^{Z}Al_6[^{T}(Si_{5.94}Al_{0.06})_{\Sigma 6.00}O_{18}](BO_3)_3{}^{V}(OH)_3{}^{W}[(OH)_{0.63}F_{0.23}O_{0.14}]_{\Sigma 1.00}$

[a] Empirical formulae were based on the Mn_2O_3 content calculated by OAS data

All these compositions are consistent with a tourmaline belonging to the alkali-group, subgroup 2 (Henry et al., 2011): they are Na-dominant at the X position of the general formula of tourmaline and hydroxy-dominant at W with (OH+F) > O and (OH) >> F, except for the OGR overgrowth and the prismatic section of fragment I, which are fluor-species as F > OH.

All the studied compositions are ^{Z}Al- and ^{Y}($Al_{1.5}Li_{1.5}$)-dominant, thus they are elbaitic, $Na(Li_{1.5}Al_{1.5})Al_6Si_6O_{18}(BO_3)_3(OH)_3(OH,F)$, from a nomenclature viewpoint (Henry et al., 2011). In particular, the overgrowths OGX, OGY and OGZ can be classified as Mnr-ich elbaite, whereas the overgrowth OGR is Mn-rich fluor-elbaite. Regarding the prismatic sections, fragments I and II correspond to fluor-elbaite and elbaite, respectively.

Optical absorption spectroscopy

Optical absorption spectra (**E⊥c** and **E||c**) recorded at selected spots within the differently colored overgrowths are reported in Figure 3.19. All the **E⊥c**-spectra of the OGX, OGY and OGZ overgrowths display a main absorption band centred at ~18800 cm^{-1} and a weaker absorption band at ~22000 cm^{-1}. The spectrum of the OGX overgrowth recorded at spot 1 reveals additional absorption bands at ~24500 and ~9500 cm^{-1}. In contrast, the **E⊥c**-spectrum recorded within the OGR overgrowth shows a different absorption pattern with two very broad bands at ~30700 and ~22700 cm^{-1}, and very weak bands at ~27000 and ~24500 cm^{-1}. Additional relatively weak and broad bands occur in the NIR region at ~9000 and ~14000 cm^{-1}. All the spectra recorded in light polarized parallel to the crystallographic **c**-axis (**E//c**), show a weaker absorption and additional very sharp bands between 6700–7200 cm^{-1} in the NIR range ascribed to overtones of the fundamental (OH)-stretching modes.

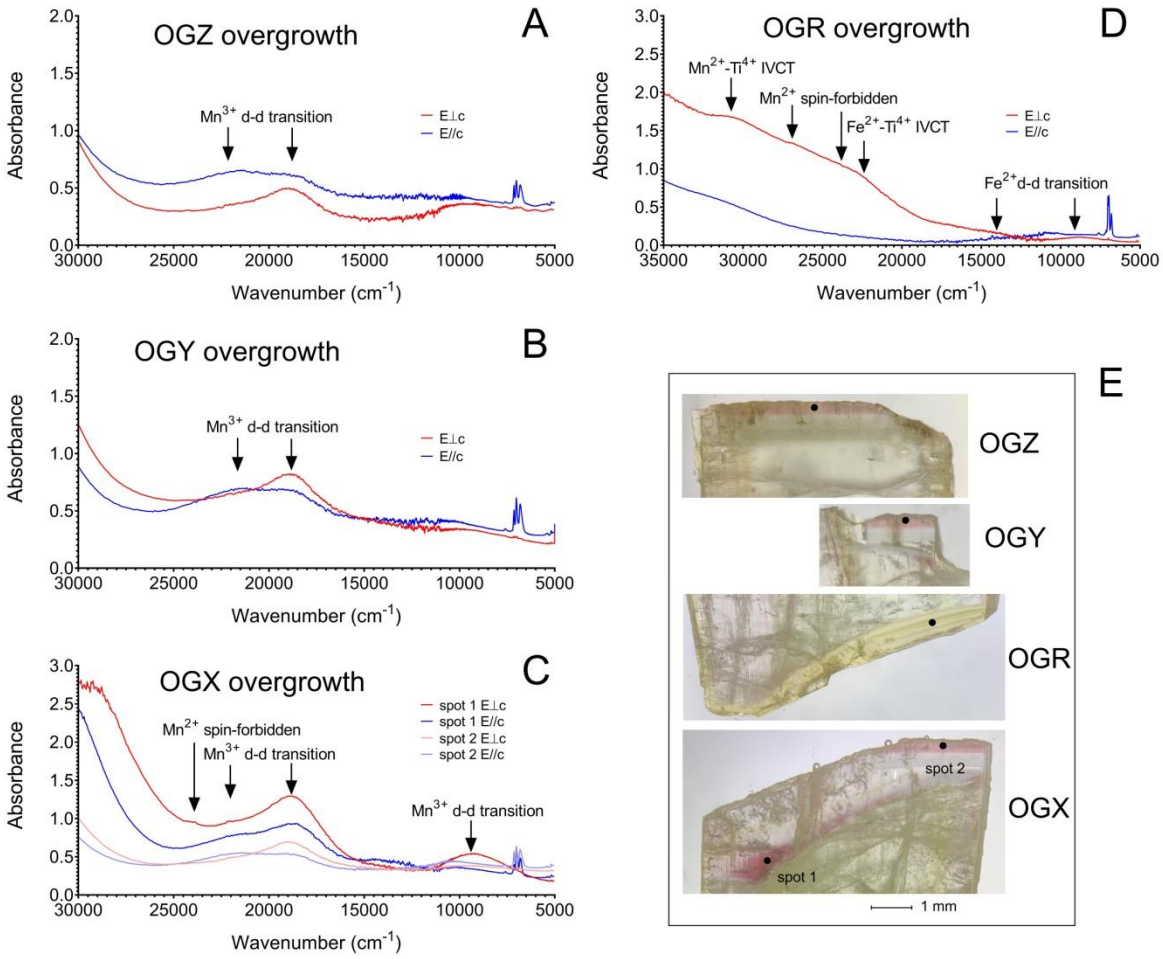

Figure 3.19. Optical absorption spectra of the dark coloured overgrowths polarised perpendicular (E⊥c) and parallel (E||c) to the **c**-axis direction of selected spots in the OGZ (A), OGY (B), OGX (C) and OGR (D) overgrowths. Optical microscopy images of the OGX, OGR, OGY and OGZ overgrowths. The location of spots used for OAS are indicated. Sample thickness: OGX = 820 μm; OGY = 902 μm; OGZ = 658 μm; OGR = 437 μm. Scale bar = 1 mm.

3.4.4 Discussion

Composition analysis

The four overgrowths (OGX, OGR, OGY and OGZ) of the two tourmaline crystal fragments are characterized by a dark color and a sudden increase in MnO, which rises up to 7 wt%. In contrast, the prismatic section of fragment I and II has a very low MnO content, with the exception of the initial part of fragment I (up to 2 wt%) (Fig. 3.16). Although the four overgrowths have similar composition, OGR has slightly more TiO_2, CaO and F, which increases, respectively up to 0.40 wt%, 0.35

wt% and 1.2 wt% (Fig. 3.17; Tables 3.5, 3.6). It should be noted that the overgrowths OGX, OGY and OGZ were formed in the direction of the analogous pole, wherease the overgrowth OGR was formed at the antilogous pole of fragment II. Although the Mn increase at the overgrowths is confirming a significant chemical evolution, the mineralogical species remain elbaite and F-elbaite. This compositional evolution trend is evident in the ternary plots of *X*- and *Y*-site occupancy (Fig. 3.18 A,B), where overgrowths are characterized by an enrichment in Na and Mn, respectively. The increase in Mn at the overgrowths is consistent with the substitution of Li and Al at the *Y* site. A plot of content of 2Li vs. (Mn + Fe) at *Y* site (Fig. 3.18 C), confirms that the analysis points relating to the prismatic sections are close to an elbaite/F-elbaite composition. In contrast, data relating to the overgrowths are distributed along a trend line corresponding to a total or partial replacement of Li and Al with Mn/Fe. A plot of the content of F vs. Na (Fig. 3.18 D) confirms the Na enrichment that characterizes the overgrowths.
Furthermore, in many graphs it is possible to observe a different distribution of the data relating to the overgrowth at the antilogous pole (OGR) compared to the other overgrowths (OGX, OGY and OGZ). This different trend is particularly evident in the Ca vs. Ti plot (Fig. 3.18 E), where most of the data points of the OGR overgrowth lie apart from the other ones. Interestingly, the data related to the different overgrowths follow a different compositional evolution trend in the ternary plot of Na/(Na + $^{X}\square$) vs. Mn/(Mn + 2Li) vs. F (Fig. 3.18 F).

Comparison of the dark overgrowths

The dark overgrowths were compared to ascertain if they were formed simultaneously in the same crystallization environment. As stated above, all overgrowths are characterized by a comparable chemical composition, which is consistent with their formation in the same environment. The antilogous overgrowth OGR compared to the analogous ones shows some differences in Ti, Ca and F content, as well as a smaller length (~500 μm for OGR, ~1000 μm for

OGX and OGZ, and ~700 μm for the lateral overgrowth OGY) (Fig. 3.17; Tables 3.5, 3.6).

Additional evidence supporting the formation of the four overgrowths in the same crystallization environment is provided by OAS data (Fig. 3.19). The overgrowth at the analogous poles (OGX, OGY and OGZ) share the same ~22000 and ~18800 cm^{-1} absorption bands that can be assigned to Mn^{3+} *d-d* transitions (Reinitz and Rossman, 1988; Taran et al., 1993 ; Ertl et al., 2005; Bosi et al., 2021). The additional bands at ~9500 and ~24500 cm^{-1} observed in the spectrum recorded at spot 1 of the OGX overgrowth can be ascribed to a Mn^{3+} spin-allowed *d-d* transition and a Mn^{2+} spin-forbidden transition, respectively (Bosi et al., 2021). These assignments agree with the same purplish-red color of these overgrowths, mainly ascribed to the presence of Mn^{3+} as color-causing agent (Pezzotta and Laurs, 2011). On the basis of the intensity of the Mn^{3+} band at ~18800 cm^{-1} in the spectra perpendicular to the **c**-axis of the analogous overgrowths OGX, OGY and OGZ (Fig. 3.19), and using the molar extinction coefficient suggested by Reinitz and Rossman (1988), the Mn_2O_3 content in these overgrowths was calculated (Table 3.10). The top of the overgrowths OGX, OGY and OGZ are characterized by the same contents of Mn_2O_3 (1.3 wt%) with a Mn^{3+}/Mn_{tot}-ratio ranging from 0.27 to 0.39. This observation, together with the similar composition, is consistent with overgrowths formed simultaneously in the crystallization environment. It should be noted that a second OAS analysis on the bottom part of the OGX overgrowth (spot 1), revealed a greater amount of Mn_2O_3 (2.93 wt%) and a higher Mn^{3+}/Mn_{tot}-ratio. The presence of Mn^{3+} suggests an oxidizing environment during the crystallization of the overgrowths.

Table 3.10. Summary of the OAS results for selected data points on the overgrowths including observed absorption bands, total content of MnO and relative amount of Mn^{3+} calculated by the molar extinction coefficient

Absorption band and assignment	OGX spot 1	OGX spot 2	OGY	OGZ	OGR
~30700 cm^{-1} Mn^{2+}-Ti^{4+} IVCT transition					+
~27000 cm^{-1} Mn^{2+} spin-forbidden transition					+
~24500 cm^{-1} Mn^{2+} spin-forbidden transition	+				+
~22700 cm^{-1} Fe^{2+}-Ti^{4+} IVCT transition					+
~22000 cm^{-1} Mn^{3+} *d-d* transition	+	+	+	+	
~18800 cm^{-1} Mn^{3+} *d-d* transition	+	+	+	+	
~14000 cm^{-1} Fe^{2+} *d-d* transition					+
~9500 cm^{-1} Mn^{3+} *d-d* transition	+				
~9000 cm^{-1} Fe^{2+} *d-d* transition					+
MnO_{tot} (wt%)#	4.18	3.11	3.51	4.31	6.76
Mn_2O_3 (wt%)*	2.93	1.34	1.30	1.30	0
Mn^{3+}/Mn_{tot}	0.63	0.39	0.33	0.27	0

+: absorption band present

#: MnO_{tot} content at the OAS spot was determined on the basis of the chemical analysis conducted along the considered traverses

*: calculated considering the intensity of the Mn^{3+}-band at 18800 cm^{-1} in **E⊥c**-spectra, in combination with the molar extinction coefficient of 7.5 for that absorption band (suggested by Reinitz and Rossman, 1988). Values of absorber thickness: OGX = 820 μm; OGY = 902 μm; OGZ = 658 μm; OGR = 437 μm.

The optical absorption spectra of the OGR overgrowth revealed only the presence of very weak Mn^{2+} spin-forbidden bands (~27000 and ~24500 cm^{-1}), in addition to strong and very broad bands at ~30700 and ~22700 cm^{-1}, which are caused by Mn^{2+}-Ti^{4+} and Fe^{2+}-Ti^{4+} IVCT (Intervalence Charge Transfer) transitions, respectively (Rossman and Mattson, 1986; Taran et al., 1993). The two latter are consistent with compositional data, which revealed an increased amount of Ti in

the OGR overgrowth compared to the other ones. The broad and moderately intense bands in the NIR region at ~9000 and ~14000 cm^{-1}, which are caused by spin-allowed transitions in Fe^{2+} (Mattson and Rossman, 1987) do not contribute to the color of the samples. The band assignments for the OGR overgrowth agree with its yellow-orange coloration due to the presence of Mn^{2+} and Mn^{2+}-Ti^{4+} IVCT as color-causing agents (Rossman and Mattson, 1986; Laurs et al., 2007; Pezzotta and Laurs, 2011). Considering the comparable total MnO contents of all the dark-colored overgrowths (about 4.5 wt%), and that OGZ, OGY and OGR belong to the same crystal fragment and therefore grew at the same time, the absence of Mn^{3+} *d-d* transitions in the OGR spectra suggests a strong preferential incorporation of Mn^{2+} ions in the antilogous overgrowth, even in the presence of Mn^{3+} in the crystallization environment. A similar crystal-chemical behaviour is observed for Ti, Ca and F, which are preferentially incorporated at the antilogous pole (Fig. 3.17; Table 3.5). As a result, the antilogous pole shows a different growth history, with a preferential incorporation of Ca, F and Ti, as well as a selective uptake of Mn^{2+} over Mn^{3+}, leading to a different coloration and tourmaline species (fluor-elbaite instead of elbaite, typical of the other overgrowths). This different behaviour is also evident in several compositional diagrams, where OGR data points occupy a different position in the plot compared to the other overgrowths spots (Fig. 3.18).

The differences observed in the composition and spectroscopic analysis between the analogous and antilogous overgrowths can be related to differences in the growing process occurring at the two poles (surface energy, nucleation speed, piezo- and pyro-electrical properties) (e.g. Henry and Dutrow, 1992).

The formation of the dark-colored overgrowths is likely the result of a pocket rupture. This event changed the chemical environment within the pocket, leading to a sudden increase in the availability of Mn in the geochemical system. Although the initial part of fragment I contains a slight enrichment in MnO (up to 2 wt%), this is related to the amount of Mn remaining available in the pegmatitic system

after the early crystallization of spessartine. The subsequent progressive decrease in MnO content in fragment I is the result of Mn depletion in the system due to tourmaline crystallization. Spessartine crystallization is recognized as an important mechanism for regulating the Mn content during the evolution of the pegmatite systems (Novak et al., 2000; Laurs et al., 2007) and, in Elba pegmatites, spessartine garnet represents the main competitor for Mn during the evolution of pegmatite system (Bosi et al., 2022a). Indeed, spessartine garnet in the Rosina pegmatite is present in the intermediate zone of the pegmatite, close to the miarolitic cavity (Fig. 3.15).

The very limited amount of Fe in the OGR overgrowth, in addition to limited amounts in all the other overgrowths, led us to exclude that this may represent the root part of the crystal. Therefore, it is reasonable to assume that this dark termination was formed on a new growth surface as a consequence of a natural breakage event which the prismatic section of the crystal underwent. Observing the two crystal fragments and disregarding the dark-colored overgrowths, the shape of analogous termination of fragment I and the antilogous one of fragment II match perfectly. This demonstrates that they are two crystal fragments belonging to the same original tourmaline crystal which broke during pocket collapse and on which late-stage overgrowths (OGR and OGX) occurred.

Comparison of the prismatic sections

In support of the evidence that the fragments (I and II) were part of the same original crystal, the analytical data document a perfect continuity (Fig. 3.20). Disregarding the data points related to the OGX and OGR overgrowths, compositional analysis revealed no significant variations for the different oxide components between the two prismatic sections, as expected if they had been joined together (Fig. 3.20; Tables 3.7, 3.8). As consequence of the crystal breakage, OGX and OGR overgrowths have been formed on the new growth surfaces generated by the break.

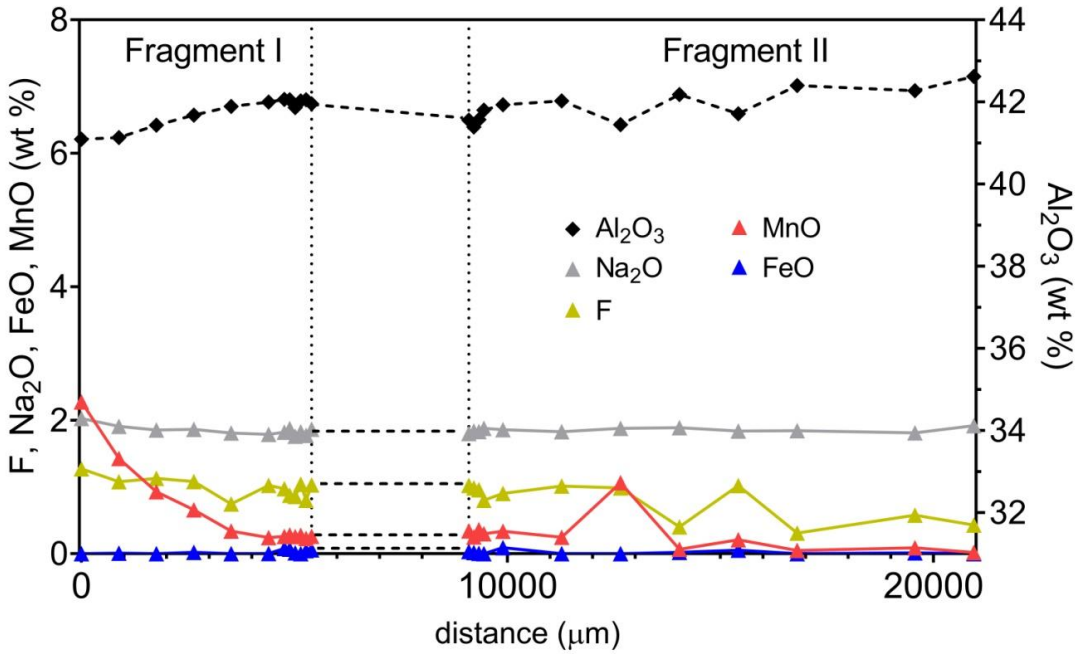

Figure 3.20. Compositional analysis of the two prismatic sections close to OGX/OGR breakage.

Genetic model for the dark-colored overgrowths

Elba tourmalines are renowned all over the world for their characteristic dark terminations, which are due to the incorporation of elements, such as Fe and/or Mn during the latest stages of crystallization in miarolic cavities (Pezzotta, 2021). However, the mechanisms that led to the availability of these elements in the residual fluids have previously been unclear.

Microstructural and paragenetic observations of the cavities in which tourmaline crystals with dark-colored overgrowths were formed, provide evidence that such pockets are characterized by: i) thin fractures penetrating from the cavity into the enclosing pegmatite; ii) leaching and corrosion of early-formed cavity-lining and cavity-coating Fe- and Mn-rich minerals crosscut by the fractures; iii) partial collapse of quartz and feldspar crystal aggregates and iv) the breakage of some tourmaline crystals as consequence of a partial pocket collapse (Bosi et al., 2022a; Altieri et al., 2022). These features are particularly evident in the Rosina pegmatite from which the tourmaline crystals originated (Fig. 3.15). The pocket rupture occurred during the formation of a series of fractures penetrating the surrounding

pegmatite, in which more primitive accessory minerals such as spessartine garnet and Fe-rich mica crystals were present (Fig. 3.15). Highly-reactive late-stage cavity fluids penetrating the fractures, allowed the corrosion of the Fe- and Mn--rich minerals causing a sudden change in the chemical composition of the pocket crystallization environment. Etching of spessartine garnet by late-stage reactive fluids has aleady been reported by London (2006) and Felch et al. (2016), and similar evidence of corroded spessartine crystals occurs in the Rosina pegmatite (Figure 3.21). To account for the presence of Mn both in +2 and +3 redox states in the dark-colored overgrowths, corrosion and alteration phenomena likely occurred in a relatively oxidizing environment.

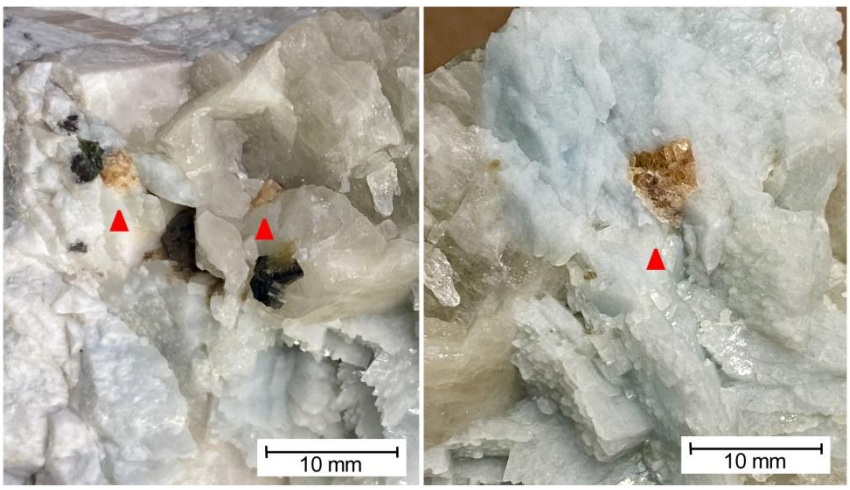

Figure 3.21. Examples of heavily fractured and partially corroded spessartine crystals (red arrows) "frozen" in quartz and feldspars in proximity of cavities of the Rosina pegmatite. Crystals up to 6 mm in diameter. Scale bar = 10 mm.

The pocket rupture was responsible for the breakage of the crystal studied in this work, allowing for the formation of two new growth surfaces (OGX and OGR). In our model, OGZ represents the overgrowth at the termination of the original analogous pole of the crystal, whereas OGX and OGR correspond to the overgrowths formed at the new analogous and antilogous pole surfaces, respectively, as a result of the crystal breakage. The OGY overgrowth is related to a smaller lateral crystal breakage (Figure 3.22).

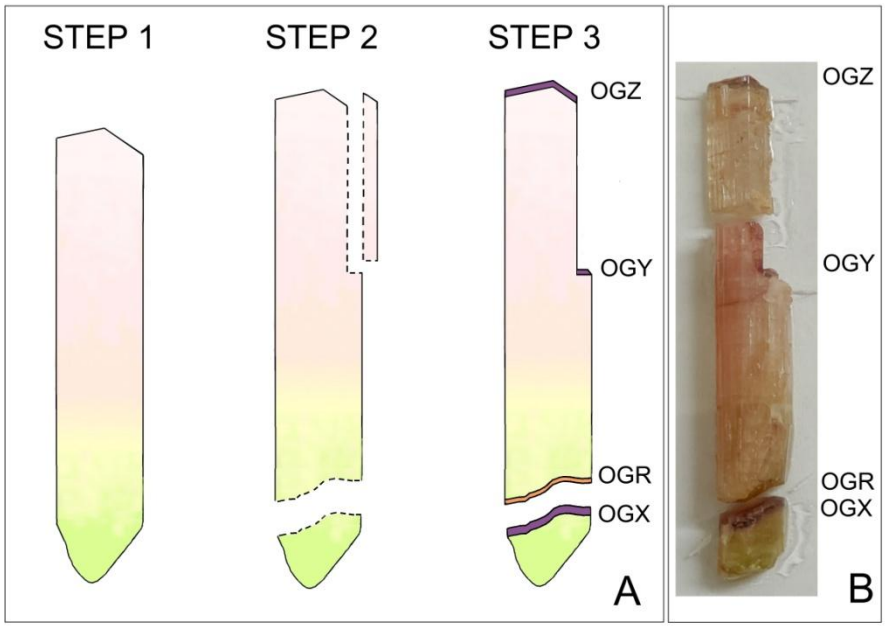

Figure 3.22. Schematic representation of the history of growth of the tourmaline crystals investigated. A) Step 1: tourmaline crystal growth from light green to pale pink in the direction of the analogous pole (**c**- side). Step 2: breakage of the crystal as a result of the pocket rupture event followed by changes in the chemical composition of the crystallisation environment. Step 3: generation of late-stage dark-coloured overgrowths at the analogous (OGX, OGY, OGZ) and at the antilogous (OGR) poles in a Mn-rich environment. B) Image of the tourmaline crystals investigated.

The crystal breakage strengthens the hypothesis that the cavity has undergone a mechanical destabilisation. Consequently, the studied tourmaline crystal fragments preserved important records not only in terms of compositional variations of the geochemical system, represented by the dark overgrowths, but also in the mechanical events, that is the crystal breakage.

A comparison of the overgrowths at the analogous and antilogous poles provides evidence of a preferential incorporation of elements at these growth surfaces. In fact, the antilogous pole is characterized by a different growth rate and higher concentrations of Ca, F and Ti. The differential uptake of these elements at the analogous and antilogous pole have been described by Henry and Dutrow (1992) and van Hinsberg et al. (2006) as a result of combined effect of "lattice site morphology" on the different growth faces and dipolar surface charge related to systematic orientation of the ring of tetrahedra. Here we report a further preference at level of the ionic charge of the same element. OAS data show a

selective uptake of Mn^{2+} at the antilogous pole in the presence of a substantial amount of Mn^{3+} ions, which preferred the analogous one. This different uptake has never been reported before and could be related to a greater partition coefficient for Mn^{3+} at the analogous surface. The preferential uptake of Mn^{3+} ions by the analogous growing surfaces led to a decrease in the Mn^{3+}/Mn_{tot}-ratio in the crystallizing fluids. A change in this ratio can be deduced by analyzing the OAS data of the more extended OGX overgrowth. In fact, OGX is characterized by a marked decrease in Mn^{3+} content along the growth direction, maintaining approximately the same MnO_{tot} content.

3.4.5 Conclusions

The tourmaline crystal fragments analyzed in this work represent a key witness of the mechanical and compositional changes during the latest stages of cavity evolution as a consequence of a pocket rupture event. The comparison of the dark overgrowths formed on the direction of the analogous pole and the antilogous one in the same crystal, has provided new evidence on the different growing process occurring at the two poles involving Mn^{2+}/Mn^{3+} ions.

This work clearly correlates structural information (i.e., fracturing of the pocket and breakage of tourmaline crystals) to the late-stage tourmaline growth, and allowed us to define and propose a genetic model for the dark-colored overgrowths in Elba tourmaline crystals.

3.5 CASE STUDY 3 - Genetic model for the color anomalies at the termination of pegmatitic gem tourmaline crystals from Elba Island (Tyrrhenian Sea, ITALY)

3.5.1 Introduction

Elba tourmalines gained interest among mineral connoisseurs during the 19th century for the perfection of their crystal shape and the variety of colors displayed (Pezzotta, 2021). The most unusual and famous Elba tourmaline variety is represented by the "black cap" crystals (the so-called "Moor's head" textural types), which are characterized by transparent yellow-green, olive-green, pink or colorless prismatic sections with sharp transitions to black color at the analogous terminations (Pezzotta, 2021). Such termination shows a wide range of morphological characteristics: it may occur as a narrow overgrowth with a sharp and lustrous pedion face ending the crystal (Fig. 3.23 A), or as a thick overgrowth with rough pyramidal faces characterized by a rather fibrous texture (Fig. 3.23 B) that, occasionally, can be composed of an aggregate of long parallel needles (Fig. 3.23 C); all intermediate morphological cases are also present.

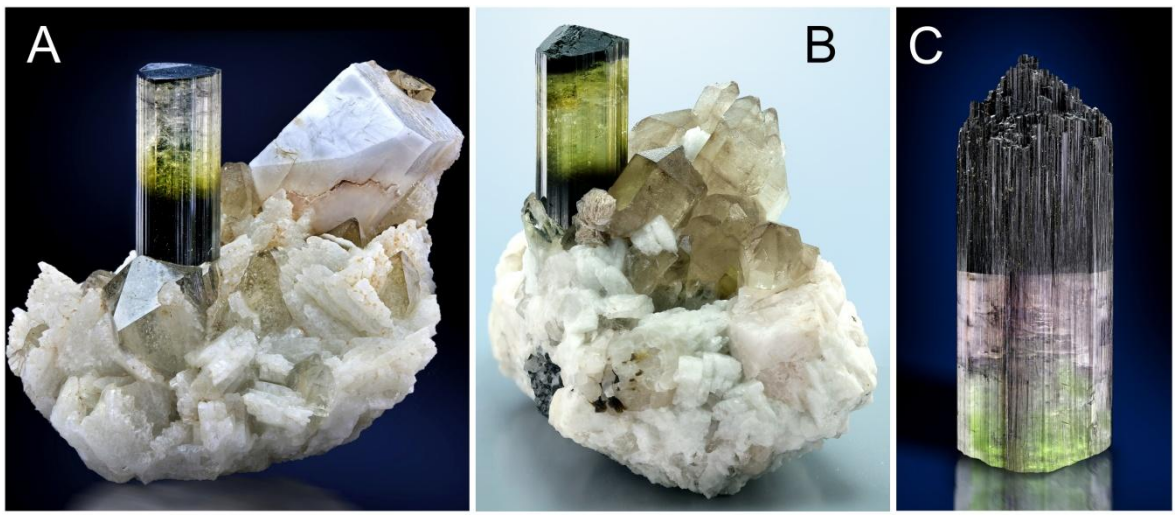

Figure 3.23. A) Thin black overgrowth evidenced by a lustrous pedion face at the termination of a multicolored tourmaline crystal on matrix; B) Thick black overgrowth with rough pyramidal faces at the termination of a multicolored tourmaline crystal on matrix; C) Fibrous black overgrowth on a multicolored tourmaline crystal. All specimens are from Elba Island (Italy). Private collection. A. Miglioli photo.

However, in some pegmatitic veins the terminations of the tourmaline crystals are not simply black, but they are made up by multiple thin growth-zones of bluish, greenish, brownish or even purplish-to-reddish colors (Pezzotta, 2021; Bosi et al., 2022a; Altieri et al., 2022, 2023). These dark-colored terminations can be generally ascribed as *color anomalies*.

It is well known that tourmaline crystals are able to register the physicochemical changes in the crystallization environment during their growth (Hawthorne and Dirlam, 2011). Therefore, it is reasonable to assume that the color anomalies at the analogous termination observed in tourmaline crystals from Elba Island likely reflect processes that occurred in tourmaline-rich pegmatites during the latest stages of crystallization. Recently, Altieri et al. (2023) provided evidence that such processes in Elba Island pegmatites are the result of a more-or-less partial opening of the geochemical system, related to a pocket rupture event.

The goal of this study is to describe through chemical and spectroscopic analyses the crystal zones characterized by such color anomalies in different tourmaline samples. The studied tourmaline crystals have been collected from several cavities found during some mining acrivity for mineral specimens, within four representative pegmatitic veins located in the area of the villages of San Piero and Sant'Ilario in Campo (Elba Island, Italy); each crystal has been selected for representing a dark overgrowth with a different color and crystal texture. The four pegmatitic veins from which the studied tourmaline crystals were collected belong to the second (the Rosina and the San Silvestro pegmatites) and the third group (the Federico and the Pastori pegmatites) of the Monte Capanne aplitic-pegmatitic veins classification system according to Pezzotta (2000) criteria (Fig. 3.24).

Rosina and San Silvestro are two parallel aplite-pegmatite veins (approximately 5 meters apart), with direction approximately North-South and a variable dipping to the West from 60° to 80°. Both veins are hosted by monzogranite in the San Piero in Campo locality and have been deeply mined in the past for mineral specimens (Pezzotta, 2021; Bosi et al., 2022a). Among the two bodies, the Rosina

pegmatite is by far the largest one and it is composed by a central section of about 10 m long, up to 2 m thick, which has been mined down for about 6 meters. From this central section, a series of pegmatite strings extend along the emplacement direction in the monzogranite. During the mining activity, the Rosina vein revealed a quite large number of small to medium-large sized elongated or tabular pockets, up to a maximum of ~ 80 dm^3 in volume. The body shows a complex and well-structured internal asymmetric zoning with a mostly aplitic-layered unit at the footwall. The pocket paragenesis ranges from primitive to highly evolved, with euhedral crystals of quartz and feldspars, together with lepidolite, gem-tourmaline, beryl, petalite, pollucite and several other accessory minerals (Pezzotta, 2021). The axial core-miarolitic zone divides a medium-grained lower section enriched in albite with minor K-feldspar, quartz, spessartine garnet, patches of sekaninaite and tourmaline in graphic aggregates with quartz, from an upper coarse-grained section enriched in feldspar with minor albite, quartz, and graphic to comb-textured tourmaline. Thin radial fractures and phenomena of cavity collapse are evident around the larger pockets. The presence in the pegmatitic rock around the cavities of corroded and/or altered crystals and masses of "biotite", sekaninaite, and spessartine garnet, more-or-less associated with extensive albitization of K-feldspar and locally a new generation of K-feldspar and quartz, suggest that a fluid circulation occurred during the latest stages of evolution of the vein (Orlandi and Pezzotta, 1996; Pezzotta, 2000; Bosi et al., 2022a; Altieri et al., 2023).

The San Silvestro pegmatite is very similar to the Rosina pegmatite, but it is smaller, being the central productive section no more of 3.5 m long. In such central section a large, flat, irregularly oblate pocket of approximately 350 dm^3 in volume (2.30 x 0.35 x 0.70 m) was discovered. A "pocket plane" divides the pegmatitic core into a lower and an upper unit, with structures and mineralogy similar to what has already been already described for the Rosina pegmatite. Around the "main pocket", radial microfractures were present, more-or-less lined with tiny crystals

of quartz, albite and dark-yellow-green tourmaline. Along such fractures, a widespread alteration of biotite crystals and a significant albitization of the K-feldspar were evident (Pezzotta, 2000; Altieri et al., 2022).

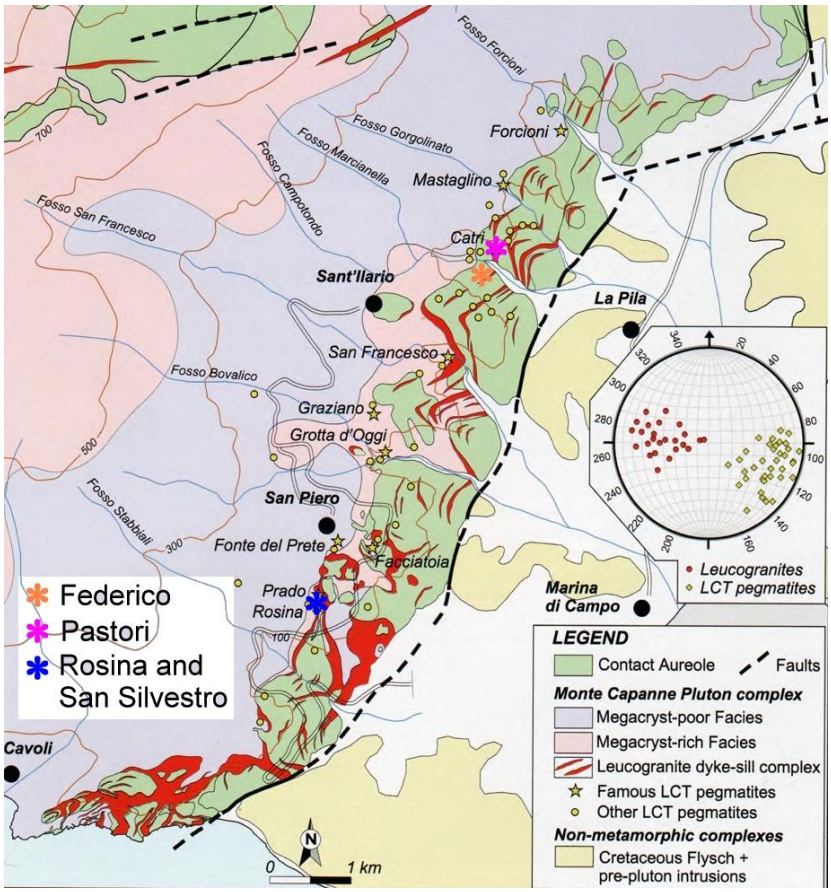

Figure 3.24. Geologic map of the eastern border of Monte Capanne monzogranite pluton. The areas of occurrence of the gem-bearing pegmatites from which the studied tourmaline samples were collected are indicated the by different colored asterisks (modified after Pezzotta 2021).

The Federico dyke and the Pastori dyke are both miarolitic and Li-bearing and are characterized by a simple asymmetric zoning. These dykes have a North-South direction, they are dipping to the West at about 70° to 80°, and they are hosted in the porphyritic monzogranite close to the contact with the country rocks of the thermometamorphic aureole, in the Sant'Ilario in Campo locality. Both dykes are 7-8 meters long and they do not exceed the thickness of 25 centimeters. Miarolitic cavities are locally abundant. The cavity plane divides the veins in two different units, a mostly medium grained and albitic lower one, typically characterized by

tourmaline in comb texture, and a coarse grained upper one rich in K-feldspar crystals. Mineral assemblages and pocket paragenesis are similar to the highly evolved ones of the group II dykes above described. A remarkable mineral segregation is present in the cavities of such veins, with most of the K-feldspar crystals confined to the roof, and most of the albite and of the tourmaline, the petalite and the pollucite confined at the base. Two fracturing events can be distinguished in such veins and cavities: a first one which is very limited and it is associated with the formation of a dark overgrowth at the termination of the tourmaline crystals; and a local, second, more dramatic one which is associated with a deep late-stage corrosion of feldspars and tourmaline, and occasionally even quartz (Orlandi and Pezzotta, 1996; Pezzotta, 2000).

Chemical and spectroscopic investigations, combined with microstructural and paragentic observations of the cavities in which the tourmaline crystals were collected, have been used to corroborate a general genetic model for the color anomalies in Elba tourmaline crystals, which represent an evolution and a better definition of a model already proposed in Bosi et al. (2022a) and Altieri et al. (2022, 2023).

The results obtained from this study represent a draft of a manuscript to be submitted to a peer-reviewed international journal. In this paper, the candidate is the first author and the main responsible for the analytical work, data interpretation, figures and tables production and the manuscript draft.

3.5.2 Analytical methods

The studied samples

From the above mentioned four pegmatitic dykes, nine tourmaline samples collected in nine different miarolitic cavities were studied (Fig. 3.25 A-I and Table 3.11). The sample selection criteria were based on the crystal features, choosing those samples that are better representative of the variety of the color anomalies at the termination of Elba tourmalines. Although the samples “Rosina 2” and “Violet Cap” were characterized in previously studies (Bosi et al., 2022a; Altieri et al.,

2023), they were included in this work because they are representative of two typical color and texture types.

Table 3.11. Occurrence and distribution of the tourmaline samples analyzed for this study (Elba Island, Italy).

Sample	Pegmatite	Pocket	Pegmatitic group	Geographical coordinates	Locality
Rosina 2	Rosina	Polluciti	II	41°44'51,62 N – 10°12'37,90 E	San Piero in Campo
Testa Scura	"	"	II	"	
Giganti Storti	"	Giganti storti	II	"	
Testa Rossa	"	Farfalle	II	"	
Testa Viola	"	Candele	II	"	
Violet Cap	"	Violet Cap	II	"	
San Silvestro	San Silvestro	Central cavity	II	41°44'51,62 N – 10°12'37,90 E	
Federico	Federico	-	III	42°46'05,24 N – 10°13'21,57 E	San't Ilario in Campo
Pastori	Pastori	-	III	42°46'01,71 N – 10°13'18,79 E	

Samples preparation

All the tourmaline samples were glued to a glass-slide using epoxy resin, with their length parallel to the surface of the slide. A slice of each crystal was cut along the fastest growth direction (crystallographic **c**-axis) and subsequently ground and polished to produce a flat surface with a uniform thickness of 500 μm for electron microprobe analysis (EMPA).

Based on quantitative chemical data obtained by EMPA, crystal fragments from zones of the colored overgrowths with significant Fe contents were extracted for Mössbauer spectroscopy analysis. Small amounts (1-2 mg) of the material were finely ground under acetone in an agate mortar, mixed with thermoplastic resin and then shaped to a millimetric-sized cylindrical absorber under mild heating.

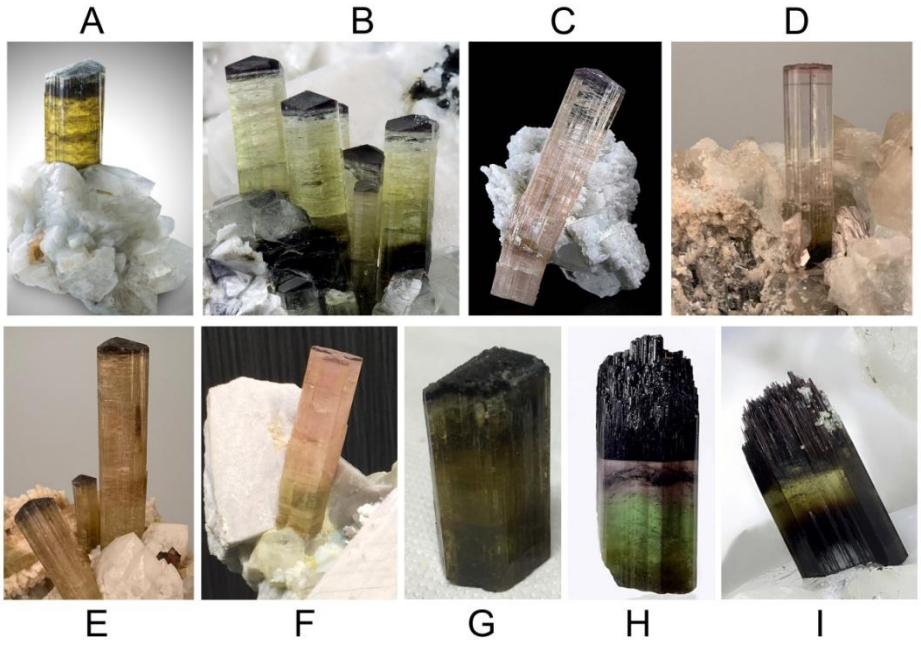

Figure 3.25. The tourmaline samples analyzed for this work. A) Rosina 2: an olive-green to yellow-green tourmaline crystal characterized by a dark purplish-bluish-grey overgrowth at the analogous pole. Crystal 17 mm tall. Photo by F. Picciani; B) Testa Scura: a brownish to light green tourmaline crystal with a thick black overgrowth at the termination. Crystals up to 18 mm. Photo by M. Chinellato; C) Giganti storti: a pale pink tourmaline crystal with a thin violet termination. Crystal 30 mm across. Photo by P. Rustemeyer; D) Testa Rossa: a light green to pink tourmaline crystal characterized by a thin purplish-red overgrowth at the termination. Specimen 90 mm across. Photo by M. Lorenzoni; E) Testa Viola: a yellowish brown tourmaline crystal with a thick dark purple termination. Crystal 70 mm across. Photo by M. Lorenzoni; F) Violet Cap: a light green to pink tourmaline crystal characterized by a purplish overgrowth at the termination. Specimen 70 mm across. Photo by F. Pezzotta; G) San Silvestro: a brownish tourmaline crystal with a thick black termination, 40 mm across. Photo by F. Pezzotta; H) Federico: multi-colored tourmaline crystal from green to light pink with a thick black overgrowth characterized by a fibrous texture. Crystal 30 mm tall. Photo by M. Chinellato; I) Pastori: a brownish to yellow-green tourmaline crystal with a black overgrowth composed by an arrangement of needles, 12 mm tall. Photo by M. Chinellato.

Electron Microprobe analysis (EMPA)

Compositional data were collected along a straight traverse parallel to the **c**-axis from the base to the termination of each crystal (Figure 3.26 A-I) with an average step size of 300 μm, using a CAMECA SX50 electron-microprobe (in WDS mode) at the "Istituto di Geologia Ambientale e Geoingegneria (Rome, Italy), CNR". EMP analysis was done operating in wavelength-dispersion mode with an accelerating potential of 15 kV, a sample current of 15 nA and a beam diameter of 10 μm. A total of 334 spot analysis were collected (Federico: 24 spots; Giganti Storti: 34

spots; Pastori: 52 spots; Rosina 2: 31 spots; San Silvestro: 39 spots; Testa Rossa: 19 spots; Testa Scura: 30 spots; Testa Viola: 22 spots; Violet Cap: 87 spots). Minerals and synthetic compounds were used as standards as follows: wollastonite (Si, Ca), magnetite (Fe), rhodonite (Mn), rutile (Ti), corundum (Al), karelianite (V), fluorphlogopite (F), periclase (Mg), jadeite (Na), orthoclase (K), sphalerite (Zn), metallic Cr and Cu. The PAP correction procedure for quantitative electron probe micro analysis was applied (Pouchou and Pichoir, 1991). Relative error on data was < 5% and detection limits < 0.03 wt%.

Mössbauer spectroscopy (MS)

The ^{57}Fe Mössbauer spectra of the Fe-rich zones of the dark-colored overgrowths in Federico, Rosina 2, and San Silvestro samples were collected using a conventional spectrometer with ^{57}Co source of 0.99 GBq (25 mCi) embedded in a Rh matrix at the Earth Sciences Department, Sapienza University of Rome (Italy). The spectra were collected in transmission mode, at room temperature and at velocities between –4 to + mm/s, and recorded in a multichannel analyzer with 512 channels. The velocity was calibrated with a 25-μm thick α-iron foil. For Pastori sample, measurements were performed using a conventional spectrometer system equipped with a 10 mCi point source and operated in constant acceleration mode at the Swedish Museum of Natural History (Stockholm, Sweden). The absorber was mounted on strip tape and positioned close (<1 mm) to the tip of the point source. Data were collected at room temperature over the velocity range ±4.2 mm/s and recorded in a multichannel analyzer with 1024 channels. The velocity was calibrated with an α-Fe foil. The obtained spectrum from Federico, Rosina 2 and San Silvestro overgrowth was fitted to Lorentzian line-shapes using the RECOIL 1.04 fitting program (Lagarec and Rancourt, 1998), whereas that of Pastori using the MossA fitting program (Prescher et al., 2012)

Determination of site populations

The wt% of element oxides determined by EMPA was used to calculate the atomic

fractions (atoms per formula unit, apfu). The B content was assumed to be stoichiometric (B = 3.00 apfu). Lithium was calculated in accord with Pesquera et al. (2016). The (OH) content was calculated by charge balance with the assumption (T + Y + Z) = 15.00 apfu and 31 anions. Iron oxidation state of the Fe-rich zones of the dark-coloured overgrowths in Federico, Rosina 2, San Silvestro and Pastori samples was determined by MS. Based on the apfu, the site populations and the empirical formulae were calculated following the site allocation of ions recommended by Henry et al. (2011).

3.5.3 Results

Chemical composition

On the basis of the compositional data and colour displayed, each sample has been divided in different zones relatively homogeneous in composition. For each zone, atoms per formula unit (apfu) were calculated and the relative empirical formula was assessed (Tables 3.12-3.22). Figures 3.26 (A-I) display the pattern of selected elements (as wt% oxides) determined along the considered traverse for each tourmaline sample.

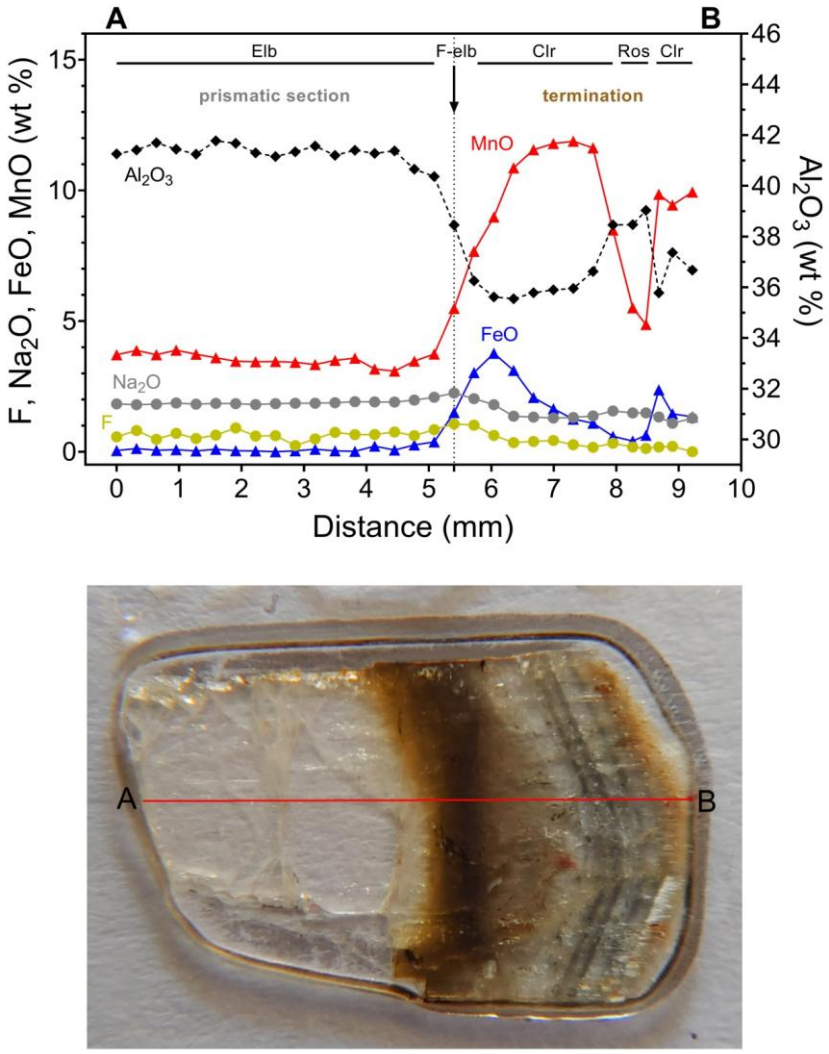

Fig. 3.26A. EMP analysis of **Rosina 2** sample along a straight traverse parallel to the **c**-axis (only selected oxides are reported). See Table 3.12 for complete chemistry.

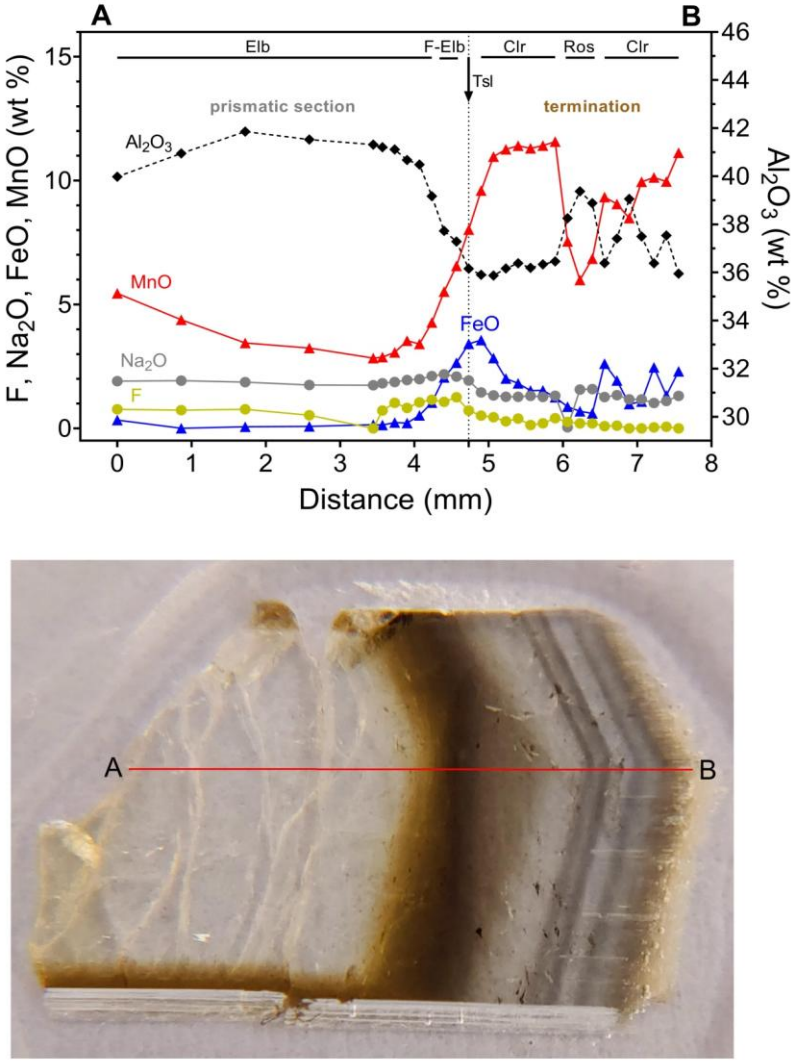

Fig. 3.26B. EMP analysis of **Testa Scura** sample along a straight traverse parallel to the **c**-axis (only selected oxides are reported). See Table 3.13 for complete chemistry.

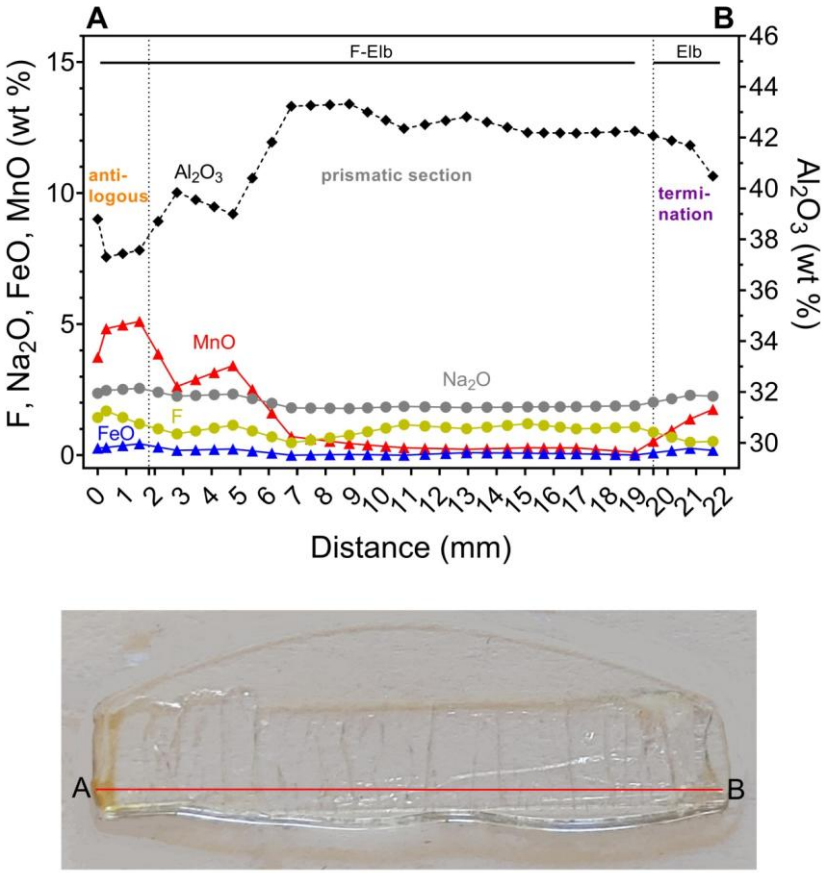

Fig. 3.26C. EMP analysis of **Giganti storti** sample along a straight traverse parallel to the **c**-axis (only selected oxides are reported). See Table 3.14 for complete chemistry.

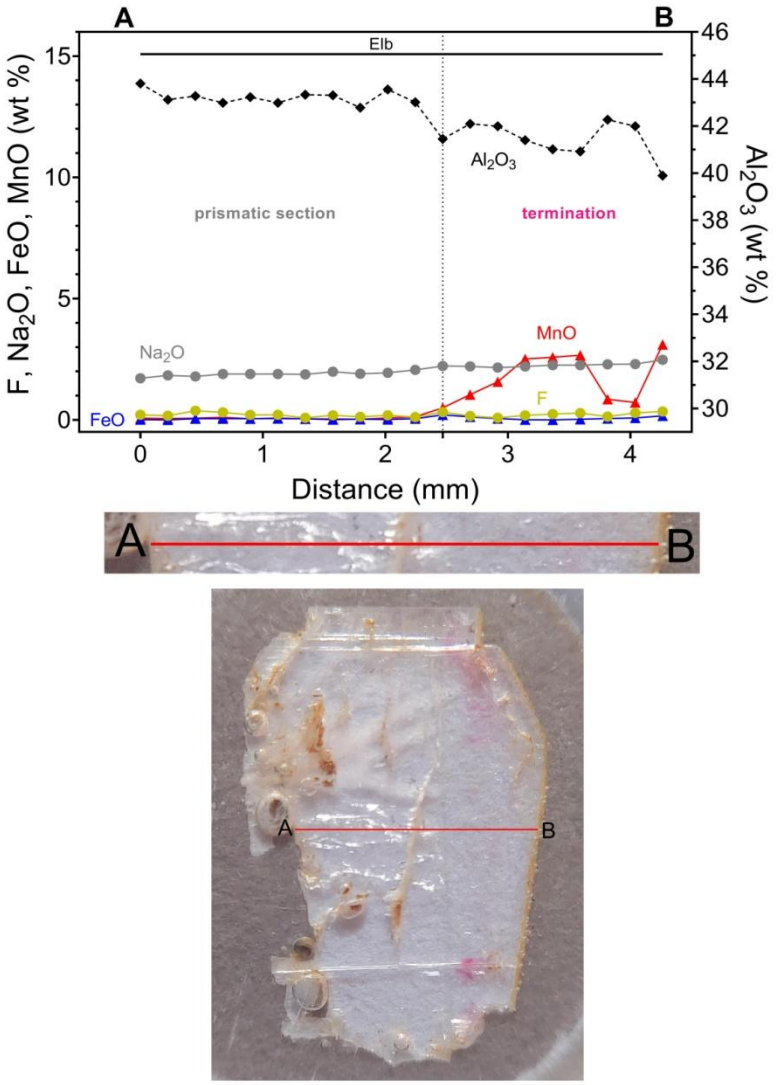

Fig. 3.26D. EMP analysis of **Testa Rossa** sample along a straight traverse parallel to the **c**-axis (only selected oxides are reported). See Table 3.15 for complete chemistry.

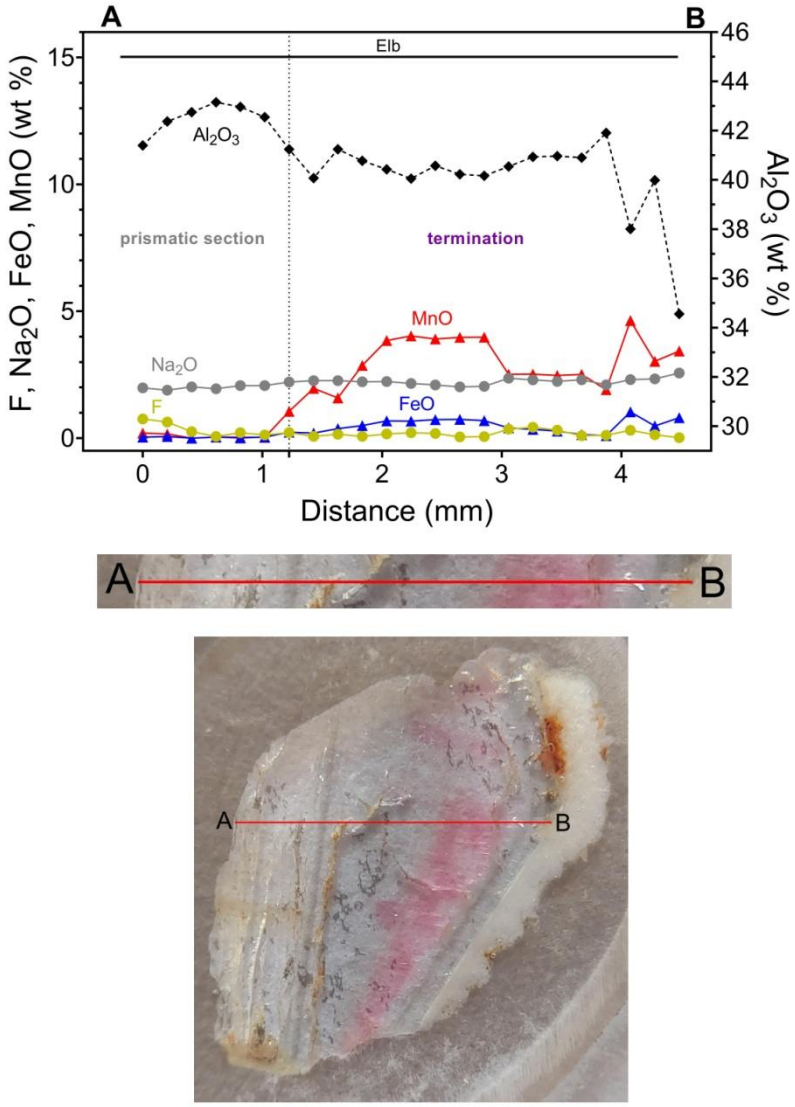

Fig. 3.26E. EMP analysis of **Testa Viola** sample along a straight traverse parallel to the **c**-axis (only selected oxides are reported). See Table 3.16 for complete chemistry.

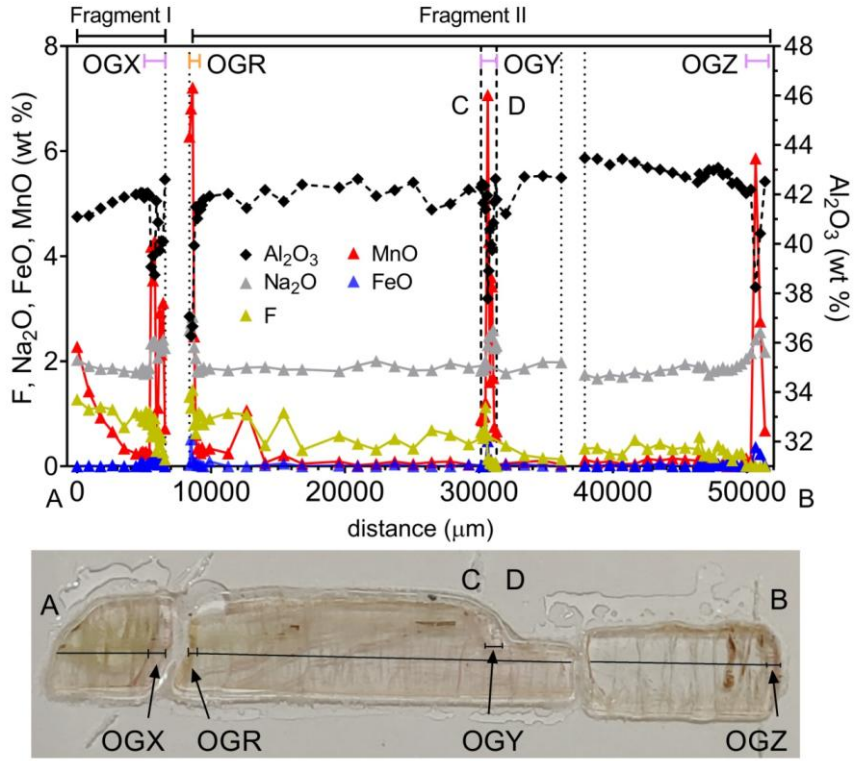

Fig. 3.26F. EMP analysis of **Violet Cap** sample along a straight traverse parallel to the **c**-axis (only selected oxides are reported). See Tables 3.17-3-19 for complete chemistry.

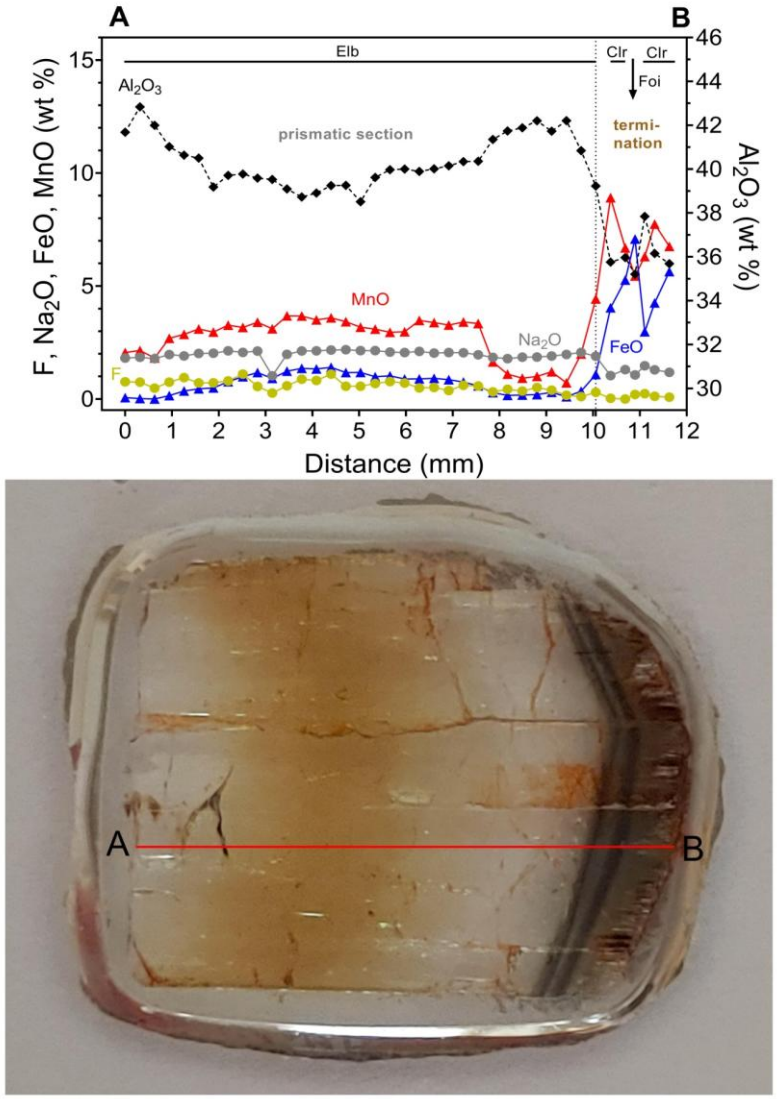

Fig. 3.26G. EMP analysis of **San Silvestro** sample along a straight traverse parallel to the **c**-axis (only selected oxides are reported). See Table 3.20 for complete chemistry.

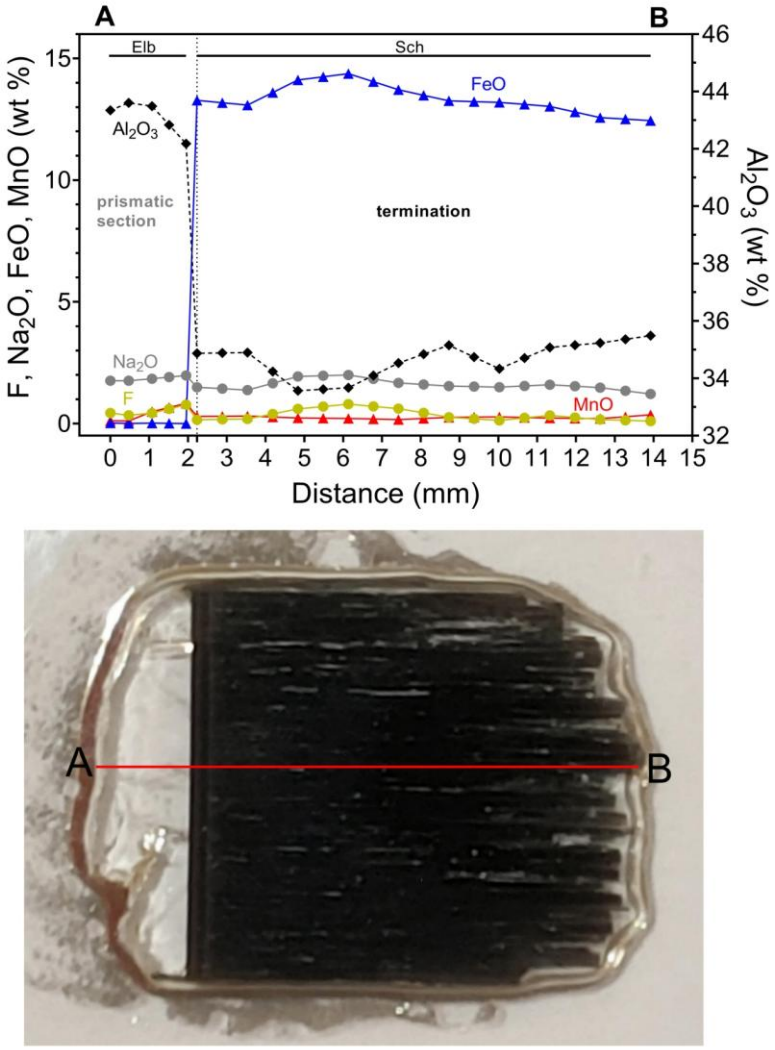

Fig. 3.26H. EMP analysis of **Federico** sample along a straight traverse parallel to the **c**-axis (only selected oxides are reported). See Table 3.21 for complete chemistry.

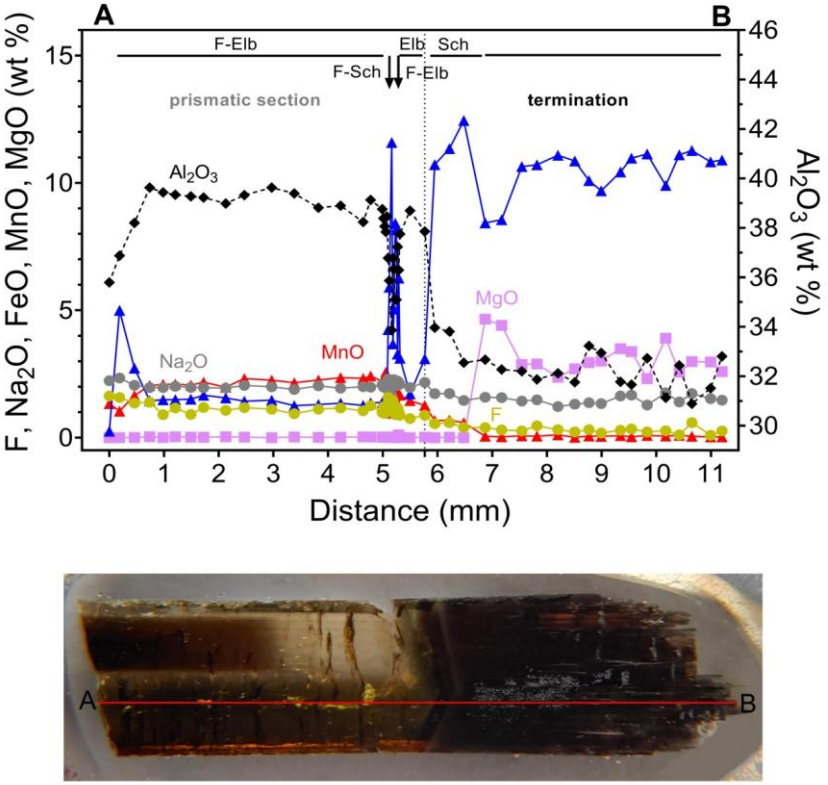

Figure 3.26I. EMP analysis of **Pastori** sample along a straight traverse parallel to the **c**-axis (only selected oxides are reported). See Tables 3.22 for complete chemistry.

Table 3.12. Average chemical composition and atoms per formula unit (a.p.f.u) for the different zones of Rosina 2 sample (San Piero in Campo, Elba Island, Italy) with the relative empirical formula.

	Prismatic section		**Termination**					
	Z1	**Z2**	**Z3**	**Z4**	**Z5**	**Z6**	**Z7**	**Z8**
	n = 17	*n* = 1	*n* = 5	*n* = 1	*n* = 1	*n* = 1	*n* = 1	*n* = 2
SiO_2 wt%	37.65(32)	36.91	36.43(30)	37.77	36.98	37.62	37.09	37.48(4)
TiO_2	0.12(3)	0.24	0.13(3)	0.09	0.05	0.06	0.09	0.05(1)
B_2O_3	11.04[a]	10.76[a]	10.61[a]	10.95[a]	10.74[a]	10.89[a]	10.68[a]	10.83[a]
Al_2O_3	41.30(35)	38.46	35.96(40)	38.46	38.47	39.03	35.78	37.02(49)
FeO_{tot}	0.09(10)	1.50	1.83(81)	0.59	0.41	0.63	2.36	1.39(8)
MnO	3.54(22)	5.48	11.55(40)	8.49	5.51	4.87	9.85	9.69(35)
MgO	-	0.02	0.02(1)	0.01	-	0.05	0.03	0.05(1)
CaO	0.06(3)	0.07	0.01(1)	0.03	0.01	0.02	-	-
Na_2O	1.87(7)	2.25	1.33(3)	1.56	1.48	1.49	1.33	1.19(13)
K_2O	0.01(1)	0.00	0.01(1)	0.03	0.00	0.04	0.01	0.02(2)
Li_2O [b]	1.44[b]	1.12[b]	0.33[b]	0.91[b]	1.32[b]	1.40[b]	0.61[b]	0.71[b]
F	0.63(16)	1.07	0.32(10)	0.32	0.18	0.12	0.18	0.10(14)
H_2O	3.28[a]	2.92[a]	3.39[a]	3.51[a]	3.68[a]	3.75[a]	3.59[a]	3.71[a]
$-O \equiv F$	–0.27	–0.45	–0.13	–0.13	–0.07	–0.05	–0.08	–0.04
FeO	0.09	-	1.83	0.59	0.41	0.63	2.27[c]	1.39
Fe_2O_3	-	-	-	-	-	-	0.09[c]	-
Total	100.80	100.35	101.82	102.60	98.77	99.97	101.56	102.23
	Atoms normalized to 31 anions							
Si apfu	5.927	5.963	5.976	5.994	5.986	6.001	6.038	6.016
Ti	0.014	0.029	0.016	0.011	0.006	0.007	0.011	0.006
B	3.000	3.000	3.000	3.000	3.000	3.000	3.000	3.000
Al	7.663	7.322	6.942	7.193	7.338	7.339	6.864	7.003
Fe^{3+}	-	-	-	-	-	-	0.012	-
Fe^{2+}	0.012	0.203	0.251	0.078	0.055	0.084	0.309	0.187
Mn^{2+}	0.472	0.750	1.602	1.141	0.755	0.658	1.358	1.317
Mg	0.000	0.000	0.005	0.002	0.000	0.012	0.007	0.012
Ca	0.010	0.012	0.002	0.005	0.002	0.007	0.000	0.001
Na	0.572	0.704	0.422	0.480	0.407	0.459	0.419	0.369
K	0.002	0.000	0.002	0.005	0.000	0.008	0.001	0.003
Li	0.912	0.728	0.217	0.581	0.859	0.898	0.399	0.458
F	0.316	0.545	0.167	0.161	0.092	0.062	0.093	0.058
OH	3.449	3.144	3.704	3.714	3.975	3.985	3.900	3.975
OH+F	3.765	3.689	3.871	3.875	4.067	4.048	3.992	4.026
Species	**Elbaite**	**Fluor-elbaite**	**Celleriite**	**Celleriite**	**Rossmanite**	**Rossmanite**	**Celleriite**	**Celleriite**

[a] Calculated by stoichiometry (see text);
[b] Estimated with the procedure of Pesquera et al. (2016);
[c] Determined by Mössbauer spectroscopy
Errors for oxides and fluorine are standard deviations (in brackets)

Empirical chemical formulae

Z1
$$^{X}(Na_{0.57}\square_{0.42}Ca_{0.01})_{\Sigma 1.00}\,^{Y}(Al_{1.59}Li_{0.91}Fe^{2+}_{0.01}Mn^{2+}_{0.47}Ti_{0.01})_{\Sigma 3.00}\,^{Z}Al_6[^{T}(Si_{5.93}Al_{0.07})O_{18}](BO_3)_3\,^{V}(OH)_{\Sigma 3.00}\,^{W}(OH_{0.45}F_{0.32}O_{0.23})_{\Sigma 1.00}$$

Z2
$$^{X}(Na_{0.70}\square_{0.29}Ca_{0.01})_{\Sigma 1.00}\,^{Y}(Al_{1.28}Li_{0.73}Fe^{2+}_{0.20}Mn^{2+}_{0.75}Ti_{0.03})_{\Sigma 3.00}\,^{Z}Al_6[^{T}(Si_{5.96}Al_{0.04})O_{18}](BO_3)_3\,^{V}(OH)_{\Sigma 3.00}\,^{W}(OH_{0.14}F_{0.54}O_{0.32})_{\Sigma 1.00}$$

Z3
$$^{X}(Na_{0.42}\square_{0.58})_{\Sigma 1.00}\,^{Y}(Al_{0.92}Li_{0.22}Fe^{2+}_{0.25}Mn^{2+}_{1.60}Ti_{0.02})_{\Sigma 3.00}\,^{Z}Al_6[^{T}(Si_{5.98}Al_{0.02})O_{18}](BO_3)_3\,^{V}(OH)_{\Sigma 3.00}\,^{W}(OH_{0.70}F_{0.17}O_{0.13})_{\Sigma 1.00}$$

Z4
$$^{X}(Na_{0.48}\square_{0.51}Ca_{0.01})_{\Sigma 1.00}\,^{Y}(Al_{1.18}Li_{0.58}Fe^{2+}_{0.08}Mn^{2+}_{1.14}Ti_{0.01})_{\Sigma 3.00}\,^{Z}Al_6[^{T}(Si_{5.99}Al_{0.01})O_{18}](BO_3)_3\,^{V}(OH)_{\Sigma 3.00}\,^{W}(OH_{0.71}F_{0.16}O_{0.13})_{\Sigma 1.00}$$

Z5
$$^{X}(Na_{0.41}\square_{0.59})_{\Sigma 1.00}\,^{Y}(Al_{1.33}Li_{0.86}Fe^{2+}_{0.06}Mn^{2+}_{0.76}Ti_{0.01})_{\Sigma 3.00}\,^{Z}Al_6[^{T}(Si_{5.99}Al_{0.01})O_{18}](BO_3)_3\,^{V}(OH)_{\Sigma 3.00}\,^{W}(OH_{0.97}F_{0.03})_{\Sigma 1.00}$$

Z6
$$^{X}(Na_{0.46}\square_{0.53}Ca_{0.01})_{\Sigma 1.00}\,^{Y}(Al_{1.34}Li_{0.90}Fe^{2+}_{0.08}Mn^{2+}_{0.66}Ti_{0.01})_{\Sigma 3.00}\,^{Z}Al_6(^{T}Si_{6.00}O_{18})(BO_3)_3\,^{V}(OH)_{\Sigma 3.00}\,^{W}(OH_{0.98}F_{0.02})_{\Sigma 1.00}$$

Z7
$$^{X}(Na_{0.42}\square_{0.58})_{\Sigma 1.00}\,^{Y}(Al_{0.86}Li_{0.40}Fe^{2+}_{0.31}Mn^{2+}_{1.36}Ti_{0.01})_{\Sigma 2.96}\,^{Z}Al_6(^{T}Si_{6.04}O_{18})(BO_3)_3\,^{V}(OH)_{\Sigma 3.00}\,^{W}(OH_{0.90}F_{0.09}O_{0.01})_{\Sigma 1.00}$$

Z8
$$^{X}(Na_{0.37}\square_{0.63})_{\Sigma 1.00}\,^{Y}(Al_{1.00}Li_{0.46}Fe^{2+}_{0.19}Mn^{2+}_{1.32}Ti_{0.01})_{\Sigma 2.98}\,^{Z}Al_6(^{T}Si_{6.02}O_{18})(BO_3)_3\,^{V}(OH)_{\Sigma 3.00}\,^{W}(OH_{0.98}F_{0.02})_{\Sigma 1.00}$$

Table 3.13. Average chemical composition and atoms per formula unit (a.p.f.u) for the different zones of Testa Scura sample (San Piero in Campo, Elba Island, Italy) with the relative empirical formula.

	Prismatic section		Termination						
	Z1	**Z2**	**Z3**	**Z4**	**Z5**	**Z6**	**Z7**	**Z8**	**Z9**
	n = 10	*n* = 2	*n* = 1	*n* = 7	*n* = 3	*n* = 2	*n* = 1	*n* = 3	n = 1
SiO_2 wt%	37.89(54)	37.53(5)	36.95	36.80(11)	37.58(25)	37.10(23)	37.51	36.99(27)	36.29
TiO_2	0.15(3)	0.26(1)	0.24	0.13(3)	0.0682)	0.10(1)	0.04	0.03(1)	0.07
B_2O_3	11.05[a]	10.82[a]	10.67[a]	10.69[a]	10.88[a]	10.76[a]	10.96[a]	10.76[a]	10.63[a]
Al_2O_3	40.83(79)	37.50(32)	36.16	36.19(23)	38.84(56)	36.90(72)	39.06	37.14(66)	35.95
FeO_{tot}	0.28(31)	2.35(42)	3.41	2.08(83)	0.72(14)	2.27(48)	0.98	1.62(74)	2.30
MnO	3.65(82)	6.04(73)	8.02	11.08(68)	6.80(78)	9.20(20)	8.49	10.01(10)	11.12
ZnO	0.02(4)	0.06(4)	-	0.05(5)	0.07(5)	0.05(2)	-	-	0.13
MgO	-	0.01(1)	0.01	0.03(1)	0.03(1)	0.07(2)	0.03	0.07(3)	0.30
CaO	0.08(2)	0.08(1)	0.05	0.02(1)	0.01(1)	0.03(3)	-	-	-
Na_2O	1.89(11)	2.13(6)	1.93	1.32(6)	1.06(88)	1.30(5)	1.17	1.10(7)	1.31
K_2O	-	0.01(1)	0.02	0.02(1)	0.02(1)	0.03(1)	0.03	0.02	0.00
Li_2O	1.47[b]	1.08[b]	0.66[b]	0.38[b]	1.01[b]	0.60[b]	0.73[b]	0.54[b]	0.29[b]
F	0.76(32)	1.16(13)	0.72	0.34(14)	0.22(4)	0.10(1)	0.00	0.03(3)	0.00
$-O \equiv F$	–0.32	–0.49	–0.30	–0.14	–0.09	–0.04	–0.00	–0.01	–0.00
H_2O	3.26[a]	2.99[a]	3.11[a]	3.43[a]	3.76[a]	3.61[a]	3.66[a]	3.68[a]	3.63[a]
Total	100.99	101.51	101.65	102.39	100.82	102.07	102.68	102.00	102.05
			Atoms normalized to 31 anions						
Si apfu	5.960	6.028	6.021	5.982	6.003	5.990	5.950	5.973	5.932
Ti	0.018	0.031	0.030	0.016	0.008	0.012	0.005	0.004	0.008
B	3.000	3.000	3.000	3.000	3.000	3.000	3.000	3.000	3.000
Al	7.569	7.099	6.944	6.933	7.310	7.022	7.302	7.067	6.926
Fe^{2+}	0.036	0.316	0.465	0.282	0.096	0.307	0.130	0.219	0.314
Mn^{2+}	0.486	0.821	1.107	1.525	0.919	1.258	1.140	1.369	1.540
Zn	0.002	0.007	-	0.006	0.008	0.006	-	-	0.016
Mg	-	0.001	0.000	0.007	0.007	0.017	0.007	0.017	0.073
Ca	0.014	0.014	0.009	0.000	0.000	0.005	-	-	-
Na	0.577	0.665	0.609	0.415	0.329	0.408	0.360	0.344	0.415
K	0.000	0.001	0.003	0.003	0.000	0.005	0.005	0.002	-
Li	0.930	0.698	0.433	0.248	0.649	0.390	0.466	0.351	0.191
F	0.376	0.590	0.370	0.175	0.110	0.051	0.000	0.017	-
OH	3.423	3.198	3.377	3.722	3.879	3.890	3.878	3.959	3.963
OH+F	3.799	3.788	3.747	3.897	3.989	3.941	3.878	3.976	3.963
Species	**Elbaite**	**Fluor-elbaite**	**Tsilaisite**	**Celleriite**	**Rossmanite**	**Celleriite**	**Celleriite**	**Celleriite**	**Celleriite**

[a] Calculated by stoichiometry (see text);
[b] Estimated with the procedure of Pesquera et al. (2016)
Errors for oxides and fluorine are standard deviations (in brackets)

Empirical chemical formulae

Z1 $^{X}(Na_{0.58}\square_{0.41}Ca_{0.01})_{\Sigma 1.00}{}^{Y}(Al_{1.53}Li_{0.93}Mn^{2+}{}_{0.49}Fe^{2+}{}_{0.04}Ti_{0.02})_{\Sigma 3.00}{}^{Z}Al_6[{}^{T}(Si_{5.96}Al_{0.04}O_{18})](BO_3)_3{}^{V}(OH)_{\Sigma 3.00}{}^{W}(OH_{0.42}F_{0.38}O_{0.20})_{\Sigma 1.00}$

Z2 $^{X}(Na_{0.67}\square_{0.32}Ca_{0.01})_{\Sigma 1.00}{}^{Y}(Al_{1.10}Li_{0.70}Mn^{2+}{}_{0.82}Fe^{2+}{}_{0.32}Ti_{0.03})_{\Sigma 2.97}{}^{Z}Al_6{}^{T}(Si_{6.03}O_{18})(BO_3)_3{}^{V}(OH)_{\Sigma 3.00}{}^{W}(OH_{0.20}F_{0.59}O_{0.21})_{\Sigma 1.00}$

Z3 $^{X}(Na_{0.61}\square_{0.38}Ca_{0.01})_{\Sigma 1.00}{}^{Y}(Al_{0.94}Li_{0.43}Mn^{2+}{}_{1.11}Fe^{2+}{}_{0.47}Ti_{0.03})_{\Sigma 2.98}{}^{Z}Al_6{}^{T}(Si_{6.02}O_{18})(BO_3)_3{}^{V}(OH)_{\Sigma 3.00}{}^{W}(OH_{0.38}F_{0.59}O_{0.03})_{\Sigma 1.00}$

Z4 $^{X}(Na_{0.42}\square_{0.58})_{\Sigma 1.00}{}^{Y}(Al_{0.91}Li_{0.25}Mn^{2+}{}_{1.53}Fe^{2+}{}_{0.28}Ti_{0.02})_{\Sigma 3.00}{}^{Z}Al_6[{}^{T}(Si_{5.98}Al_{0.02}O_{18})](BO_3)_3{}^{V}(OH)_{\Sigma 3.00}{}^{W}(OH_{0.72}F_{0.18}O_{0.10})_{\Sigma 1.00}$

Z5 $^{X}(Na_{0.33}\square_{0.67})_{\Sigma 1.00}{}^{Y}(Al_{1.31}Li_{0.65}Mn^{2+}{}_{0.92}Fe^{2+}{}_{0.10}Ti_{0.01})_{\Sigma 3.00}{}^{Z}Al_6{}^{T}(Si_{6.00}O_{18})(BO_3)_3{}^{V}(OH)_{\Sigma 3.00}$ $^{W}(OH_{0.88}F_{0.11}O_{0.01})_{\Sigma 1.00}$

Z6 $^{X}(Na_{0.41}\square_{0.59})_{\Sigma 1.00}{}^{Y}(Al_{1.01}Li_{0.39}Mn^{2+}{}_{1.26}Fe^{2+}{}_{0.31}Ti_{0.01})_{\Sigma 3.00}{}^{Z}Al_6[{}^{T}(Si_{5.99}Al_{0.01}O_{18})](BO_3)_3{}^{V}(OH)_{\Sigma 3.00}{}^{W}(OH_{0.89}F_{0.05}O_{0.06})_{\Sigma 1.00}$

Z7 $^{X}(Na_{0.36}\square_{0.64})_{\Sigma 1.00}{}^{Y}(Al_{1.25}Li_{0.47}Mn^{2+}{}_{1.14}Fe^{2+}{}_{0.13}Ti_{0.01})_{\Sigma 3.00}{}^{Z}Al_6[{}^{T}(Si_{5.95}Al_{0.05}O_{18})](BO_3)_3{}^{V}(OH)_{\Sigma 3.00}{}^{W}(OH_{0.88}O_{0.12})_{\Sigma 1.00}$

Z8 $^{X}(Na_{0.34}\square_{0.66})_{\Sigma 1.00}{}^{Y}(Al_{1.05}Li_{0.35}Mn^{2+}{}_{1.38}Fe^{2+}{}_{0.22})_{\Sigma 3.00}{}^{Z}Al_6[{}^{T}(Si_{5.97}Al_{0.03}O_{18})](BO_3)_3{}^{V}(OH)_{\Sigma 3.00}{}^{W}(OH_{0.96}F_{0.02}O_{0.02})_{\Sigma 1.00}$

Z9 $^{X}(Na_{0.41}\square_{0.59})_{\Sigma 1.00}{}^{Y}(Al_{0.86}Li_{0.19}Mn^{2+}{}_{1.54}Fe^{2+}{}_{0.31}Ti_{0.01})_{\Sigma 3.00}{}^{Z}Al_6[{}^{T}(Si_{5.93}Al_{0.07}O_{18})](BO_3)_3{}^{V}(OH)_{\Sigma 3.00}{}^{W}(OH_{0.96}O_{0.04})_{\Sigma 1.00}$

Table 3.14. Average chemical composition and atoms per formula unit (a.p.f.u) for the different zones of Giganti Storti sample (San Piero in Campo, Elba Island, Italy) with the relative empirical formula.

	Analogous		Prismatic section			Termination
	Z1	**Z2**	**Z3**	**Z4**	**Z5**	**Z6**
	n = 1	*n* = 3	*n* = 6	*n* = 11	*n* = 10	n = 4
SiO_2 wt%	38.42	37.95(15)	38.58(23)	38.55(29)	38.71(26)	38.17(71)
TiO_2	0.04	0.21(1)	0.06(4)	0.03(2)	0.03(2)	0.07(2)
B_2O_3	10.98[a]	10.83[a]	11.04[a]	11.24[a]	11.22[a]	11.08[a]
Al_2O_3	38.79	37.44(13)	39.46(61)	42.81(47)	42.25(15)	41.36(76)
FeO_{tot}	0.27	0.36(7)	0.22(5)	0.03(3)	0.06(3)	0.21(5)
MnO	3.73	4.97(14)	3.07(51)	0.51(40)	0.26(11)	1.36(40)
CaO	0.15	0.45(14)	0.15(4)	0.17(7)	0.26(6)	0.04(3)
Na_2O	2.36	2.51(4)	2.29(8)	1.83(6)	1.87(6)	2.23(7)
Li_2O	1.77[b]	1.66[b]	1.83[b]	1.87[b]	1.99[b]	1.83[b]
F	1.44	1.44(24)	0.97(11)	0.86(24)	1.06(9)	0.57(10)
H_2O	3.04[a]	2.87[a]	3.27[a]	3.30[a]	3.23[a]	3.37[a]
Total	100.50	100.16	100.62	100.95	100.61	100.11
Atomic fractions normalized to 31 anions						
Si apfu	6.083	6.091	6.072	5.958	5.996	5.986
Ti	0.004	0.026	0.008	0.004	0.004	0.008
B	3.000	3.000	3.000	3.000	3.000	3.000
Al	7.238	7.083	7.320	7.800	7.713	7.644
Fe^{2+}	0.035	0.049	0.028	0.004	0.007	0.027
Mn^{2+}	0.501	0.675	0.410	0.067	0.035	0.180
Ca	0.026	0.077	0.025	0.029	0.043	0.008
Na	0.724	0.781	0.697	0.549	0.561	0.678
Li	1.127	1.072	1.158	1.163	1.240	1.154
F	0.719	0.731	0.484	0.419	0.521	0.282
OH	3.213	3.078	3.438	3.400	3.341	3.530
OH+F	3.932	3.808	3.922	3.819	3.862	3.812
Species	**Fluor-elbaite**	**Fluor-elbaite**	**Fluor-elbaite**	**Fluor-elbaite**	**Fluor-elbaite**	**Elbaite**

[a] Calculated by stoichiometry (see text)
[b] Estimated with the procedure of Pesquera et al. (2016)
Errors for oxides and fluorine are standard deviations (in brackets)

Empirical chemical formulae

Z1
$$^{X}(Na_{0.72}\square_{0.25}Ca_{0.03})_{\Sigma 1.00}\,^{Y}(Al_{1.24}Li_{1.13}Fe^{2+}_{0.04}Mn^{2+}_{0.50}Ti_{0.004})_{\Sigma 2.92}\,^{Z}Al_6(^{T}Si_{6.08}O_{18})(BO_3)_3\,^{V}(OH)_{\Sigma 3.00}\,^{W}(OH_{0.21}F_{0.72}O_{0.07})_{\Sigma 1.00}$$

Z2
$$^{X}(Na_{0.78}\square_{0.14}Ca_{0.08})_{\Sigma 1.00}\,^{Y}(Al_{1.08}Li_{1.07}Fe^{2+}_{0.05}Mn^{2+}_{0.68}Ti_{0.03})_{\Sigma 2.91}\,^{Z}Al_6(^{T}Si_{6.09}O_{18})(BO_3)_3\,^{V}(OH)_{\Sigma 3.00}\,^{W}(OH_{0.08}F_{0.73}O_{0.19})_{\Sigma 1.00}$$

Z3
$$^{X}(Na_{0.70}\square_{0.27}Ca_{0.03})_{\Sigma 1.00}\,^{Y}(Al_{1.32}Li_{1.16}Fe^{2+}_{0.03}Mn^{2+}_{0.41}Ti_{0.01})_{\Sigma 2.93}\,^{Z}Al_6(^{T}Si_{6.07}O_{18})(BO_3)_3\,^{V}(OH)_{\Sigma 3.00}\,^{W}(OH_{0.44}F_{0.48}O_{0.08})_{\Sigma 1.00}$$

Z4
$$^{X}(Na_{0.55}\square_{0.42}Ca_{0.03})_{\Sigma 1.00}\,^{Y}(Al_{1.76}Li_{1.16}Mn^{2+}_{0.07}Ti_{0.004})_{\Sigma 3.00}\,^{Z}Al_6[^{T}(Si_{5.96}Al_{0.04})O_{18}](BO_3)_3\,^{V}(OH)_{\Sigma 3.00}\,^{W}(OH_{0.40}F_{0.42}O_{0.18})_{\Sigma 1.00}$$

Z5
$$^{X}(Na_{0.56}\square_{0.40}Ca_{0.04})_{\Sigma 1.00}\,^{Y}(Al_{1.71}Li_{1.24}Fe^{2+}_{0.01}Mn^{2+}_{0.04}Ti_{0.004})_{\Sigma 3.00}\,^{Z}Al_6(^{T}Si_{6.00}O_{18})(BO_3)_3\,^{V}(OH)_{\Sigma 3.00}\,^{W}(OH_{0.34}F_{0.52}O_{0.14})_{\Sigma 1.00}$$

Z6
$$^{X}(Na_{0.56}\square_{0.40}Ca_{0.04})_{\Sigma 1.00}\,^{Y}(Al_{1.63}Li_{1.15}Fe^{2+}_{0.03}Mn^{2+}_{0.18}Ti_{0.01})_{\Sigma 3.00}\,^{Z}Al_6[^{T}(Si_{5.99}Al_{0.01})O_{18}](BO_3)_3\,^{V}(OH)_{\Sigma 3.00}\,^{W}(OH_{0.53}F_{0.28}O_{0.05})_{\Sigma 1.00}$$

Table 3.15. Average chemical composition and atoms per formula unit (a.p.f.u) for the different zones of Testa Rossa sample (San Piero in Campo, Elba Island, Italy) with the relative empirical formula.

	Prismatic section	**Termination**		
	Z1	**Z2**	**Z3**	**Z4**
	n = 11	*n* = 6	*n* = 1	*n* = 2
SiO_2 wt%	39.35(52)	38.97(36)	35.65	38.03(31)
TiO_2	-	0.03(3)	0.01	-
B_2O_3	11.40[a]	11.26[a]	10.63[a]	11.10[a]
Al_2O_3	43.22(29)	41.59(45)	40.92	42.13(20)
FeO_{tot}	0.03(2)	0.08(9)	0.02	0.06(2)
MnO	0.06(3)	1.64(91)	2.66	0.78(10)
ZnO	-	0.06(4)	-	-
MgO	-	0.05(10)	-	0.01
CaO	0.01(1)	0.01(3)	0.01	0.01
Na_2O	1.89(9)	2.21(4)	2.26	2.30(1)
Li_2O	1.99[b]	1.88[b]	1.39[b]	1.84[b]
F	0.20(8)	0.20(9)	0.28	0.21(11)
$-O \equiv F$	–0.08	–0.08	–0.12	–0.09
H_2O	3.74[a]	3.68[a]	3.22[a]	3.52[a]
Total	101.78	101.58	96.88	99.92
Atoms normalized to 31 anions				
Si apfu	6.000	6.017	5.830	5.955
Ti	-	0.003	0.001	-
B	3.000	3.000	3.000	3.000
Al	7.767	7.569	7.887	7.775
Fe^{2+}	0.004	0.010	0.003	0.008
Mn^{2+}	0.008	0.214	0.369	0.103
Zn	-	0.007	-	-
Mg	-	0.012	-	0.001
Ca	0.001	0.001	0.001	0.001
Na	0.558	0.661	0.715	0.697
Li	1.221	1.168	0.914	1.159
F	0.095	0.096	0.143	0.102
OH	3.801	3.792	3.509	3.673
OH+F	3.895	3.888	3.652	3.775
Species	**Elbaite**	**Elbaite**	**Elbaite**	**Elbaite**

[a] Calculated by stoichiometry (see text)
[b] Estimated with the procedure of Pesquera et al. (2016)
Errors for oxides and fluorine are standard deviations (in brackets)

Empirical chemical formulae

Z1 $^{X}(Na_{0.56}\square_{0.44})_{\Sigma 1.00}{}^{Y}(Al_{1.77}Li_{1.22}Mn^{2+}{}_{0.01})_{\Sigma 3.00}{}^{Z}Al_6(^{T}Si_{6.00}O_{18})(BO_3)_3{}^{V}(OH)_{\Sigma 3.00}{}^{W}(OH_{0.80}F_{0.10}O_{0.10})_{\Sigma 1.00}$

Z2 $^{X}(Na_{0.66}\square_{0.34})_{\Sigma 1.00}{}^{Y}(Al_{1.57}Li_{1.17}Fe^{2+}{}_{0.01}Mn^{2+}{}_{0.21})_{\Sigma 2.98}{}^{Z}Al_6(^{T}Si_{6.02}O_{18})(BO_3)_3{}^{V}(OH)_{\Sigma 3.00}{}^{W}(OH_{0.79}F_{0.10}O_{0.11})_{\Sigma 1.00}$

Z3 $^{X}(Na_{0.72}\square_{0.28})_{\Sigma 1.00}{}^{Y}(Al_{1.72}Li_{0.91}Mn^{2+}{}_{0.37})_{\Sigma 3.00}{}^{Z}Al_6[^{T}(Si_{5.83}Al_{0.17}O_{18})(BO_3)_3{}^{V}(OH)_{\Sigma 3.00}{}^{W}(OH_{0.51}F_{0.14}O_{0.35})_{\Sigma 1.00}$

Z4 $^{X}(Na_{0.70}\square_{0.30})_{\Sigma 1.00}{}^{Y}(Al_{1.72}Li_{1.16}Fe^{2+}{}_{0.01}Mn^{2+}{}_{0.10})_{\Sigma 3.00}{}^{Z}Al_6[^{T}(Si_{5.96}Al_{0.04}O_{18})(BO_3)_3{}^{V}(OH)_{\Sigma 3.00}{}^{W}(OH_{0.67}F_{0.10}O_{0.23})_{\Sigma 1.00}$

Table 3.16. Average chemical composition and atoms per formula unit (a.p.f.u) for the different zones of Testa Viola sample (San Piero in Campo, Elba Island, Italy) with the relative empirical formula.

	Prismatic section			Termination	
	Z1	**Z2**	**Z3**	**Z4**	**Z5**
	$n = 4$	$n = 1$	$n = 1$	$n = 4$	$n = 12$
SiO_2 wt%	38.08(91)	39.46	37.01	38.78(29)	37.80(40)
TiO_2	0.02(2)	0.02	-	0.03(1)	0.04(2)
B_2O_3	11.11[a]	11.40[a]	10.94[a]	11.16[a]	10.99[a]
Al_2O_3	42.42(72)	42.97	42.55	40.83(55)	40.39(92)
FeO_{tot}	0.04(3)	0.01	0.04	0.32(13)	0.52(28)
MnO	0.10(10)	0.04	0.03	1.87(76)	3.28(87)
ZnO	0.01(1)	0.03	0.01	0.05	0.04(4)
CaO	0.12(13)	0.02	0.01	0.01(1)	0.03(2)
Na_2O	1.96(6)	2.07	2.07	2.24(3)	2.21(12)
Li_2O	1.92[b]	2.04[b]	1.78[b]	1.86[b]	1.53[b]
F	0.43(32)	0.22	0.12	0.13(7)	0.20(12)
$-O \equiv F$	–0.18	–0.09	–0.05	–0.05	–0.08
H_2O	3.47[a]	3.69[a]	3.48[a]	3.69[a]	3.49[a]
Total	99.52	101.86	98.01	100.93	100.44
Atoms normalized to 31 anions					
Si apfu	5.956	6.018	5.882	6.041	5.980
Ti	0.002	0.002	-	0.003	0.005
B	3.000	3.000	3.000	3.000	3.000
Al	7.818	7.723	7.970	7.497	7.530
Fe^{2+}	0.005	0.001	0.006	0.042	0.069
Mn^{2+}	0.013	0.005	0.004	0.246	0.439
Zn	0.002	0.003	0.001	0.005	0.004
Ca	0.020	0.003	0.001	-	0.006
Na	0.594	0.612	0.639	0.677	0.677
Li	1.208	1.251	1.138	1.165	0.973
F	0.210	0.104	0.061	0.062	0.100
OH	3.622	3.759	3.695	3.834	3.687
OH+F	3.832	3.863	3.755	3.895	3.787
Species	**Elbaite**	**Elbaite**	**Elbaite**	**Elbaite**	**Elbaite**

[a] Calculated by stoichiometry (see text)
[b] Estimated with the procedure of Pesquera et al. (2016)
Errors for oxides and fluorine are standard deviations (in brackets)

Empirical chemical formulae

Z1
$$^{X}(Na_{0.59}\square_{0.39}Ca_{0.02})_{\Sigma 1.00}\,^{Y}(Al_{1.78}Li_{1.21}Mn^{2+}_{0.01})_{\Sigma 3.00}\,^{Z}Al_6[T(Si_{5.96}Al_{0.04}O_{18})](BO_3)_3\,^{V}(OH)_{\Sigma 3.00}\,^{W}(OH_{0.62}F_{0.21}O_{0.27})_{\Sigma 1.00}$$

Z2
$$^{X}(Na_{0.61}\square_{0.39})_{\Sigma 1.00}\,^{Y}(Al_{1.72}Li_{1.25}Mn^{2+}_{0.01})_{\Sigma 2.98}\,^{Z}Al_6(^{T}Si_{6.02}O_{18})(BO_3)_3\,^{V}(OH)_{\Sigma 3.00}\,^{W}(OH_{0.76}F_{0.10}O_{0.14})_{\Sigma 1.00}$$

Z3
$$^{X}(Na_{0.64}\square_{0.36})_{\Sigma 1.00}\,^{Y}(Al_{1.85}Li_{1.14}Fe^{2+}_{0.01})_{\Sigma 3.00}\,^{Z}Al_6[^{T}(Si_{5.88}Al_{0.12}O_{18})(BO_3)_3\,^{V}(OH)_{\Sigma 3.00}\,^{W}(OH_{0.70}F_{0.07}O_{0.23})_{\Sigma 1.00}$$

Z4
$$^{X}(Na_{0.68}\square_{0.32})_{\Sigma 1.00}\,^{Y}(Al_{1.50}Li_{1.17}Fe^{2+}_{0.04}Mn^{2+}_{0.25})_{\Sigma 2.96}\,^{Z}Al_6(^{T}Si_{6.04}O_{18})(BO_3)_3\,^{V}(OH)_{\Sigma 3.00}\,^{W}(OH_{0.83}F_{0.06}O_{0.11})_{\Sigma 1.00}$$

Z5
$$^{X}(Na_{0.68}\square_{0.30}Ca_{0.02})_{\Sigma 1.00}\,^{Y}(Al_{1.51}Li_{0.97}Fe^{2+}_{0.07}Mn^{2+}_{0.44})_{\Sigma 3.00}\,^{Z}Al_6[^{T}(Si_{5.98}Al_{0.02}O_{18})(BO_3)_3\,^{V}(OH)_{\Sigma 3.00}\,^{W}(OH_{0.69}F_{0.10}O_{0.21})_{\Sigma 1.00}$$

Table 3.17. Average chemical composition and atoms per formula unit (a.p.f.u) for the different zones of the prismatic section of fragment I and OGX of Violet Cap sample (San Piero in Campo, Elba Island, Italy) with the relative empirical formula.

	Fragment I				
	Prismatic section I	OGX			
	Z1	Z2	Z3	Z4	Z5
	$n = 12$	$n = 3$	$n = 2$	$n = 3$	$n = 1$
SiO_2 wt%	37.95(20)	37.75(41)	38.12(12)	38.01(3)	35.93
TiO_2	0.05(2)	0.14(7)	0.06(4)	0.06(4)	0.01
B_2O_3	11.06[a]	10.89[a]	11.06[a]	10.97[a]	10.77[a]
Al_2O_3	41.77(33)	39.11(39)	41.30(61)	39.98(21)	42.60
FeO_{tot}	0.03(3)	0.13(6)	0.05(2)	0.07(2)	-
MnO_{tot}	0.62(51)	4.00(40)	0.93(26)	2.72(52)	0.72
CaO	0.34(7)	0.06(4)	0.03	0.07(1)	0.06
Na_2O	1.85(4)	2.36(3)	2.18(16)	2.31(11)	2.25
K_2O	0.01(1)	0.01(1)	0.02(1)	0.01(2)	-
Li_2O	1.90[b]	1.63[b]	1.93[b]	1.78[b]	1.54[b]
F	0.99(9)	0.73(17)	0.49(28)	0.41(14)	0.13
$-O \equiv F$	–0.42	–0.31	–0.21	–0.17	–0.05
H_2O	3.18[a]	3.10[a]	3.43[a]	3.34[a]	3.22[a]
MnO	0.62	2.85[d]	0.60[d]	1.75[d]	0.458[d]
Mn_2O_3	-	1.28[d]	0.37[d]	1.08[d]	0.290[d]
Total	99.35	99.66	99.41	99.59	97.19
Atoms normalized to 31 anions					
Si apfu	5.967	6.024	5.992	6.021	5.799
Ti	0.006	0.017	0.007	0.007	0.001
B	3.000	3.000	3.000	3.000	3.000
Al	7.740	7.355	7.651	7.464	8.102
Fe^{3+}	-	0.017[c]	0.006[c]	0.009[c]	-[c]
Fe^{2+}	0.003	-[c]	-[c]	-[c]	-[c]
Mn^{3+}	-	0.155	0.044	0.130	0.036
Mn^{2+}	0.083	0.385	0.080	0.235	0.063
Ca	0.057	0.010	0.005	0.013	0.011
Na	0.563	0.732	0.664	0.708	0.704
K	0.002	0.003	0.005	0.003	-
Li	1.201	1.046	1.220	1.134	1.000
F	0.494	0.370	0.243	0.205	0.067
OH	3.334	3.301	3.595	3.529	3.505
OH+F	3.828	3.671	3.838	3.734	3.572
Species	**Fluor-elbaite**	**Elbaite**	**Elbaite**	**Elbaite**	**Elbaite**

[a] Calculated by stoichiometry (see text);
[b] Estimated with the procedure of Pesquera et al. (2016);
[c] All Fe was considered to be Fe^{3+} based on the OAS results;
[d] Determined by OAS (Altieri et al., 2023)
Errors for oxides and fluorine are standard deviations (in brackets)

Empirical chemical formulae

Z1 $^{X}(Na_{0.56}\square_{0.38}Ca_{0.06})_{\Sigma 1.00}{}^{Y}(Al_{1.71}Li_{1.20}Mn^{2+}_{0.08}Ti_{0.01})_{\Sigma 3.00}{}^{Z}Al_6[{}^{T}(Si_{5.97}Al_{0.03})O_{18}](BO_3)_3{}^{V}(OH)_{\Sigma 3.00}{}^{W}(OH_{0.33}F_{0.49}O_{0.18})_{\Sigma 1.00}$

Z2 $^{X}(Na_{0.73}\square_{0.26}Ca_{0.01})_{\Sigma 1.00}{}^{Y}(Al_{1.36}Li_{1.05}Mn^{2+}_{0.38}Mn^{3+}_{0.16}Fe^{3+}_{0.02}Ti_{0.01})_{\Sigma 2.98}{}^{Z}Al_6({}^{T}Si_{6.02}O_{18})(BO_3)_3{}^{V}(OH)_{\Sigma 3.00}{}^{W}(OH_{0.30}F_{0.37}O_{0.33})_{\Sigma 1.00}$

Z3 $^{X}(Na_{0.66}\square_{0.33}Ca_{0.01})_{\Sigma 1.00}{}^{Y}(Al_{1.64}Li_{1.22}Mn^{2+}_{0.08}Mn^{3+}_{0.04}Fe^{3+}_{0.01}Ti_{0.01})_{\Sigma 3.00}{}^{Z}Al_6[{}^{T}(Si_{5.99}Al_{0.01})O_{18}](BO_3)_3{}^{V}(OH)_{\Sigma 3.00}{}^{W}(OH_{0.59}F_{0.24}O_{0.16})_{\Sigma 1.00}$

Z4 $^{X}(Na_{0.71}\square_{0.28}Ca_{0.01})_{\Sigma 1.00}{}^{Y}(Al_{1.36}Li_{1.13}Mn^{2+}_{0.24}Mn^{3+}_{0.13}Fe^{3+}_{0.01}Ti_{0.01})_{\Sigma 2.98}{}^{Z}Al_6({}^{T}Si_{6.02}O_{18})(BO_3)_3{}^{V}(OH)_{\Sigma 3.00}{}^{W}(OH_{0.53}F_{0.21}O_{0.26})_{\Sigma 1.00}$

Z5 $^{X}(Na_{0.70}\square_{0.29}Ca_{0.01})_{\Sigma 1.00}{}^{Y}(Al_{1.90}Li_{1.00}Mn^{2+}_{0.06}Mn^{3+}_{0.04})_{\Sigma 3.00}{}^{Z}Al_6[{}^{T}(Si_{5.80}Al_{0.20})O_{18}](BO_3)_3{}^{V}(OH)_{\Sigma 3.00}{}^{W}(OH_{0.51}F_{0.07}O_{0.42})_{\Sigma 1.00}$

Table 3.18. Average chemical composition and atoms per formula unit (a.p.f.u) for the different zones of OGR and the prismatic section of fragment II of Violet Cap sample (San Piero in Campo, Elba Island, Italy) with the relative empirical formula.

	Fragment II						
	OGR		Prismatic section II		OGZ		
	Z6	Z7	Z8	Z9	Z10	Z11	Z12
	$n = 3$	$n = 1$	$n = 17$	$n = 30$	$n = 1$	$n = 1$	$n = 1$
SiO_2 wt%	37.14(31)	36.77	36.81(20)	38.23(95)	37.29	37.68	35.79
TiO_2	0.26(11)	0.20	0.03	0.01	0.12	0.02	-
B_2O_3	10.67[a]	10.76[a]	10.85[a]	11.16[a]	10.79[a]	10.95[a]	10.74[a]
Al_2O_3	36.66(39)	39.93	41.79(45)	42.64(58)	38.25	40.42	42.52
FeO_{tot}	0.23(25)	0.08	0.02	0.02(2)	0.37	0.23	0.03
MnO	6.77(47)	2.47	0.29(11)	0.08(5)	5.86	2.76	0.68
CaO	0.24(10)	0.11	0.19(13)	0.02(3)	0.02	0.01	0.06
Na_2O	2.73(13)	2.27	1.87	1.86(11)	2.42	2.55	2.18
K_2O	0.02(1)	0.02	0.01	0.01(1)	0.03	0.05	-
Li_2O	1.39[b]	1.67[b]	1.81[b]	1.92[b]	1.34[b]	1.65[b]	1.53[b]
F	1.30(17)	0.80	0.75(18)	0.31(16)	-	-	-
$-O \equiv F$	–0.55	–0.34	–0.31	–0.13	–0.00	–0.00	–0.00
H_2O	2.84[a]	3.15[a]	3.22[a]	3.60[a]	3.29[a]	3.40[a]	3.30[a]
MnO	6.77[d]	2.47[d]	0.29	0.08	4.27[d]	2.01[d]	0.49[d]
Mn_2O_3	-[d]	-[d]	-	-	1.77[d]	0.83[d]	0.21[d]
Total	99.69	97.88	97.33	99.72	99.81	99.84	96.85
Atoms normalized to 31 anions							
Si apfu	6.052	5.939	5.897	5.955	6.007	5.981	5.794
Ti	0.032	0.025	0.004	0.001	0.015	0.003	-
B	3.000	3.000	3.000	3.000	3.000	3.000	3.000
Al	7.040	7.602	7.891	7.828	7.261	7.561	8.113
Fe^{3+}	-[c]	-[c]	-	-	0.049[c]	0.031[c]	0.004[c]
Fe^{2+}	0.031[c]	0.010[c]	0.003	0.002	-[c]	-[c]	-[c]
Mn^{3+}	-	-			0.217	0.100	0.026
Mn^{2+}	0.934	0.339	0.039	0.010	0.583	0.271	0.068
Ca	0.041	0.018	0.033	0.003	0.003	0.002	0.011
Na	0.862	0.711	0.582	0.563	0.755	0.786	0.683
K	0.003	0.004	0.002	0.003	0.006	0.010	-
Li	0.911	1.085	1.166	1.203	0.868	1.053	0.996
F	0.669	0.408	0.378	0.154	-	-	-
OH	3.086	3.396	3.445	3.736	3.531	3.595	3.521
OH+F	3.755	3.804	3.823	3.890	3.531	3.595	3.521
Species	**Fluor-elbaite**	**Fluor-elbaite**	**Elbaite**	**Elbaite**	**Elbaite**	**Elbaite**	**Elbaite**

[a] Calculated by stoichiometry (see text);
[b] Estimated with the procedure of Pesquera et al. (2016);
[c] All Fe was considered to be Fe^{3+}, with the exception of the OGR overgrowth, based on the OAS results;
[d] Determined by OAS (Altieri et al., 2023)
Errors for oxides and fluorine are standard deviations (in brackets)

Empirical chemical formulae

Z6 $^{X}(Na_{0.86}\square_{0.38}Ca_{0.04})_{\Sigma 1.00}{}^{Y}(Al_{1.04}Li_{0.91}Mn^{2+}_{0.93}Fe^{2+}_{0.03}Ti_{0.03})_{\Sigma 2.95}{}^{Z}Al_6(^{T}Si_{6.05}O_{18})(BO_3)_3{}^{V}(OH)_{\Sigma 3.00}{}^{W}(OH_{0.09}F_{0.67}O_{0.24})_{\Sigma 1.00}$

Z7 $^{X}(Na_{0.71}\square_{0.27}Ca_{0.02})_{\Sigma 1.00}{}^{Y}(Al_{1.56}Li_{1.08}Mn^{2+}_{0.34}Fe^{2+}_{0.01}Ti_{0.03})_{\Sigma 3.00}{}^{Z}Al_6[^{T}(Si_{5.94}Al_{0.06})O_{18}](BO_3)_3{}^{V}(OH)_{\Sigma 3.00}{}^{W}(OH_{0.40}F_{0.41}O_{0.19})_{\Sigma 1.00}$

Z8 $^{X}(Na_{0.58}\square_{0.39}Ca_{0.03})_{\Sigma 1.00}{}^{Y}(Al_{1.79}Li_{1.17}Mn^{2+}_{0.04})_{\Sigma 3.00}{}^{Z}Al_6[^{T}(Si_{5.90}Al_{0.10})O_{18}](BO_3)_3{}^{V}(OH)_{\Sigma 3.00}{}^{W}(OH_{0.45}F_{0.38}O_{0.17})_{\Sigma 1.00}$

Z9 $^{X}(Na_{0.56}\square_{0.44})_{\Sigma 1.00}{}^{Y}(Al_{1.79}Li_{1.20}Mn^{2+}_{0.01})_{\Sigma 3.00}{}^{Z}Al_6[^{T}(Si_{5.96}Al_{0.06})O_{18}](BO_3)_3{}^{V}(OH)_{\Sigma 3.00}{}^{W}(OH_{0.74}F_{0.15}O_{0.11})_{\Sigma 1.00}$

Z10 $^{X}(Na_{0.76}\square_{0.24})_{\Sigma 1.00}{}^{Y}(Al_{1.26}Li_{0.87}Mn^{2+}_{0.58}Mn^{3+}_{0.22}Fe^{3+}_{0.05}Ti_{0.02})_{\Sigma 2.99}{}^{Z}Al_6(^{T}Si_{6.01}O_{18})(BO_3)_3{}^{V}(OH)_{\Sigma 3.00}{}^{W}(OH_{0.53}O_{0.47})_{\Sigma 1.00}$

Z11 $^{X}(Na_{0.79}\square_{0.21})_{\Sigma 1.00}{}^{Y}(Al_{1.54}Li_{1.05}Mn^{2+}_{0.27}Mn^{3+}_{0.10}Fe^{3+}_{0.03})_{\Sigma 3.00}{}^{Z}Al_6[^{T}(Si_{5.98}Al_{0.02})O_{18}](BO_3)_3{}^{V}(OH)_{\Sigma 3.00}{}^{W}(OH_{0.56}O_{0.44})_{\Sigma 1.00}$

Z12 $^{X}(Na_{0.68}\square_{0.31}Ca_{0.01})_{\Sigma 1.00}{}^{Y}(Al_{1.90}Li_{1.00}Mn^{2+}_{0.07}Mn^{3+}_{0.03})_{\Sigma 3.00}{}^{Z}Al_6[^{T}(Si_{5.79}Al_{0.21})O_{18}](BO_3)_3{}^{V}(OH)_{\Sigma 3.00}{}^{W}(OH_{0.52}O_{0.48})_{\Sigma 1.00}$

Table 3.19. Average chemical composition and atoms per formula unit (a.p.f.u) for the different zones of the lateral overgrowth (OGY) of Violet Cap sample (San Piero in Campo, Elba Island, Italy) with the relative empirical formula.

	Fragment II					
	OGY					
	Z13	**Z14**	**Z15**	**Z16**	**Z17**	**Z18**
	n = 1	*n* = 1	*n* = 1	*n* = 2	*n* = 2	*n* = 2
SiO_2 wt%	37.32	37.77	38.06	38.02(22)	37.03(93)	35.56(52)
TiO_2	0.07	0.07	-	0.01(1)	0.02(3)	0.01(2)
B_2O_3	10.78[a]	10.88[a]	11.00[a]	10.98[a]	10.87[a]	10.67[a]
Al_2O_3	37.78	38.91	40.59	39.85(15)	41.27(59)	42.21(59)
FeO_{tot}	0.48	0.11	0.09	0.11(2)	0.03(3)	0.03(1)
MnO	7.07	4.27	1.61	3.51(12)	1.22(66)	0.62(6)
CaO	0.05	0.02	-	0.01	0.02(2)	0.05(1)
Na_2O	2.31	2.48	2.49	2.48(1)	2.42(25)	2.29(2)
K_2O	0.01	0.02	0.02	-	0.01(1)	-
Li_2O	1.18[b]	1.62[b]	1.89[b]	1.66[b]	1.75[b]	1.55[b]
F	0.15	0.14	0.08	0.08(3)	0.03(2)	0.04(5)
$-O \equiv F$	–0.06	–0.06	–0.03	–0.03	–0.01	–0.02
MnO[d]	4.71	2.85	0.10	2.34	0.81	0.23
Mn_2O_3[d]	2.62	1.58	1.07	1.30	0.45	0.42
H_2O	3.38[a]	3.36[a]	3.54[a]	3.35	3.43[a]	3.26[a]
Total	100.58	99.78	99.33	99.41	98.14	96.31
	Atoms normalized to 31 anions					
Si apfu	6.017	6.033	6.013	6.020	5.923	5.791
Ti	0.008	0.008	-	0.001	0.003	0.002
B	3.000	3.000	3.000	3.000	3.000	3.000
Al	7.180	7.325	7.558	7.436	7.780	8.102
Fe^{3+} [c]	0.065	0.015	0.011	0.014	0.004	0.005
Fe^{2+} [c]	-	-	-	-	-	-
Mn^{3+}	0.322	0.192	0.072	0.158	0.055	0.029
Mn^{2+}	0.644	0.386	0.143	0.318	0.110	0.058
Ca	0.008	0.003	-	0.002	0.003	0.008
Na	0.721	0.768	0.762	0.762	0.751	0.723
K	0.002	0.004	0.005	0.001	0.002	-
Li	0.765	1.041	1.201	1.057	1.126	1.015
F	0.076	0.069	0.038	0.039	0.017	0.019
OH	3.521	3.581	3.727	3.673	3.659	3.537
OH+F	3.697	3.650	3.765	3.712	3.676	3.556
Species	**Elbaite**	**Elbaite**	**Elbaite**	**Elbaite**	**Elbaite**	**Elbaite**

[a] Calculated by stoichiometry (see text);
[b] Estimated with the procedure of Pesquera et al. (2016);
[c] All Fe was considered to be Fe^{3+} based on the OAS results;
[d] Determined by OAS (Altieri et al., 2023)
Errors for oxides and fluorine are standard deviations (in brackets)

Empirical chemical formulae

Z13 $^{X}(Na_{0.72}\square_{0.27}Ca_{0.01})_{\Sigma 1.00}{}^{Y}(Al_{1.18}Li_{0.77}Mn^{2+}_{0.64}Mn^{3+}_{0.32}Fe^{3+}_{0.07}Ti_{0.01})_{\Sigma 2.98}{}^{Z}Al_6(^{T}Si_{6.02}O_{18})(BO_3)_3{}^{V}(OH)_{\Sigma 3.00}{}^{W}(OH_{0.52}F_{0.08}O_{0.40})_{\Sigma 1.00}$

Z14 $^{X}(Na_{0.77}\square_{0.23})_{\Sigma 1.00}{}^{Y}(Al_{1.33}Li_{1.04}Mn^{2+}_{0.39}Mn^{3+}_{0.19}Fe^{3+}_{0.02}Ti_{0.01})_{\Sigma 2.97}{}^{Z}Al_6(^{T}Si_{6.03}O_{18})O_{18}](BO_3)_3{}^{V}(OH)_{\Sigma 3.00}{}^{W}(OH_{0.58}F_{0.07}O_{0.35})_{\Sigma 1.00}$

Z15 $^{X}(Na_{0.76}\square_{0.24})_{\Sigma 1.00}{}^{Y}(Al_{1.56}Li_{1.20}Mn^{2+}_{0..14}Mn^{3+}_{0.07}Fe^{3+}_{0.01})_{\Sigma 2.99}{}^{Z}Al_6(^{T}Si_{6.01}O_{18})(BO_3)_3{}^{V}(OH)_{\Sigma 3.00}{}^{W}(OH_{0.73}F_{0.04}O_{0.23})_{\Sigma 1.00}$

Z16 $^{X}(Na_{0.76}\square_{0.24})_{\Sigma 1.00}{}^{Y}(Al_{1.44}Li_{1.06}Mn^{2+}_{0.32}Mn^{3+}_{0.16}Fe^{3+}_{0.01})_{\Sigma 2.98}{}^{Z}Al_6(^{T}Si_{6.02}O_{18})O_{18}](BO_3)_3{}^{V}(OH)_{\Sigma 3.00}{}^{W}(OH_{0.67}F_{0.04}O_{0.29})_{\Sigma 1.00}$

Z17 $^{X}(Na_{0.75}\square_{0.25})_{\Sigma 1.00}{}^{Y}(Al_{1.70}Li_{1.13}Mn^{2+}_{0.11}Mn^{3+}_{0.06})_{\Sigma 3.00}{}^{Z}Al_6[^{T}(Si_{5.92}Al_{0.08})O_{18}](BO_3)_3{}^{V}(OH)_{\Sigma 3.00}{}^{W}(OH_{0.66}F_{0.02}O_{0.32})_{\Sigma 1.00}$

Z18 $^{X}(Na_{0.73}\square_{0.26}Ca_{0.01})_{\Sigma 1.00}{}^{Y}(Al_{1.89}Li_{1.02}Mn^{2+}_{0.06}Mn^{3+}_{0.03}Fe^{3+}_{0.01})_{\Sigma 3.00}{}^{Z}Al_6[^{T}(Si_{5.79}Al_{0.21})O_{18}](BO_3)_3{}^{V}(OH)_{\Sigma 3.00}{}^{W}(OH_{0.54}F_{0.02}O_{0.44})_{\Sigma 1.00}$

Table 3.20. Average chemical composition and atoms per formula unit (a.p.f.u) for the different zones of San Silvestro sample (San Piero in Campo, Elba Island, Italy) with the relative empirical formula.

	Prismatic section				Termination				
	Z1	**Z2**	**Z3**	**Z4**	**Z5**	**Z6**	**Z7**	**Z8**	**Z9**
	$n = 6$	$n = 23$	$n = 3$	$n = 1$	$n = 1$	$n = 1$	$n = 1$	$n = 1$	$n = 2$
SiO_2 wt%	37.88(31)	37.22(48)	38.11(9)	37.54	36.48	36.83	37.58	37.08	36.46(22)
TiO_2	0.05(3)	0.14(6)	0.05(2)	0.07	0.07	0.09	0.04	0.09	0.11(2)
B_2O_3	11.06[a]	10.86[a]	11.09[a]	10.88[a]	10.57[a]	10.63[a]	10.69[a]	10.79[a]	10.63[a]
Al_2O_3	41.45(90)	39.96(98)	41.59(17)	39.23	35.76	35.96	35.20	37.84	35.92(33)
FeO_{tot}	0.17(19)	0.85(38)	0.24(13)	1.08	4.04	5.27	7.08	2.98	4.94(98)
MnO	2.44(51)	2.93(86)	1.30(64)	4.43	8.91	6.69	5.44	6.30	7.25(70)
MgO	0.01(1)	0.01	0.01(1)	-	0.06	0.11	0.11	0.18	0.44(18)
CaO	0.06(2)	0.13(8)	0.04(2)	0.06	0.02	0.03	0.02	0.12	0.04(2)
Na_2O	1.89(9)	1.99(24)	1.98(8)	1.89	1.03	1.30	1.06	1.47	1.23(8)
K_2O	0.02(2)	0.03(2)	0.01	0.01	0.00	0.03	0.02	0.02	0.03
Li_2O	1.61[b]	1.51[b]	1.80[b]	1.35[b]	0.39[b]	0.55[b]	0.61[b]	0.82[b]	0.48[b]
F	0.73(15)	0.62(22)	0.22(15)	0.29	0.03	0.00	0.20	0.23	0.10(3)
H_2O	3.29[a]	3.27[a]	3.60[a]	3.47[a]	3.62[a]	3.61[a]	3.62[a]	3.50[a]	3.64[a]
$-O \equiv F$	–0.31	–0.26	–0.09	–0.12	–0.01	-	–0.08	–0.10	–0.04
FeO	0.17	0.85	0.24	1.08	4.04	5.27	6.72[c]	2.98	4.94
Fe_2O_3	-	-	-	-	-	-	0.35[c]	-	-
Total	100.40	99.28	99.97	100.23	100.99	101.08	101.57	101.33	101.26
Atoms normalized to 31 anions									
Si apfu	5.952	5.958	5.972	5.996	5.996	6.023	6.113	5.972	5.962
Ti	0.006	0.017	0.006	0.008	0.009	0.011	0.005	0.011	0.013
B	3.000	3.000	3.000	3.000	3.000	3.000	3.000	3.000	3.000
Al	7.674	7.538	7.681	7.385	6.927	6.932	6.749	7.182	6.922
Fe^{3+}	-	-	-	-	-	-	0.043	-	-
Fe^{2+}	0.023	0.114	0.031	0.145	0.555	0.720	0.915	0.401	0.676
Mn^{2+}	0.325	0.398	0.173	0.599	1.241	0.927	0.749	0.860	1.003
Mg	0.001	0.001	0.001	-	0.015	0.027	0.027	0.043	0.107
Ca	0.009	0.022	0.007	0.011	0.004	0.005	0.003	0.021	0.007
Na	0.575	0.619	0.602	0.585	0.329	0.362	0.335	0.458	0.391
K	0.005	0.005	0.002	0.001	0.000	0.006	0.003	0.005	0.005
Li	1.017	0.972	1.135	0.867	0.258	0.362	0.399	0.531	0.316
F	0.362	0.313	0.109	0.147	0.016	0.000	0.102	0.119	0.050
OH	3.452	3.496	3.764	3.699	3.965	3.938	3.952	3.760	3.974
OH+F	3.814	3.809	3.873	3.846	3.980	3.938	4.027	3.879	4.024
Species	**Elbaite**	**Elbaite**	**Elbaite**	**Elbaite**	**Celleriite**	**Celleriite**	**Foitite**	**Celleriite**	**Celleriite**

[a] Calculated by stoichiometry (see text);
[b] Estimated with the procedure of Pesquera et al. (2016);
[c] Determined by Mössbauer spectroscopy.
Errors for oxides and fluorine are standard deviations (in brackets)

Empirical chemical formulae

Z1 $^{X}(Na_{0.58}\square_{0.41}Ca_{0.01})_{\Sigma 1.00}{}^{Y}(Al_{1.62}Li_{1.02}Fe^{2+}_{0.02}Mn^{2+}_{0.32}Ti_{0.01})_{\Sigma 3.00}{}^{Z}Al_6[{}^{T}(Si_{5.95}Al_{0.05})O_{18}](BO_3)_3{}^{V}(OH)_{\Sigma 3.00}{}^{W}(OH_{0.45}F_{0.36}O_{0.19})_{\Sigma 1.00}$

Z2 $^{X}(Na_{0.62}\square_{0.36}Ca_{0.02})_{\Sigma 1.00}{}^{Y}(Al_{1.50}Li_{0.97}Fe^{2+}_{0.11}Mn^{2+}_{0.40}Ti_{0.02})_{\Sigma 3.00}{}^{Z}Al_6[{}^{T}(Si_{5.96}Al_{0.04})O_{18}](BO_3)_3{}^{V}(OH)_{\Sigma 3.00}{}^{W}(OH_{0.50}F_{0.31}O_{0.19})_{\Sigma 1.00}$

Z3 $^{X}(Na_{0.60}\square_{0.39}Ca_{0.01})_{\Sigma 1.00}{}^{Y}(Al_{1.65}Li_{1.14}Fe^{2+}_{0.31}Mn^{2+}_{0.17}Ti_{0.01})_{\Sigma 3.00}{}^{Z}Al_6[{}^{T}(Si_{5.97}Al_{0.03})O_{18}](BO_3)_3{}^{V}(OH)_{\Sigma 3.00}{}^{W}(OH_{0.76}F_{0.11}O_{0.13})_{\Sigma 1.00}$

Z4 $^{X}(Na_{0.59}\square_{0.40}Ca_{0.01})_{\Sigma 1.00}{}^{Y}(Al_{1.65}Li_{1.14}Fe^{2+}_{0.31}Mn^{2+}_{0.17}Ti_{0.01})_{\Sigma 3.00}{}^{Z}Al_6({}^{T}Si_{6.00}O_{18})(BO_3)_3{}^{V}(OH)_{\Sigma 3.00}{}^{W}(OH_{0.70}F_{0.15}O_{0.15})_{\Sigma 1.00}$

Z5 $^{X}(Na_{0.33}\square_{0.67})_{\Sigma 1.00}{}^{Y}(Al_{0.93}Li_{0.26}Fe^{2+}_{0.56}Mn^{2+}_{1.24}Ti_{0.01})_{\Sigma 3.00}{}^{Z}Al_6({}^{T}Si_{6.00}O_{18})(BO_3)_3{}^{V}(OH)_{\Sigma 3.00}{}^{W}(OH_{0.97}F_{0.02}O_{0.01})_{\Sigma 1.00}$

Z6 $^{X}(Na_{0.36}\square_{0.64})_{\Sigma 1.00}{}^{Y}(Al_{0.93}Li_{0.36}Fe^{2+}_{0.72}Mn^{2+}_{0.93}Ti_{0.01})_{\Sigma 2.98}{}^{Z}Al_6({}^{T}Si_{6.02}O_{18})(BO_3)_3{}^{V}(OH)_{\Sigma 3.00}{}^{W}(OH_{0.94}O_{0.06})_{\Sigma 1.00}$

Z7 $^{X}(Na_{0.34}\square_{0.66})_{\Sigma 1.00}{}^{Y}(Al_{0.75}Li_{0.40}Fe^{2+}_{0.92}Fe^{3+}_{0.04}Mn^{2+}_{0.75}Ti_{0.01})_{\Sigma 2.89}{}^{Z}Al_6({}^{T}Si_{6.11}O_{18})(BO_3)_3{}^{V}(OH)_{\Sigma 3.00}{}^{W}(OH_{0.95}F_{0.05})_{\Sigma 1.00}$

Z8 $^{X}(Na_{0.46}\square_{0.52}Ca_{0.02})_{\Sigma 1.00}{}^{Y}(Al_{1.15}Li_{0.53}Fe^{2+}_{0.40}Mn^{2+}_{0.86}Ti_{0.01})_{\Sigma 3.00}{}^{Z}Al_6[{}^{T}(Si_{5.97}Al_{0.03})O_{18}](BO_3)_3{}^{V}(OH)_{\Sigma 3.00}{}^{W}(OH_{0.76}F_{0.12}O_{0.12})_{\Sigma 1.00}$

Z9 $^{X}(Na_{0.39}\square_{0.60}Ca_{0.01})_{\Sigma 1.00}{}^{Y}(Al_{0.88}Li_{0.32}Fe^{2+}_{0.68}Mn^{2+}_{1.00}Ti_{0.01})_{\Sigma 3.00}{}^{Z}Al_6[{}^{T}(Si_{5.96}Al_{0.04})O_{18}](BO_3)_3{}^{V}(OH)_{\Sigma 3.00}{}^{W}(OH_{0.97}F_{0.03})_{\Sigma 1.00}$

Table 3.21. Average chemical composition and atoms per formula unit (a.p.f.u) for the different zones of Federico sample (Catri, Sant' Ilario in Campo, Elba Island, Italy) with the relative empirical formula.

	Prismatic section	**Termination**
	Z1	**Z2**
	n =5	n = 19
SiO_2 wt%	38.77(34)	35.99(35)
TiO_2	0.03(2)	0.03(2)
B_2O_3	11.30[a]	10.32[a]
Al_2O_3	43.09(59)	34.66(59)
FeO_{tot}	0.01(1)	13.33(57)
MnO	0.44(32)	0.25(5)
CaO	0.03(2)	0.14(8)
Na_2O	1.85(9)	1.59(21)
Li_2O	1.88[b]	0.21[b]
F	0.51(17)	0.35(23)
H_2O	3.51[a]	3.00[a]
$-O \equiv F$	–0.22	–0.14
FeO	0.01[c]	13.33[c]
Fe_2O_3	-	-
Total	101.25	99.81
Atoms normalized to 31 anions		
Si apfu	6.004	6.059
Ti	0.003	0.004
B	3.000	3.000
Al	7.780	6.877
Fe^{3+}	-	-
Fe^{2+}	0.001	1.877
Mn^{2+}	0.057	0.035
Ca	0.004	0.025
Na	0.551	0.519
Li	1.163	0.142
F	0.250	0.184
OH	3.650	3.371
OH+F	3.851	3.555
Species	**Elbaite**	**Schorl**

[a] Calculated by stoichiometry (see text)
[b] Estimated with the procedure of Pesquera et al. (2016)
[c] Determined by Mössbauer spectroscopy
Errors for oxides and fluorine are standard deviations (in brackets)

Empirical chemical formulae

Z1 $^{X}(Na_{0.55}\square_{0.45})_{\Sigma 1.00}{}^{Y}(Al_{1.78}Li_{1.16}Mn^{2+}{}_{0.06}Ti_{0.003})_{\Sigma 3.00}{}^{Z}Al_6(^{T}Si_6O_{18})(BO_3)_3{}^{V}(OH)_{\Sigma 3.00}{}^{W}(OH_{0.65}F_{0.25}O_{0.10})_{\Sigma 1.00}$

Z2 $^{X}(Na_{0.52}\square_{0.45}Ca_{0.03})_{\Sigma 1.00}{}^{Y}(Al_{0.88}Li_{0.14}Fe^{2+}{}_{1.88}Mn^{2+}{}_{0.04}Ti_{0.004})_{\Sigma 2.94}{}^{Z}Al_6(^{T}Si_{6.06}O_{18})(BO_3)_3{}^{V}(OH)_{\Sigma 3.00}$ $^{W}(OH_{0.37}F_{0.18}O_{0.45})_{\Sigma 1.00}$

Table 3.22. Average chemical composition and atoms per formula unit (a.p.f.u) for the different zones of Pastori sample (Catri, Sant'Ilario in Campo, Elba Island, Italy) with the relative empirical formula.

	Prismatic section									Termination	
	Z1	**Z2**	**Z3**	**Z4**	**Z5**	**Z6**	**Z7**	**Z8**	**Z9**	**Z10**	**Z11**
	n = 21	*n* = 1	*n* = 1	*n* = 1	*n* = 2	*n* = 2	*n* = 1	*n* = 1	*n* = 3	*n* = 3	*n* = 16
SiO_2 wt%	37.63(30)	37.45	37.13	35.92	37.68(29)	36.48(1)	37.37	37.49	38.20(15)	36.04(72)	36.85(32)
TiO_2	0.30(4)	0.22	0.26	0.35	0.26(1)	0.30(1)	0.26	0.25	0.25(2)	0.40(5)	0.29(13)
B_2O_3	10.83[a]	10.67[a]	10.57[a]	10.27[a]	10.71[a]	10.43[a]	10.69[a]	10.69[a]	10.89[a]	10.25[a]	10.55[a]
Al_2O_3	38.65(95)	36.78	35.87	33.87	36.55(32)	35.10(1)	37.23	36.30	38.10(52)	33.44(78)	33.30(66)
FeO_{tot}	1.59(88)	4.24	5.91	11.59	4.37(97)	8.29(18)	3.28	6.26	2.64(80)	11.50(87)	10.41(88)
MnO	2.07(37)	1.40	1.61	0.96	1.83(44)	1.09(12)	1.80	1.23	1.46(20)	0.65(5)	0.06(3)
ZnO	0.04(4)	-	0.06	0.12	0.10	0.19(11)	0.06	0.13	0.05(4)	0.06(2)	0.03(3)
MgO	-	0.03	-	-	-	-	-	0.11	0.01(1)	-	3.13(68)
CaO	0.51(7)	0.24	0.13	0.04	0.17(2)	0.09(3)	0.18	0.17	0.21(6)	0.07(3)	0.09(12)
Na_2O	2.01(10)	2.30	2.26	1.65	2.23(7)	2.04(1)	2.22	2.17	2.08(10)	1.64(15)	1.49(16)
Li_2O	1.73[b]	1.57[b]	1.31[b]	0.49[b]	1.53[b]	0.98[b]	1.61[b]	1.30[b]	1.78[b]	0.63[b]	0.33[b]
F	1.17(20)	1.59	1.24	1.05	1.38(10)	1.03(18)	1.17	1.01	0.83(7)	0.51(10)	0.29(12)
H_2O	3.04	2.83	2.94	2.85	2.99	2.96	3.07[a]	3.11[a]	3.36[a]	3.12[a]	3.50[a]
$-O \equiv F$	−0.49	−0.67	−0.52	−0.44	−0.58	−0.43	−0.49	−0.43	−0.35	−0.21	−0.12
FeO	1.59	4.24	5.91	11.59	4.37	8.29	3.28	6.26	2.64	11.09[c]	10.41
Fe_2O_3	-	-	-	-	-	-	-	-	-	0.41[c]	-
Total	99.15	98.66	98.76	98.72	99.23	98.55	98.45	99.80	99.52	98.10	100.33
Atomic fractions normalized to 31 anions											
Si apfu	6.038	6.102	6.115	6.097	6.116	6.080	6.078	6.098	6.099	6.112	6.068
Ti	0.036	0.027	0.032	0.044	0.031	0.037	0.031	0.030	0.030	0.051	0.036
B	3.000	3.000	3.000	3.000	3.000	3.000	2.990	3.000	3.000	3.000	3.000
Al	7.309	7.064	6.952	6.753	6.993	6.894	7.131	6.958	7.170	6.682	6.463
Fe^{3+}	-	-	-	-	-	-	-	-	-	0.052	-
Fe^{2+}	0.213	0.578	0.813	1.640	0.593	1.155	0.446	0.852	0.353	1.572	1.434
Mn^{2+}	0.282	0.193	0.224	0.138	0.251	0.154	0.248	0.169	0.198	0.093	0.008
Zn	0.004	-	0.007	0.015	0.012	0.023	0.007	0.016	0.006	0.008	0.000
Mg	-	0.007	-	-	-	-	-	0.027	0.002	-	0.768
Ca	0.087	0.042	0.023	0.007	0.030	0.016	0.031	0.029	0.036	0.012	0.016
Na	0.627	0.727	0.721	0.541	0.701	0.659	0.700	0.685	0.643	0.539	0.475
Li	1.116	1.029	0.867	0.333	0.999	0.657	1.053	0.850	1.143	0.429	0.219
F	0.594	0.817	0.645	0.562	0.710	0.543	0.602	0.522	0.420	0.274	0.150
OH	3.250	3.076	3.229	3.220	3.238	3.295	3.334	3.369	3.578	3.529	3.844
OH+F	3.844	3.893	3.874	3.782	3.948	3.838	3.936	3.891	3.998	3.803	3.994
Species	**Fluor-elbaite**	**Fluor-elbaite**	**Fluor-elbaite**	**Fluor-schorl**	**Fluor-elbaite**	**Fluor-elbaite**	**Fluor-elbaite**	**Fluor-elbaite**	**Elbaite**	**Schorl**	**Foitite**

[a] Calculated by stoichiometry (see text);
[b] Estimated with the procedure of Pesquera et al. (2016);
[c] Determined by Mössbauer spectroscopy
Errors for oxides and fluorine are standard deviations (in brackets)

Empirical chemical formulae

Z1 $^{X}(Na_{0.63}\square_{0.28}Ca_{0.09})_{\Sigma 1.00}{}^{Y}(Al_{1.31}Li_{1.12}Fe^{2+}_{0.21}Mn^{2+}_{0.28}Ti_{0.04})_{\Sigma 2.96}{}^{Z}Al_6(^{T}Si_{6.04}O_{18})(BO_3)_3{}^{V}(OH)_{\Sigma 3.00}{}^{W}(OH_{0.25}F_{0.59}O_{0.16})_{\Sigma 1.00}$

Z2 $^{X}(Na_{0.73}\square_{0.23}Ca_{0.04})_{\Sigma 1.00}{}^{Y}(Al_{1.06}Li_{1.03}Fe^{2+}_{0.58}Mn^{2+}_{0.19}Ti_{0.03})_{\Sigma 2.90}{}^{Z}Al_6(^{T}Si_{6.10}O_{18})(BO_3)_3{}^{V}(OH)_{\Sigma 3.00}{}^{W}(OH_{0.08}F_{0.82}O_{0.10})_{\Sigma 1.00}$

Z3 $^{X}(Na_{0.72}\square_{0.26}Ca_{0.02})_{\Sigma 1.00}{}^{Y}(Al_{0.95}Li_{0.87}Fe^{2+}_{0.81}Mn^{2+}_{0.22}Ti_{0.03})_{\Sigma 2.88}{}^{Z}Al_6(^{T}Si_{6.12}O_{18})(BO_3)_3{}^{V}(OH)_{\Sigma 3.00}{}^{W}(OH_{0.23}F_{0.65}O_{0.12})_{\Sigma 1.00}$

Z4 $^{X}(Na_{0.54}\square_{0.45}Ca_{0.01})_{\Sigma 1.00}{}^{Y}(Al_{0.75}Li_{0.33}Fe^{2+}_{1.64}Mn^{2+}_{0.14}Ti_{0.04})_{\Sigma 2.90}{}^{Z}Al_6(^{T}Si_{6.10}O_{18})(BO_3)_3{}^{V}(OH)_{\Sigma 3.00}{}^{W}(OH_{0.20}F_{0.56}O_{0.24})_{\Sigma 1.00}$

Z5 $^{X}(Na_{0.70}\square_{0.27}Ca_{0.03})_{\Sigma 1.00}{}^{Y}(Al_{0.99}Li_{1.00}Fe^{2+}_{0.59}Mn^{2+}_{0.25}Ti_{0.03})_{\Sigma 2.88}{}^{Z}Al_6(^{T}Si_{6.12}O_{18})(BO_3)_3{}^{V}(OH)_{\Sigma 3.00}{}^{W}(OH_{0.24}F_{0.71}O_{0.05})_{\Sigma 1.00}$

Z6 $^{X}(Na_{0.66}\square_{0.32}Ca_{0.02})_{\Sigma 1.00}{}^{Y}(Al_{0.89}Li_{0.66}Fe^{2+}_{1.15}Mn^{2+}_{0.15}Ti_{0.03})_{\Sigma 2.92}{}^{Z}Al_6(^{T}Si_{6.08}O_{18})(BO_3)_3{}^{V}(OH)_{\Sigma 3.00}{}^{W}(OH_{0.30}F_{0.54}O_{0.16})_{\Sigma 1.00}$

Z7 $^{X}(Na_{0.70}\square_{0.27}Ca_{0.03})_{\Sigma 1.00}{}^{Y}(Al_{1.31}Li_{1.05}Fe^{2+}_{0.45}Mn^{2+}_{0.25}Ti_{0.03})_{\Sigma 2.92}{}^{Z}Al_6(^{T}Si_{6.08}O_{18})(BO_3)_3{}^{V}(OH)_{\Sigma 3.00}{}^{W}(OH_{0.33}F_{0.60}O_{0.07})_{\Sigma 1.00}$

Z8 $^{X}(Na_{0.69}\square_{0.28}Ca_{0.03})_{\Sigma 1.00}{}^{Y}(Al_{0.96}Li_{0.85}Fe^{2+}_{0.85}Mn^{2+}_{0.17}Ti_{0.03})_{\Sigma 2.90}{}^{Z}Al_6(^{T}Si_{6.10}O_{18})(BO_3)_3{}^{V}(OH)_{\Sigma 3.00}{}^{W}(OH_{0.37}F_{0.52}O_{0.11})_{\Sigma 1.00}$

Z9 $^{X}(Na_{0.64}\square_{0.32}Ca_{0.04})_{\Sigma 1.00}{}^{Y}(Al_{1.17}Li_{1.14}Fe^{2+}_{0.35}Mn^{2+}_{0.20}Ti_{0.03})_{\Sigma 2.90}{}^{Z}Al_6(^{T}Si_{6.10}O_{18})(BO_3)_3{}^{V}(OH)_{\Sigma 3.00}{}^{W}(OH_{0.58}F_{0.42})_{\Sigma 1.00}$

Z10 $^{X}(Na_{0.54}\square_{0.45}Ca_{0.01})_{\Sigma 1.00}{}^{Y}(Al_{0.68}Li_{0.43}Fe^{2+}_{1.57}Fe^{3+}_{0.05}Mn^{2+}_{0.09}Ti_{0.05})_{\Sigma 2.89}{}^{Z}Al_6(^{T}Si_{6.11}O_{18})(BO_3)_3{}^{V}(OH)_{\Sigma 3.00}{}^{W}(OH_{0.53}F_{0.27}O_{0.20})_{\Sigma 1.00}$

Z11 $^{X}(Na_{0.48}\square_{0.50}Ca_{0.02})_{\Sigma 1.00}{}^{Y}(Al_{0.46}Li_{0.22}Fe^{2+}_{1.43}Mn^{2+}_{0.01}Ti_{0.04})_{\Sigma 2.93}{}^{Z}Al_6(^{T}Si_{6.07}O_{18})(BO_3)_3{}^{V}(OH)_{\Sigma 3.00}{}^{W}(OH_{0.84}F_{0.15}O_{0.01})_{\Sigma 1.00}$

In general, chemical analysis revealed that the termination of each crystal is characterized by a sudden increase in Mn and/or Fe that is responsible for the color variation at the analogous pole. As expected, in the tourmaline crystals with the most significant Mn and/or Fe increase at the termination (MnO > 5 wt% and FeO > 2 wt%), the color variation is resulting more dramatic, and the species changes from an initial elbaite/fluor-elbaite, $Na(Li_{1.5}Al_{1.5})Al_6Si_6O_{18}(BO_3)_3(OH)_3(OH,F)$, to celleriite, $\square(Mn^{2+}_2Al)Al_6(Si_6O_{18})(BO_3)_3(OH)_3(OH)$, foitite, $\square(Fe^{2+}_2Al)Al_6(Si_6O_{18})(BO_3)_3(OH)_3(OH)$ or schorl $NaFe^{2+}_3Al_6(Si_6O_{18})(BO_3)_3(OH)_3(OH)$ at the crystal termination.

Such chemical evolution is clear evident in Rosina 2, Testa Scura and San Silvestro samples (Fig. 3.26 A, B, G), where the increase in Mn over Fe led to the formation of celleriite. On the other hand, in Pastori and Federico samples, the increase in Fe over Mn led to the formation of foitite and schorl, respectively (Fig. 3.26 H, I). The identified species for the different zones relative to the prismatic section and the dark-colored termination of each tourmaline sample are summarized in Tables 3.12-3.22.

In most of the studied samples, the content in MnO and FeO at the dark-colored termination follows a rhythmic behaviour and, in some cases, this oscillatory pattern led to an alternation of either celleriite, $\square(Mn^{2+}_2Al)Al_6(Si_6O_{18})(BO_3)_3(OH)_3(OH)$, and rossmanite, $\square(Li_2Al)Al_6(Si_6O_{18})(BO_3)_3(OH)_3(OH)$, or celleriite and foitite, $\square(Fe^{2+}_2Al)Al_6(Si_6O_{18})(BO_3)_3(OH)_3(OH)$, compositions (Fig. 3.27).

In Figure 3.28 are summarized all compositional data that confirm an increase in Mn and/or Fe at the analogous termination, which is more evident in those samples wherein a chemical evolution occurred.

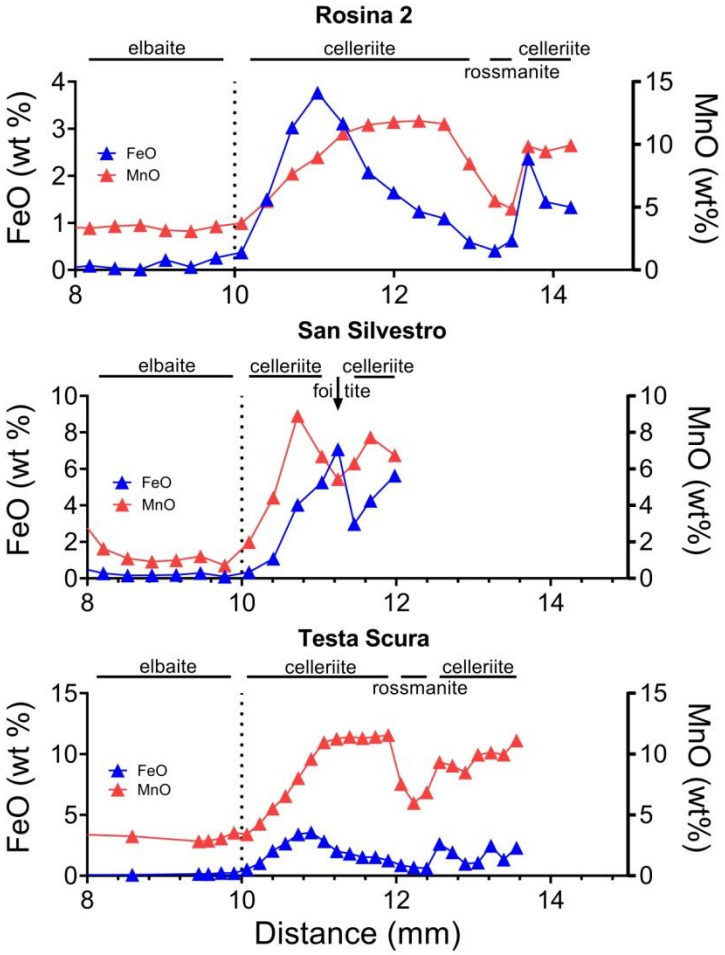

Figure 3.27. Variation in MnO and FeO (wt%) along a straight traverse parallel to the **c**-axis of Rosina 2, San Silvestro and Testa Scura tourmaline crystals, from the upper section to the dark termination. The dashed line marks the transition between the upper section and the dark colored termination of the crystals.

MS data and iron speciation

Portions of the dark-colored overgrowths of Federico, Rosina 2, San Silvestro and Pastori samples, characterized by the highest Fe content, were subjected to MS analysis to evaluate the Fe redox state. The obtained spectra were deconvoluted using Lorentzian doublets and their hyperfine parameters were interpreted according with the model described in Andreozzi et al. (2008). The hyperfine parameters of MS doublets and the relative Fe oxidation state and site assignment for each sample analyzed are summarized in Table 3.23. The spectrum of Federico sample was accurately fitted with three doubles consistent with Fe^{2+} at the *Y* site. No indication of absorption due to Fe^{3+} was observed (Fig. 3.29A).

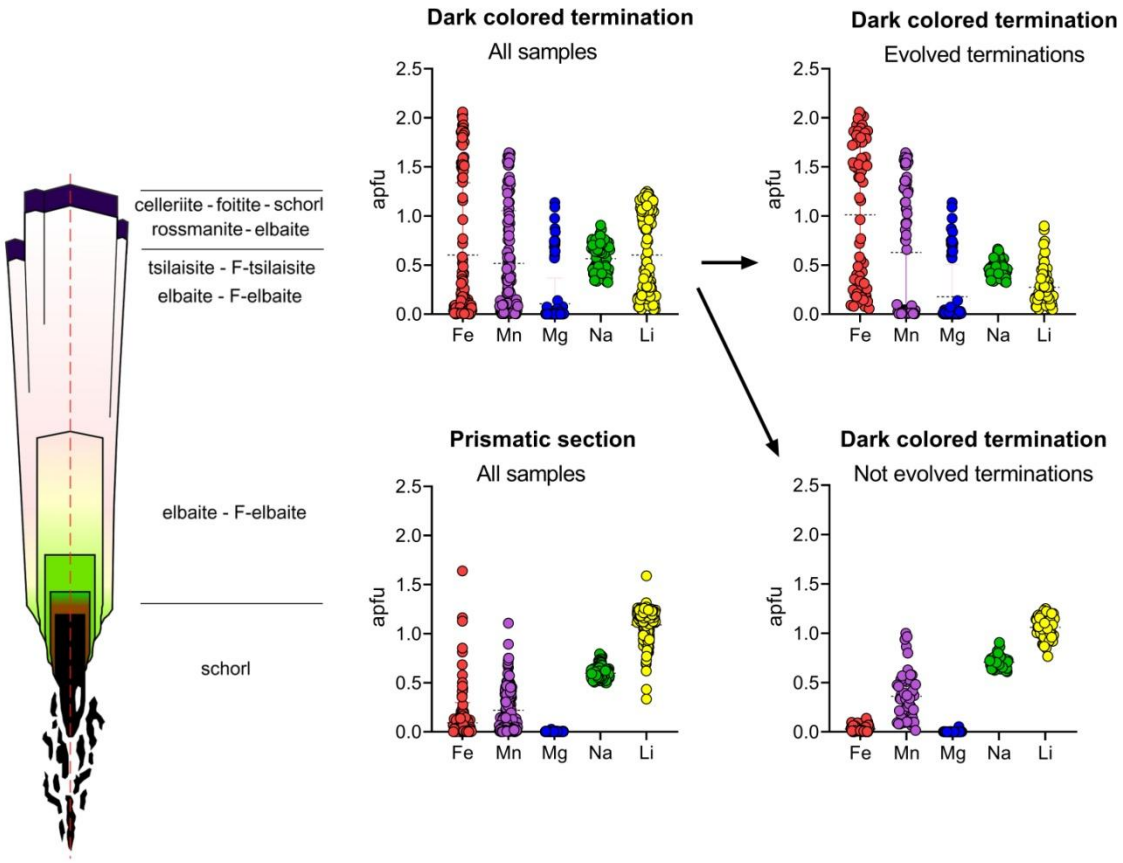

Figure 3.28. Compositional variations in typical tourmaline crystals from Elba pegmatites. The representative abundances of Fe, Mn, Mg, Na, Li (apfu) are reported for the prismatic sections and the dark colored terminations. Each point represents the result of a spot analysis (about 400).

For San Silvestro and Pastori samples, a different model with four absorption doublets was adopted. The first three doublets of San Silvestro and Pastori samples were interpreted as Fe^{2+} at the *Y* site (*Y*1, *Y*2 and *Y*3). Differently, the fourth doublets of San Silvestro and Pastori samples are consistent with Fe^{3+} (5% and 4% of Fe_{tot} for San Silvestro and Pastori samples, respectively) (Fig. 3.29B,C).

For Rosina 2 sample, Fe oxidation state and site assignment are similar to San Silvestro and Pastori samples, with most of Fe^{2+} at *Y* site (87% of Fe_{tot}) and a small amount of Fe^{3+} assigned at the *Y* site (4% of Fe_{tot}) (Bosi et al., 2022a). However, Rosina 2 sample is characterized by the presence of Fe^{2+} at the *Z* site (9% of Fe_{tot}), which could be explained by the preferential occupation of the *Y* site by Mn^{2+} respect to Fe^{2+} (e.g., Bosi, 2018). In fact, as above reported by EMPA, the FeO-rich portion of Rosina 2 dark-coloured overgrowth is characterised by the highest Mn

concentration (MnO ~ 9 wt%). Because the Fe^{3+}/Fe_{tot}-ratio in all the tourmaline samples analysed is ≤ 0.05, very low oxidizing conditions during the late-stage of Federico, Rosina 2, San Silvestro and Pastori crystals growth can be hypothesized.

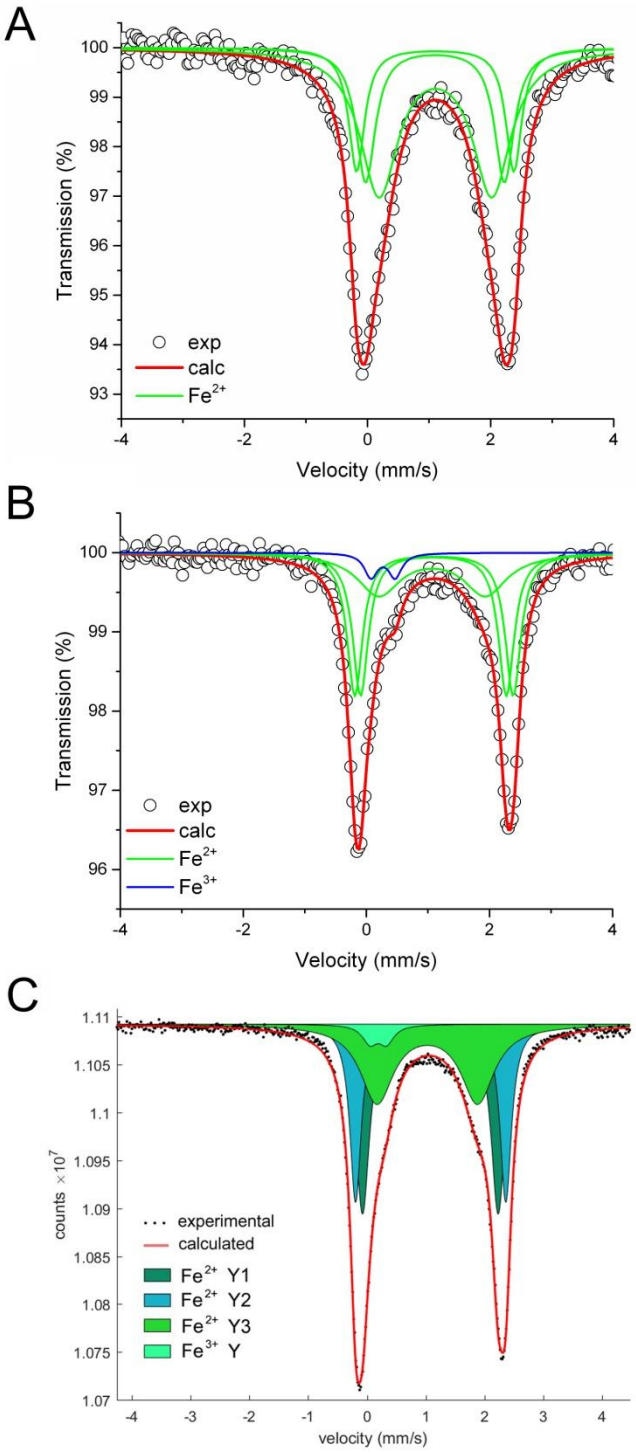

Figure 3.29. Room temperature ^{57}Fe Mössbauer spectra for the dark-colored overgrowths of Federico, San Silvestro and Pastori samples. For Federico and San Silvestro samples (A,B), experimental spectrum (exp) is represented by open circles, calculated spectrum (calc) by thick red curve. Lorentzian absorption doublets assigned to $^{[6]}Fe^{2+}$ are represented by thin green lines, whereas the absorption doublet assigned to $^{[6]}Fe^{3+}$ is represented by thin blues line. For Pastori sample (C), experimental spectrum (exp) is

represented by dots, calculated spectrum (calc) by thick red curve. Lorentzian absorption doublets assigned to $^{[6]}Fe^{2+}$ are represented by dark-green, light blue and light green colored areas. The neon-green colored area refers to the assignment of $^{[6]}Fe^{3+}$.

Table 3.23. Room temperature ^{57}Fe Mössbauer parameters for FeO-rich portions of the dark-colored overgrowths in selected tourmaline samples

Sample	δ mm/s	ΔE_Q mm/s	Γ mm/s	Assignment	%Area	Fe^{3+}/Fe_{Tot}
Federico	1.10	2.55	0.32	Fe^{2+} (*Y*1)	20	
	1.10	2.25	0.38	Fe^{2+} (*Y*2)	30	0.00
	1.10	1.83	0.75	Fe^{2+} (*Y*3)	50	
Rosina 2	1.09	2.47	0.36	Fe^{2+} (*Y*1)	81	
(Bosi et al. 2022a)	1.12	2.06	0.20	Fe^{2+} (*Y*2)	6	
	1.12	1.45	0.42	Fe^{2+} (*Z*)	9	
	0.42	0.16	0.24	Fe^{3+} (*Y*)	4	0.04
San Silvestro	1.10	2.57	0.30	Fe^{2+} (*Y*1)	34	
	1.09	2.37	0.30	Fe^{2+} (*Y*2)	34	
	1.07	1.73	0.84	Fe^{2+} (*Y*3)	27	
	0.27	0.39	0.26	Fe^{3+} (*Y*)	5	0.05
Pastori	1.08	2.55	0.24	Fe^{2+} (*Y*1)	27	
	1.08	2.30	0.29	Fe^{2+} (*Y*2)	35	
	1.02	1.71	0.68	Fe^{2+} (*Y*3)	34	
	0.19	0.28	0.31	Fe^{3+} (*Y*)	4	0.04

Centroid shift (δ) in mm/s relative to α-Fe foil; errors are estimated no less than ± 0.02 mm/s for δ, quadrupole splitting (ΔE_Q), and peak width (Γ), and no less than ± 3% for doublets areas. Site assigment is based on Andreozzi et al. (2008)

3.5.4 Discussion

Overall, EMPA data revealed a sharp increase in Mn and/or Fe at the analogous termination of all analyzed samples, which is responsible at the same time for the color anomalies and for the chemical evolution, with in some samples relatively high changes (MnO > 5 wt% and FeO > 2 wt%). Such increase in Mn/Fe suggests that a sudden chemical variation in the crystallization environment, with a new supply in Fe/Mn during the latest stages of tourmaline growth, occurred.

In the studied samples, the increase in Mn and Fe is consistent with the substitution of Li and Al at the *Y* site. However, this substitution can occur in different ways according to whether Mn and Fe totally or partially replace Li and Al.

Total substitution of Li and Al by Mn/Fe

$$(Li_{1.5} + Al_{1.5})^{\Sigma charge = 6+} \leftrightarrow 3(Fe^{2+}/Mn^{2+})^{\Sigma charge = 6+} \quad \text{Equation 1}$$

Partial substitution of Li and Al by Mn/Fe:

$$(Li_{1.5} + Al_{0.5})^{\Sigma charge = 3+} \leftrightarrow 2(Fe^{2+}/Mn^{2+})^{\Sigma charge = 4+} \quad \text{Equation 2}$$

$$(Li_{1.0} + Al_{1.0})^{\Sigma charge = 4+} \leftrightarrow 2(Fe^{2+}/Mn^{2+})^{\Sigma charge = 4+} \quad \text{Equation 3}$$

To gain information about which kind of substitution occurred during the chemical evolution of the samples studied, the content of 2Li vs (Mn + Fe) at *Y* site, calculated for each spot analysis, was plotted. As shown in Figure 3.30, the left part of the graph is mainly occupied by data points corresponding to geochemically evolved species. Interestingly, compositional data are preferentially distributed along a trend line corresponding to a partial substitution with a total charge variation at *Y* site (Equation 2), indicating that this is the most favored type of substitution in the crystals from Elba Island. As this substitution determines a total charge variation, it needs to be balanced by the incorporation of a cation vacancy (□) replacing Na at the *X* site: $Na^{+} + (1.5Li + 0.5Al)^{\Sigma 3+} \leftrightarrow \square + 2(Mn,Fe)^{\Sigma 4+}$.

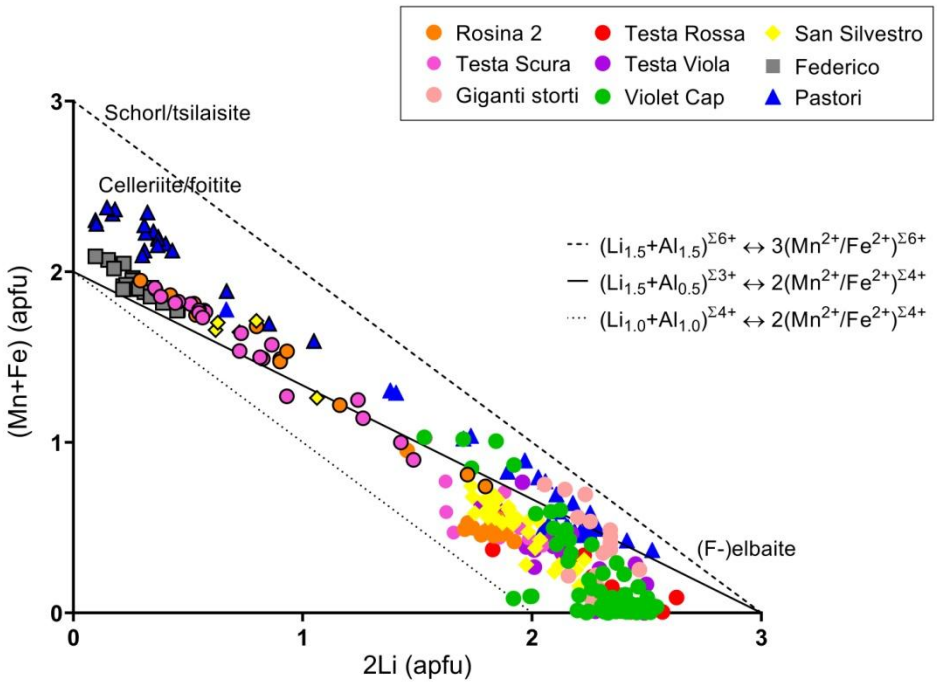

Figure 3.30. Plot of the content of 2Li vs. (Mn+Fe) at the *Y* site for each spot analysis of the tourmaline samples studied. The three lines (dashed, dotted and full) represent different degree of substitution. Symbols with black border indicate the compositions relative to the dark terminations of the different samples. For Pastori sample the Mg content was also considered.

In support of this simplified mechanism, Na and OH occupations at *X* and *W* sites calculated for each data point, were plotted (Fig. 3.31). It can be observed that most of the data points corresponding to the evolved termination are characterized by a low content in Na at the *X* site and a higher content in OH at the *W* site. In fact, OH is structurally more compatible with a cation vacancy at the *X* site for electrostatic reason (Bosi, 2010; 2018).

By analyzing the occupation at *X*, *Y* and *W* sites for the different data points of the studied samples (Fig. 3.32), a clear linear relationship in plotted data can be observed. This trend is consistent with the crystal-chemical evolution observed in most of the tourmalines analyzed, which follow a transition from an initial elbaite/fluor-elbaite composition to celleriite, foitite and schorl, that can be described by following general chemical substitution:

$$^{X}Na^{+} + {}^{Y}(Li_{1.5} + Al_{0.5})^{3+} + {}^{W}F^{-} \leftrightarrow {}^{X}\square + 2^{Y}(Fe/Mn)^{2+} + {}^{W}OH^{-}$$

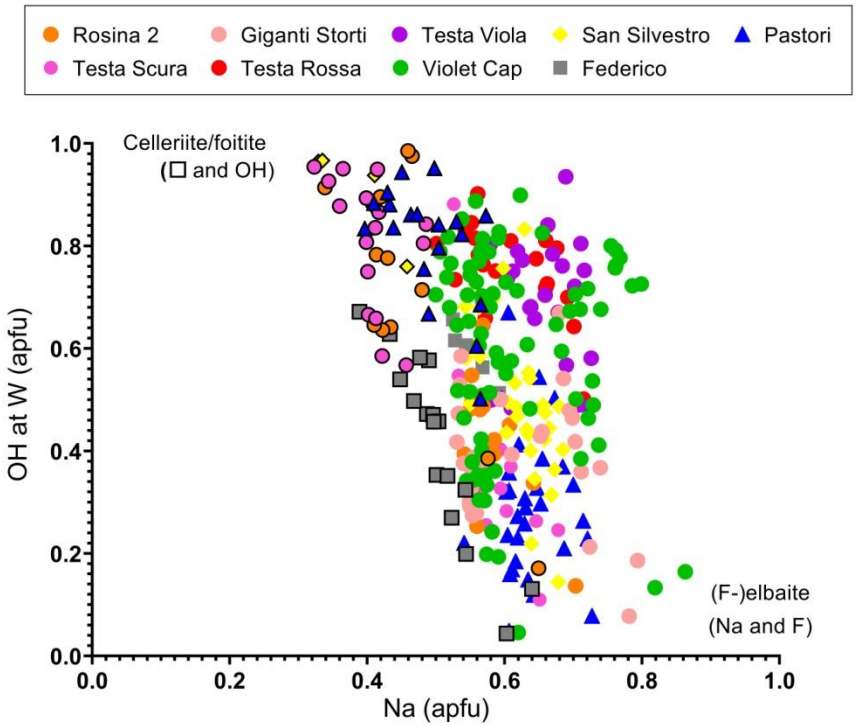

Figure 3.31. Plot of the content of Na vs. ^{W}OH for each spot analysis of the tourmaline samples studied. Symbols with black border indicate the compositions relative to the dark terminations of the different samples.

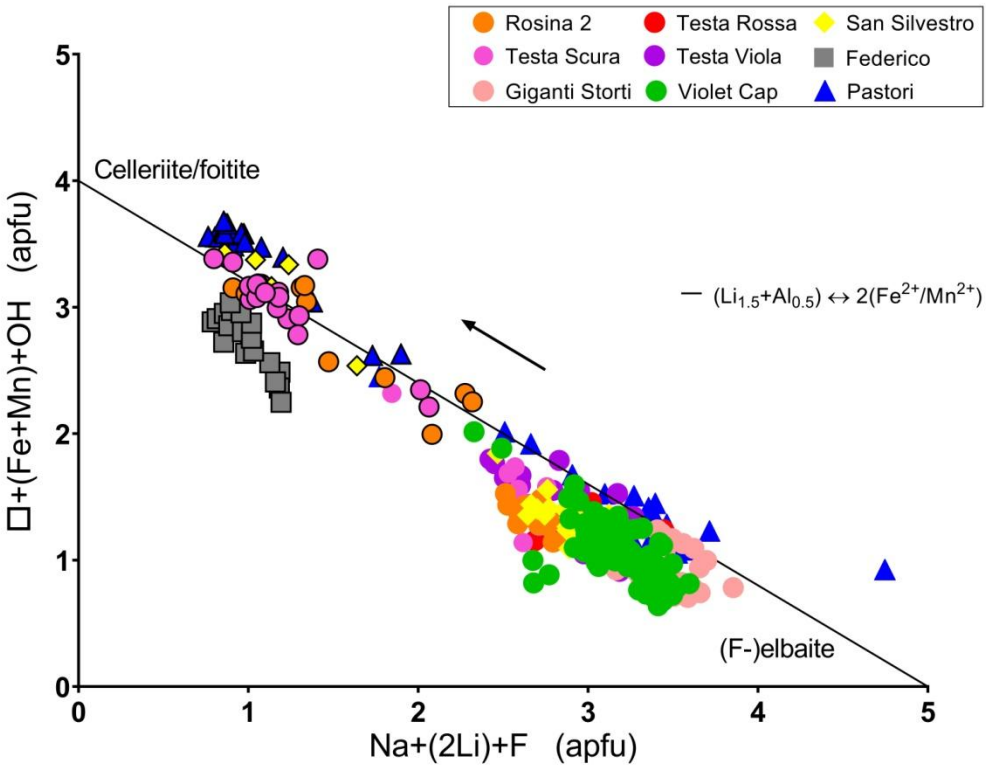

Figure 3.32. Plot of the content of Na+(2Li)+F vs. $^{X}\square$+(Mn+Fe)+^{W}OH for each spot analysis of the tourmaline samples studied. Symbols with black border indicate the compositions relative to the dark terminations of the different samples. For Pastori sample the Mg content was also considered. The arrow highlights the compositional evolution trend followed by the tourmaline samples investigated.

Depending on the relative increase in Mn and Fe, and thus the dominant cation at *Y* site, different type of geochemically evolved species can occur at the termination of each sample. Rosina 2 and Testa Scura are characterized by a consistent Mn enrichment respect Fe at the analogous pole (MnO up to 12 wt%, FeO < 5 wt%), which result in a dark brownish-purplish termination of celleriite composition (Fig. 3.26 A,B). Additionally, a local decrease in Mn at the termination led to a rossmanite compostion in alternation with celleriite. The termination of San Silvestro is enriched in both Mn and Fe. This led to a cellerite composition when Mn is over Fe and foitite in the opposite condition (Fig. 3.26 G). Differently, in Federico and Pastori samples the Fe content is always much higher than Mn (FeO >10 wt%), leading to two different mineralogical species (Fig. 3.26 H,I). Indeed, the black termination of Federico is consistent with a schorl composition, which generally requires a complete substitution at *Y* site (Equation 1), differently from

the behaviour observed for all the other samples. However, the empirical chemical formula calculated, $^{X}(Na_{0.51}\square_{0.46}K_{0.01}Ca_{0.02})_{\Sigma 1.00}{}^{Y}(Al_{0.94}Li_{0.14}Mn^{2+}_{0.04}Fe^{2+}_{1.87}Ti_{0.01})_{\Sigma 3.00}$ $^{Z}Al_{6}{}^{T}Si_{6.06}B_{3}O_{27}{}^{V}(OH)_{3}{}^{W}(OH_{0.39}F_{0.18}O_{0.43})_{\Sigma 1.00}$, is barely enough to assign it as schorl. The increase in Fe content at the termination of Pastori leads to a foitite composition. A singular feature of this sample is that the increase in Fe is also accompanied by a significant increase in Mg and a simultaneously lack of Mn. A first sudden and temporary chemical variation, with FeO up to 10 wt%, is concentrated in a small region of the crystal (about 0.4 mm) where a rapid transition from fluor-elbaite to fluor-schorl to fluor-elbaite/elbite composition occurred. A further increase in FeO (up to 10 wt%) results in a color change from bright green to black (Fig. 3.26 I). The peculiar characteristic of this termination is the presence of Mg instead of Mn, related to a different chemical environment that led to Mg availability instead of Mn. The increase in Mg is concomitant with the transition from a schorl composition to foitite.

In the other analyzed tourmaline samples (Testa Rossa, Testa Viola and Violet Cap), although they resulted characterized by an increase in Mn at the termination (MnO > 3 wt%), the chemical variations are not enough for a change in the name of the species, and thus the mineralogical species remains elbaite/F-elbaite (Fig. 3.26 D-F).

Genetic geochemical model for the colour anomalies of Elba tourmaline crystals

Compositional data suggest that a sharp increase in Mn and/or Fe must have occurred in the latest stage of tourmaline crystal growth, leading to the formation of dark-colored overgrowths generally ascribed as color anomalies. The formation of such color anomalies is related to a sudden physicochemical change in the crystallization environment, here considered the consequence of an opening of the geochemical system related to the mechanic destabilization of the pocket in which tourmalines grew. Bosi et al. (2022a) and Altieri et al. (2022; 2023) already proposed a genetic model for some dark-colored overgrowths in Elba tourmaline crystals based on a pocket rupture event followed by leaching and corrosion

processes of the Fe- and Mn-rich cavity-lining minerals. In agreement with this model, all pockets from which the tourmaline samples were collected are characterized by thin radial fractures penetrating from the cavity into the enclosing pegmatite, suggesting fracturing of the pockets and, in some cases, phenomena of partial cavity collapse. Additionally, the occurrence of fractured and corroded primitive Fe- and Mn-rich minerals in proximity of the cavities is particularly evident (Altieri et al., 2023).

Paragenetic observations of the cavities in which the tourmaline samples were collected reveal abundant petalite, pollucite and lepidolite. The occurrence of such mineral phases provides evidence that the initial steps of crystal growth occurred in pegmatite portions characterized by an advanced degree of geochemical evolution (Pezzotta 2000; 2021). At this stage, the pegmatitic melt appears to be depleted in Mn and Fe, as such elements were stored in the early-crystallized minerals, such as spessartine and biotite present in the pegmatitic rock surrounding the cavities. Therefore, tourmalines in the cavities initially crystallized as elbaite/F-elbaite. However, compositional analyses revealed a sudden increase in Fe and/or Mn at the analogous termination leading, in some cases, to the evolution from an initial elbaite/fluor-elbaite composition to celleriite, foitite or schorl. We ascribe this sudden chemical change to the pocket rupture event, likely related to a rigid mechanical shock to which the cavity underwent, caused, for instance, by a thermal contraction during pegmatite cooling, possibly coupled with residual tectonic stress along the border of the granodioritic pluton of Monte Capanne. In this scenario, the highly reactive late-stage cavity fluids were allowed to permeate the fractures in the pegmatitic rock surrounding the cavity where the early-crystallized minerals were formed (i.e., spessartine and biotite, and in some cases even sekaninaite). The hydrothermal alteration of such minerals through leaching and corrosion processes ascribed to the late-stage fluids connected with the cavities, led to the release of Fe/Mn in the pockets. Thus, the incorporation of Mn and Fe during the latest stages of crystallization, coupled with the presence of abundant B, was responsible for both the color anomalies

observed at the termination of the tourmaline crystals and for their chemical changes. In addition, the late-stage hydrothermal cavity fluids promoted OH incorporation at *W* site and the consequent loss of Na at *X* site, explaining the partial substitution at *Y* observed in the tourmaline samples during the latest stage of crystallization (Fig. 3.33).

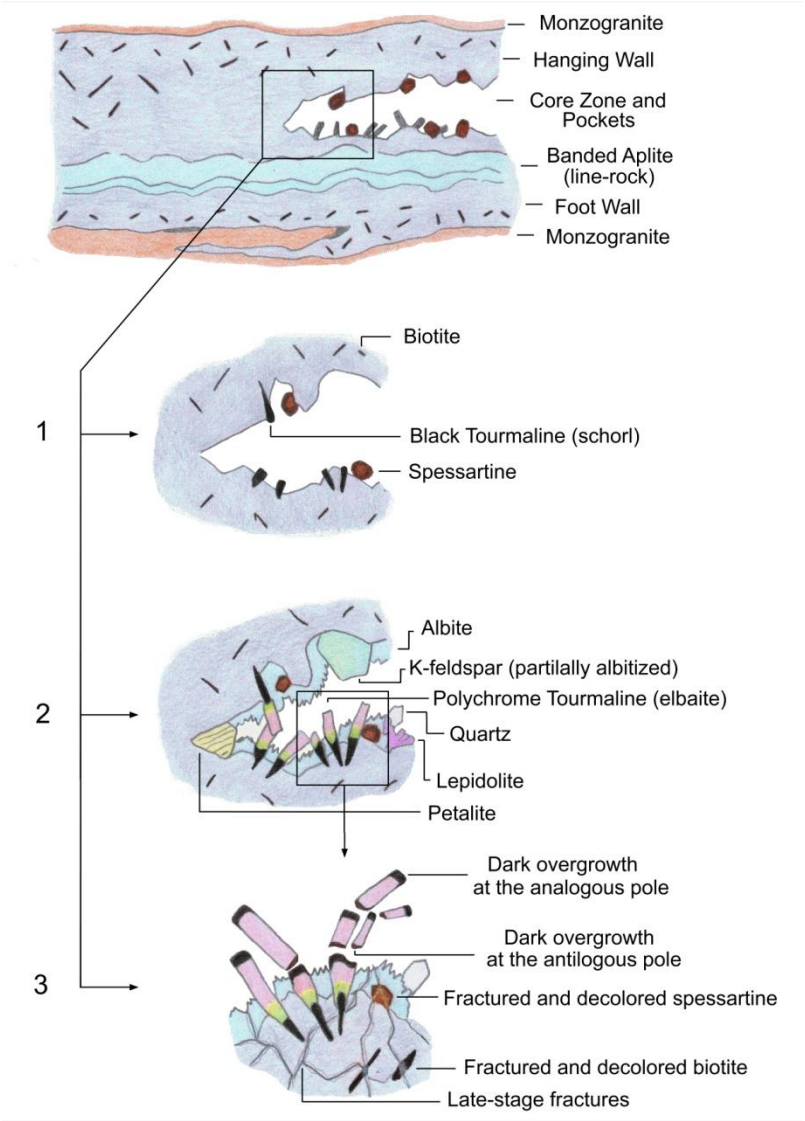

Figure 3.33. Schematic representation of the evolution of a miarolitic cavity in an Elba tourmaline-bearing pegmatite. 1) Early-stage of cavity evolution marked by the crystallization of primary schorl and spessartine garnet. 2) Growth of polychrome elbaite crystals with abundant lepidolite and petalite. The occurrence of these latter mineral phases, along with the presence of early-crystallized spessartine garnet, indicates that the initial steps of tourmaline crystals growth occurred in pegmatite portions characterized by an advanced degree of geochemical evolution. 3) Fracturing of the cavity as a consequence of a rigid mechanical shock. At the same time some tourmaline crystals underwent breakage. The pocket rupture event allowed the highly-reactive cavity-fluids to permeate the fractures in the enclosing pegmatite where the primitive accessory minerals were hosted. Leaching and corrosion of biotite and spessartine caused a sudden

increase in Fe and Mn availability in the pocket environment, and the consequent crystallization of the dark-colored overgrowths at the analogous poles and also at the antilogous poles of the broken tourmaline crystals.

The case, previously reported in Altieri et al. (2023) of a tourmaline crystal found naturally broken in several fragments within a wide miarolitic cavity in the Rosina pegmatite, and characterized by dark-colored overgrowths at both analogous and antilogous poles, strengthens this genetic model, as it records a strict relationship between the crystal rupture and the dark-colored overgrowths.

Based on variations in Mn and Fe observed at the termination of the analyzed tourmaline samples, and considering both the pegmatitic veins and the cavities in which tourmalines originated, some remarks can be made. Tourmaline samples from the Rosina pegmatite, which belong to group II, are characterized by the presence of Mn and low Fe contents at the termination. On the contrary, tourmalines from Federico and Pastori pegmatitic veins, which belong to group III, share very low Mn contents and high amount in Fe at the dark termination (Table 3.24).

In the case of the celleriite-bearing pockets of Rosina (Polluciti cavity) and San Silvestro (Central cavity) pegmatites, the abundance of spessartine coupled with the relative scarcity of biotite and others Fe-rich minerals in the pegmatitic rock surrounding the cavities may account for a Mn-rich, Fe-poor source in the late-stage cavity fluids. This was responsible for the crystallization of a brownish-purplish overgrowth composed by celleriite in Rosina 2, Testa Scura and San Silvestro samples.

In the case of the Giganti storti, Testa Rossa and Testa Viola samples, the miarolitic cavities in which they originated were subject to a less efficient late-stage fluid interaction with the early crystallized minerals in the surrounding pegmatite, which generated a late-stage tourmaline overgrowth characterized by a more limited Mn and/or Fe enrichment. As a result, the mineralogical species of these tourmaline samples remains elbaite/fluor-elbaite even at the purplish-to-reddish overgrowths.

Table 3. Summary of compositional characteristics of the different dark-colored overgrowths in relation to the primitive accessory minerals occurring close to the pocket in which the tourmaline crystals studied were formed.

Sample	Pegmatite	Pocket	Mn-and Fe-rich accessory minerals	Pegmatitic group	Dark termination	
					MnO, FeO and MgO range (wt%)	Mineral Species
Rosina 2	Rosina	Polluciti	Spessartine (+++) Biotite (+)	II	MnO 5-12 FeO 0-4 MgO 0	Celleriite
Testa Scura	"	"		II	MnO 5-12 FeO 0-4 MgO 0	Celleriite
Giganti Storti	"	Giganti storti	Spessartine (+)	II	MnO 0-1.5 FeO 0 MgO 0	Elbaite
Testa Rossa	"	Farfalle	Spessartine (+)	II	MnO 0-3 FeO 0 MgO 0	Elbaite
Testa Viola	"	Candele	Spessartine (+) scarce Biotite	II	MnO 0-5 FeO 0-1.5 MgO 0	Elbaite
Violet Cap	"	Violet Cap	Spessartine (++) scarce Biotite	II	MnO 0-8 FeO 0-1 MgO 0	Elbaite/F-elbaite
San Silvestro	San Silvestro	Central cavity	Spessartine (++) Biotite (++)	II	MnO 1-9 FeO 0-7 MgO 0	Celleriite
Federico	Federico	-	Biotite (+++)	III	MnO 0 FeO 1-14 MgO 0	Schorl
Pastori	Pastori	-	scarce Spessartine Biotite (+++)	III	MnO 0-1 FeO 1-13 MgO 0-3	Foitite

+: abundance of the accessory mineral

On the basis of the color displayed by Mn-rich overgrowth, information on the redox environment can be obtained. Previously obtained optical absorption spectroscopy data, demonstrated that the purplish overgrowths, characterizing the analogous termination of the Violet Cap sample, are the result of Mn^{3+} *d-d* transitions and thus occurred in an oxidizing environment (Altieri et al., 2023). This suggests that a relative oxidizing environment characterizes the formation of all the other overgrowths displaying the same purplish-to-reddish colour (Giganti storti, Testa Rossa and Testa Viola).

As a final remark, it should be point out that tourmalines grown in Polluciti and San Silvestro pockets are characterized by a rhythmic behavior of Mn and Fe at the

crystal termination, leading to an alternation of different mineralogical species. Such compositional oscillatory zoning is assessed to variations in composition (*X*), temperature (*T*) and pressure (*P*) of the crystallizing fluid by Lussier and Hawthorne (2011). In the specific case of Rosina 2, Testa Scura and San Silvestro samples, the apparent non-random distribution of the compositional zone suggests that above variations could be the result of changes in the diffusion rate of Mn and Fe, released by corrosion and alteration phenomena of the earlier crystallized Mn/Fe-rich minerals, at the crystal-melt interface.

The black overgrowth composed of foitite and schorl observed in Pastori and Federico samples, respectively, was produced by significant Fe enrichment in the geochemical system, caused by the hydrothermal alteration of the biotite occurring in the monzogranite which is hosting the narrow veins. The lack of early crystallized Mn-rich minerals (spessartine, for instance) in such pegmatitic dykes is accounting for the very low Mn content in the overgrowths of Pastori and Federico samples. The termination of Federico sample is characterized by a sharp transition from colorless to black with a huge increase in Fe up to 13 wt%. This suggests an intense fracturing of the pocket, which associated to the leaching of biotite, allowed the release and the availability of large amounts of Fe in the system. Differently, chemical data suggest that the pocket in which Pastori sample grew have suffered two successive destabilization events, as supported by structural evidences. A first minor event was responsible for a sudden but limited increase in Fe availability leading to the formation of the narrow fluor-schorl zone. Successive and more intense fracturing phenomena led to a new increase in the availability of Fe, allowing for the formation of the foitite termination. Additionally, the termination of Pastori sample is characterized by an increased amount in Mg linked to the hydrothermal alteration of Mg-rich minerals. In this case the biotite from porphyritic monzogranite in which the Pastori vein is hosted is much richer in Mg than the biotite occurring in the Rosina and the San Sivestro pegmatites.

3.5.5 Conclusions

In this work we strengthen the previously proposed genetic model for the dark-colored overgrowths in Elba tourmaline crystals (Altieri et al., 2023). Based on the size of the cavity, the extent of the fracturing phenomena and the consequent leaching processes, as well as the relative abundance of different primitive minerals in the enclosing pegmatite (such as biotite and spessartine), the chemical composition of the residual cavity fluids underwent a variation in concentration of Fe and Mn. This can result in a simple color change up to a chemical evolution from an initial elbaite/fluor-elbaite composition to foitite, celleriite or schorl at the termination of the tourmaline crystals. For instance, the "blue-cap" tourmalines, found in small cavities within the San Silvestro and Fucili veins, are characterized by a bluish growth zone in the upper part of the crystal, slightly richer in Fe^{2+} (Altieri et al., 2022). The slight enrichment in Fe is consistent with a partial opening of the cavity system associated with a minor fracturing phenomenon. Moreover, the presence of Fe only in the divalent state suggests persisting reducing conditions in the pocket environment (Altieri et al., 2022). On the contrary, in the cavities of the "dark cap" crystals (such as Rosina 2, Testa Scura and San Silvestro samples) more extensive fracturing phenomena associated with the presence of abundant Fe/Mn-rich cavity-lining minerals, allowed the release of high amounts of Fe/Mn to the residual cavity fluids. In these conditions, a chemical evolution at the analogous termination of the tourmaline crystals occurred. Depending on the prevalence of Mn or Fe, the overgrowths can result in celleriite, foitite or schorl composition.

A similar scenario occurred in the cavity of Rosina pegmatite where the Violet Cap sample, characterized by late-stage Mn-rich dark-colored overgrowths, respectively purplish-red at the analogous pole (Mn^{3+} dependent), and yellow–orange at the antilogous one (Mn^{2+} dependent), was collected (Altieri et al., 2023). In this case, the partial collapse of the cavity caused not only an intense leaching and corrosion of the primitive Mn-rich minerals in enclosing pegmatite, but also the breakage in several fragments of some tourmaline crystals, allowing for the

formation of new growth surfaces in the direction of the analogous and the antilogous poles. Although the Mn increase at the overgrowths confirmed a significant chemical evolution, the mineralogical species remain elbaite/fluor-elbaite. The presence of Mn of both in the redox state +3 and +2 suggests that corrosion and alteration phenomena occurred in a relatively oxidizing environment (Altieri et al., 2023). In the case of late-stage fracturing of narrow dykes (such as the Federico and the Pastori dykes), pocket fluids interacted with Fe and Mg-rich minerals occurring in the host rock, producing a sudden and more massive contamination of the geochemical environment of the cavities, resulting in the formation of a thick black tourmaline overgrowth, rich in iron and, occasionally even magnesium.

The results obtained in this work, as well as previously published data, improved the knowledge on the opening of geochemical systems in which tourmaline crystallized, and allowed the definition of a genetic model for the formation of the color anomalies in Elba tourmaline crystals. This model could probably be exported to explain late-stage color and composition anomalies of gem tourmaline crystals of many other gem-pegmatite deposits in the world.

4. MOZAMBIQUE – Chemical and spectroscopic characterization of gem-quality tourmalines from the Alto Ligonha pegmatite district (Mavuco locality, NE Mozambique)

4.1 Introduction

Tourmaline crystals from the Alto Ligonha pegmatite district, in NE Mozambique, are among the most renowned gemstones for the combination of color, durability and rarity. These features make them unique from a gemological viewpoint and therefore with a high commercial value, limiting the information regarding their crystal-chemical characteristics. For example, few data are available on the chemical composition and, in particular, studies relating the chemical composition of tourmalines to their color are lacking. To fill this gap, several tourmaline samples from the secondary deposit of Mavuco, in the eastern portion of the Alto Ligonha pegmatite district (Nampula Province, NE Mozambique), were studied (Fig. 4.1).

These tourmaline samples were provided by ongoing mining projects, and were subjected to an in-depth analysis. Specifically, a detailed chemical characterization, as well as a correlation study between compositional data and color displayed, was conducted. In addition, on selected samples with particular chromatic features, optical absorption spectroscopy analyses were performed. For all the tourmaline samples analyzed, the gemological variety, according to the color displayed, was identified.

Some of the tourmaline crystals from the secondary deposit of Mavuco are characterized by a prismatic dark-colored overgrowth, which genetic mechanisms have not already been defined as the pegmatitic source from which these tourmalines originated was still uncertain. This uncertainty was essentially due to the strong NYF (Niobium-Yttrium-Fluorine) geochemical affinity (Li- and B-poor composition) of the Alto Ligonha pegmatites found quite close the secondary deposit of Mavuco, as well as the rudimentary excavation techniques, which did not allow the exploration of new pegmatitic deposits in the Alto Ligonha district.

Figure 4.1. Cu-bearing tourmalines are found in northeastern Mozambique, in Nampula Province, near the village of Mavuco. From Nampula, Mavuco can be reached via Murrupula (from Laurs et al. 2008).

To gain information about the pegmatitic sources of the detrital samples of the Mavuco area and the processes that led to the formation of the observed dark-colored overgrowths, selected tourmaline crystals from a recently discovered pegmatitic field, the so-called "Marina" pegmatite, were analyzed. The "Marina" pegmatite was hypothesized to be a source of the detrital tourmaline grains of the Mavuco area, given its proximity to the secondary deposit, and its LCT geochemical signature.

Studies on tourmaline crystals from the "Marina" pegmatite were carried out to confirm the above hypothesis, through the comparison of the compositional data obtained from such tourmaline crystals, with those obtained from the detrital

tourmalines of the secondary deposit of Mavuco. The same studies allowed obtain detailed information on the genesis of the prismatic dark-colored overgrowths, which also characterize some of the detrital tourmalines

4.2 Geological setting

4.2.1 Summary of the geological frame in the Mavuco area (NE Mozambique)

The basement rocks in the Mavuco area (NE Mozambique), constitute part of the Mozambique Belt (1100–800 Ma), which extends from the Mediterranean Sea down to central Mozambique (Lächelt, 2004). The Mozambique belt covers a large area from Mozambique through Tanzania and Kenya, and is extremely rich in gems and minerals (Bettencourt Dias and Wilson, 2000). In the northeastern Mozambique, the basement consists mostly of strongly metamorphosed gneisses (migmatites) that were deformed during the Pan-African tectonic event (800-550 Ma). During the period 600-400 Ma, such rocks were intruded by granitoid masses and rare-element granite pegmatite rocks, which currently constitute the Pegmatitic District of Alto Ligonha (Pinna et al., 1993; Lächelt, 2004; Fig. 4.2). The Alto Ligonha pegmatitic district covers an area of approximately 200 km^2 (Laurs et al., 2008) and, since the 1930s, it is well known for producing superb gem material such as specimens of tourmaline, beryl and topaz hosted in miarolitic cavities. Additionally, the Alto Ligonha pegmatitic rocks have been mined for a variety of raw materials including rare metals (Li, Be, Nb and Ta) and industrial minerals such as quartz, mica, feldspar and clay. (Bettencourt Dias and Wilson, 2000; Lächelt, 2004).

The Mavuco area is tropically weathered and mostly covered by deep lateritic soil thanks to its tropical humid climate.

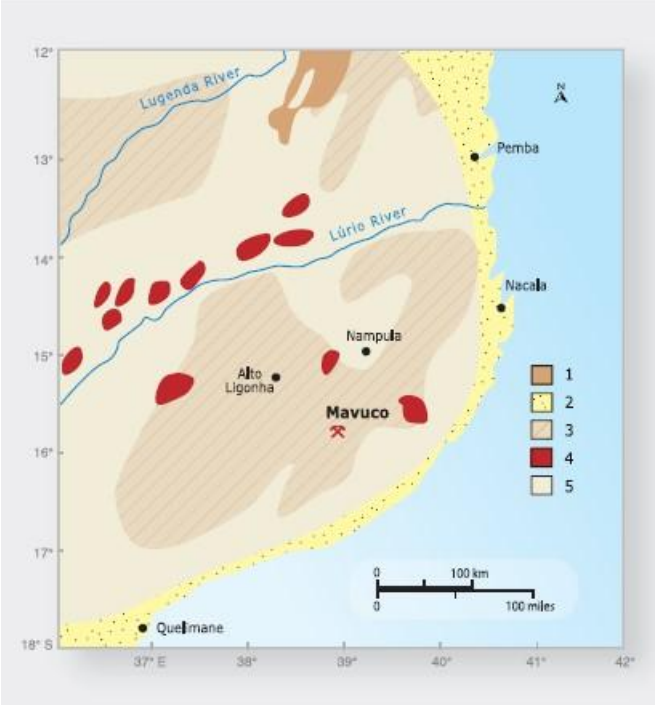

Figure 4.2. The area where the Cu-bearing tourmalines are found lies on the eastern side of the Alto Ligonha pegmatite district. This geologic sketch map shows the principal tectonic-geologic units: (1) rift of the East African Rift System; (2) Mesozoic and Cenozoic sedimentary rocks; (3) pegmatite fields; (4) Pan-African intrusions; (5) Mozambican areas, part of the Mozambique Belt and mostly remetamorphosed during the Pan-African tectonic event. Modified after Lächelt (2004) (from Laurs et al. 2008).

4.2.2 Lithological characteristics of the secondary deposit of Mavuco

The mining area of the Mavuco locality consists of an alluvial deposit of approximately 3 km^2. In this secondary deposit, tourmalines can be found as waterworn grains of subangular to subrounded shapes, along with fine- to medium-sized gravels of 0.2-30 mm, quartz and rare feldspar. The tourmaline-bearing gravel layer, called *kamada* in local language, has a thickness ranging from a few centimeters to 1 meter. The *kamada* layer rests on top of an altered biotite gneiss bedrock, and is covered by a red-brown to black bauxitic horizon, called *cororò*. The bauxite varies in thickness from approximately 0.5 m to typically 3-5 m, and its color is due to the weathering of the iron-bearing materials (Laurs et al. 2008) (Fig. 4.3).

Because the gravels are clast-supported and dominated by subangular clasts (> 90% of the whole sediment), the sedimentology and internal architecture of the tourmaline-bearing layer suggest a braided fluvial depositional environment.

Specifically, the event that favored the formation of this alluvial deposit, which is most likely composed of residual material derived from the granitic pegmatites of the Alto Ligonha district, is a fluvial transport characterized by energetically high hydrodynamic conditions during rainy seasons. This is consistent with the climate of Mavuco that is tropical humid with an average rainfall of 250-260 mm in January-February. In this period, the tourmaline-bearing sediments from the Alto Ligonha pegmatites were eroded and transported by the season streams through spasmodic flash floods downhill to the Mavuco area where were deposited (Slater, 2006; Laurs, 2008).

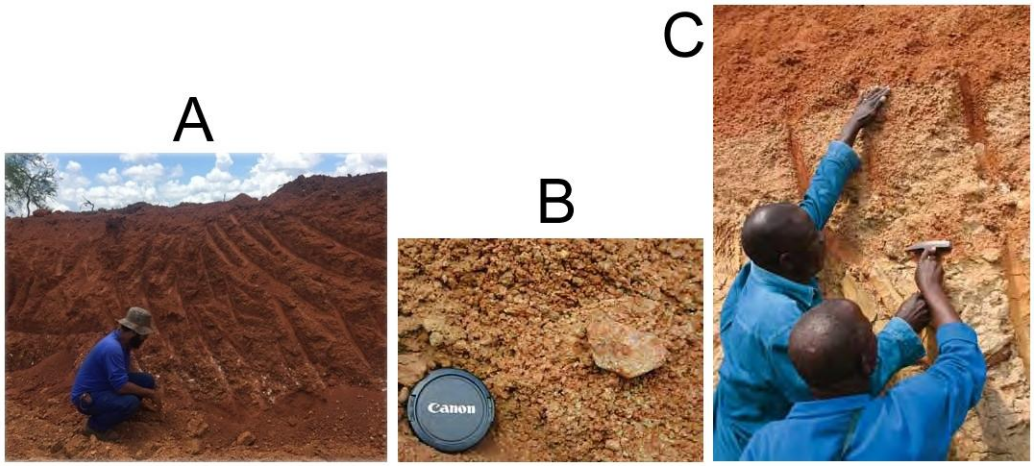

Figure 4.3. A) Cross-section of the geology of the secondary deposit of Mavuco. Photo by F. Pezzotta. The tourmalines are found in a light reddish brown quartz-rich gravel layer on top of a light tan weathered bedrock, and underneath a top layer of red-brown clayey soil. B) The tourmaline-bearing layer is a clast-supported gravel. Many of the clasts are angular, such as the larger (5 cm) quartz pebble toward the right in this image. Photo by J. C. Zwaan. C) The gravel layer can be found between 0.5 m and 5 m below the surface in the Mavuco area. The thickness of the tourmaline-bearing gravel layer is indicated by the men in the image B. Photo by J. C. Zwaan.

4.2.3 The Alto Ligonha pegmatitic district

Alto Ligonha Pegmatite Province

The Pan African rare-element pegmatites of the Alto Ligonha Pegmatite Province of northern Mozambique, are famous for their gemstones, industrial minerals and rare metals (REE, Be, Nb–Ta, Li, U–Th). Pegmatites of the Alto Ligonha district are characterized by a LCT geochemical signature with a variable NYF affinity, and are sourced from late- to post-orogenic subaluminous to peraluminous A-type

granites of Pan-African age (Cronwright, 2005; Melcher et al., 2015). The Alto Ligonha pegmatites can be subdivided into four groups of economically important rare-element pegmatites: 1) Sodic; 2) Potassic with beryl and columbotantalite; 3) Potassic rich in uranium, thorium and rare-earth bearing minerals; 4) Amazonite-bearing and tourmaline–bearing pegmatite. These pegmatites were dated at between 481-440 Ma, thereby post-dating the intrusion of the late undeformed Pan African granites (~521-495 Ma) (Cronwright, 2005).

The sodic pegmatites (also referred to as "sodalithic" due to the occurrence of plagioclase and lithium minerals in these rocks), are usually well zoned and contain beryl, tourmaline, lepidolite, spodumene, and a variety of accessory minerals. These pegmatites constitute the most important group and occur mainly in amphibole schists, amphibolites and mica schists. They correspond to the complex spodumene and lepidolite–albite–spodumene types of the LCT family of Černý (1991).

The potassic pegmatites (beryl-columbite subtype, LCT family) are characterized by beryl, minor polycrase–euxenite, monazite, ilmenite and bismuthite.

The potassic pegmatites with metamict U, Th and REE minerals show attributes of both the LCT and NYF families.

Lastly, the amazonite-bearing and tourmaline-bearing pegmatites have similar degrees of fractionation to the sodalithic and potassic pegmatites respectively (Cronwright, 2005 and Melcher et al., 2015).

The "Marina" pegmatite: a possible source of the detrital tourmalines from the secondary deposit of Mavuco

The Mavuco area is probably the world's largest known alluvial deposit of Cu-bearing *Paraiba-type* tourmalines (Laurs et al., 2008). Mavuco actually produces tourmalines with a wide range of colors, typically purple, violet to blue, blue to green, and green to yellowish green (Fig. 4.4). Among them, tourmalines with bright blue-to-green hues are the most sought after in the gem market, as they closely resemble the renowned and appreciated tourmalines from Brazil's Paraíba

State. The *Paraiba* variety is very uncommon and represents only 10% of the rough tourmaline mined from the Mavuco area (Laurs et al., 2008).

Figure 4.4. Cu-bearing tourmalines found as waterworn pebbles of different coloration in the secondary deposit of Mavuco. Photo by F. Pezzotta.

Several hypotheses were put forward about the origin of the Cu-bearing tourmalines from the Mavuco area. The presence of Cu in these tourmalines suggested that the primary deposit from which they originated, must have the same chemical signature. However, until 2016, all granitic pegmatites mined in the Pegmatitic District of the Alto Ligonha, close to the Mavuco alluvial deposit, resulted Cu-free, also with a significant NYF affinity. Recently, thanks to the improved excavation techniques and the effort of the Mozambique-Gems Company, owner of the mining license in the Alto Ligonha pegmatite district, it was possible to discover a new primary deposit, the so-called "Marina" granitic pegmatite, which identification was hindered by the rudimentary excavation techniques. This pegmatite, which got its name for surface occurrences of gem crystals of beryl variety *aquamarine*, is a relatively large body (Fig. 4.5). At the surface it is more than 140 m long and 15 m thick, and it is hosted in meta-amphibolites. The "Marina" pegmatite represents the first discovered primary deposit of the Alto Ligonha pegmatite district close to the secondary deposit of Mavuco, in which Cu-bearing tourmalines were found. For this reason, it can be hypothesized that the detrital tourmalines hosted in the *kamada* layer of the alluvial deposit of Mavuco, were originated from tourmaline crystals grown within miarolitic cavities of the "Marina" pegmatite, as source of the residual material.

Figure 4.5. Vew of the "Marina" pegmatite, hosted in anfibolite rock, in Mavuco, Alto Ligonha, Mozambique. Photo by F. Pezzotta.

4.3 Analytical Methods

4.3.1 Samples description

Sixteen selected tourmaline samples from the secondary deposit of Mavuco, located in the Pegmatitic District of Alto Ligonha, were studied (Fig. 4.6). The samples collected were found as waterworn grains with a sub-angular to sub-rounded shape. Most of them show a dark-colored prismatic overgrowth that surrounds completely, or in part, a multicolored core ranging from blue, green, yellow to purple-red, even within the same crystal. All samples analyzed are representative of a crystal section perpendicular to the **c**-axis.

In addition, a multicolored tourmaline crystal from the "Marina" pegmatite, a recently discovered primary deposit in the Alto Ligona district from which the detrital tourmalines of the Mavuco locality are supposed to derive, was analyzed (Fig. 4.7).

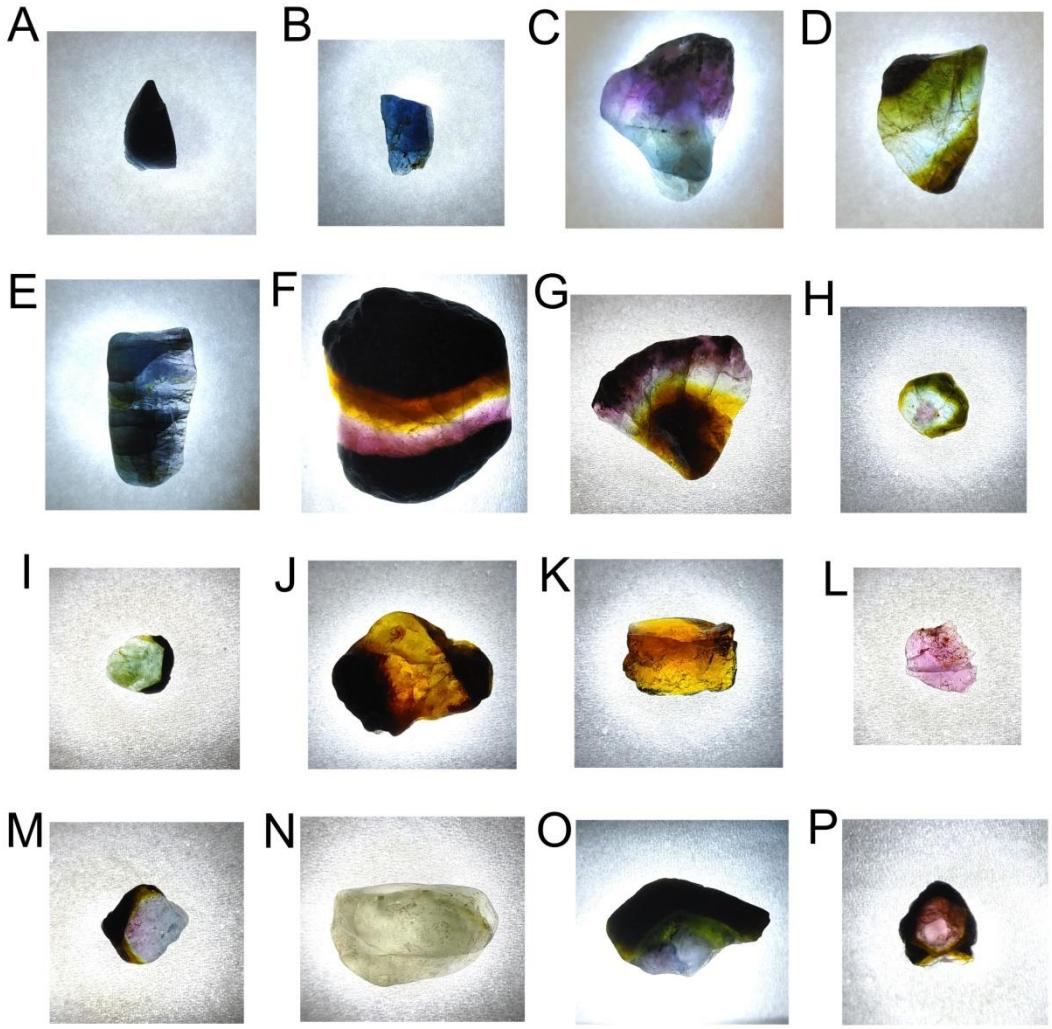

Figure 4.6. The tourmaline grains analyzed for this study. A) MAV 1; B) MAV 2; C) MAV 3; D) MAV 4; E); MAV 5; F) MAV 6; G) MAV 7; H) MAV 8; I) MAV 10; J) MAV 11; K) MAV 12; L) MAV 13; M) MAV 14; N) MAV 15; O) MAV 17; P) MAV 18.

Here is reported a brief description of the tourmaline samples analyzed in this study, as well as their appearance and weight:

MAV 1: Eye-shaped dark colored fragment corresponding to the core of a tourmaline crystal. Weight: 1.05 gr (Fig. 4.6 A).

MAV 2: Fragment of a dark tourmaline core. The crystal shows portions of weathering alteration. Weight: 5.65 gr (Fig. 4.6 B).

MAV 3: Polychrome tourmaline grain characterized by a purplish core and a dark green rim. Weight: 11.69 gr (Fig. 4.6 C).

MAV 4: Polychrome tourmaline grain with a greenish core. Weight: 21.45 gr (Fig. 4.6 D).

MAV 5: Tourmaline grain with a blue core. Weight: 12.61 gr (Fig. 4.6 E).

MAV 6: Polychrome tourmaline grain of 12.75 gr. The crystal is characterized by a black core, an intermediate polychromatic zone and a dark-colored rim (Fig. 4.6 F).

MAV 7: Polychrome tourmaline grain of 9.48 gr. The crystal displays a brownish core, an intermediate polychromatic zone and a black rim (Fig. 4.6 G).

MAV 8: Prismatic section of a tourmaline crystal with a black overgrowth surrounding a polychromatic core. Weight: 4.18 gr (Fig. 4.6 H).

MAV 10: Prismatic section of a tourmaline crystal with a black overgrowth surrounding a green core. Weight: 2.00 gr (Fig. 4.6 I).

MAV 11: Tourmaline grain of 4.69 gr with a yellow zone surrounded by two dark-colored zones (Fig. 4.6 J).

MAV 12: Fragment of a yellow tourmaline core. Weight: 0.63 gr (Fig. 4.6 K).

MAV 13: Fragment of a pink-reddish tourmaline core. Weight: 0.54 gr (Fig. 4.6 L).

MAV 14: Polychrome tourmaline grain of 1.01 gr. The crystal is characterized by a bluish to pink-reddish core and a black rim (Fig. 4.6 M).

MAV 15: Fragment of a greenish tourmaline core. Weight: 3.81 gr (Fig. 4.6 N).

MAV 17: Polychrome tourmaline grain of 3.61 gr. The crystal displays a bluish to greenish core and a wide black rim (Fig. 4.6 O).

MAV 18: Prismatic section of a tourmaline crystal with a black overgrowth surrounding a pink-reddish core. Weight 1.13 gr (Fig. 4.6 P).

MAV 21: Multicolored tourmaline crystal with a dark-colored overgrowth at the analogous termination, characterized by several zones of brownish, yellowish, green and pink-reddish colors. A couple of bluish-green thin growth-sectors are observable in the upper part of the crystal (Fig. 4.7).

Figure 4.7. MAV 21 sample from the "Marina" pegmatite, Alto Ligonha, Mavuco, Mozambique. A) The crystal under polarized light reveals its polychromatic nature. B) Crystal at natural light illumination. Specimen 30 mm across. Photo by F. Pezzotta.

4.3.2 Samples preparation

All the detrital tourmaline samples were glued to a glass-slide using epoxy resin. A slice of each sample was cut perpendicular to the **c**-axis and subsequently ground and polished to produce a flat surface with a uniform thickness of 500 μm for electron microprobe analysis (EMPA). The different colorations assumed by the core and the dark overgrowths, when present, can be better distinguished once thin section for each detrital sample was realized.

The sample from the "Marina" pegmatite, in which the base and the termination of the crystal can be recognized, was glued to the glass-slide with its length parallel to the surface of the slide. A slice of this tourmaline sample was cut along the growth direction (crystallographic **c**-axis) and subsequently ground and polished to produce a flat surface with a uniform thickness of 500 μm for electron microprobe analysis (EMPA).

Compositional analyses were carried out in order to reveal the chemical composition of the tourmaline samples studied, define their mineralogical species and verify the occurrence of any chemical evolution at the dark-colored overgrowth.

The gemological variety that characterizes the core zone of the detrital tourmalines was identified according to the color displayed and the relative chemical

composition. Moreover, to get information on the causes of color, optical absorption spectroscopy analyses (OAS) were performed on selected tourmaline grains.

4.3.3 Electron-microprobe analysis (EMPA)

Compositional data of all the detrital samples were collected along a straight traverse perpendicular to the **c**-axis with an average step size of 300 μm, using a CAMECA SX50 electron-microprobe at the Istituto di Geologia Ambientale e Geoingegneria (CNR of Rome, Italy). The traverse analyzed in each sample included, when occurring, all the dark-colored overgrowths. The segment of the traverse crossing the core of the crystal was labeled as "C", while that crossing the overgrowth was labeled "OG". In the presence of dark-colored overgrowths at both side of the traverse, they were differentiated as left (OGL) and right (OGR) overgrowths. A total of 501 spot analyses were obtained. EMP analyses were done operating in wavelength-dispersion mode with an accelerating potential of 15 kV, a sample current of 15 nA and a beam diameter of 10 μm. Minerals and synthetic compounds were used as primary standards: wollastonite (Si, Ca), magnetite (Fe), rutile (Ti), corundum (Al), karelianite (V), fluorphlogopite (F), periclase (Mg), jadeite (Na), orthoclase (K), rhodonite (Mn), metallic Cr, Cu and Zn. The PAP correction procedure for quantitative electron probe micro analysis was applied (Pouchou and Pichoir, 1991). Relative error on data was < 5% and detection limits < 0.03 wt%.

Compositional data of MAV 21 sample was collected along a straight traverse parallel to the **c**-axis with an average step size of 300 μm, using a CAMECA SX50 electron-microprobe as above described for the detrital samples. On the basisi of chemical homogeneity, the sample was divided in different zones. A total of 90 spot analyses were obtained.

4.3.4 Optical absorption spectroscopy (OAS)

Polarised room temperature optical absorption spectra of MAV 5, MAV 6 and

MAV 10 core regions in the range of 30000–9000 cm^{-1} (286–1111 nm) were obtained at a spectral resolution of 1 nm on doubly polished sections, using an AVASPEC-ULS2048×16 spectrometer attached via a 400 μm ultraviolet (UV) optical fibre cable to a Zeiss Axiotron UV-microscope. The diameter of the circular measure aperture was 50 μm. A 75 W Xenon arc lamp was used as light source and Zeiss Ultrafluar 10× lenses served as objective and condenser. An UV-quality Glan-Thompson prism, with a working range from 40000 to 3704 cm^{-1} was used as a polariser. The beam was collimated using an adjustable rectangular aperture with edges varying from 50–80 μm.

4.3.5 Determination of atomic fractions

The wt% of element oxides determined by EMPA was used to calculate the atomic fractions (apfu). The B^{3+} content was assumed to be stoichiometric (B = 3.00 apfu). Lithium was calculated in accord with Pesquera et al. (2016). All Fe and Mn were assumed to be in the reduced state +2. The (OH) content and the apfu werecalculated by charge balance with the assumption (T + Y + Z) = 15.00 apfu and 31 anions.

4.4 Results and Discussion

4.4.1 Tourmaline samples from the secondary deposit of Mavuco

Chemical composition of the Mavuco tourmaline grains

Based on the overall appearance, the samples can be classified in two types: grains characterized by a prismatic dark-colored overgrowth, which, in some cases, surrounds the whole crystal, and grains with no overgrowth and mostly homogeneous in color.

It is possible to hypothesize that the original tourmaline crystals from which the analyzed grains derived, were characterized by a dark-colored overgrowth at the crystal termination that developed all over the tourmaline surfaces, including the prism faces. For this reason the chemical analysis for each sample was conducted perpendicularly to the **c**-axis to evaluate any difference in composition between

the crystal core and rim, determine the mineralogical species to which the samples belong, and verify if a chemical evolution occurred within the same tourmaline sample.

On the basis of the variation in chemical homogeneity and color displayed, each sample was divided in different zones. The area corresponding to the dark-colored overgrowth was labeled "OG", while the core zone "C". The "OG" and "C" regions were further subdivided by adding a progressive numerical suffix starting from the rim to the core of the crystal, in presence of changes in composition or color.

The following figures (Figures 4.8–4.23) display the pattern of selected elements (as wt% oxides) determined along the considered traverse of all tourmaline samples from the secondary deposit of Mavuco analyzed. Tables 4.1–4.16 summarized the chemical composition in wt%, apfu for each zone of the studied samples and the relative empirical formula.

MAV 1: the sample represents a fragment of a tourmaline core (C) and, as thin section, shows a blue coloration, which is darker on one side. The chemical composition is quite homogeneous along the analyzed traverse and is characterized by a significant content in Fe and Mn (FeO ~ 3 wt% and MnO ~ 4.5 wt%). CuO content shows some oscillation within 0.03 wt%.

The slight difference in the color displayed is not apparently related to variations in the chemical composition. The blue coloration displayed by this tourmaline sample can be related to the presence of both Fe and Mn as mainly color-causing agents (Fig. 4.8 and Table 4.1).

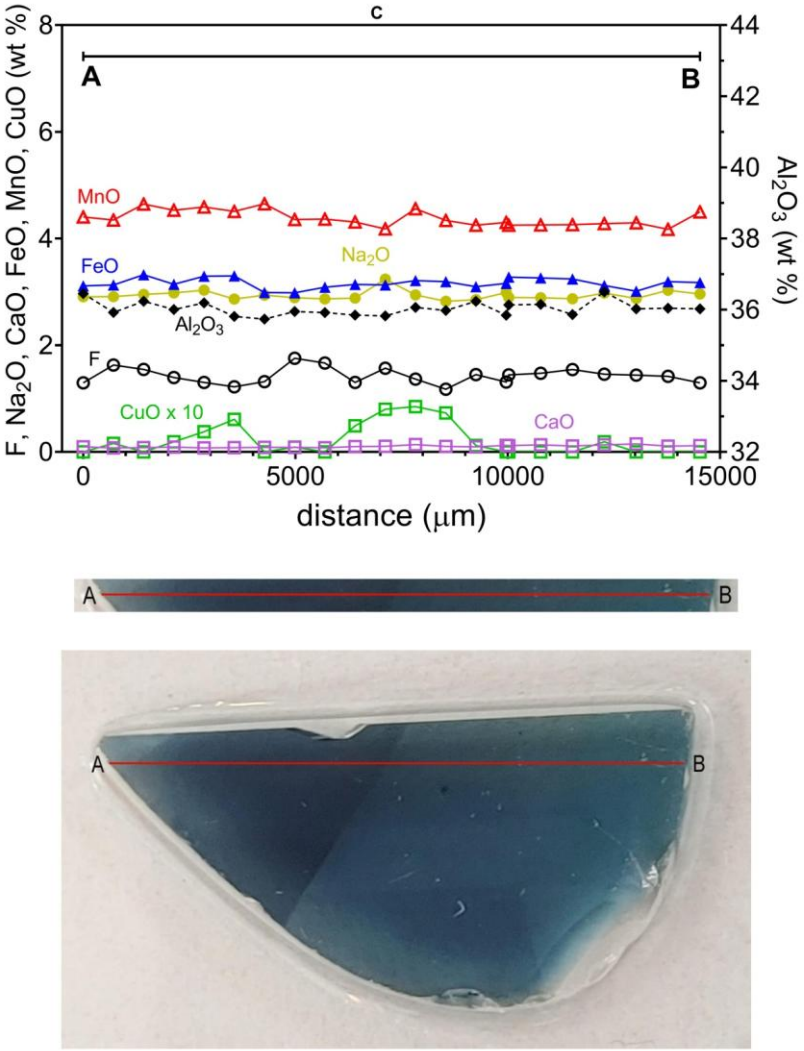

Figure 4.8. EMP analysis of the **MAV 1** sample along a straight traverse perpendicular to the c-axis (only selected oxides are reported. See Table 4.1 for complete chemistry.

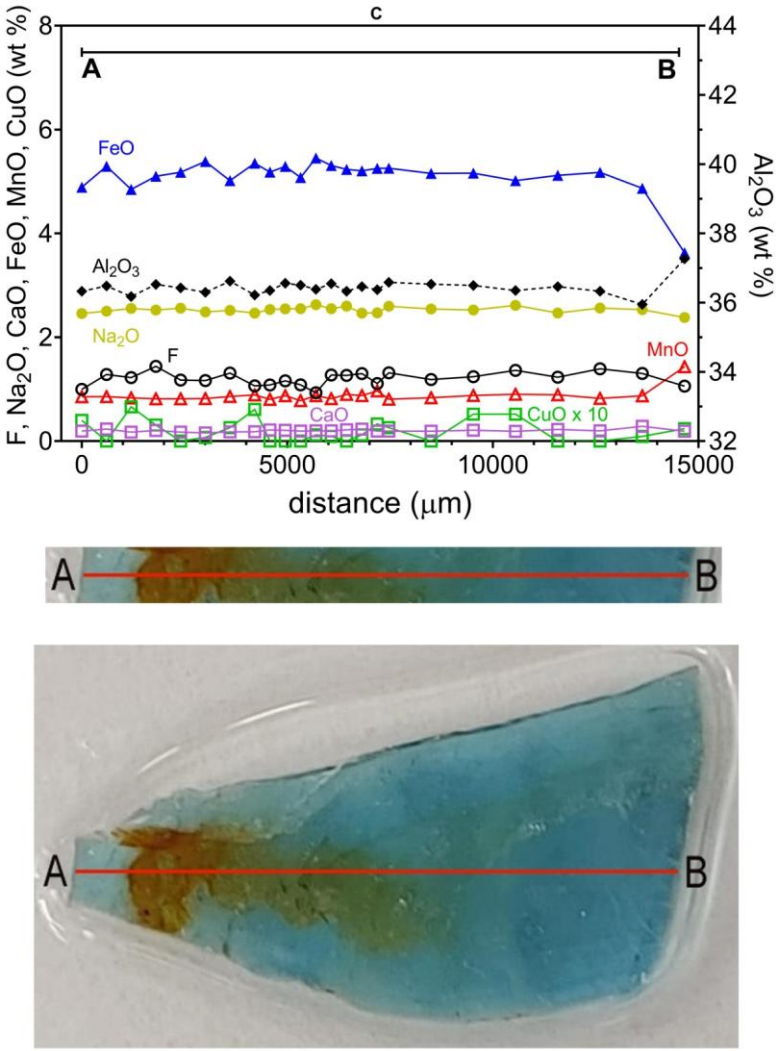

Figure 4.9. EMP analysis of the **MAV 2** sample along a straight traverse perpendicular to the c-axis (only selected oxides are reported. See Table 4.2 for complete chemistry.

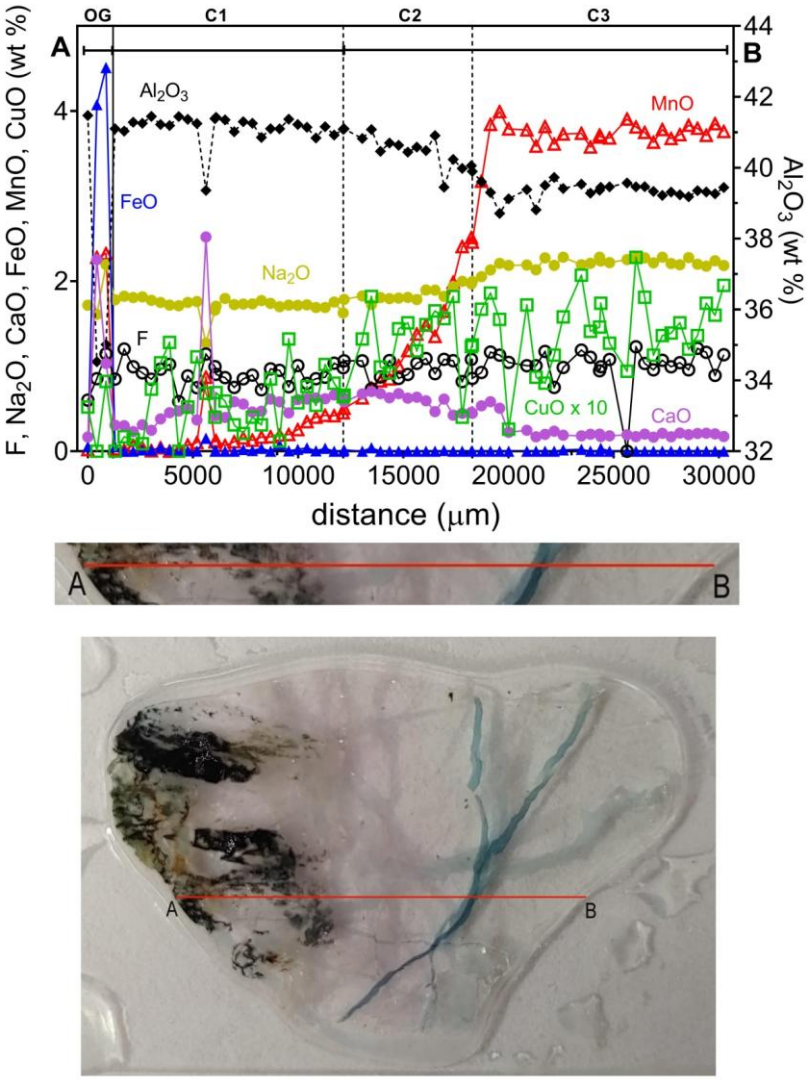

Figure 4.10. EMP analysis of the **MAV 3** sample along a straight traverse perpendicular to the c-axis (only selected oxides are reported. See Table 4.3 for complete chemistry.

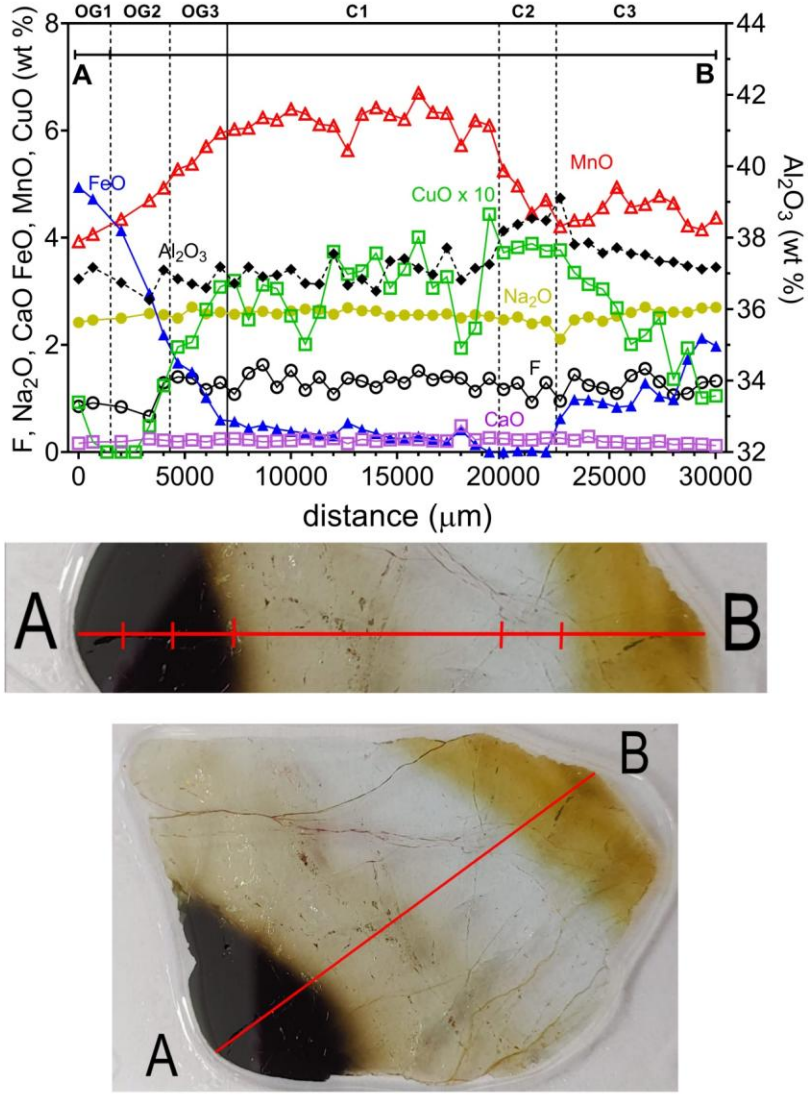

Figure 4.11. EMP analysis of the **MAV 4** sample along a straight traverse perpendicular to the c-axis (only selected oxides are reported. See Table 4.4 for complete chemistry.

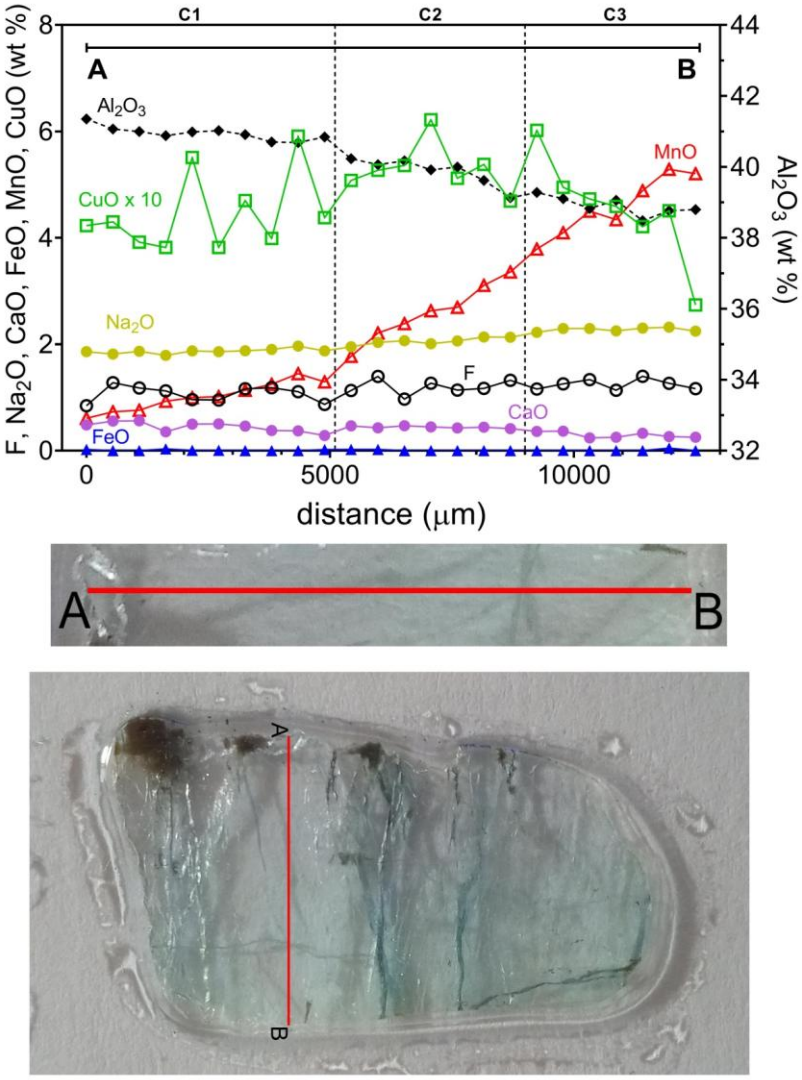

Figure 4.12. EMP analysis of the **MAV 5** sample along a straight traverse perpendicular to the c-axis (only selected oxides are reported. See Table 4.5 for complete chemistry.

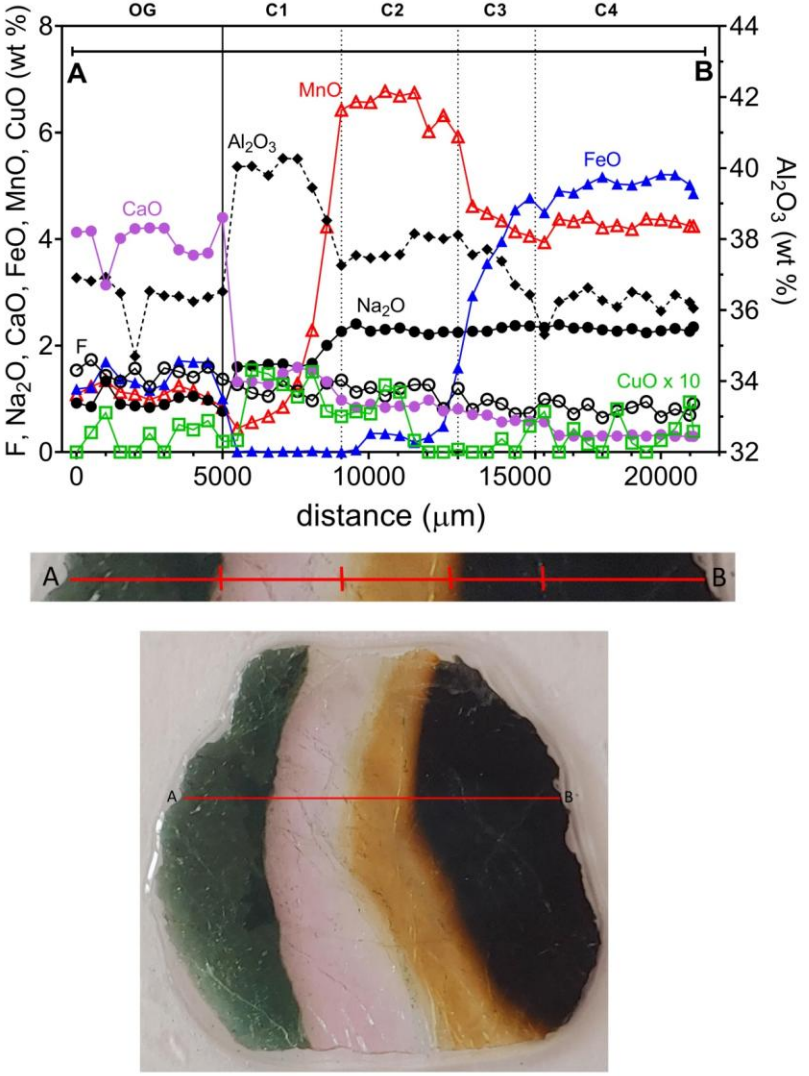

Figure 4.13. EMP analysis of the **MAV 6** sample along a straight traverse perpendicular to the c-axis (only selected oxides are reported. See Table 4.6 for complete chemistry.

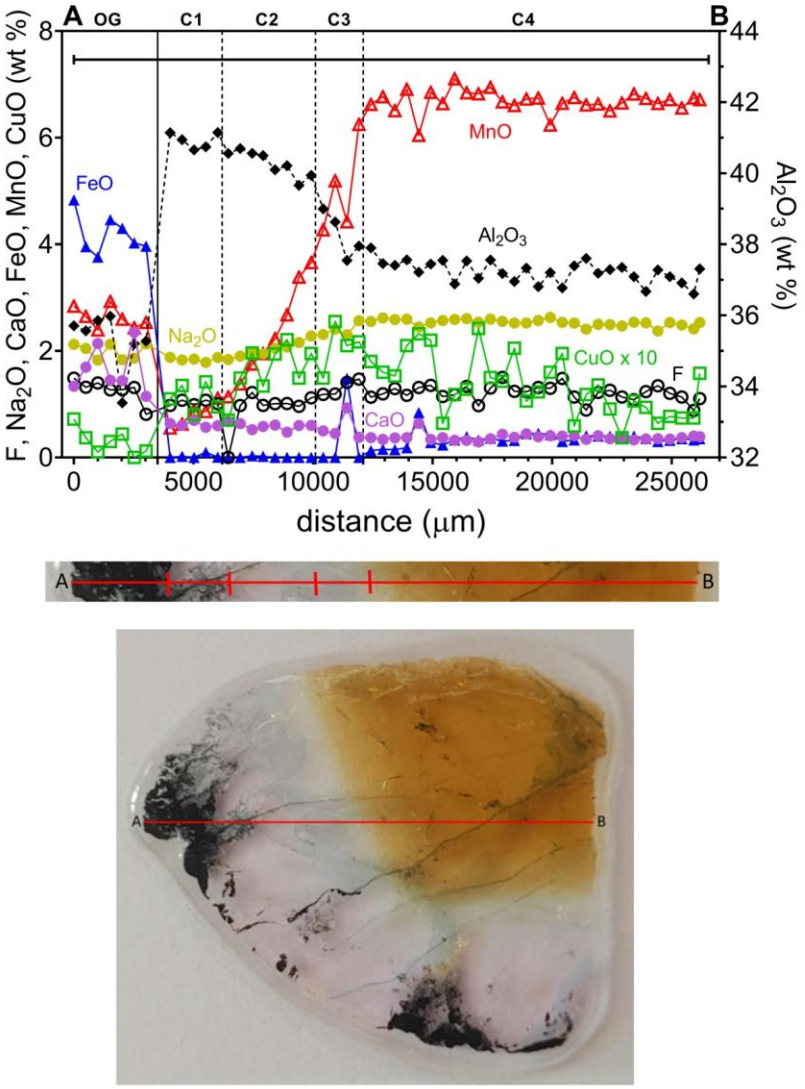

Figure 4.14. EMP analysis of the **MAV 7** sample along a straight traverse perpendicular to the c-axis (only selected oxides are reported. See Table 4.7 for complete chemistry.

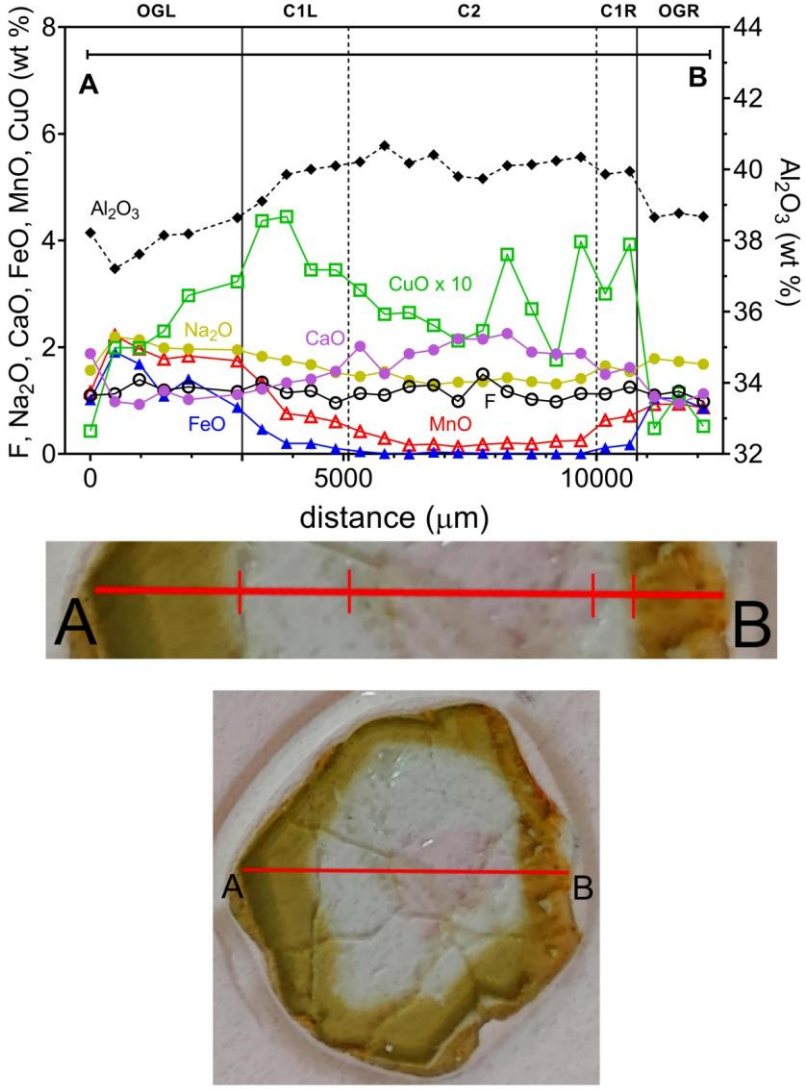

Figure 4.15. EMP analysis of the **MAV 8** sample along a straight traverse perpendicular to the c-axis (only selected oxides are reported. See Table 4.8 for complete chemistry.

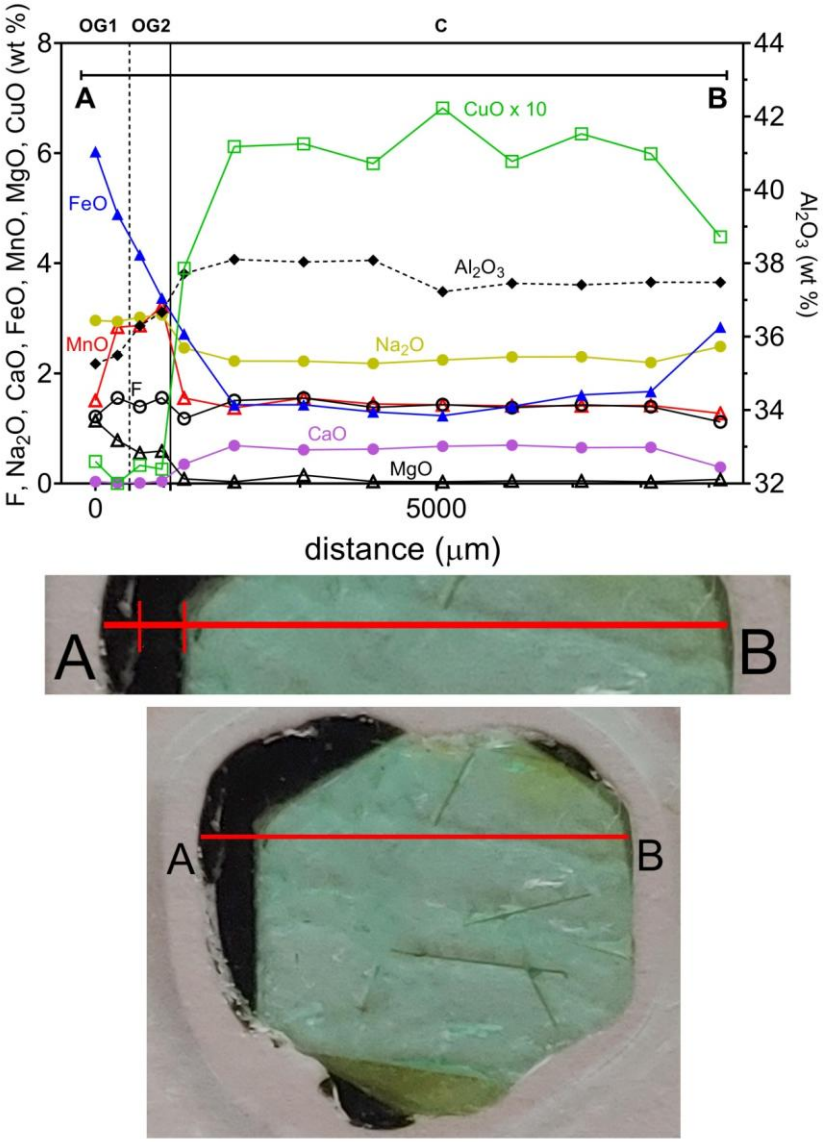

Figure 4.16. EMP analysis of the **MAV 10** sample along a straight traverse perpendicular to the c-axis (only selected oxides are reported. See Table 4.9 for complete chemistry.

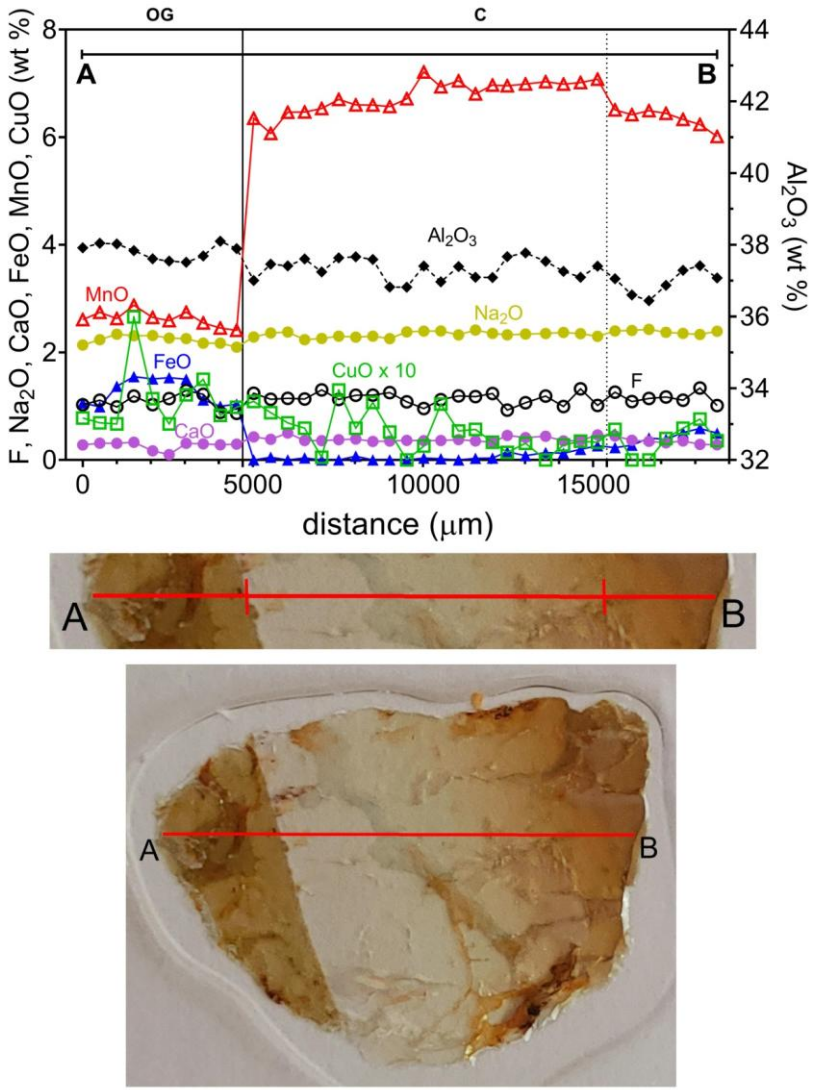

Figure 4.17. EMP analysis of the **MAV 11** sample along a straight traverse perpendicular to the c-axis (only selected oxides are reported. See Table 4.10 for complete chemistry.

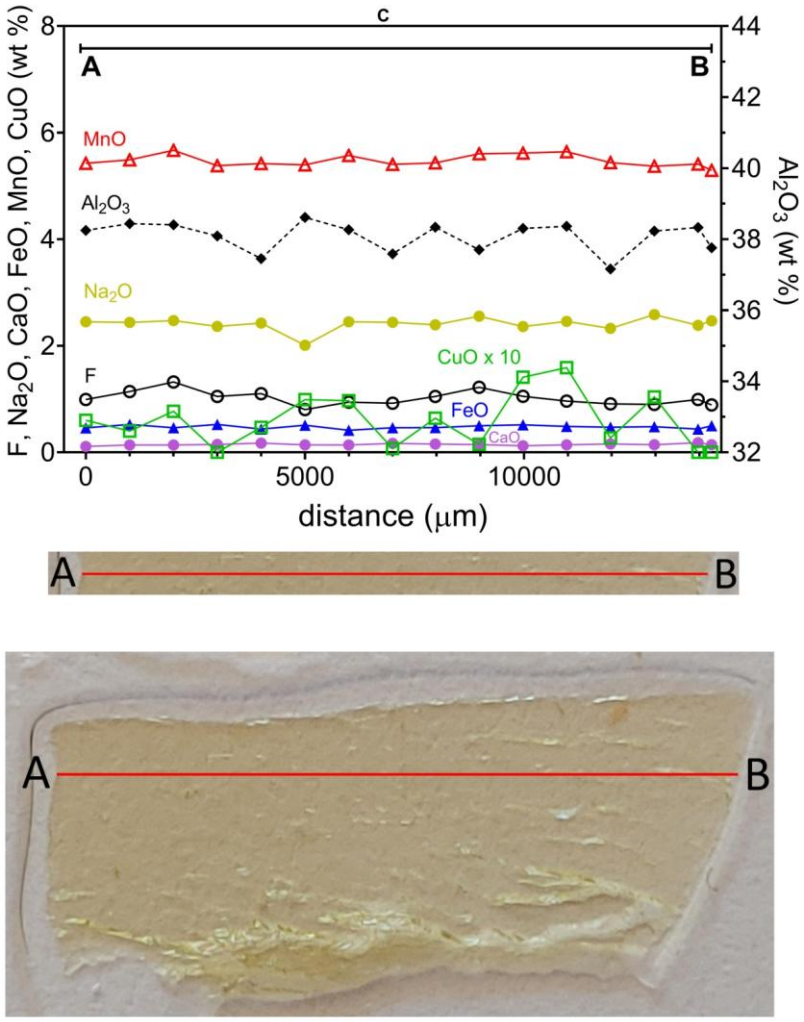

Figure 4.18. EMP analysis of the **MAV 12** sample along a straight traverse perpendicular to the c-axis (only selected oxides are reported. See Table 4.11 for complete chemistry.

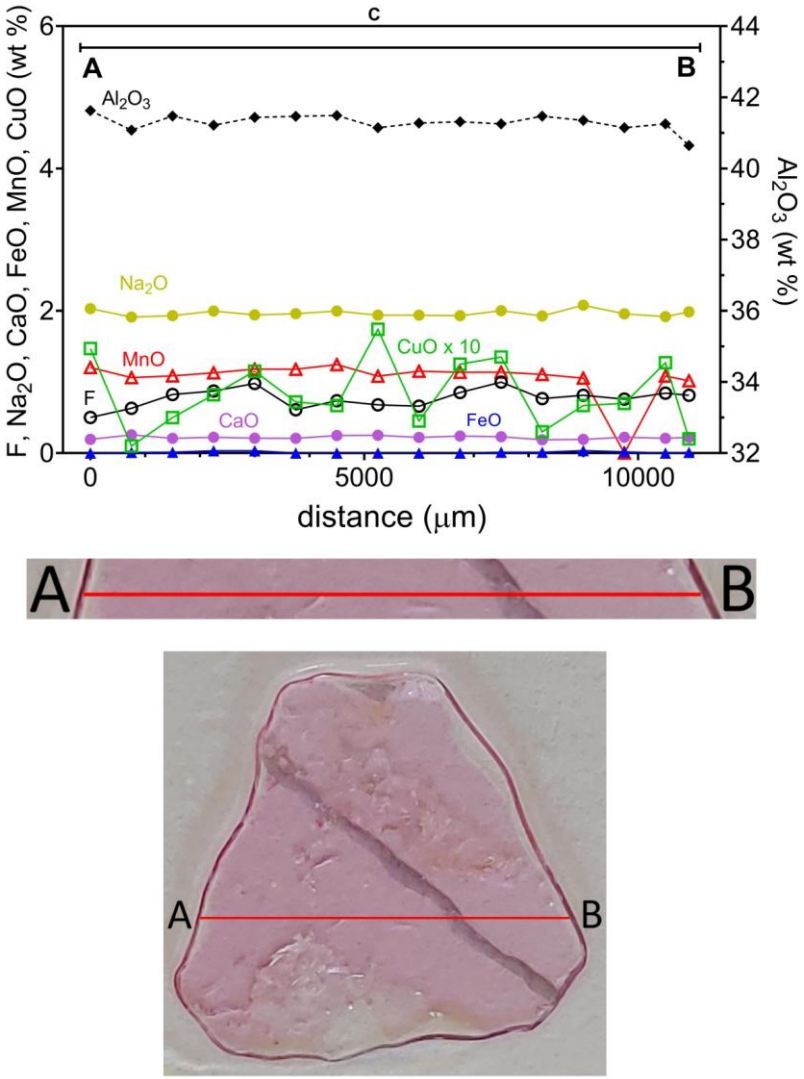

Figure 4.19. EMP analysis of the **MAV 13** sample along a straight traverse perpendicular to the c-axis (only selected oxides are reported. See Table 4.12 for complete chemistry.

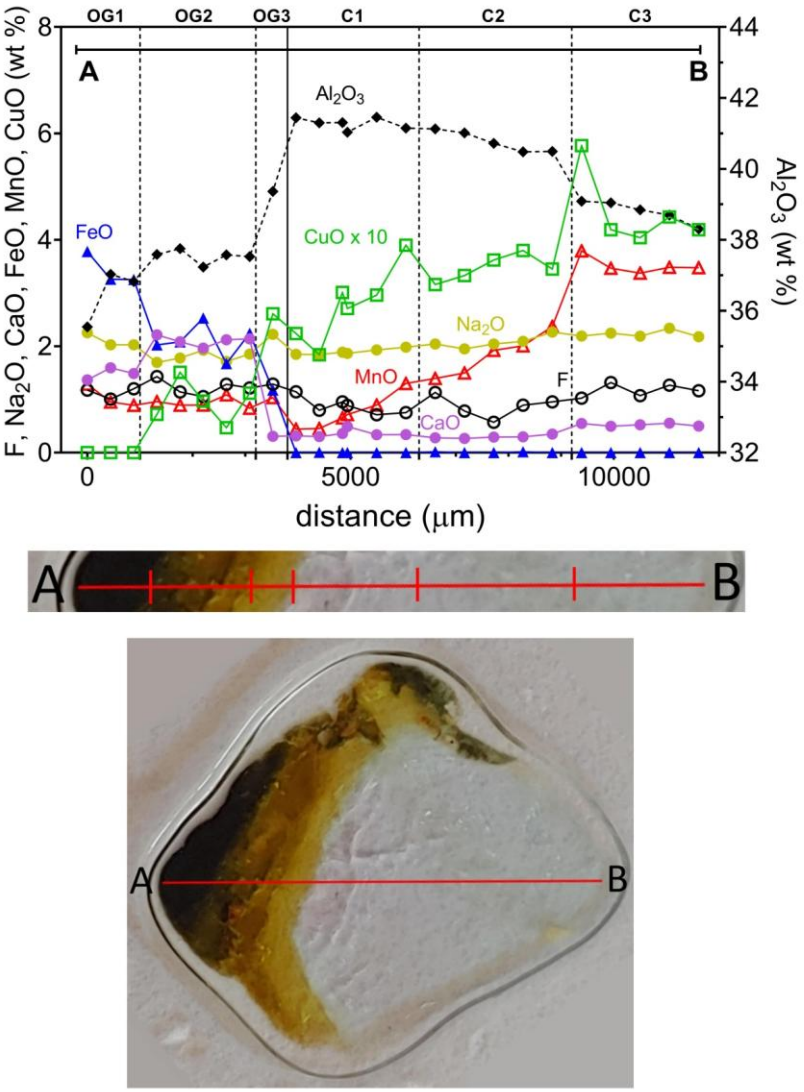

Figure 4.20. EMP analysis of the **MAV 14** sample along a straight traverse perpendicular to the c-axis (only selected oxides are reported. See Table 4.13 for complete chemistry.

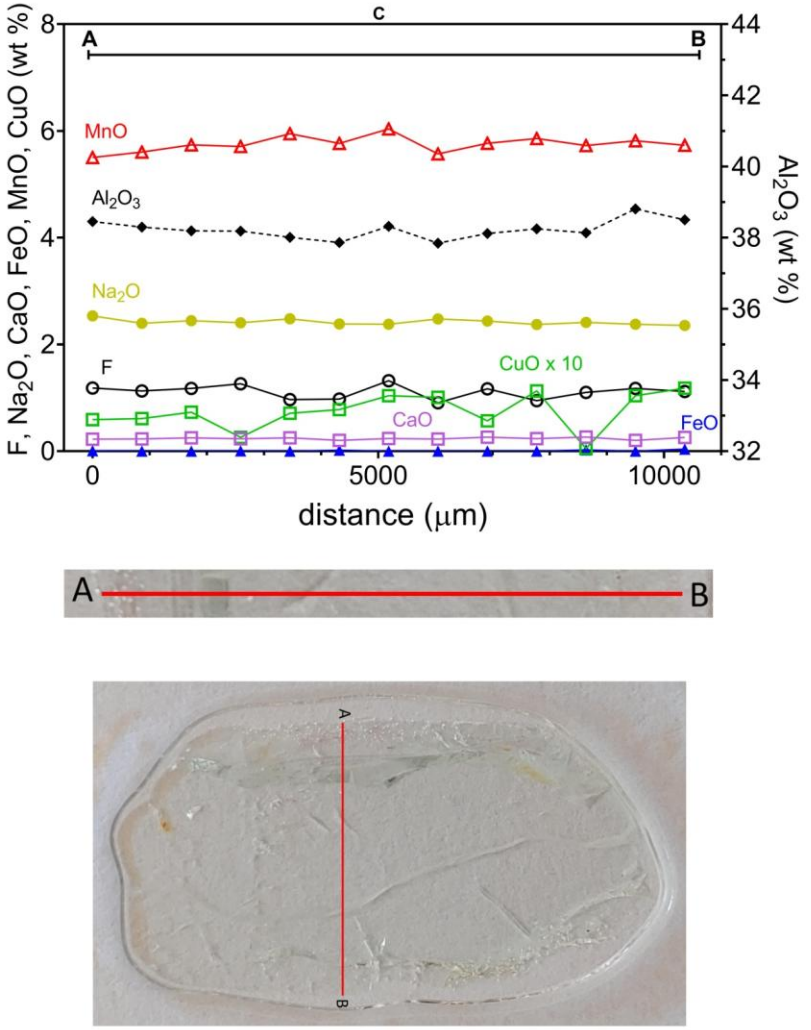

Figure 4.21. EMP analysis of the **MAV 15** sample along a straight traverse perpendicular to the c-axis (only selected oxides are reported. See Table 4.14 for complete chemistry.

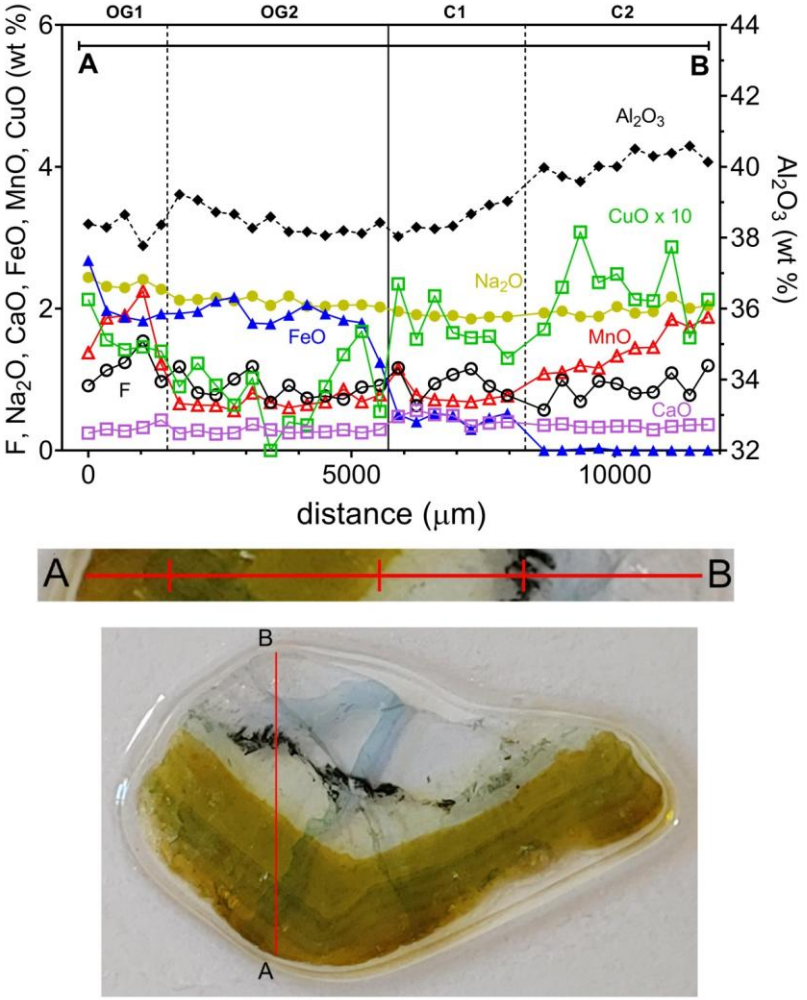

Figure 4.22. EMP analysis of the **MAV 17** sample along a straight traverse perpendicular to the c-axis (only selected oxides are reported. See Table 4.15 for complete chemistry.

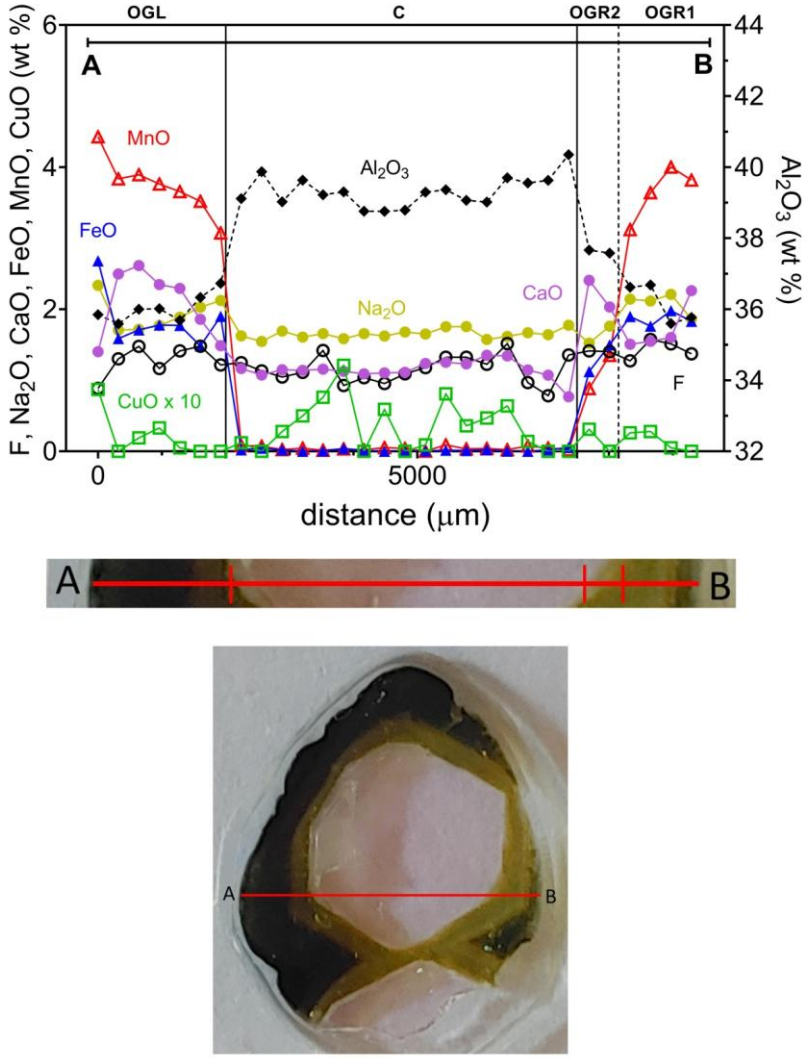

Figure 4.23. EMP analysis of the **MAV 18** sample along a straight traverse perpendicular to the c-axis (only selected oxides are reported. See Table 4.16 for complete chemistry.

Table 4.1. Average chemical composition and atoms per formula unit (a.p.f.u) for the core zone of the MAV1 sample (Mavuco, Mozambique) with the relative empirical formula.

	C *n* = 22
SiO_2 (wt%)	37.26(31)
TiO_2	0.02(2)
B_2O_3[a]	10.60
Al_2O_3	36.03(20)
FeO	3.16(10)
MnO	4.38(15)
MgO	0.01(1)
CuO	0.04(3)
CaO	0.10(2)
Na_2O	2.94(9)
Li_2O[b]	1.34
K_2O	0.05(2)
F	1.43(15)
H_2O[a]	2.72
$-O \equiv F$	−0.60
Total	99.47
Atoms normalized to 31 anions	
Si (a.p.f.u)	6.108
Ti^{4+}	0.003
B	3.000
Al	6.962
Fe^{2+}	0.434
Mn^{2+}	0.608
Mg	0.002
Cu	0.004
Ca	0.018
Na	0.933
Li	0.884
K	0.010
F	0.739
OH	2.972

[a] Calculated by stoichiometry (see text)
[b] Estimated with the procedure of Pesquera et al. (2016)
Errors for oxides and fluorine are standard deviations (in brackets)

Empirical chemical formulae

C $^{X}(Na_{0.93}K_{0.01}\square_{0.04}Ca_{0.02})_{\Sigma 1.00}{}^{Y}(Al_{0.96}Li_{0.88}Fe^{2+}{}_{0.43}Mn^{2+}{}_{0.61}Ti_{0.003})_{\Sigma 2.88}{}^{Z}Al_6({}^{T}Si_{6.11}O_{18})(BO_3)_3$ $^{V}(OH_{2.97}O_{0.03})_{\Sigma 3.00}{}^{W}(F_{0.74}O_{0.26})_{\Sigma 1.00}$

Table 4.2. Average chemical composition and atoms per formula unit (a.p.f.u) for the core zone of the MAV 2 sample (Mavuco, Mozambique) with the relative empirical formula.

	C
	n = 24
SiO_2 (wt%)	37.24(27)
TiO_2	0.01(1)
B_2O_3[a]	10.58
Al_2O_3	36.44(23)
FeO	5.10(35)
MnO	0.88(13)
MgO	0.01(1)
CuO	0.04(2)
CaO	0.20(3)
Na_2O	2.53(6)
Li_2O[b]	1.51
K_2O	0.03(1)
F	1.21(13)
H_2O[a]	2.90
–O ≡ F	−0.508
Total	98.17
Atoms normalized to 31 anions	
Si (a.p.f.u)	6.119
Ti^{4+}	0.001
B	3.000
Al	7.057
Fe^{2+}	0.701
Mn^{2+}	0.122
Mg	0.002
Cu	0.004
Ca	0.035
Na	0.805
Li	0.998
K	0.006
F	0.627
OH	3.180

[a] Calculated by stoichiometry (see text)
[b] Estimated with the procedure of Pesquera et al. (2016)
Errors for oxides and fluorine are standard deviations (in brackets)

Empirical chemical formulae

C $^{X}(Na_{0.81}K_{0.01}\square_{0.15}Ca_{0.04})_{\Sigma 1.00}{}^{Y}(Al_{1.06}Li_{1.00}Fe^{2+}{}_{0.70}Mn^{2+}{}_{0.12}Ti_{0.001})_{\Sigma 2.88}{}^{Z}Al_6({}^{T}Si_{6.12}O_{18})(BO_3)_3{}^{V}(OH)_{3.00}{}^{W}[(OH)_{0.18}F_{0.63}O_{0.19})]_{\Sigma 1.00}$

Table 4.3. Average chemical composition and atoms per formula unit (a.p.f.u) for the overgrowth and core zones of the MAV 3 sample (Mavuco, Mozambique) with the relative empirical formula.

	OG	**C1**	**C2**	**C3**
	n = 2	*n* = 26	*n* = 15	*n* = 26
SiO_2 (wt%)	37.36(12)	38.80(21)	38.09(40)	37.66(54)
TiO_2	0.30(14)	0.00(1)	0.04(3)	0.13(3)
B_2O_3[a]	10.65	11.14	10.99	10.89
Al_2O_3	34.77(34)	41.20(17)	40.46(46)	39.34(22)
FeO	4.29(31)	0.02(2)	0.00(1)	0.00(1)
MnO	2.30(3)	0.16(14)	1.40(68)	3.73(15)
MgO	0.84(13)	0.00(0)	0.00(0)	0.00(1)
CuO	0.04(6)	0.06(4)	0.13(4)	0.14(4)
CaO	1.64(86)	0.47(13)	0.58(10)	0.24(11)
Na_2O	1.90(41)	1.74(5)	1.86(9)	2.21(6)
Li_2O[b]	1.64	2.15	1.96	1.66
K_2O	0.04(2)	0.03(5)	0.03(3)	0.02(1)
F	1.00(21)	0.89(13)	0.97(12)	1.01(23)
H_2O[a]	3.14	3.38	3.19	3.09
$-O \equiv F$	−0.42	−0.38	−0.41	−0.42
Total	99.49	99.68	99.30	99.71
	Atoms normalized to 31 anions			
Si (a.p.f.u)	6.094	6.053	6.022	6.012
Ti^{4+}	0.036	0.001	0.005	0.015
B	3.000	3.000	3.000	3.000
Al	6.685	7.574	7.539	7.402
Fe^{2+}	0.586	0.002	0.001	0.000
Mn^{2+}	0.318	0.021	0.187	0.504
Mg	0.204	0.000	0.000	0.000
Cu	0.005	0.007	0.016	0.017
Ca	0.287	0.079	0.098	0.040
Na	0.602	0.525	0.569	0.685
Li	1.076	1.349	1.246	1.066
K	0.007	0.006	0.007	0.005
F	0.516	0.441	0.483	0.508
OH	3.421	3.515	3.360	3.288

[a] Calculated by stoichiometry (see text)
[b] Estimated with the procedure of Pesquera et al. (2016)
Errors for oxides and fluorine are standard deviations (in brackets)

Empirical chemical formulae

OG
$$^{X}(Na_{0.60}K_{0.01}\square_{0.10}Ca_{0.29})_{\Sigma 1.00}{}^{Y}(Al_{0.68}Li_{1.08}Fe^{2+}_{0.59}Mn^{2+}_{0.32}Mg_{0.20}Cu_{0.01}Ti_{0.04})_{\Sigma 2.88}{}^{Z}Al_6$$
$$(^{T}Si_{6.09}O_{18})(BO_3)_3{}^{V}(OH)_{3.00}{}^{W}[(OH)_{0.42}F_{0.52}O_{0.06})]_{\Sigma 1.00}$$

C1
$$^{X}(Na_{0.53}K_{0.01}\square_{0.39}Ca_{0.08})_{\Sigma 1.00}{}^{Y}(Al_{1.57}Li_{1.35}Fe^{2+}_{0.002}Mn^{2+}_{0.02}Cu_{0.01}Ti_{0.001})_{\Sigma 2.95}{}^{Z}Al_6$$
$$(^{T}Si_{6.05}O_{18})(BO_3)_3{}^{V}(OH)_{3.00}{}^{W}[(OH)_{0.52}F_{0.44}O_{0.04})]_{\Sigma 1.00}$$

C2
$$^{X}(Na_{0.57}K_{0.01}\square_{0.33}Ca_{0.10})_{\Sigma 1.00}{}^{Y}(Al_{1.54}Li_{1.25}Fe^{2+}_{0.001}Mn^{2+}_{0.19}Cu_{0.02}Ti_{0.005})_{\Sigma 3.00}{}^{Z}Al_6$$
$$(^{T}Si_{6.02}O_{18})(BO_3)_3{}^{V}(OH)_{3.00}{}^{W}[(OH)_{0.36}F_{0.48}O_{0.16})]_{\Sigma 1.00}$$

C3
$$^{X}(Na_{0.69}K_{0.01}\square_{0.27}Ca_{0.04})_{\Sigma 1.00}{}^{Y}(Al_{1.40}Li_{1.07}Mn^{2+}_{0.50}Cu_{0.02}Ti_{0.02})_{\Sigma 3.00}{}^{Z}Al_6$$
$$(^{T}Si_{6.09}O_{18})(BO_3)_3{}^{V}(OH)_{3.00}{}^{W}[(OH)_{0.29}F_{0.51}O_{0.20})]_{\Sigma 1.00}$$

Table 4.4. Average chemical composition and atoms per formula unit (a.p.f.u) for the overgrowth and core zones of the MAV 4 sample (Mavuco, Mozambique) with the relative empirical formula.

	OG1	**OG2**	**OG3**	**C1**	**C2**	**C3**
	$n = 2$	$n = 3$	$n = 4$	$n = 19$	$n = 4$	$n = 12$
SiO_2 (wt%)	35.91(31)	35.47(34)	35.50(28)	35.37(82)	37.19(63)	37.43(53)
TiO_2	0.24(2)	0.19(1)	0.13(4)	0.08(4)	0.00(1)	0.16(6)
B_2O_3[a]	10.48	10.37	10.38	10.36	10.74	10.75
Al_2O_3	37.00(23)	36.70(42)	36.83(26)	37.03(32)	38.40(15)	37.61(53)
FeO	4.83(15)	3.09(98)	1.19(48)	0.34(7)	0.01(1)	1.20(48)
MnO	4.00(10)	4.66(29)	5.58(31)	6.19(24)	4.84(34)	4.48(25)
MgO	0.01(1)	0.02(2)	0.02(0)	0.01(1)	0.00(0)	0.02(1)
CuO	0.06(5)	0.06(6)	0.24(5)	0.31(7)	0.38(1)	0.23(9)
CaO	0.18(2)	0.22(3)	0.21(3)	0.24(7)	0.24(2)	0.19(5)
Na_2O	2.44(3)	2.55(5)	2.60(9)	2.59(5)	2.46(5)	2.55(16)
Li_2O[b]	0.82	1.01	1.19	1.2	1.53	1.51
K_2O	0.03(1)	0.04(1)	0.04(1)	0.03(1)	0.02(1)	0.02(1)
F	0.88(5)	0.94(32)	1.31(11)	1.33(16)	1.17(17)	1.25(18)
H_2O[a]	2.72	2.73	2.61	2.57	2.86	2.87
$-O \equiv F$	−0.37	−0.39	−0.55	−0.56	−0.49	−0.53
Total	99.61	98.07	97.30	97.12	99.37	99.77
	Atoms normalized to 31 anions					
Si (a.p.f.u)	5.955	5.945	5.947	5.931	6.017	6.052
Ti^{4+}	0.030	0.024	0.016	0.010	0.001	0.020
B	3.000	3.000	3.000	3.000	3.000	3.000
Al	7.233	7.250	7.272	7.290	7.321	7.166
Fe^{2+}	0.670	0.434	0.167	0.047	0.002	0.162
Mn^{2+}	0.562	0.661	0.791	0.880	0.634	0.613
Mg	0.002	0.005	0.005	0.002	0.000	0.005
Cu	0.008	0.008	0.030	0.039	0.046	0.028
Ca	0.031	0.040	0.038	0.043	0.042	0.032
Na	0.785	0.828	0.844	0.843	0.770	0.799
Li	0.547	0.681	0.802	0.809	0.996	0.982
K	0.007	0.008	0.008	0.006	0.004	0.005
F	0.464	0.496	0.695	0.706	0.599	0.640
OH	3.006	3.054	2.912	2.880	3.082	3.100

[a] Calculated by stoichiometry (see text)
[b] Estimated with the procedure of Pesquera et al. (2016)
Errors for oxides and fluorine are standard deviations (in brackets)

Empirical chemical formulae

OG1
$$^{X}(Na_{0.79}K_{0.01}\square_{0.18}Ca_{0.03})_{\Sigma 1.00}{}^{Y}(Al_{1.18}Li_{0.55}Fe^{2+}_{0.67}Mn^{2+}_{0.56}Mg_{0.002}Cu_{0.01}Ti_{0.03})_{\Sigma 3.00}{}^{Z}Al_6$$
$$[^{T}(Si_{5.95}Al_{0.05})O_{18}](BO_3)_3{}^{V}(OH)_{3.00}{}^{W}[(OH)_{0.01}F_{0.46}O_{0.54})]_{\Sigma 1.00}$$

OG2
$$^{X}(Na_{0.83}K_{0.01}\square_{0.12}Ca_{0.04})_{\Sigma 1.00}{}^{Y}(Al_{1.19}Li_{0.68}Fe^{2+}_{0.43}Mn^{2+}_{0.66}Mg_{0.01}Cu_{0.01}Ti_{0.02})_{\Sigma 3.00}{}^{Z}Al_6$$
$$[^{T}(Si_{5.94}Al_{0.06})O_{18}](BO_3)_3{}^{V}(OH)_{3.00}{}^{W}[(OH)_{0.05}F_{0.50}O_{0.45})]_{\Sigma 1.00}$$

OG3
$$^{X}(Na_{0.84}K_{0.01}\square_{0.11}Ca_{0.04})_{\Sigma 1.00}{}^{Y}(Al_{1.22}Li_{0.80}Fe^{2+}_{0.17}Mn^{2+}_{0.79}Mg_{0.005}Cu_{0.03}Ti_{0.02})_{\Sigma 3.00}{}^{Z}Al_6$$
$$[^{T}(Si_{5.95}Al_{0.05})O_{18}](BO_3)_3{}^{V}(OH_{2.91}O_{0.09})_{3.00}{}^{W}(F_{0.70}O_{0.30})_{\Sigma 1.00}$$

C1
$$^{X}(Na_{0.84}K_{0.01}\square_{0.11}Ca_{0.04})_{\Sigma 1.00}{}^{Y}(Al_{1.22}Li_{0.81}Fe^{2+}_{0.05}Mn^{2+}_{0.88}Mg_{0.002}Cu_{0.04}Ti_{0.01})_{\Sigma 3.00}{}^{Z}Al_6$$
$$[^{T}(Si_{5.93}Al_{0.07})O_{18}](BO_3)_3{}^{V}(OH_{2.88}O_{0.12})_{3.00}{}^{W}(F_{0.71}O_{0.29})_{\Sigma 1.00}$$

C2
$$^{X}(Na_{0.77}\square_{0.18}Ca_{0.04})_{\Sigma 1.00}{}^{Y}(Al_{1.32}Li_{1.00}Fe^{2+}_{0.002}Mn^{2+}_{0.63}Cu_{0.05}Ti_{0.001})_{\Sigma 3.00}{}^{Z}Al_6$$
$$^{T}(Si_{6.02})O_{18}(BO_3)_3{}^{V}(OH)_{3.00}{}^{W}[(OH)_{0.08}F_{0.60}O_{0.32})]_{\Sigma 1.00}$$

C3
$$^{X}(Na_{0.77}\square_{0.18}Ca_{0.04})_{\Sigma 1.00}{}^{Y}(Al_{1.32}Li_{1.00}Fe^{2+}_{0.002}Mn^{2+}_{0.63}Cu_{0.05}Ti_{0.001})_{\Sigma 3.00}{}^{Z}Al_6$$
$$^{T}(Si_{6.02})O_{18}(BO_3)_3{}^{V}(OH)_{3.00}{}^{W}[(OH)_{0.08}F_{0.60}O_{0.32})]_{\Sigma 1.00}$$

Table 4.5. Average chemical composition and atoms per formula unit (a.p.f.u) for the core zones of the MAV 5 sample (Mavuco, Mozambique) with the relative empirical formula.

	C1	**C2**	**C3**
	$n = 10$	$n = 7$	$n = 7$
SiO_2 (wt%)	38.43(16)	38.16(20)	37.98(18)
TiO_2	0.01(1)	0.03(1)	0.05(3)
B_2O_3[a]	11.08	10.98	10.92
Al_2O_3	40.94(19)	39.88(38)	38.90(26)
FeO	0.12(33)	0.01(1)	0.01(2)
MnO	1.02(27)	2.60(54)	4.59(56)
MgO	0.01(1)	0.00(1)	0.00(0)
CuO	0.45(7)	0.53(5)	0.45(10)
CaO	0.45(9)	0.44(2)	0.30(6)
Na_2O	1.87(5)	2.06(7)	2.28(4)
Li_2O[b]	1.98	1.84	1.61
K_2O	0.01(1)	0.02(1)	0.03(1)
F	1.07(15)	1.20(14)	1.25(10)
H_2O[a]	3.12	2.97	2.9
$-O \equiv F$	−0.45	−0.51	−0.53
Total	100.12	100.23	100.75
Atoms normalized to 31 anions			
Si (a.p.f.u)	6.028	6.038	6.045
Ti^{4+}	0.001	0.004	0.006
B	3.000	3.000	3.000
Al	7.568	7.437	7.298
Fe^{2+}	0.016	0.001	0.001
Mn^{2+}	0.136	0.348	0.619
Mg	0.002	0.000	0.000
Cu	0.053	0.063	0.054
Ca	0.076	0.075	0.051
Na	0.569	0.632	0.704
Li	1.249	1.171	1.031
K	0.002	0.004	0.006
F	0.531	0.601	0.629
OH	3.260	3.130	3.077

[a] Calculated by stoichiometry (see text)

[b] Estimated with the procedure of Pesquera et al. (2016)

Errors for oxides and fluorine are standard deviations (in brackets)

Empirical chemical formulae

C1

$$^{X}(Na_{0.57}\square_{0.35}Ca_{0.08})_{\Sigma 1.00}{}^{Y}(Al_{1.57}Li_{1.25}Fe^{2+}{}_{0.02}Mn^{2+}{}_{0.14}Ti_{0.001})_{\Sigma 2.98}{}^{Z}Al_6$$
$$(^{T}Si_{6.03}O_{18})(BO_3)_3{}^{V}(OH)_{3.00}{}^{W}(OH_{0.26}F_{0.53}O_{0.21})_{\Sigma 1.00}$$

C2

$$^{X}(Na_{0.63}\square_{0.30}Ca_{0.07})_{\Sigma 1.00}{}^{Y}(Al_{1.44}Li_{1.17}Fe^{2+}{}_{0.001}Mn^{2+}{}_{0.35}Ti_{0.004})_{\Sigma 2.96}{}^{Z}Al_6$$
$$(^{T}Si_{6.04}O_{18})(BO_3)_3{}^{V}(OH)_{3.00}{}^{W}(OH_{0.13}F_{0.60}O_{0.27})_{\Sigma 1.00}$$

C3

$$^{X}(Na_{0.70}K_{0.01}\square_{0.24}Ca_{0.05})_{\Sigma 1.00}{}^{Y}(Al_{1.30}Li_{1.03}Fe^{2+}{}_{0.001}Mn^{2+}{}_{0.62}Ti_{0.01})_{\Sigma 2.96}{}^{Z}Al_6$$
$$(^{T}Si_{6.05}O_{18})(BO_3)_3{}^{V}(OH)_{3.00}{}^{W}(OH_{0.08}F_{0.63}O_{0.29})_{\Sigma 1.00}$$

Table 4.6. Average chemical composition and atoms per formula unit (a.p.f.u) for the overgrowth and core zones of the MAV 6 sample (Mavuco, Mozambique) with the relative empirical formula.

	OG	**C1**	**C2**	**C3**	**C4**
	n = 11	*n* = 6	*n* = 10	*n* = 5	*n* = 12
SiO_2 (wt%)	39.56(39)	39.25(47)	37.55(54)	36.45(16)	37.16(27)
TiO_2	0.05(2)	0.03(5)	0.45(9)	0.65(4)	0.45(2)
B_2O_3[a]	11	11.15	10.83	10.62	10.66
Al_2O_3	36.78(61)	39.98(31)	37.82(40)	37.16(56)	36.21(34)
FeO	1.37(26)	0.01(1)	0.36(46)	3.95(75)	4.99(20)
MnO	1.20(14)	1.02(69)	6.23(76)	4.33(23)	4.27(13)
MgO	0.20(6)	0.00(1)	0.00(1)	0.01(1)	0.03(1)
CuO	0.03(3)	0.12(5)	0.06(5)	0.01(2)	0.04(3)
CaO	3.86(35)	1.42(13)	0.92(16)	0.63(7)	0.33(8)
Na_2O	1.00(15)	1.63(3)	2.26(10)	2.32(5)	2.31(4)
Li_2O[b]	2.37	2.22	1.36	0.97	1.00
K_2O	0.01(1)	0.02(1)	0.02(1)	0.03(1)	0.03(1)
F	1.51(14)	1.15(14)	1.18(15)	0.83(12)	0.82(12)
H_2O[a]	2.62	3.1	2.74	2.71	2.93
$-O \equiv F$	−0.64	−0.48	−0.50	−0.35	−0.35
Total	100.94	100.62	101.29	100.35	100.92
	Atoms normalized to 31 anions				
Si (a.p.f.u)	6.250	6.120	6.023	5.968	6.057
Ti^{4+}	0.005	0.004	0.054	0.079	0.055
B	3.000	3.000	3.000	3.000	3.000
Al	6.850	7.348	7.151	7.170	6.955
Fe^{2+}	0.181	0.002	0.048	0.541	0.680
Mn^{2+}	0.160	0.134	0.846	0.600	0.590
Mg	0.047	0.000	0.000	0.002	0.007
Cu	0.004	0.014	0.007	0.001	0.005
Ca	0.653	0.237	0.157	0.110	0.057
Na	0.307	0.493	0.702	0.738	0.731
Li	1.506	1.392	0.878	0.639	0.655
K	0.003	0.003	0.005	0.007	0.006
F	0.754	0.567	0.598	0.430	0.423
OH	2.760	3.227	2.930	2.965	3.180

[a] Calculated by stoichiometry (see text)

[b] Estimated with the procedure of Pesquera et al. (2016)

Errors for oxides and fluorine are standard deviations (in brackets)

Empirical chemical formulae

OG
$$^{X}(Na_{0.31}\square_{0.04}Ca_{0.65})_{\Sigma 1.00}{}^{Y}(Al_{0.85}Li_{1.51}Fe^{2+}_{0.18}Mn^{2+}_{0.16}Mg_{0.05}Ti_{0.08})_{\Sigma 2.83}{}^{Z}Al_6(^{T}Si_{6.25}O_{18})(BO_3)_3{}^{V}(OH_{2.76}O_{0.24})_{\Sigma 3.00}{}^{W}(F_{0.75}O_{0.25})_{\Sigma 1.00}$$

C1
$$^{X}(Na_{0.49}\square_{0.27}Ca_{0.24})_{\Sigma 1.00}{}^{Y}(Al_{1.35}Li_{1.39}Mn^{2+}_{0.13}Cu_{0.01}Ti_{0.004})_{\Sigma 2.88}{}^{Z}Al_6(^{T}Si_{6.12}O_{18})(BO_3)_3{}^{V}(OH)_{3.00}{}^{W}(OH_{0.23}F_{0.57}O_{0.20})_{\Sigma 1.00}$$

C2
$$^{X}(Na_{0.70}\square_{0.14}Ca_{0.16})_{\Sigma 1.00}{}^{Y}(Al_{1.15}Li_{0.88}Fe^{2+}_{0.05}Mn^{2+}_{0.85}Cu_{0.01}Ti_{0.05})_{\Sigma 2.99}{}^{Z}Al_6(^{T}Si_{6.02}O_{18})(BO_3)_3{}^{V}(OH_{2.93}O_{0.07})_{\Sigma 3.00}{}^{W}(F_{0.60}O_{0.40})_{\Sigma 1.00}$$

C3
$$^{X}(Na_{0.74}K_{0.01}\square_{0.14}Ca_{0.11})_{\Sigma 1.00}{}^{Y}(Al_{1.14}Li_{0.64}Fe^{2+}_{0.54}Mn^{2+}_{0.60}Ti_{0.08})_{\Sigma 3.00}{}^{Z}Al_6[(^{T}Si_{5.97}Al_{0.03})O_{18}](BO_3)_3{}^{V}(OH_{2.97}O_{0.03})_{\Sigma 3.00}{}^{W}(F_{0.43}O_{0.57})_{\Sigma 1.00}$$

C4
$$^{X}(Na_{0.73}K_{0.01}\square_{0.21}Ca_{0.06})_{\Sigma 1.00}{}^{Y}(Al_{0.96}Li_{0.66}Fe^{2+}_{0.68}Mn^{2+}_{0.59}Mg_{0.01}Ti_{0.06})_{\Sigma 2.96}{}^{Z}Al_6(^{T}Si_{6.06}O_{18})(BO_3)_3{}^{V}(OH)_{3.00}{}^{W}(OH_{0.18}F_{0.42}O_{0.40})_{\Sigma 1.00}$$

Table 4.7. Average chemical composition and atoms per formula unit (a.p.f.u) for the overgrowth and core zones of the MAV 7 sample (Mavuco, Mozambique) with the relative empirical formula.

	OG	**C1**	**C2**	**C3**	**C4**
	n = 7	*n* = 5	*n* = 8	*n* = 4	*n* = 26
SiO_2 (wt%)	38.05(97)	39.66(25)	39.23(30)	38.68(13)	38.51(25)
TiO_2	0.22(6)	0.03(2)	0.09(4)	0.27(7)	0.42(3)
B_2O_3[a]	10.78	11.29	11.20	11.03	10.96
Al_2O_3	35.30(83)	40.93(22)	40.28(36)	38.28	37.23(31)
FeO	4.19(37)	0.02(4)	0.01(1)	0.37(74)	0.34(13)
MnO	2.62(20)	0.81(22)	2.27(91)	5.03(91)	6.68(20)
MgO	0.61(24)	0.01(1)	0.00(1)	0.03(5)	0.00(1)
CuO	0.03(2)	0.11(3)	0.16(5)	0.21(4)	0.13(6)
CaO	1.65(44)	0.62(5)	0.59(6)	0.56(25)	0.38(6)
Na_2O	1.99(14)	1.84(4)	2.03(14)	2.40(12)	2.53(6)
Li_2O[b]	1.63	2.19	1.98	1.64	1.48
K_2O	0.03(1)	0.01(1)	0.02(1)	0.03(2)	0.03(2)
F	1.27(22)	1.03(5)	0.91(38)	1.31(15)	1.21(15)
H_2O[a]	2.94	3.34	3.26	2.89	2.95
$-O \equiv F$	−0.53	−0.43	−0.38	−0.55	−0.51
Total	100.78	101.47	101.65	102.21	102.35
	Atoms normalized to 31 anions				
Si (a.p.f.u)	6.136	6.105	6.088	6.093	6.106
Ti^{4+}	0.027	0.003	0.010	0.032	0.050
B	3.000	3.000	3.000	3.000	3.000
Al	6.710	7.425	7.367	7.108	6.957
Fe^{2+}	0.565	0.003	0.001	0.049	0.045
Mn^{2+}	0.358	0.105	0.299	0.672	0.898
Mg	0.147	0.002	0.000	0.007	0.000
Cu	0.004	0.013	0.019	0.025	0.016
Ca	0.285	0.102	0.098	0.095	0.064
Na	0.623	0.550	0.609	0.732	0.777
Li	1.057	1.356	1.236	1.039	0.944
K	0.005	0.002	0.004	0.006	0.006
F	0.646	0.499	0.446	0.654	0.606
OH	3.166	3.426	3.373	3.041	3.118

[a] Calculated by stoichiometry (see text)
[b] Estimated with the procedure of Pesquera et al. (2016)
Errors for oxides and fluorine are standard deviations (in brackets)

Empirical chemical formulae

OG
$$^{X}(Na_{0.62}\square_{0.09}Ca_{0.29})_{\Sigma 1.00}{}^{Y}(Al_{0.71}Li_{1.06}Fe^{2+}{}_{0.57}Mn^{2+}{}_{0.36}Mg_{0.15}Ti_{0.03})_{\Sigma 2.88}{}^{Z}Al_6(^{T}Si_{6.14}O_{18})(BO_3)_3{}^{V}(OH)_{3.00}{}^{W}(OH_{0.17}F_{0.65}O_{0.18})_{\Sigma 1.00}$$

C1
$$^{X}(Na_{0.55}\square_{0.35}Ca_{0.10})_{\Sigma 1.00}{}^{Y}(Al_{1.43}Li_{1.36}Mn^{2+}{}_{0.11}Cu_{0.01}Ti_{0.003})_{\Sigma 2.91}{}^{Z}Al_6(^{T}Si_{6.11}O_{18})(BO_3)_3{}^{V}(OH)_{3.00}{}^{W}(OH_{0.43}F_{0.50}O_{0.07})_{\Sigma 1.00}$$

C2
$$^{X}(Na_{0.61}\square_{0.29}Ca_{0.10})_{\Sigma 1.00}{}^{Y}(Al_{1.37}Li_{1.24}Mn^{2+}{}_{0.30}Cu_{0.01}Ti_{0.01})_{\Sigma 2.93}{}^{Z}Al_6(^{T}Si_{6.09}O_{18})(BO_3)_3{}^{V}(OH)_{3.00}{}^{W}(OH_{0.37}F_{0.45}O_{0.18})_{\Sigma 1.00}$$

C3
$$^{X}(Na_{0.73}\square_{0.17}K_{0.01}Ca_{0.10})_{\Sigma 1.00}{}^{Y}(Al_{1.11}Li_{1.04}Fe^{2+}{}_{0.05}Mn^{2+}{}_{0.67}Mg_{0.01}Cu_{0.03}Ti_{0.03})_{\Sigma 2.88}{}^{Z}Al_6(^{T}Si_{6.09}O_{18})(BO_3)_3{}^{V}(OH)_{3.00}{}^{W}(OH_{0.04}F_{0.65}O_{0.31})_{\Sigma 1.00}$$

C4
$$^{X}(Na_{0.78}K_{0.01}\square_{0.15}Ca_{0.06})_{\Sigma 1.00}{}^{Y}(Al_{0.96}Li_{0.94}Fe^{2+}{}_{0.05}Mn^{2+}{}_{0.90}Cu_{0.02}Ti_{0.05})_{\Sigma 2.92}{}^{Z}Al_6(^{T}Si_{6.11}O_{18})(BO_3)_3{}^{V}(OH)_{3.00}{}^{W}(OH_{0.12}F_{0.61}O_{0.27})_{\Sigma 1.00}$$

Table 4.8. Average chemical composition and atoms per formula unit (a.p.f.u) for the overgrowth and core zones of the MAV 8 sample (Mavuco, Mozambique) with the relative empirical formula.

	OGL $n = 6$	**C1L** $n = 4$	**C2** $n = 10$	**C1R** $n = 2$	**OGR** $n = 3$
SiO_2 (wt%)	38.15(28)	38.19(21)	38.27(19)	38.15(10)	39.18(15)
TiO_2	0.14(5)	0.04(2)	0.01(1)	0.05(0)	0.20(1)
B_2O_3[a]	10.84	10.94	10.97	10.94	11.06
Al_2O_3	38.00(51)	39.77(45)	40.18(27)	39.91(6)	38.70(6)
FeO	1.33(41)	0.24(16)	0.01(2)	0.15(4)	0.98(11)
MnO	1.79(35)	0.85(32)	0.23(8)	0.67(6)	0.91(4)
MgO	0.02(2)	-	-	-	-
CuO	0.22(10)	0.39(6)	0.27(7)	0.35(7)	0.07(4)
CaO	1.18(35)	1.38(14)	1.96(21)	1.56(9)	1.05(9)
Na_2O	1.97(22)	1.70(13)	1.39(7)	1.60(8)	1.73(5)
Li_2O[b]	1.96	2.10	2.20	2.12	2.21
K_2O	1.97(22)	0.02(2)	0.02(1)	0.01(0)	0.01(1)
F	0.03(1)	1.16(16)	1.16(16)	1.19(9)	1.09(10)
H_2O[a]	2.92	2.91	2.86	2.87	3.25
$-O \equiv F$	−0.51	−0.49	−0.49	−0.50	−0.46
Total	99.27	99.20	99.06	99.07	100.01
	Atoms normalized to 31 anions				
Si (a.p.f.u)	6.115	6.065	6.063	6.060	6.159
Ti^{4+}	0.017	0.004	0.001	0.005	0.023
B	3.000	3.000	3.000	3.000	3.000
Al	7.179	7.444	7.503	7.470	7.170
Fe^{2+}	0.178	0.032	0.002	0.019	0.129
Mn^{2+}	0.242	0.114	0.030	0.091	0.121
Mg	0.005	-	-	-	-
Cu	0.027	0.047	0.032	0.042	0.008
Ca	0.203	0.234	0.332	0.265	0.177
Na	0.611	0.522	0.427	0.492	0.528
Li	1.264	1.341	1.402	1.354	1.397
K	0.007	0.005	0.004	0.002	0.001
F	0.611	0.582	0.580	0.597	0.540
OH	3.124	3.086	3.025	3.045	3.409

[a] Calculated by stoichiometry (see text)
[b] Estimated with the procedure of Pesquera et al. (2016)
Errors for oxides and fluorine are standard deviations (in brackets)

Empirical chemical formulae

OGL
$$^{X}(Na_{0.61}K_{0.01}\square_{0.18}Ca_{0.20})_{\Sigma 1.00}{}^{Y}(Al_{1.18}Li_{1.26}Fe^{2+}_{0.18}Mn^{2+}_{0.24}Mg_{0.01}Cu_{0.03}Ti_{0.02})_{\Sigma 2.92}{}^{Z}Al_6$$
$$(^{T}Si_{6.12}O_{18})(BO_3)_3{}^{V}(OH)_{3.00}{}^{W}(OH_{0.12}F_{0.61}O_{0.27})_{\Sigma 1.00}$$

C1L
$$^{X}(Na_{0.52}K_{0.01}\square_{0.24}Ca_{0.23})_{\Sigma 1.00}{}^{Y}(Al_{1.44}Li_{1.34}Fe^{2+}_{0.03}Mn^{2+}_{0.11}Cu_{0.05}Ti_{0.004})_{\Sigma 2.97}{}^{Z}Al_6$$
$$(^{T}Si_{6.07}O_{18})(BO_3)_3{}^{V}(OH)_{3.00}{}^{W}(OH_{0.09}F_{0.58}O_{0.33})_{\Sigma 1.00}$$

C2
$$^{X}(Na_{0.43}\square_{0.24}Ca_{0.33})_{\Sigma 1.00}{}^{Y}(Al_{1.50}Li_{1.40}Mn^{2+}_{0.03}Cu_{0.03}Ti_{0.001})_{\Sigma 2.96}{}^{Z}Al_6$$
$$(^{T}Si_{6.06}O_{18})(BO_3)_3{}^{V}(OH)_{3.00}{}^{W}(OH_{0.06}F_{0.58}O_{0.36})_{\Sigma 1.00}$$

C1R
$$^{X}(Na_{0.60}\square_{0.24}Ca_{0.27})_{\Sigma 1.00}{}^{Y}(Al_{1.47}Li_{1.35}Fe^{2+}_{0.02}Mn^{2+}_{0.09}Cu_{0.04}Ti_{0.01})_{\Sigma 2.98}{}^{Z}Al_6$$
$$(^{T}Si_{6.06}O_{18})(BO_3)_3{}^{V}(OH)_{3.00}{}^{W}(OH_{0.05}F_{0.60}O_{0.35})_{\Sigma 1.00}$$

OGR
$$^{X}(Na_{0.53}\square_{0.29}Ca_{0.18})_{\Sigma 1.00}{}^{Y}(Al_{1.17}Li_{1.40}Fe^{2+}_{0.13}Mn^{2+}_{0.12}Cu_{0.01}Ti_{0.02})_{\Sigma 2.85}{}^{Z}Al_6$$
$$(^{T}Si_{6.16}O_{18})(BO_3)_3{}^{V}(OH)_{3.00}{}^{W}(OH_{0.41}F_{0.54}O_{0.05})_{\Sigma 1.00}$$

Table 4.9. Average chemical composition and atoms per formula unit (a.p.f.u) for the overgrowth and core zones of the MAV 10 sample (Mavuco, Mozambique) with the relative empirical formula.

	OG1	**OG2**	**C**
	n = 2	*n* = 2	*n* = 9
SiO_2 (wt%)	37.86(32)	37.36(5)	37.54(79)
TiO_2	0.23(3)	0.16(2)	0.03(4)
B_2O_3[a]	10.82	10.74	10.70
Al_2O_3	35.38(16)	36.48(26)	37.67(33)
FeO	5.46(80)	3.76(55)	1.74(61)
MnO	2.17(94)	3.04(25)	1.43(9)
MgO	0.96(25)	0.57(2)	0.06(4)
CuO	0.02(3)	0.03(0)	0.57(9)
CaO	0.02(2)	0.02(2)	0.58(15)
Na_2O	2.95(1)	3.04(3)	2.29(11)
Li_2O [b]	1.45	1.41	1.91
K_2O	0.03(2)	0.02(0)	0.03(1)
F	1.39(24)	1.48(11)	1.37(14)
H_2O[a]	3.10	2.87	2.83
$-O \equiv F$	−0.58	−0.62	−0.58
Total	101.32	100.38	98.18
	Atoms normalized to 31 anions		
Si (a.p.f.u)	6.081	6.044	6.095
Ti^{4+}	0.028	0.019	0.004
B	3.000	3.000	3.000
Al	6.696	6.956	7.208
Fe^{2+}	0.733	0.509	0.236
Mn^{2+}	0.296	0.417	0.196
Mg	0.230	0.137	0.015
Cu	0.002	0.004	0.070
Ca	0.004	0.004	0.101
Na	0.919	0.954	0.721
Li	0.937	0.918	1.247
K	0.006	0.004	0.005
F	0.703	0.755	0.706
OH	3.302	3.098	3.060

[a] Calculated by stoichiometry (see text)

[b] Estimated with the procedure of Pesquera et al. (2016)

Errors for oxides and fluorine are standard deviations (in brackets)

Empirical chemical formulae

OG1

$$^{X}(Na_{0.92}K_{0.01}\square_{0.07})_{\Sigma 1.00}{}^{Y}(Al_{0.70}Li_{0.94}Fe^{2+}_{0.73}Mn^{2+}_{0.30}Mg_{0.23}Ti_{0.03})_{\Sigma 2.92}{}^{Z}Al_6$$
$$(^{T}Si_{6.08}O_{18})(BO_3)_3{}^{V}(OH)_{3.00}{}^{W}(OH_{0.30}F_{0.70})_{\Sigma 1.00}$$

OG2

$$^{X}(Na_{0.95}\square_{0.05})_{\Sigma 1.00}{}^{Y}(Al_{0.96}Li_{0.92}Fe^{2+}_{0.51}Mn^{2+}_{0.42}Mg_{0.14}Ti_{0.02})_{\Sigma 2.96}{}^{Z}Al_6$$
$$(^{T}Si_{6.04}O_{18})(BO_3)_3{}^{V}(OH)_{3.00}{}^{W}(OH_{0.10}F_{0.76}O_{0.14})_{\Sigma 1.00}$$

C

$$^{X}(Na_{0.72}K_{0.01}\square_{0.17})_{\Sigma 1.00}{}^{Y}(Al_{1.21}Li_{1.25}Fe^{2+}_{0.24}Mn^{2+}_{0.20}Mg_{0.02}Cu_{0.07}Ti_{0.004})_{\Sigma 2.99}{}^{Z}Al_6$$
$$(^{T}Si_{6.10}O_{18})(BO_3)_3{}^{V}(OH)_{3.00}{}^{W}(OH_{0.06}F_{0.71}O_{0.24})_{\Sigma 1.00}$$

Table 4.10. Average chemical composition and atoms per formula unit (a.p.f.u) for the overgrowth and core zones of the MAV 11 sample (Mavuco, Mozambique) with the relative empirical formula.

	OG	**C**
	n = 10	*n* = 28
SiO_2 (wt%)	38.70(10)	37.53(28)
TiO_2	0.19(5)	0.32(6)
B_2O_3[a]	10.96	10.78
Al_2O_3	37.82(21)	37.24(34)
FeO	1.27(24)	0.15(18)
MnO	2.63(14)	6.66(32)
MgO	0.07(1)	0.00(1)
CuO	0.11(6)	0.05(4)
CaO	0.27(7)	0.38(5)
Na_2O	2.23(8)	2.34(5)
Li_2O[b]	1.93	1.40
K_2O	0.02(1)	0.03(2)
F	1.07(14)	1.15(11)
H_2O[a]	3.28	2.96
$-O \equiv F$	−0.45	−0.48
Total	100.13	100.53
Atoms normalized to 31 anions		
Si (a.p.f.u)	6.139	6.039
Ti^{4+}	0.023	0.039
B	3.000	3.000
Al	7.070	7.074
Fe^{2+}	0.168	0.020
Mn^{2+}	0.353	0.910
Mg	0.017	0.000
Cu	0.013	0.006
Ca	0.046	0.065
Na	0.686	0.733
Li	1.231	0.908
K	0.004	0.006
F	0.539	0.585
OH	3.463	3.183

[a] Calculated by stoichiometry (see text)
[b] Estimated with the procedure of Pesquera et al. (2016)
Errors for oxides and fluorine are standard deviations (in brackets)

Empirical chemical formulae

OG

$$^{X}(Na_{0.69}\square_{0.26}Ca_{0.05})_{\Sigma 1.00}{}^{Y}(Al_{1.07}Li_{1.23}Fe^{2+}_{0.17}Mn^{2+}_{0.35}Mg_{0.02}Cu_{0.01}Ti_{0.02})_{\Sigma 2.86}{}^{Z}Al_6(^{T}Si_{6.14}O_{18})(BO_3)_3{}^{V}(OH)_{3.00}{}^{W}(OH_{0.46}F_{0.54})_{\Sigma 1.00}$$

C

$$^{X}(Na_{0.73}\square_{0.20}Ca_{0.07})_{\Sigma 1.00}{}^{Y}(Al_{1.07}Li_{0.91}Fe^{2+}_{0.02}Mn^{2+}_{0.91}Cu_{0.01}Ti_{0.04})_{\Sigma 2.96}{}^{Z}Al_6(^{T}Si_{6.04}O_{18})(BO_3)_3{}^{V}(OH)_{3.00}{}^{W}(OH_{0.18}F_{0.59}O_{0.23})_{\Sigma 1.00}$$

Table 4.11. Average chemical composition and atoms per formula unit (a.p.f.u) for the zone of the MAV12 sample (Mavuco, Mozambique) with the relative empirical formula.

	C
	n = 16
SiO_2 (wt%)	38.78(60)
TiO_2	0.17(2)
B_2O_3[a]	11.03
Al_2O_3	38.08(42)
FeO	0.48(3)
MnO	5.47(11)
MgO	0.01(1)
CuO	0.06(5)
CaO	0.15(2)
Na_2O	2.41(13)
Li_2O[b]	1.59
K_2O	0.02(1)
F	1.02(13)
H_2O[a]	3.2
$-O \equiv F$	−0.43
Total	102.06
Atoms normalized to 31 anions	
Si (a.p.f.u)	6.108
Ti^{4+}	0.020
B	3.000
Al	7.070
Fe^{2+}	0.063
Mn^{2+}	0.730
Mg	0.002
Cu	0.007
Ca	0.025
Na	0.736
Li	1.007
K	0.005
F	0.506
OH	3.364

[a] Calculated by stoichiometry (see text)
[b] Estimated with the procedure of Pesquera et al. (2016)
Errors for oxides and fluorine are standard deviations (in brackets)

Empirical chemical formulae

C $^{X}(Na_{0.74}K_{0.01}\square_{0.23}Ca_{0.03})_{\Sigma 1.00}{}^{Y}(Al_{1.07}Li_{1.00}Fe^{2+}{}_{0.06}Mn^{2+}{}_{0.73}Cu_{0.01}Ti_{0.02})_{\Sigma 2.89}{}^{Z}Al_6$ $(^{T}Si_{6.11}O_{18})(BO_3)_3{}^{V}(OH)_{3.00}{}^{W}(OH_{0.36}F_{0.51}O_{0.13})_{\Sigma 1.00}$

Table 4.12. Average chemical composition and atoms per formula unit (a.p.f.u) for the core zones of the MAV 13 sample (Mavuco, Mozambique) with the relative empirical formula.

	C
	$n = 16$
SiO_2 (wt%)	39.23(35)
TiO_2	0.02(1)
B_2O_3[a]	11.25
Al_2O_3	41.29(23)
FeO	0.01(1)
MnO	1.05(29)
MgO	-
CuO	0.08(5)
CaO	0.22(2)
Na_2O	1.97(5)
Li_2O[b]	2.05
K_2O	0.01(1)
F	0.77(13)
H_2O[a]	3.45
$-O \equiv F$	−0.33
Total	101.09
Atoms normalized to 31 anions	
Si (a.p.f.u)	6.063
Ti^{4+}	0.002
B	3.000
Al	7.521
Fe^{2+}	0.001
Mn^{2+}	0.138
Mg	-
Cu	0.009
Ca	0.036
Na	0.589
Li	1.274
K	0.003
F	0.377
OH	3.559

[a] Calculated by stoichiometry (see text)
[b] Estimated with the procedure of Pesquera et al. (2016)
Errors for oxides and fluorine are standard deviations (in brackets)

Empirical chemical formulae

C $^{X}(Na_{0.59}\square_{0.37}Ca_{0.04})_{\Sigma 1.00}{}^{Y}(Al_{1.52}Li_{1.27}Mn^{2+}{}_{0.14}Cu_{0.01}Ti_{0.002})_{\Sigma 2.94}{}^{Z}Al_6$ $(^{T}Si_{6.06}O_{18})(BO_3)_3{}^{V}(OH)_{3.00}{}^{W}(OH_{0.56}F_{0.38}O_{0.26})_{\Sigma 1.00}$

Table 4.13. Average chemical composition and atoms per formula unit (a.p.f.u) for the overgrowth and core zones of the MAV 14 sample (Mavuco, Mozambique) with the relative empirical formula.

	OG1	**OG2**	**OG3**	**C1**	**C2**	**C3**
	n = 3	*n* = 5	*n* = 1	*n* = 5	*n* = 6	*n* = 5
SiO_2 (wt%)	38.09(64)	37.94(35)	37.67	38.61(24)	36.93(45)	38.46(98)
TiO_2	0.43(14)	0.26(6)	0.16	-	0.02(2)	0.01(1)
B_2O_3[a]	10.82	10.81	10.89	11.13	10.83	10.97
Al_2O_3	36.47(80)	37.53(19)	39.36	41.31(17)	40.83(31)	38.80(31)
FeO	3.43(30)	2.11(31)	1.18	-	0.01(1)	-
MnO	1.04(21)	0.93(10)	1.03	0.63(19)	1.75(42)	3.52(16)
MgO	0.45(8)	0.25(2)	0.21	-	-	-
CuO	-	0.10(4)	0.26	0.26(5)	0.35(3)	0.45(7)
CaO	1.48(11)	2.10(9)	0.31	0.36(8)	0.30(3)	0.52(3)
Na_2O	2.10(13)	1.79(10)	2.22	1.88(4)	2.06(11)	2.23(7)
Li_2O[b]	1.89	1.99	1.89	2.04	1.71	1.86
K_2O	0.03(1)	0.02(2)	0.01	0.01(1)	0.03(4)	0.01(1)
F	1.13(11)	1.23(14)	1.29	0.90(16)	0.85(19)	1.17(12)
H_2O[a]	3.01	2.77	3.02	3.28	3.03	3.01
$-O \equiv F$	−0.48	−0.52	−0.54	−0.38	−0.36	−0.49
Total	99.94	99.36	98.99	100.03	98.35	100.53
	Atoms normalized to 31 anions					
Si (a.p.f.u)	6.116	6.089	6.004	6.010	5.929	6.094
Ti^{4+}	0.052	0.032	0.019	-	0.002	0.001
B	3.000	3.000	3.000	3.000	3.000	3.000
Al	6.901	7.111	7.406	7.604	7.686	7.246
Fe^{2+}	0.461	0.284	0.157	-	0.001	-
Mn^{2+}	0.142	0.127	0.130	0.084	0.238	0.472
Mg	0.108	0.060	0.040	-	-	-
Cu	-	0.012	0.031	0.031	0.042	0.054
Ca	0.255	0.363	0.053	0.060	0.052	0.089
Na	0.655	0.559	0.688	0.568	0.642	0.685
Li	1.221	1.287	1.214	1.282	1.104	1.186
K	0.006	0.005	0.003	0.002	0.006	0.002
F	0.573	0.623	0.650	0.444	0.430	0.586
OH	3.227	2.966	3.220	3.416	3.240	3.181

[a] Calculated by stoichiometry (see text)
[b] Estimated with the procedure of Pesquera et al. (2016)
Errors for oxides and fluorine are standard deviations (in brackets)

Empirical chemical formulae

OG1
$$^{X}(Na_{0.66}K_{0.01}\square_{0.08}Ca_{0.26})_{\Sigma 1.00}{}^{Y}(Al_{0.90}Li_{1.22}Fe^{2+}_{0.46}Mn^{2+}_{0.14}Mg_{0.11}Ti_{0.05})_{\Sigma 2.88}{}^{Z}Al_6$$
$$(^{T}Si_{6.12}O_{18})(BO_3)_3{}^{V}(OH)_{3.00}{}^{W}[(OH)_{0.23}F_{0.57}O_{0.20})]_{\Sigma 1.00}$$

OG2
$$^{X}(Na_{0.56}K_{0.01}\square_{0.07}Ca_{0.36})_{\Sigma 1.00}{}^{Y}(Al_{1.11}Li_{1.29}Fe^{2+}_{0.28}Mn^{2+}_{0.13}Mg_{0.06}Cu_{0.01}Ti_{0.03})_{\Sigma 2.91}{}^{Z}Al_6$$
$$(^{T}Si_{6.09}O_{18})(BO_3)_3{}^{V}(OH_{2.97}O_{0.03})_{\Sigma 3.00}{}^{W}(F_{0.62}O_{0.38})_{\Sigma 1.00}$$

OG3
$$^{X}(Na_{0.69}\square_{0.26}Ca_{0.05})_{\Sigma 1.00}{}^{Y}(Al_{1.41}Li_{1.21}Fe^{2+}_{0.16}Mn^{2+}_{0.13}Mg_{0.04}Cu_{0.03}Ti_{0.02})_{\Sigma 3.00}{}^{Z}Al_6$$
$$(^{T}Si_{6.00}O_{18})(BO_3)_3{}^{V}(OH)_{3.00}{}^{W}[(OH)_{0.22}F_{0.65}O_{0.13})]_{\Sigma 1.00}$$

C1
$$^{X}(Na_{0.57}\square_{0.37}Ca_{0.06})_{\Sigma 1.00}{}^{Y}(Al_{1.60}Li_{1.28}Mn^{2+}_{0.08}Cu_{0.03})_{\Sigma 2.99}{}^{Z}Al_6$$
$$(^{T}Si_{6.01}O_{18})(BO_3)_3{}^{V}(OH)_{3.00}{}^{W}[(OH)_{0.42}F_{0.44}O_{0.14})]_{\Sigma 1.00}$$

C2
$$^{X}(Na_{0.64}K_{0.01}\square_{0.30}Ca_{0.05})_{\Sigma 1.00}{}^{Y}(Al_{1.62}Li_{1.10}Mn^{2+}_{0.24}Cu_{0.04}Ti_{0.002})_{\Sigma 3.00}{}^{Z}Al_6$$
$$[(^{T}Si_{5.93}Al_{0.07})O_{18}](BO_3)_3{}^{V}(OH)_{3.00}{}^{W}[(OH)_{0.24}F_{0.43}O_{0.13})]_{\Sigma 1.00}$$

C3
$$^{X}(Na_{0.69}\square_{0.22}Ca_{0.09})_{\Sigma 1.00}{}^{Y}(Al_{1.25}Li_{1.19}Mn^{2+}_{0.47}Ti_{0.001})_{\Sigma 2.91}{}^{Z}Al_6$$
$$(^{T}Si_{6.09}O_{18})(BO_3)_3{}^{V}(OH)_{3.00}{}^{W}[(OH)_{0.18}F_{0.59}O_{0.23})]_{\Sigma 1.00}$$

Table 4.14. Average chemical composition and atoms per formula unit (a.p.f.u) for the core zone of the MAV15 sample (Mavuco, Mozambique) with the relative empirical formula.

	C
	$n = 13$
SiO_2 (wt%)	36.29(83)
TiO_2	0.02(1)
B_2O_3[a]	10.60
Al_2O_3	38.23(26)
FeO	0.01(1)
MnO	5.75(15)
MgO	-
CuO	0.07(3)
CaO	0.24(2)
Na_2O	2.42(5)
Li_2O[b]	1.30
K_2O	0.03(1)
F	1.11(13)
H_2O[a]	2.83
$-O \equiv F$	−0.47
Total	98.45
Atoms normalized to 31 anions	
Si (a.p.f.u)	5.951
Ti^{4+}	0.003
B	3.000
Al	7.379
Fe^{2+}	0.001
Mn^{2+}	0.799
Mg	-
Cu	0.009
Ca	0.042
Na	0.769
Li	0.857
K	0.006
F	0.576
OH	3.100

[a] Calculated by stoichiometry (see text)
[b] Estimated with the procedure of Pesquera et al. (2016)
Errors for oxides and fluorine are standard deviations (in brackets)

Empirical chemical formulae

C $^{X}(Na_{0.77}K_{0.01}\square_{0.18}Ca_{0.04})_{\Sigma 1.00}{}^{Y}(Al_{1.33}Li_{0.86}Mn^{2+}_{0.80}Cu_{0.01}Ti_{0.003})_{\Sigma 3.00}{}^{Z}Al_6$
$[(^{T}Si_{5.95}Al_{0.05})O_{18}](BO_3)_3{}^{V}(OH)_{3.00}{}^{W}(OH_{0.10}F_{0.58}O_{0.32})_{\Sigma 1.00}$

Table 4.15. Average chemical composition and atoms per formula unit (a.p.f.u) for the overgrowth and core zones of the MAV 17 sample (Mavuco, Mozambique) with the relative empirical formula.

	OG1 $n = 5$	**OG2** $n = 12$	**C1** $n = 7$	**C2** $n = 10$
SiO_2 (wt%)	36.81(94)	35.05(57)	34.58(23)	37.40(79)
TiO_2	0.21(4)	0.13(2)	0.05(1)	0.01(1)
B_2O_3[a]	10.67	10.33	10.23	10.86
Al_2O_3	38.29(32)	38.47(38)	38.50(37)	40.32(32)
FeO	2.06(35)	1.88(23)	0.46(8)	-
MnO	1.72(42)	0.69(9)	0.79(16)	1.62(31)
MgO	0.13(14)	0.03(1)	0.01(1)	-
CuO	0.16(3)	0.08(5)	0.18(4)	0.22(5)
CaO	0.31(7)	0.27(4)	0.45(8)	0.34(2)
Na_2O	2.35(7)	2.09(6)	1.90(3)	2.02(8)
Li_2O[b]	1.64	1.60	1.78	1.85
K_2O	0.02(1)	0.02(1)	0.01(1)	0.02(2)
F	1.16(25)	0.88(17)	0.95(20)	0.94(19)
H_2O[a]	2.91	2.96	2.98	3.12
$-O \equiv F$	−0.49	−0.37	−0.40	−0.40
Total	98.01	94.15	92.52	98.34
	Atoms normalized to 31 anions			
Si (a.p.f.u)	5.997	5.899	5.877	5.984
Ti^{4+}	0.026	0.016	0.007	0.001
B	3.000	3.000	3.000	3.000
Al	7.323	7.622	7.683	7.584
Fe^{2+}	0.280	0.264	0.065	-
Mn^{2+}	0.238	0.098	0.114	0.219
Mg	0.032	0.008	0.008	-
Cu	0.020	0.010	0.023	0.027
Ca	0.055	0.049	0.083	0.058
Na	0.741	0.683	0.626	0.627
Li	1.075	1.083	1.217	1.191
K	0.004	0.004	0.003	0.005
F	0.598	0.471	0.510	0.476
OH	3.162	3.328	3.381	3.330

[a] Calculated by stoichiometry (see text)
[b] Estimated with the procedure of Pesquera et al. (2016)
Errors for oxides and fluorine are standard deviations (in brackets)

Empirical chemical formulae

OG1
$$^{X}(Na_{0.74}\square_{0.20}Ca_{0.06})_{\Sigma 1.00}{}^{Y}(Al_{1.32}Li_{1.08}Fe^{2+}_{0.28}Mn^{2+}_{0.24}Mg_{0.03}Cu_{0.02}Ti_{0.03})_{\Sigma 3.00}{}^{Z}Al_6 (^{T}Si_{6.00}O_{18})(BO_3)_3{}^{V}(OH)_{3.00}{}^{W}(OH_{0.16}F_{0.60}O_{0.24})_{\Sigma 1.00}$$

OG2
$$^{X}(Na_{0.68}\square_{0.26}Ca_{0.05})_{\Sigma 1.00}{}^{Y}(Al_{1.52}Li_{1.08}Fe^{2+}_{0.26}Mn^{2+}_{0.10}Mg_{0.01}Cu_{0.01}Ti_{0.02})_{\Sigma 3.00}{}^{Z}Al_6 [(^{T}Si_{5.90}Al_{0.10})O_{18}](BO_3)_3{}^{V}(OH)_{3.00}{}^{W}(OH_{0.33}F_{0.47}O_{0.20})_{\Sigma 1.00}$$

C1
$$^{X}(Na_{0.63}\square_{0.29}Ca_{0.08})_{\Sigma 1.00}{}^{Y}(Al_{1.56}Li_{1.22}Fe^{2+}_{0.07}Mn^{2+}_{0.11}Mg_{0.01}Cu_{0.02}Ti_{0.01})_{\Sigma 3.00}{}^{Z}Al_6 [(^{T}Si_{5.88}Al_{0.12})O_{18}](BO_3)_3{}^{V}(OH)_{3.00}{}^{W}(OH_{0.38}F_{0.51}O_{0.11})_{\Sigma 1.00}$$

C2
$$^{X}(Na_{0.63}\square_{0.31}Ca_{0.06})_{\Sigma 1.00}{}^{Y}(Al_{1.56}Li_{1.19}Mn^{2+}_{0.22}Cu_{0.03}Ti_{0.001})_{\Sigma 3.00}{}^{Z}Al_6 [(^{T}Si_{5.98}Al_{0.02})O_{18}](BO_3)_3{}^{V}(OH)_{3.00}{}^{W}(OH_{0.33}F_{0.48}O_{0.19})_{\Sigma 1.00}$$

Table 4.16. Average chemical composition and atoms per formula unit (a.p.f.u) for the overgrowth and core zones of the MAV 18 sample (Mavuco, Mozambique) with the relative empirical formula.

	OGL $n = 7$	**C** $n = 17$	**OGR2** $n = 2$	**OGR1** $n = 4$
SiO_2 (wt%)	37.19(96)	37.68(84)	38.13(21)	37.60(34)
TiO_2	0.14(5)	0.01(1)	0.12(3)	0.11(3)
B_2O_3[a]	10.60	10.8	10.81	10.67
Al_2O_3	36.03(39)	39.32(43)	37.62(6)	36.17(57)
FeO	1.84(39)	0.02(2)	1.31(27)	1.87(9)
MnO	3.74(41)	0.04(3)	1.12(33)	3.65(38)
MgO	0.18(7)	-	0.12(7)	0.14(3)
CuO	0.02(3)	0.04(4)	0.02(2)	0.01(1)
CaO	2.07(49)	1.15(13)	2.22(27)	1.73(36)
Na_2O	1.94(24)	1.65(6)	1.64(17)	2.08(15)
Li_2O[b]	1.67	2.26	2.12	1.72
K_2O	0.03(1)	0.01(1)	0.01(1)	0.02(1)
F	1.28(21)	1.16(20)	1.41(1)	1.43(14)
H_2O[a]	2.63	3.12	2.75	2.66
$-O \equiv F$	−0.54	−0.49	−0.59	−0.60
Total	98.83	96.782	98.83	99.29
Atoms normalized to 31 anions				
Si (a.p.f.u)	6.100	6.066	6.129	6.135
Ti^{4+}	0.017	0.001	0.015	0.014
B	3.000	3.000	3.000	3.000
Al	6.965	7.461	7.118	6.943
Fe^{2+}	0.253	0.002	0.176	0.254
Mn^{2+}	0.519	0.006	0.152	0.503
Mg	0.044	-	0.029	0.034
Cu	0.002	0.005	0.002	0.001
Ca	0.364	0.198	0.382	0.302
Na	0.617	0.516	0.512	0.658
Li	1.102	1.463	1.371	1.127
K	0.006	0.003	0.002	0.003
F	0.662	0.588	0.716	0.739
OH	2.877	3.347	2.944	2.889

[a] Calculated by stoichiometry (see text)
[b] Estimated with the procedure of Pesquera et al. (2016)
Errors for oxides and fluorine are standard deviations (in brackets)

Empirical chemical formulae

OGL
$$^{X}(Na_{0.62}K_{0.01}\square_{0.01}Ca_{0.36})_{\Sigma 1.00}{}^{Y}(Al_{0.97}Li_{1.10}Fe^{2+}{}_{0.25}Mn^{2+}{}_{0.52}Mg_{0.04}Ti_{0.02})_{\Sigma 2.90}{}^{Z}Al_6$$
$$(^{T}Si_{6.10}O_{18})(BO_3)_3{}^{V}(OH_{2.88}O_{0.12})_{\Sigma 3.00}{}^{W}(F_{0.66}O_{0.34})_{\Sigma 1.00}$$

C
$$^{X}(Na_{0.52}\square_{0.28}Ca_{0.20})_{\Sigma 1.00}{}^{Y}(Al_{1.46}Li_{1.46}Mn^{2+}{}_{0.01}Ti_{0.001})_{\Sigma 2.93}{}^{Z}Al_6$$
$$(^{T}Si_{6.07}O_{18})(BO_3)_3{}^{V}(OH)_{3.00}{}^{W}(OH_{0.35}F_{0.59}O_{0.06})_{\Sigma 1.00}$$

OGR2
$$^{X}(Na_{0.51}\square_{0.10}Ca_{0.38})_{\Sigma 1.00}{}^{Y}(Al_{1.12}Li_{1.37}Fe^{2+}{}_{0.18}Mn^{2+}{}_{0.15}Mg_{0.03}Ti_{0.02})_{\Sigma 2.88}{}^{Z}Al_6$$
$$(^{T}Si_{6.13}O_{18})(BO_3)_3{}^{V}(OH_{2.94}O_{0.06})_{\Sigma 3.00}{}^{W}(F_{0.72}O_{0.28})_{\Sigma 1.00}$$

OGR1
$$^{X}(Na_{0.66}\square_{0.04}Ca_{0.30})_{\Sigma 1.00}{}^{Y}(Al_{0.94}Li_{1.13}Fe^{2+}{}_{0.25}Mn^{2+}{}_{0.50}Mg_{0.03}Ti_{0.01})_{\Sigma 2.86}{}^{Z}Al_6$$
$$(^{T}Si_{6.14}O_{18})(BO_3)_3{}^{V}(OH_{2.89}O_{0.11})_{\Sigma 3.00}{}^{W}(F_{0.74}O_{0.26})_{\Sigma 1.00}$$

MAV 2: the sample represents a fragment of a tourmaline core (C) and, as thin section, reveals a bright blue coloration with a brownish-greenish portion. As for the sample MAV 1, the chemical composition of this tourmaline is quite homogeneous along the considered traverse, but the average amounts of Fe and Mn are different. The MAV 2 sample is characterized by a higher concentration of Fe (FeO ~ 5 wt%) and a lower Mn content (MnO ~ 1 wt%). CuO content shows some oscillation within 0.03 wt% as already observed for the MAV 1 sample.
The change of color observed along the crystal fragment seems to be not related to variations in FeO, MnO and CuO contents. Based on the chemical composition, Fe is the principle coloring agent responsible for the bright blue clororation displayed by this tourmaline sample. This because Mn is a much weaker absorber than Fe, and concentrations of 1–3 wt% MnO is usually not enough to impart a color to Li-Al tourmaline crystals (Rossman, 1997) (Fig. 4.9 and Table 4.2).

MAV 3: once reduced to a thin section, the sample displays a discontinuous black-to-green rim, which is present only on one side of the tourmaline grain. Moreover, the sample is characterized by a colored core ranging from light pink to light blue-green in the inner part of the crystal. At the dark-colored rim (OG), the sample shows high levels of Fe and Mn, with a content of FeO ~ 4.5 wt% and MnO ~ 2.2 wt%. Fe and Mn content sharply decreases below detection limit within the core. While FeO level remains so low through the entire core of the crystal, MnO rises progressively in correspondence of the light pink region of the polychrome core (C1 and C2), reaching a concentration of about 4 wt% in the initial part of the light blue-green zone of the core where it remains almost constant (C3). A similar behavior, but with a less extent, can be observed for CuO, which content is about 0.04 − 0.06 wt% in the initial part of the crystal (OG and C1), and 0.13 − 0.14 wt% in the remaining (C2 and C3). The dark-colored overgrowth (OG) also shows a slight increase in CaO reaching values up to ~2 wt%. The first part of the light pink zone (C1) is characterized by a low MnO content, which increases in the second part (C2) along with CuO. This gives rise to a light blue-green shading in the C2 zone.

The blue-green zone (C3) is instead characterized by the highest level in MnO and CuO. Consequently, the blue-green hue of the C3 zone can be ascribed to Cu and Mn in combination with Ti (TiO_2 ~0.10 wt%) (Fig. 4.10 and Table 4.3).

MAV 4: the sample, as thin section, exhibits an extended blackish rim and a polychromatic core where it can be distinguished at least three different shade of yellow color: yellow (C1), pale yellow (C2) and ochre (C3). The dark-colored overgrowth is characterized by an average high content in Fe and Mn. While FeO decreases from an initial value of about 5 wt% at the rim edge to 0.6 wt% at the transition rim-core, MnO rises from 4 wt% to 6 wt%. On the basis of these variations, the dark-colored overgrowth was subdivided in OG1, OG2 and OG3. FeO level remains below 0.5 wt% in the yellow and pale-yellow zones of the core (C1 and C2), rising to 1.5 wt% in the ochre zone (C3). MnO content remains quite constant at about 6 wt% in the first core region (C1), decreases in the C2 zone to about 4.5 wt%, remaining around this level in the last zone of the core (C3). CuO content rises in the inner part of the dark-colored overgrowth (OG3) reaching a value of about 0.3 wt%. Its level remains constant through the C1 and C2 zones, decreasing to ~ 0.1 wt% in the ochre zone (C3).

Overall, the yellow zone (C1) is characterized by the highest level of Mn (MnO ~ 6 wt%) and the lowest of Fe (FeO > 0.5 wt%). In the pale-yellow zone (C2) a progressive decrease in Mn content can be observed (MnO ~ 4 wt%), wherease FeO level remains quite low. The ochre zone (C3) is the result of an increased amount of FeO content, which is always > 1 wt%, reaching up to 2 wt% at the end of the fragment. In the same zone, CuO content decreases from 0.30 wt% to 0.10 wt% (Fig. 4.11 and Table 4.4). Due to the very low FeO content in the C1 and C2 zones, Mn may be responsible for the yellow to pale yellow coloration displayed by these zones. The yellow-green coloration of the C3 zone, may instead be ascribed to both Fe and Mn, with the influence of Ti (TiO_2 ~ 0.3 wt%). It is not to be excluded that Cu, given its not negligibile content (CuO ~ 0.3 wt%), may play a role in the greenish hue of the crystal core zone (Fig. 4.11 and Table 4.4).

MAV 5: the sample represents a fragment of a tourmaline core and, as thin section, shows a light blue color. FeO content is always below the detection limit. MnO progressively increases through the entire length of the crystal fragment, starting from an initial value of 0.6 wt% to 5.2 wt% at the end. Considering this variation, the core was subdivided in three parts: C1, C2 and C3. CuO level is quite significant with an average value of 0.5 wt%, showing a rhythmic behavior in the range 0.4 wt% − 0.5 wt%. Despite the increase in Mn, the color displayed by this tourmaline sample remains blue along the whole crystal, suggesting that Cu is the main color-causing agent (Fig. 4.12 and Table 4.5).

MAV 6: in thin section, the sample reveals a dark-green overgrowth and a core where are clearly distinguishable three differently colored zones: pink to pale green (C1), ochre (C2) and an extended blackish core (C3 and C4). The dark-green overgrowth is characterized by a quite significant amount of CaO, which reaches an average value of 4 wt%, and a lower content in FeO and MnO, in the range of 1-2 wt%. The multicolored core shows, for several oxides, a different behavior. FeO amount sharply decreases below detection limits in the C1 zone, rises a little bit in the C2 zone (about 0.4 wt%) and then sharply increases in the C3 zone reaching the highest value of about 4 wt %. FeO level remains constant, always around 4 wt%, in the C4 zone. Differently, the content in MnO initially decreases below 0.5 wt% at the beginning of the C1 zone, and then progressively increases reaching the highest value (about 6.7 wt%) at the beginning of the C2 zone. MnO content is always over 6 wt% in the C2 zone and then sharply decreases to about 4 wt% in the C3 and C4 zone. CaO also abrutely decreases in the C1 zone below 1.5 wt%, and then progressively decreases up to 0.3 wt% in the C4 zone.

CuO levels are low along the whole sample with the highest values (~0.2 wt%) mainly concentrated in the C1 zone and the initial part of the C2 one. TiO_2 level are below 0.05 wt% in the OG and C1 zones, and becomes quite elevate in the ochre (C2) and blackish (C3 and C4) zones of the sample, with values ranging from 0.45 w% to 0.65 wt%. (Fig. 4.13 and Table 4.6).

Considering all these compositional data, the dark-green color of the overgrowth (OG), which is characterized by an unusual enrichment in Ca, maybe mainly the result of the combination of yellow and blue hues related to Mn and Fe as color-causing agents, respectively. The pink color displayed by the initial part of the C1 zone could be related to Mn as the only color-causing agent, because the absence of FeO in this part of the sample. The last part of the C1 zone shows a light blue-green color that can be related to the sharp increases in MnO, which content rises from 1 wt% to about 7 wt%. However, this latter zone is also characterized by the highest level of CuO, which cannot be excluded as color-causing agent. The ochre color of the C2 zone is mainly the result of the highest content in Mn. However, it cannot be excluded the contribution of Ti due to the discrete amount of TiO_2 in this zone (~0.45 wt%). The blackish color of the inner part of the sample (C3 and C4) is related to the high and quite constant content in FeO and MnO, with a value of about 5 wt% and 4 wt%, respectively (Fig. 4.13 and Table 4.6).

MAV 7: once reduced to a thin section, the sample displays a discontinuous black rim (OG), which is present only on one side of the tourmaline grain, and a colored core ranging from light pink (C1 and C2), to light blue-green (C3) to ochre in the inner part of the crystal (C4). The sample shows compositional and chromatic characteristics similar to MAV 3. In fact, the black overgrowth is characterized by a high content in FeO and MnO, with an average value of 4 wt% and 2 wt%, respectively. Both oxides sharply decrease at the rim-core transition. FeO level remains below detection limits in C1, C2 and C3 zones, and then rises a little in the C4 zone, with a value always below 0.5 wt%. Differently, MnO level progressively rises from ~1 wt% to ~7 wt% through the C1, C2 and C3 zones, and then remains constant to the highest level in the C4 zone. CuO content is quite low in the dark-colored overgrowth, rising up to an average level of 0.2 wt% in the core zone. Similar to the MAV 3 sample, the dark-colored overgrowth is characterized by an increased amount of Ca (CaO up to ~2 wt%) (Fig. 4.14 and Table 4.7).

Considering the color displayed, the light pink and the light blue-green zones (C1

− C3), are characterized by the same behavior in Mn as observed for the C2 zones of MAV 3 and MAV 6 samples. In fact, these zones are characterized by a wide change in Mn content, which increases at the transition from the light pink to the light blue-green zone. The C4 ochre zone, as the C1 zone of the sample MAV 6, displays the highest concentration of MnO and low level of FeO. Similarly, is characterized by a discrete amount of Ti (TiO_2 ~0.4 wt%) (Table 4.7). Therefore, both Mn and Ti can be the responsible of the ochre coloration of the C4 zone.

MAV 8: the sample, as thin section, reveals a polychromatic core raging from pale blue-green to light pink, surrounded by a greenish overgrowth. The overgrowth (OGR and OGL) is characterized by a slight enrichment in FeO and MnO (between 1 wt% and 2 wt%). MnO decreases progressively in the core zone, with an average value of 0.8 wt% in the C1 zone, and 0.2 wt% in the inner core zone (C2). Similarly, FeO decreases to an average value of 0.2 wt% in the C1 zone, up to a value below the detection limit in the inner core zone (C2). An opposite behavior can be observed for CuO, which content is higher in the core zone, showing values ranging from 0.3 wt% to 0.4 wt%, and then decreases at the overgrowth. Similarly, CaO shows a slight increase in the core zone, with values ranging from ~1.4 wt% and ~2 wt% (Fig. 4.15 and Table 4.8).

The greenish color of the overgrowth (OGL and OGR) that characterized this tourmaline sample, may be related to the lower enrichment in Fe and Mn, which are always below ~2 wt%, coupled with the influence of Ti (TiO_2 ~0.15 wt%). The pale blue-green color of the C1 zone, could be related to the very low content in Fe, associated with the maximum concentration of Cu (CuO up to ~0.4 wt%). The light pink color of the inner core (C2) can be associated with the absence of Fe, which is below the detection limit, and a very low amount in Mn. Although the light pink color displayed, it cannot be excluded a contribution of Cu (CuO ~0.2 wt%) (Fig. 4.15 and Table 4.8).

MAV 10: once reduced in thin section, the sample displays a bright blue-green

core surrounded by a black overgrowth. The overgrowth is characterized by very high content in FeO in the outer region (OG1), starting with a value of about 6 wt%, which progressively decreases in the inner part of the overgrowth (OG2), ranging from ~3 wt% to 4 wt%. The outer region of the overgrowth (OG1) starts with a low MnO content, which reaches the maximum at the OG2 (~3 wt%) being comparable with FeO content. The FeO and MnO content decreases in the core zone remaining almost constant with an approximately equivalent amount (~1.5 wt%). CuO level is very low in the overgrowth and abruptly increases in the core zone where it reaches a constant value of ~0.6 wt%. Similarly, CaO shows a slight increased amount in the core zone (~0.6 wt%) compared to the overgrowth, where its content is below detection limit (Fig. 4.16 and Table 4.9).

The black color of the overgrowth is surely related to the high content in Fe and Mn coupled with the presence of Ti (TiO_2 ~0.2 wt%), while the bright blue-green color displayed by the core zone could be related to the combined effects of Fe and Cu as color-causing agents (Fig. 4.16 and Table 4.9).

MAV 11: the sample, as thin section, exhibits a brownish overgrowth and a core zone characterized by an increase in the ochre coloration from the outer to the inner core. The overgrowth shows a discrete but not so high content in MnO and FeO, which remains constant within the OG with values of ~2.6 wt% and 1.3 wt%, respectively. In the core zone, MnO and FeO show a completely different behavior. MnO content abruptly increases being always over 6 wt% through all core zone, while FeO sharply decreases below the detection limit showing a slight increase in the inner part of the core. CuO content is quite low throughout the considered traverse with values always below ~0.1 wt%, while TiO_2 increases in the ochre zone of the core zone reaching values ranging from ~0.3 wt% − 0.4 wt% (Fig. 4.17 and Table 4.10).

The brownish coloration of the overgrowth is consistent with the moderate content in Fe and Mn. The very high content of Mn in the core zone could be responsible of its ochre coloration. However, being the levels of Mn quite constant,

the observed increase in the greenish hue of the ochre coloration through the inner core, could be related to higher Ti level (TiO_2 ~0.3 wt%) in this part of the crystal (Fig. 4.17 and Table 4.10).

MAV 12: the sample represents a fragment of a yellow tourmaline core (C). As previously observed for MAV 1 and MAV 2 samples, this tourmaline sample has a homogeneous chemical composition. However, it is characterized by an higher content in MnO (~5.5 wt%) and a lower content in FeO (~0.5 wt%). CuO level is quite low (~0.06 wt%). TiO_2 is about 0.15 wt% (Fig. 4.18 and Table 4.11). Considering this compositional data, the yellow color displayed by this tourmaline sample is consistent with the enrichment in Mn and the low Fe content, even if a slight contribution of Ti cannot be excluded.

MAV 13: the sample represents a fragment of a pink-reddish tourmaline core (C). Here again, the sample is characterized a homogeneous chemical composition. As observed for the MAV 12 sample, the content in MnO is higher than FeO. However, MnO level is quite lower respect to the sample MAV 12 (1 wt% vs 6 wt%). FeO is constantly below the detection limit, and CuO content is quite low (~0.1 wt%) (Fig.4.19 and Table 4.12). Overall, the pink-reddish coloration of this sample can be related to the low content in Mn and the absence of Fe.

MAV 14: the sample, as thin section, shows a wide overgrowth with colors ranging from black in the outer region (OG1), to brownish in the inner region (OG2 and OG3). The core shows a pale coloration, pink in the outer core zone (C1 and C2) and blue-green in the inner (C3). The overgrowth is characterized by FeO content greater than MnO, with initial values of ~3.8 wt% and 1.3 wt%, respectively. FeO content decreases within the overgrowth (OG1, OG2 and OG3), to reach values below the detection limit in the core zone. MnO level remains almost constant within all the overgrowth, sharply decreases below ~0.5 wt% at the rim-core transition, and then progressively increases though the C1 and C2

zones reaching the maximum in the inner core region (C3) where it remains constant (~3.5 wt%). CuO shows a similar behavior of MnO, with a very low level within the overgrowth, which progressively increase in C1 and C2, reaching a value of ~0.4 wt% in the inner core (C3). The overgrowth, compared with the core zone, is characterized by an increased content of CaO (~2 wt%) and TiO_2 (Fig. 4.20 and Table 4.13).

The black-to-brownish color change displayed by the overgrowth is related to the progressive decrease in Fe and Ti content, which allow the appearance of a yellowish coloration related to the low but constant Mn content. The pale pink color showed by C1 and C2 zones can be the result of the low Mn content in association to the absence of Fe. The pale blue-green coloration of the C3 zone can be related to the higher Mn content. Cu can contribute to the color displayed by the core (C1, C2 and C3).

MAV 15: the sample represents a fragment of a tourmaline core and, as thin section, shows a pale green coloration. It is characterized by a homogeneous chemical composition quite similar to that reported for the MAV 12 sample. In fact, they share a similar MnO content (~6 wt%). However, FeO content in MAV 15 sample is constantly below the detection limit. CuO level is quite low (below ~0.1 wt%) and TiO_2 is below detection limit (Fig. 4.21 and Table 4.14).

Despite the similar chemical composition of MAV 12 sample with a high content in Mn, the pale green coloration, quite different from the yellow one displayed by the MAV 12, could be related to Mn alone.

MAV 17: the sample, as thin section, shows a brownish-to-greenish overgrowth (OG1 and OG2), which is darker in the outer region (OG1), and a colored core ranging from green (C1) to light green (C2). The entire overgrowth is characterized by a high content in FeO (~2 wt%). MnO shows an increased concentration in OG1 (up to ~2 wt%), while is constantly below ~1 wt% in OG2. FeO content sharply decrease below 0.5 wt% in the C1 zone and became

undetectable in the C2 zone. On the contrary, MnO level remains quite constant below ~1 wt% in the C1 zone, and then progressively doubles in the C2 zone. CuO displays a behavior similar to MnO. The initial average value of 0.15 wt% in OG1 is followed by a decrease in the OG2 zone. CuO levels sharply rise at the transition rim-core to reach higher average values in the C1 and C2 zones (0.18 wt% and 0.22 wt%, respectively) (Fig. 4.22 and Table 4.15).

Differently from the MAV 14 sample, the darker greenish hue displayed by the overgrowth, is related to the decrease in Mn content, considering that Fe content is quite constant through the overgrowth. In addition, the average TiO_2 level is greater in OG1 respect to OG2 (0.21 wt% vs 0.13 wt%) (see Table 4.15). The green coloration of the C1 zone can be related to the low content in Fe and Mn. The absence of Fe and the presence of a moderate amount of Mn, could be responsible of the light green color displayed by the C2 zone. Again Cu, which content is increased in this zone, may play a role as color-causing agent.

MAV 18: the sample, as thin section, displays a black-to-greenish overgrowth surrounding a pale pink homogeneous core. The behavior of FeO and MnO is similar to that observed for the MAV 8 sample, with the overgrowth (OGL, OGR2 and OGR1) characterized by a content of MnO higher than FeO and a core depleted of these oxides. However, in this case MnO and FeO levels (~4 wt% and ~2 wt%, respectively) are higher than that reported for the MAV 8 sample. MnO and FeO content decreases at the rim-core transition abruptly on one side (OGL), and gradually on the other one (OGR). For this reason, on the basis of the chemical heterogeneity, the latter region was subdivided in OGR2 and OGR1.

Additionally, the core zone is characterized by a very low amount of Mn, constantly below ~0.1 wt%, and FeO below detection limit. Differently for the MAV 8 sample, CaO is higher in the overgrowth zones, with an averaged double amount compared to the core. CuO content is constantly very low along the considered traverse (Fig.4.23 and Table 4.16). The black-to-greenish overgrowth is related to the high content in Mn and Fe, coupled with the presence of Ti (TiO_2

~0.1 wt%) (Table 4.16). The black to greenish transition observed in the inner part of the overgrowth, more extended in one side (OGR2), is consistent with the decrease in Mn, Fe and Ti content, slower in OGR respect to OGL. The pale pink coloration of the core zone may be associated with the very low, but detectable, content in Mn and the absence of Fe.

General comments on the chemical composition and mineralogical species of the Mavuco tourmaline grains

Based on the compositional data obtained by EMPA, differences in the amount of some oxides can be evidenced. These differences can be observed not only among the tourmaline samples analyzed but also, in several cases, within the same sample. FeO and MnO are the oxides for which the greatest variations in content are observed, followed, in some samples, by CaO, MgO and CuO. This compositional heterogeneity is more marked in those samples with a dark-colored overgrowth, which may surround a colored core or be limited to one side of the tourmaline grain.

The overgrowths are generally enriched in FeO and MnO, although with a different amount and ratio. Several overgrowths are also enriched in CaO, TiO_2 and MgO..

A similar compositional heterogeneity, mainly involving MnO, followed by CuO, CaO, FeO and, in few cases, MgO and TiO_2, can be observed in the core zone of tourmaline samples with a dark-colored overgrowth. Frequently, these core zones appear polychromatic, with colors ranging from pink, blue, blue-green, green and ochre. This polychromatic feature is particularly evident in the MAV 6 sample, which core shows the highest color variability (Fig. 4.13). The chromatic variation observed in the core zone of the analyzed samples, are often related to compositional changes mainly ascribed to Mn, Fe, Ti and Cu, which are typical chromophore elements.

For samples composed only by a monochromatic core fragment, the chemical composition remains almost homogeneous within the crystal.

In all the analyzed samples, CuO can always be detected with concentrations below 1 wt% but showing a marked variability both within the same sample and among the different tourmaline grains. Therefore, it cannot be excluded that Cu can contributed to the color displayed by the tourmaline samples, especially in those zones where its concentration is higher. All other elements analyzed do not show any particular variation along the considered traverses. Vanadium, Cr and K were always below detection limit.

The site populations for each zone of the tourmaline samples analyzed were calculated following Henry et al. (2011) and the resulting empirical formulae are reported in Tables 4.1−4.16. In figure 4.24 are shown the ternary plots of X- , Y- and W-site occupancy of all analyzed zones, while in figure 4.25 are reported the ternay plots of core and overgrowth zones in the different samples, separately.

Despite the compositional variability evidenced by EMP analyses, all tourmaline samples belong to the elbaite−fluor-elbaite series, except for samples MAV 4 and MAV 6. In fact, the outermost region of MAV 4 dark-colored overgrowth (OG1) is consistent with a tourmaline belonging to the alkali-group, subgroup 3 (Henry et al., 2011): it is Na-dominant at the *X* position of the tourmaline general formula and oxy-dominant at *W* with $O^{2-} > (OH+F)^{-}$. Because is ^{Z}Al- and $^{Y}(Fe_2Al)$-dominant, its composition can be ascribed to an oxy-schorl (Henry et al., 2011) (Fig. 4.24 and 4.25). The dark-green overgrowth (OG) of MAV 6 can be, instead, classified as a tourmaline belonging to the calcic-group, subgroup 2 (Henry et al., 2011): it is Ca-dominant dominant at the *X* position and fluor-dominant with $(F+OH)^{-} > O^{2-}$ and F >> (OH). Because is ^{Z}Al- and $^{Y}(AlLi_2)$-dominant, its composition can be ascribed to a fluor-liddicoatite (Henry et al., 2011) (Fig. 4.24 and 4.25).

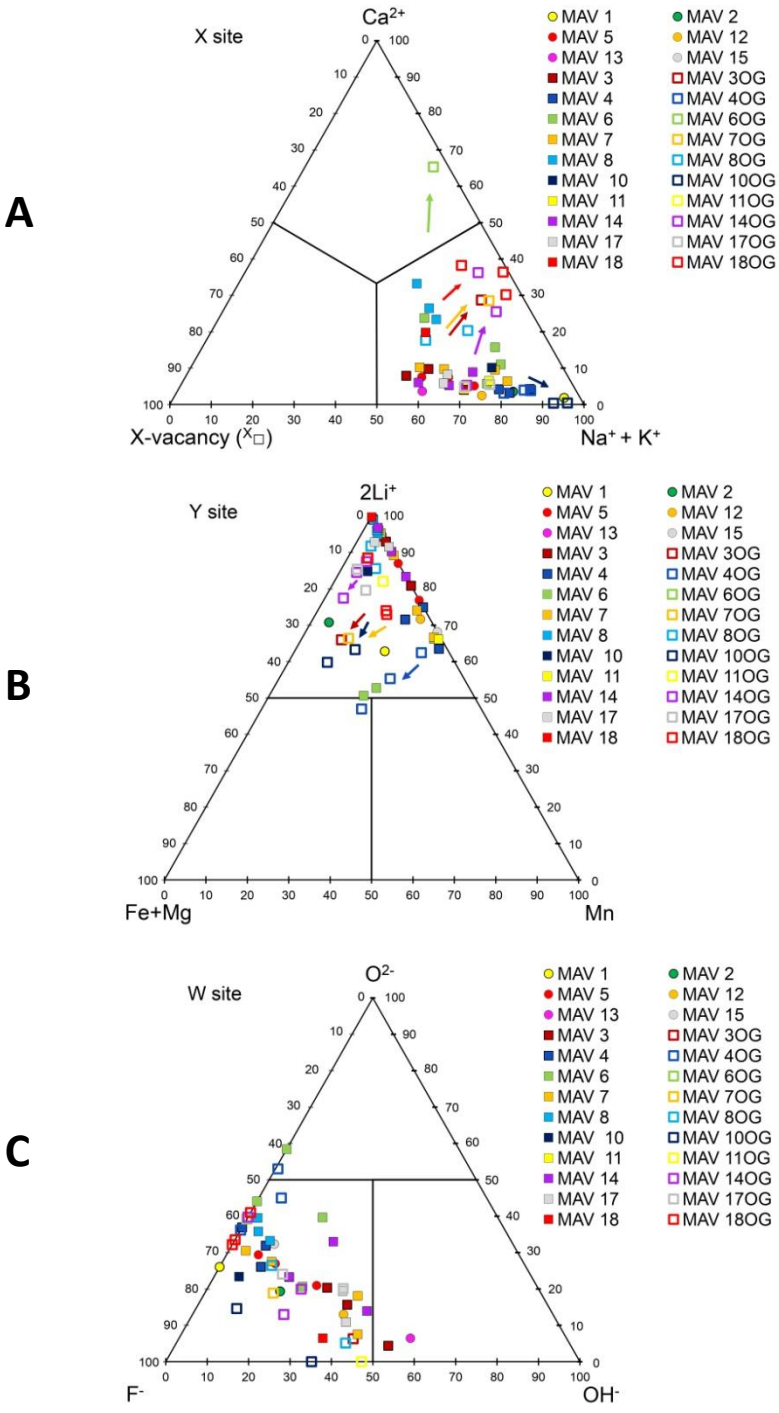

Figure 4.24. Compositional diagrams determined by EMPA. Each point represents the result in apfu of the core and overgrowth zones analyzed. (A) X-site occupancy; (B) Y-site occupancy; (C) W-site occupancy. Arrows highlight the compositional evolution trend from the core zone to the overgrowth.

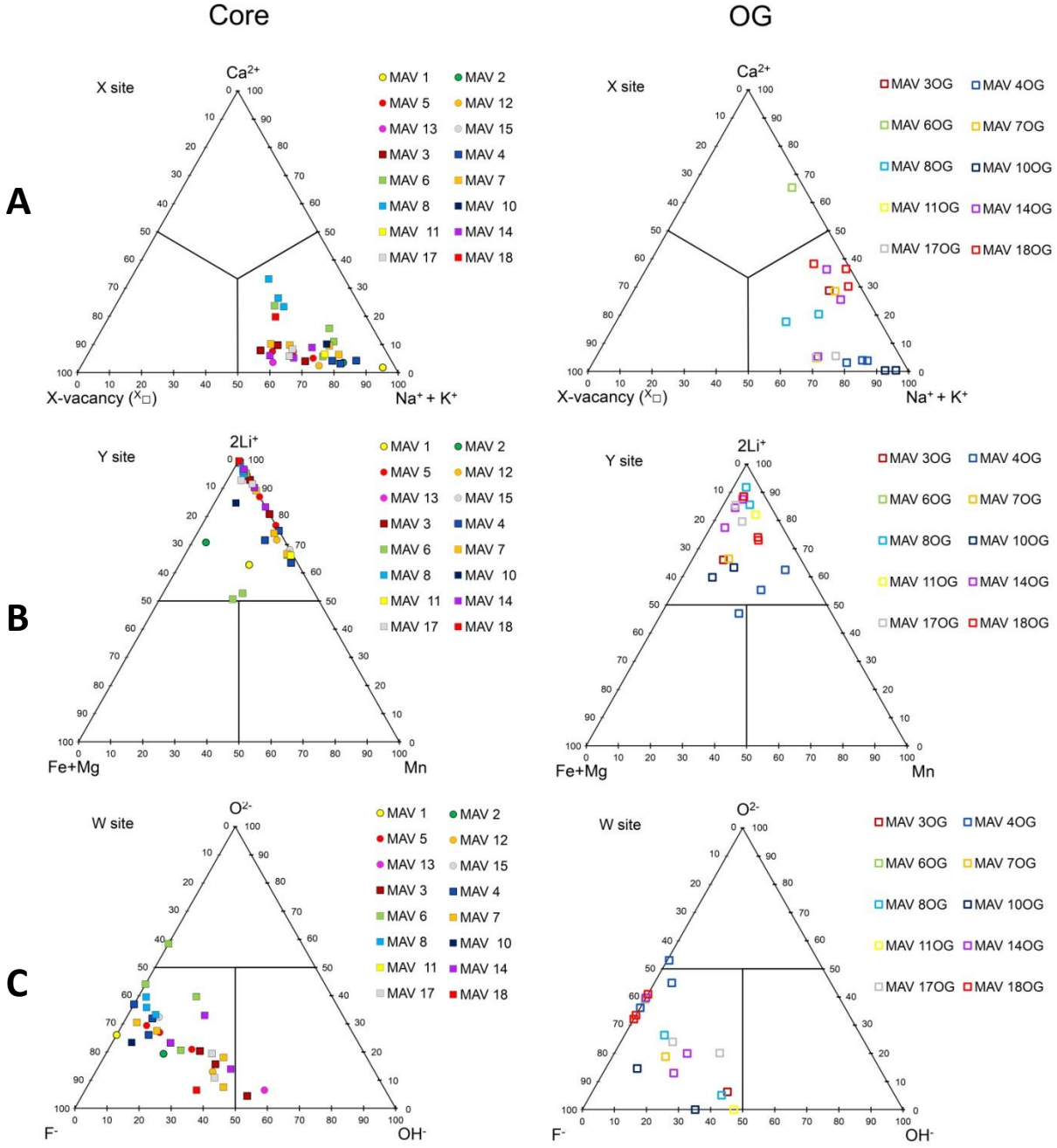

Figure 4.25. Compositional diagrams determined by EMPA. Each point represents the result in apfu of the core (left) and overgrowth (right) zones analyzed. (A) X-site occupancy; (B) Y-site occupancy; (C) W-site occupancy.

Comparison of the overgrowths in the Mavuco tourmaline grains

Chemical analyses conducted on tourmaline samples with a dark prismatic overgrowth, revealed that such overgrowths are generally characterized by an enrichment in FeO and MnO, which are responsible for the dark coloration. When

the content of FeO and MnO is limited, the overgrowths display a brownish-to-greenish coloration. In most overgrowths, Ti is present and could contribute as color-causing agent through Fe^{2+}-Ti^{4+} and Mn^{2+}-Ti^{4+} IVCT (Intervalence charge transfer) interactions.

The FeO and MnO content within the dark-colored overgrowths is always below 6 wt% and thus not sufficient to determine a chemical evolution of the crystals. In fact, as stated above, the whole tourmaline grains analyzed, from core-to-rim, remain in the elbaite–fluor-elbaite, $Na(Al_{1.5}Li_{1.5})Al_6(Si_6O_{18})(BO_3)_3(OH)_3(OH,F)$, compositional field, except for the MAV 4 sample in which the overgrowth corresponds to oxy-schorl. The evolutionary trend related to an enrichment in Fe at the *Y*-site, can be also observed in the ternary plot (Fig. 4.24B,C and 4.25B,C).

A comparison of all the analyzed overgrowths reveals that they do not have the same compositional characteristics. In fact, it is possible to distinguish samples in which the overgrowth is characterized by FeO content higher, similar or lower than MnO (Fig. 4.26).

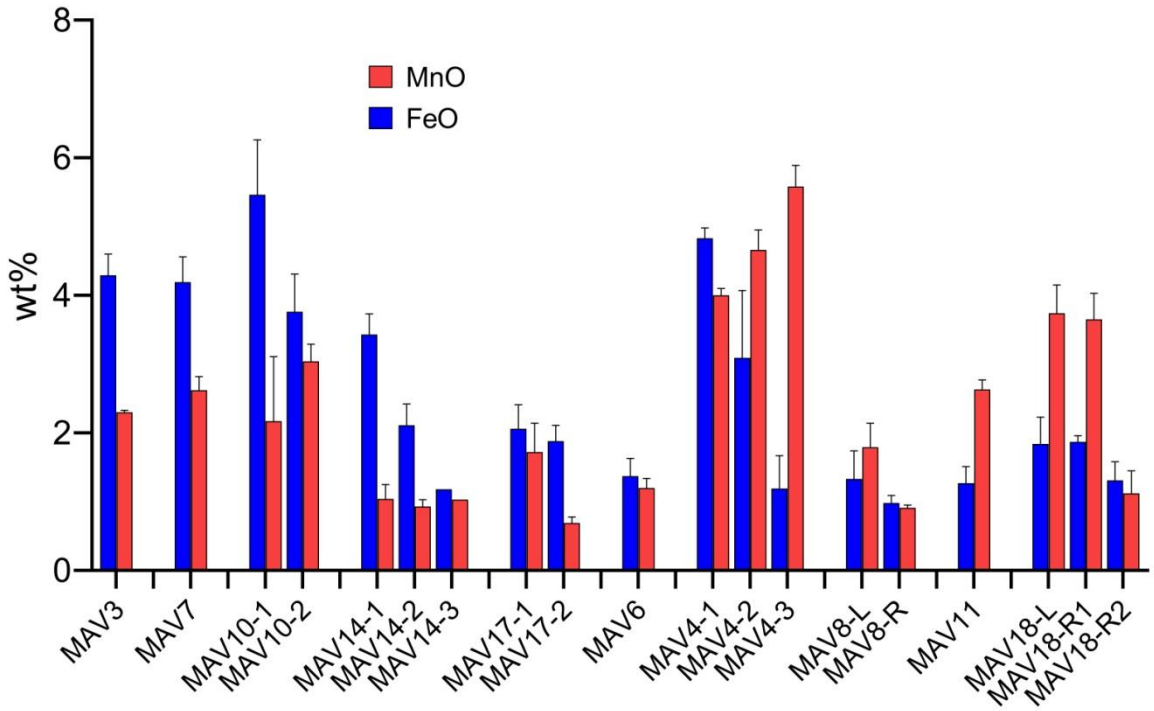

Figure 4.26. Graphical representation of the distribution of Fe and Mn content in the overgrowths of the studied tourmaline grains.

In MAV 3, MAV 7, MAV 10 and MAV 14 samples, the FeO content is significantly

higher (almost double) than MnO. In particular, in MAV 10 and MAV 14 samples, where the overgrowth was further subdivided, an increase in FeO content from the core to rim can be observed. The overgrowth of MAV 4, MAV 6 and MAV 17 samples are instead characterized by a slightly higher FeO content respect to MnO. However, in MAV 4 sample it can be observed not only a significant increase in the FeO content towards the rim, as observed for MAV 10 and MAV 14 samples, but also a concomitant decrease in MnO, which amount becomes much lower than FeO in the outermost part of the overgrowth. Differently, the overgrowths of MAV 8, MAV 11 and MAV 18 samples are characterized by a higher content in MnO respect to FeO (Fig. 4.26).

The differential distribution of Fe and Mn in the analyzed overgrowths is surely related to the different availability of these elements in the crystallizing environment during the overgrowth formation within the miarolitic cavity.

A further comparison of CaO and Na_2O in the analyzed overgrowths shows some significant differences (Fig. 4.27). Some overgrowths (MAV 6, MAV 3, MAV 7, MAV 14 and MAV 18) are characterized by a higher content in Ca (CaO ~2 wt%, with a value of ~4 wt% in MAV 6). The same increase in Ca at the *X*-site can be also observed in the ternay plot (Fig. 4.24A and 4.25A), and in the case of MAV 6 sample the overgrowth can be classified as fluor-liddicoatite. On the contrary, the overgrowths in MAV 4, MAV 11 and MAV 17 samples show very low content (CaO < 0.5 wt%). Calcium is undetectable in the overgrowth of sample MAV 10, which instead contains the highest content in NaO compared to the other overgrowths (NaO ~3 wt%). As stated above, differences in the content of CaO in the overgrowths could be related to the availability of Ca during the latest-stages of tourmaline crystallization.

There is no correlation between the Fe and Ca content in the analyzed overgrowths. In fact, while MAV 3, MAV 7 and MAV 14 samples are characterized by a high content in both Ca and Fe, the overgrowth of MAV 18 sample shows an enrichment in Ca and Mn. In addition, the overgrowth of MAV 6 sample, which can be distinguished for the highest content in CaO, shows a discrete level of MnO

and FeO (about 1.2-1.4 wt%). On the other hand, the overgrowths of MAV 4 and MAV 10 are characterized by high content in Fe and Mn, but a very low CaO level. (Fig. 4.26 and 4.27).

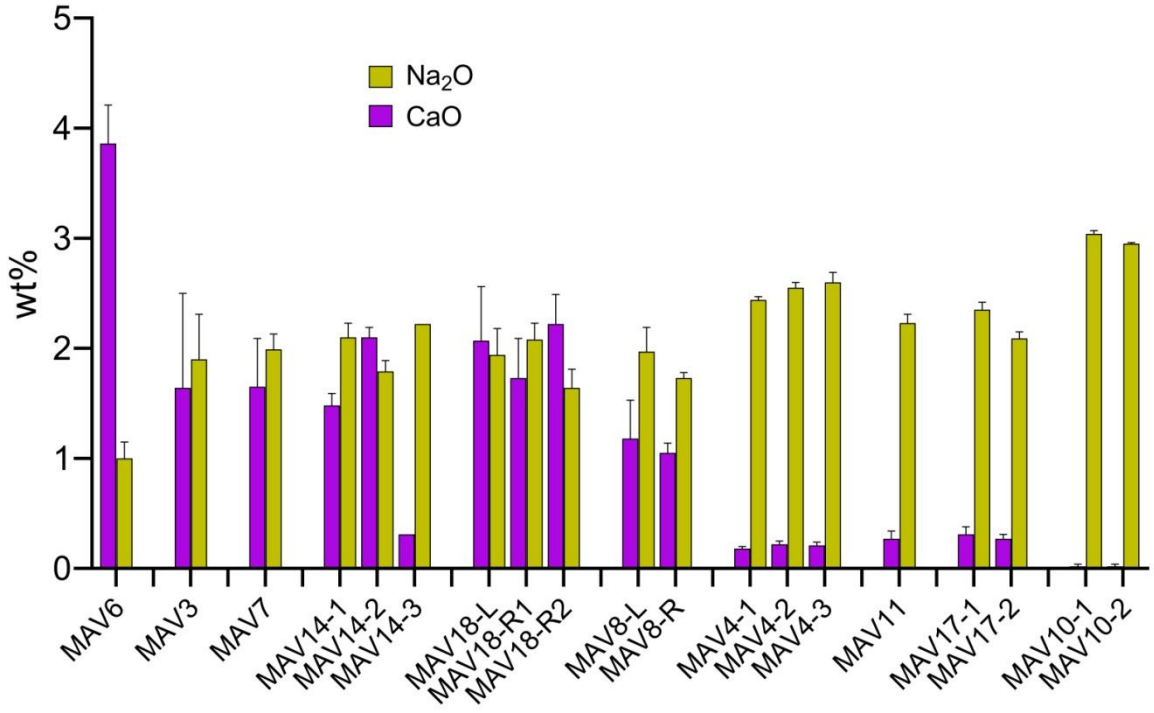

Figure 4.27. Graphical representation of the distribution of Ca and Na content in the overgrowths of the studied tourmaline grains.

Regarding the MgO content in the analyzed overgrowths, a substantial heterogeneity can be observed (Fig. 4.28). There are samples characterized by a discrete content in MgO, such as MAV 3 and MAV 10 (MgO ~ 1 wt%), and samples where MgO is present in traces (MAV 4 and MAV 8). Again, there is no correlation between MgO and FeO/MnO content. In fact, although both the overgrowths enriched in MgO (MAV 3 and MAV 10) show also high level of Fe (FeO > 4 wt%), this is not true for the overgrowths where MgO is present in trace (MAV 4, MAV 8 and MAV 11), which are characterized by higher levels of FeO and MnO (> 4 wt% for MAV 4, and > 1 wt% for MAV 8 and MAV 11) (Figures 4.26 and 4.28).

All overgrowths are characterized by a detectable amount of Cu (CuO > 0.03 wt%). In some of the overgrowths, CuO level rises significantly up to 0.2 wt%, although the enrichment is differently distributed within the same overgrowth. In fact, there

are samples in which the enrichment regards the outermost part of the overgrowth (MAV 8 and MAV 17), and others where is the inner part of the overgrowth to be enriched in CuO (MAV 4 and MAV 14) (Fig. 4.29).

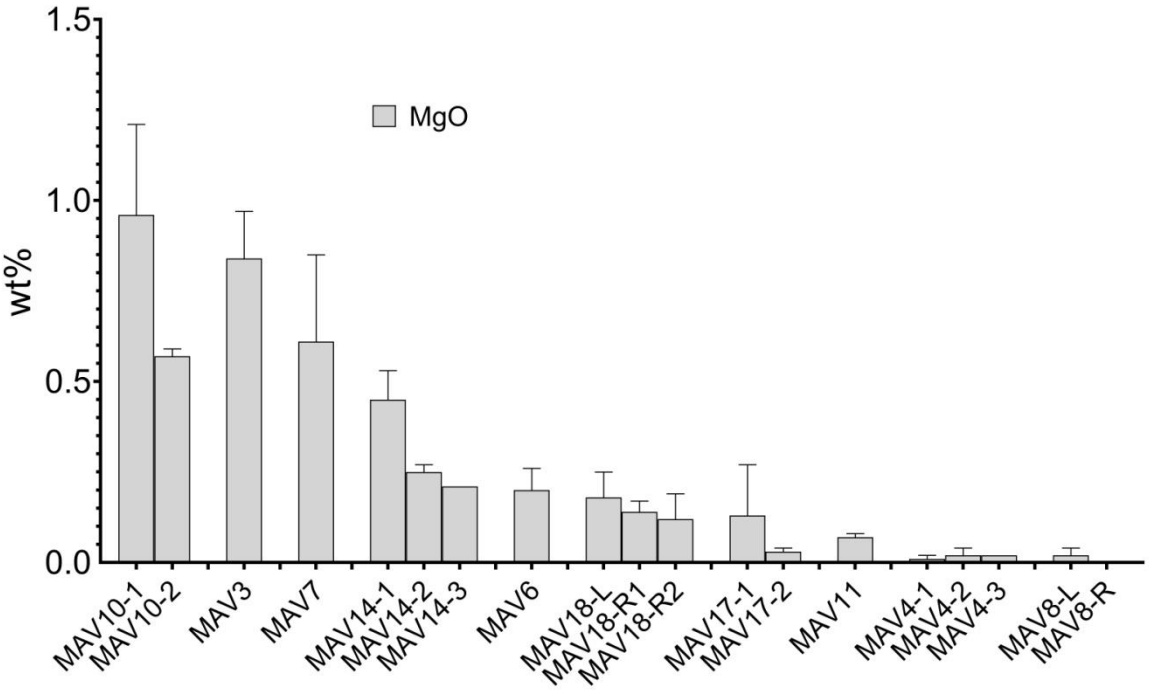

Figure 4.28. Graphical representation of the distribution of Mg content in the overgrowths of the studied tourmaline grains.

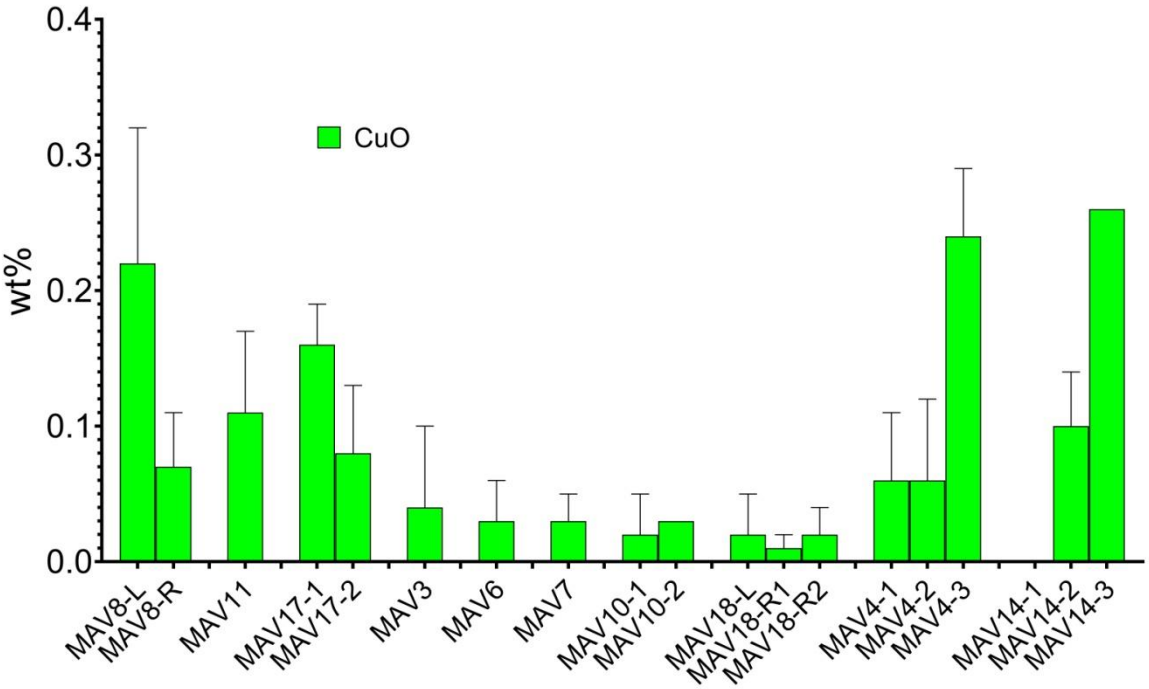

Figure 4.29. Graphical representation of the distribution of Cu content in the overgrowths of the studied tourmaline grains.

Overall, the observed dark-colored overgrowths are the result of a sudden chemical-physical change occurred within the crystallization environment during the latest-stages of tourmaline growth. Probably, similar phenomena as those previously described for Elba tourmalines occurred during the crystallization of tourmalines from which the detrital samples were originated.

In this regard, it can be assumed that the miarolitic cavities hosting the original tourmaline crystals underwent to more-or-less extensive fracturing phenomena, which involved the enclosing pegmatite, allowing the cavity fluids to infiltrate and cause leaching and corrosion of the early-crystallized Fe/Mg- and/or Mn-rich minerals in the pegmatitic rock surrounding the cavities. The typical accessory minerals, hosting those elements, in the Alto Ligonha pegmatitic system are biotite, ferromagnesian amphiboles and Mn-bearing apatite. Concerning the Ca availability, this can be supplied by the chemical alteration of apatite in proximity of some cavities. The mineral responsible for F enrichment in the tourmaline samples analyzed can be fluorite, which is quite abundant in the Alto Ligonha pegmatite district. In fact, most of the tourmaline samples analyzed are fluor-dominant species.

Comparison of the core zone in the Mavuco tourmaline grains

An overall comparison of the analyzed tourmaline samples reveals that the core zones are characterized by a marked heterogeneity in MnO content, ranging from ca. 0.5 wt% to 7 wt% (Fig. 4.30).

Samples with the higher MnO content (4 wt% − 7 wt%) are MAV 1, MAV 3, MAV 4, MAV 5, MAV 6, MAV 7, MAV 11, MAV 12, MAV 14 and MAV 15. The core zones of MAV 2, MAV 8 and MAV 13 samples are instead characterized by a low MnO content (< 1 wt%).

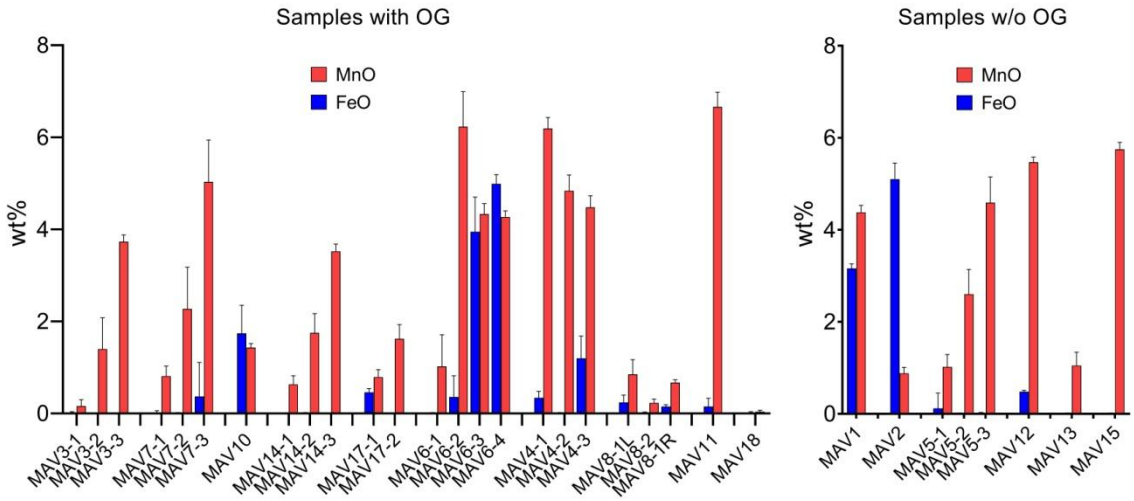

Figure 4.30. Graphical representation of the distribution of Fe and Mn content in the core zone of the studied tourmaline grains (with or without a dark overgrowth).

MnO is present in trace in the core zone of MAV 18 sample. Considering Fe, all observed core zones, show a low (< 1.0 wt%) or trace content in FeO, with the exception of MAV 1, MAV 2 and MAV 6 samples where FeO reaches values of ~3 wt% (MAV 1), and ~ 5 wt% (MAV 2 and MAV 6). These samples can be also distinguished by the MnO content, very high in MAV 1 and MAV 6 (> 4 wt%) and low in MAV 2 sample (< 1 wt%). While MAV 6 is characterized by the presence of a dark-colored overgrowth, MAV 1 and MAV 2 were collected as only core fragments.

A comparison of CaO and NaO content in the core zone of the analyzed samples, confirm the heterogeneous behavior observed for MnO, with samples characterized by an high content in CaO (MAV 8, MAV 6 and MAV 18), with a value ranging from 1 to 2 wt%, and samples depleted in CaO (MAV 1, MAV 2; MAV 4, MAV 12, MAV 13, MAV 15) (Fig. 4.31).

All core zones show a very low content in MgO (< 0.05 wt%), with the exception of the inner core of MAV 10, where MgO reaches the value of ~0.05 wt% (Fig. 4.32).

Several core zones show an enrichment in CuO with value close or above 0.4 wt% (MAV 4, MAV 5, MAV 8, MAV 10, MAV 14), a content much higher than that generally observed in the overgrowths. Other core zones are instead characterized by a very low content in CuO (MAV 1 and MAV 2) (Fig. 4.33).

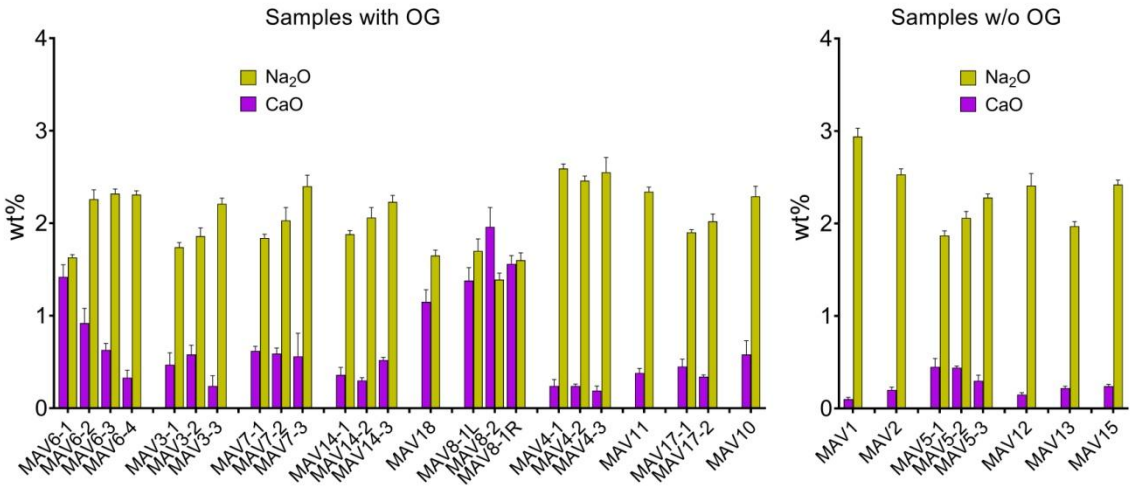

Figure 4.31. Graphical representation of the distribution of Ca and Na content in the core zone of the studied tourmaline grains (with or without a dark overgrowth).

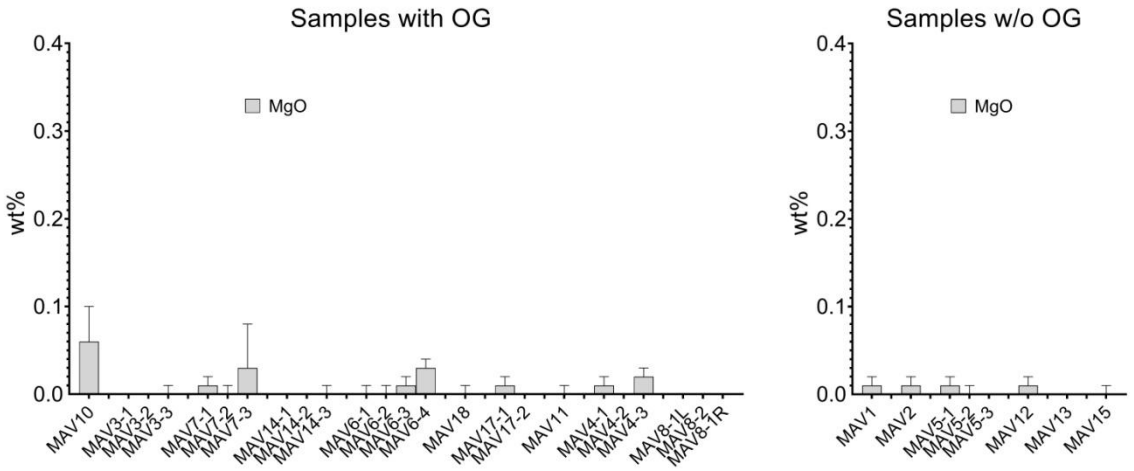

Figure 4.32. Graphical representation of the distribution of Mg content in the core zone of the studied tourmaline grains (with or without a dark overgrowth).

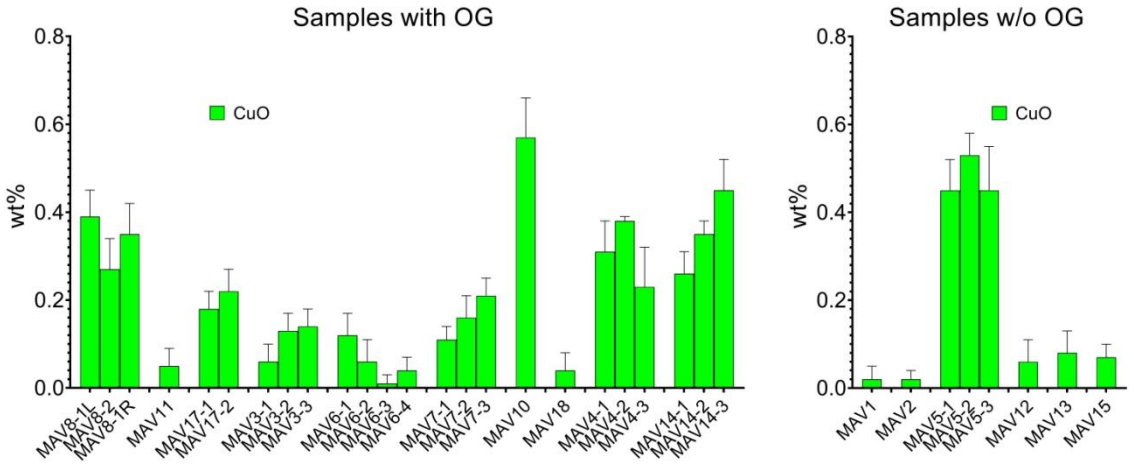

Figure 4.33. Graphical representation of the distribution of Cu content in the core zone of the studied tourmaline grains (with or without a dark overgrowth).

All these data confirm the huge compositional heterogeneity that characterizes the core zone of the tourmaline grains analyzed. For those samples consisting of only a core zone, the observed compositional heterogeneity can be explained assuming they derive from distinct tourmaline crystals grown in different chemical environments. Alternatively, they could originate from the same tourmaline crystal that has undergone to a high degree of chemical evolution during its growth, as result of significant changes in the crystallization environment likely in wide miarolitic cavities. Although the compositional heterogeneity, the mineralogical species remain elbaite/F-elbaite as confirmed by the ternary plots of X-, Y- and W-site occupancy (Fig. 4.24 and 4.25).

Considering only those samples characterized by the presence of a dark-colored overgrowth, the core zone of half of them (MAV 3, MAV 4, MAV 6, MAV 7, MAV, 11 and MAV 14) shows an high Mn content, always greater than 3 wt% with values up to 6 wt% (Fig. 4.28 left panel). This confirms the abundant availability of Mn during the growth of the tourmaline crystals from which they originated. Almost all the core zones of samples characterized by the presence of a dark-colored overgrowth (with the exception of MAV 10 and MAV 18) show compositional and/or chromatic variations. In these core zones, Mn content follows different trends. In some samples (MAV 3, MAV 6, MAV 7 and MAV 14), the level of MnO is higher in the inner part of the core and decreases in the direction of the overgrowth (MAV 3, MAV 6, MAV 7 and MAV 14). An opposite behavior can be observed in MAV 4 and MAV 8 samples, in which the MnO content increases from the inner core towards the overgrowth (Fig. 4.30 left panel). Additionally, all the core zone relative to samples featuring a dark-colored overgrowth, are characterized by a limited amount of Fe (FeO < 0.5 wt%), with the exception of MAV 4, MAV 6 and MAV 10 samples, where FeO amount reaches values ranging from 1-2 wt% (MAV 4 and MAV 10) to ~5 wt% (MAV 6). However, in MAV 4 and MAV 6, the level in FeO quite decreases towards the overgrowth (Fig. 4.30 left panel). The samples characterized by the absence of a dark-colored overgrowth (only core fragments) show a lower content in CaO, always below 0.5

wt%, MgO and CuO compared to the samples with the overgroth (with the exception of MAV 5) (Figures 4.31 – 4.33).

Chemical evolution from core to overgrowth in the Mavuco tourmaline grains

A general comparison of the compositional data obtained on the tourmaline samples from the secondary deposit of Mavuco characterized by a dark-colored overgrowth, confirms that such overgrowths are mainly the result of a sudden increase in Fe during the latest-stages of tourmaline crystallization (Fig. 4.34). In fact, all the overgrowths are characterized by the presence of FeO, which content is always greater that 1 wt%, and in some samples, reaches (MAV 4, MAV 6 and MAV 17) or exceeds (MAV 3, MAV 7, MAV 10 and MAV 14) MnO content. The content in FeO in the dark-colored overgrowth is always greater than that revealed in the core zone of the corresponding sample with the exception of MAV 6 sample. Despite the sharp increase in Fe, none of the samples show a chemical evolution at the dark-colored overgrowth, except for MAV 4, in which the overgrowth is classifiable as oxy-schorl.

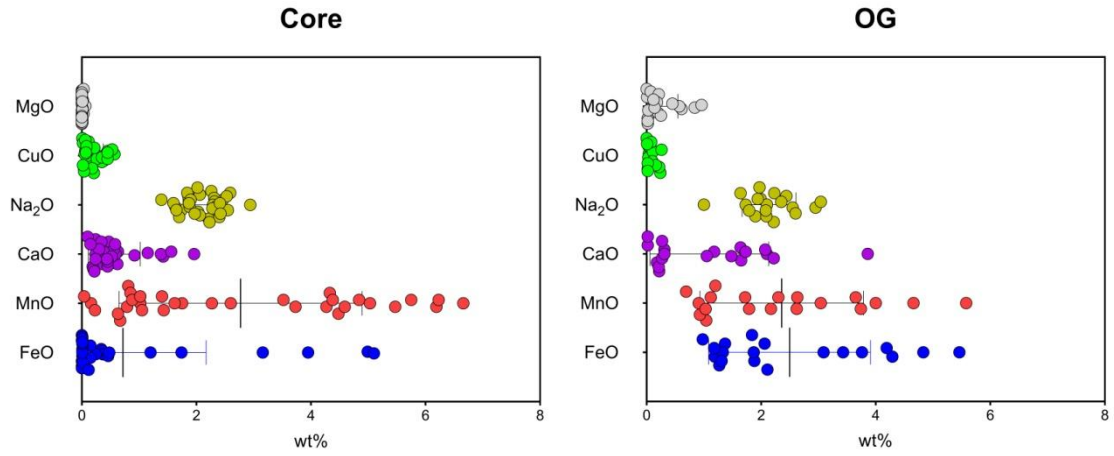

Figure 4.34. Compositional variations in the tourmaline grains from the secondary deposit of Mavuco (Alto Ligonha pegmatite district, Mozambique). The representative abundances of FeO, MnO, CaO, Na_2O, CuO and MgO (wt%) are reported for the core regions and the dark colored overgrowths. Plotted points represent the chemically homogeneous zones (52) in which each sample was divided (see Tables 4.1-4.16).

The evolutionary trend is also observable in the ternary plots of X-, Y- and W-site occupancy (Fig. 4.24). Concerning the X-site ternary plot, MAV 6 is characterized

by an overgrowth enriched in Ca, leading to a fluor-liddicoatite composition. Other evolutive trends, without chemical evolution, can be observed for MAV 3, MAV 7, MAV 10, MAV 14 and MAV 18, which composition shift to a more Na-dominant compostion (Fig. 4.24A). Regarding the Y-site ternary plot, as stated above, most of the samples show an evolutive trend from core-to-rim with an enrichment in Fe/Mg, and the only sample in which a chemical evolution occurs is MAV 4 (Fig. 4.24B,C).

The early crystallization of Fe-rich minerals during the initial steps of tourmaline growth, is considered the most likely mechanism for depleting Fe from the pegmatitic melt (Dutrow and Henry 2016, 2018; Bosi et al., 2022a; Altieri et al., 2022). However, in some samples (MAV 4, MAV 6 and MAV 10) the inner core zone is characterized by an enrichment in Fe (FeO up to 5 wt%). This is related to the amount of Fe remaining available in the pegmatitic system after the early crystallization of Fe-rich minerals, such as biotite and/or Fe-rich amphiboles, which are typical accessory minerals of the pegmatitic rock in the Alto Ligonha district. In fact, the inner core zone of MAV 4, MAV 6 and MAV 10 samples may represent the primitive part of the crystal. The subsequent progressive decrease in FeO content towards the dark-colored overgrowth, reaching an undetectable level in the outermost part of the core zone of MAV 6, is the result of Fe depletion in the system due to tourmaline crystallization.

During the late-stage of tourmaline crystallization, a sudden increase in Fe, responsible for the dark-colored overgrowths, is observable in all analyzed samples. To explain the new Fe availability in the crystallization environment, a partial opening of the geochemical system can be argued. This scenario can be similar to that observed in Elba tourmaline crystals, which are frequently characterized by a Fe-rich dark-colored overgrowth (Bosi et al., 2022a; Altieri et al., 2022, 2023). However, in Elba tourmalines the overgrowth formation is limited to the crystal termination, typically at the analogous pole, originating the so-called "Moor's head" textural types (Pezzotta, 2021). As it was argued for Elba Island petrogenetic system, a pocket rupture event, probably related to a rigid

mechanical schok to which the cavity underwent, caused, for istance, by a thermal contraction during the pegmatite cooling, led to mechanical brittle deformations of the enclosing pegmatite through the formation of late-stage fractures. In this scenario, the highly reactive late-stage cavity fluids were allowed to permeate the fractures in the pegmatitic rock surrounding the cavity, where the early-crystallized cavity-lining Fe-rich minerals (i.e., biotite and/or Fe-rich amphiboles) were formed. Leaching and corrosion processes ascribed to the late-stage cavity-fluids, led to the hydrothermal alteration of such minerals with the consequent release of Fe in the system, causing a sudden change in the chemical composition of the pocket environment. The increased availability of Fe in the residual cavity-fluids would lead to the formation of the observed dark-colored overgrowths in the tourmaline crystal from which the grains of the secondary deposit of Mavuco originated. It is important to point out that the tourmaline crystals from which the grains of the Mavuco area originated were characterized by overgrowths extending to the prismatic faces. Such extensive overgrowths are surely the result of a large availability of early-crystallized Fe/Mn-rich minerals, which underwent to hydrothermal alteration during the latest-stages of tourmaline crystallization. Additionally, a wide size of the miarolitic cavities in which the original tourmaline crystals grew, combined with an extensive fracturing of the cavities, may have played a key role in the formation of the prismatic overgrowths. In fact, a broad fracturing surface may allow more extensive alteration and corrosion phenomena of the early-crystallized cavity-lining and cavity-coating Fe/Mn-rich minerals in the enclosing pegmatite, thus leading to persistent leaching processes by the highly reactive late-stage cavity fluids. All these conditions, associated with a long lasting late-stage tourmaline crystallization ensured by B, which must be still present in the residual fluids of the cavity, allowed for the development of the dark-colored overgrowths not only at the crystal termination, but also along the prismatic faces. This hypothesis is supported by a tourmaline crystal from the "Marina" pegmatite (MAV 22, see below), which is characterized by a thick black Fe-rich overgrowth covering all over the tourmaline surfaces, including the prism

faces and the steep pyramidal faces at the antilogous pole.

A particular case is represented by the MAV 18 sample, which is characterized by a very limited amount of Fe and Mn in the core zone and a sharp increase in these elements at the overgrowth, with Mn content exceeding that of Fe. Such Mn enrichment can be likely ascribed to the leaching and corrosion of Mn-rich cavity-lining minerals during the latest-stages of tourmaline crystallization. The strong enrichment in Mn observed in this overgrowth, can be the result of the corrosion and alteration of highly-competitive minerals for this element, such as spessartine garnet (Hernández-Filiberto et al., 2021). Spessartine crystallization is recognized as an important mechanism for regulating the Mn content during the evolution of the pegmatite systems (Novak et al., 2000; Laurs et al., 2007; Bosi et al., 2022a). The high partitioning of Mn into garnet (Haralampiev and Grover, 1993), allows spessartine to store most of the Mn present in the pegmatitic melt when it crystallizes in the early-stage of cavity evolution, thus preventing the Mn enrichment in primary tourmaline within pegmatite pockets. This could explain the absence of Mn in the core zone of MAV 18 sample. Spessartine garnet, although in limited quantities, occurs in the *kamada* layer of the secondary deposit of Mavuco. Consequently, it is reasonable to assume that the absence of Mn in the core zone of MAV 18 and its subsequent increase observed at the overgrowth, is due to early-formed spessartine garnet. All these events may allow the formation of the observed Mn-rich overgrowth in MAV 18 sample. In the same sample, a similar scenario can be assumed for Fe, which was sequestered by the primitive Fe-rich minerals during the initial steps of tourmaline crystallization, and then released right after the pocket rupture, which involved the pegmatitic rock surrounding the cavity.

In general, Mn content shows a wide range of concentrations in the analyzed tourmaline samples, with values between traces and 6 wt%. The variation in the Mn content observed both within the same sample and among the analyzed samples, is most likely the result of a different availability of this element in the geochemical system.

In those samples where the core is richer in Mn than the overgrowth (MAV 6, MAV 7, MAV 3 and MAV 14), it is reasonable to assume that this element was present in the pegmatitic melt, and thus geochemically available during pegmatite crystallization. The Mn incorporation in the early-stages of tourmaline crystallization can occur when no highly-competitive mineral for Mn were crystallizing, such as spessartine garnet. Apatite is instead a fairly-competitive mineral for Mn. The presence of abundant apatite crystals in the *kamada* layer of the secondary deposit of Mavuco strongly suggests this mineral as supply of Mn during the late-stage of tourmaline crystallization as a consequence of leaching processes. The co-crystallization of apatite and tourmaline in the early-stages of cavity evolution, can explain the observed Mn enrichment in the core zone of some tourmaline grains analyzed. As apatite has low affinity for Mn, its subsequent chemical alteration results in a lower release of Mn in the system. This may be responsible for the lower content in Mn recorded by tourmalines at the overgrowth compared to the core region.

Overall, the Mn content in the tourmaline crystals, either in the core part or the overgrowth, are directly dependent on the fractionation of Mn in the pegmatitc melt and the crystallization of highly- to fairly-competitive minerals for Mn, such as spessartine garnet and Mn-bearing apatite, respectively. The observed higher enrichment in Mn at the dark-colored overgrowth compared to the core zone in specific tourmaline grains, suggests the role of spessartine as main regulator of the Mn levels during tourmaline crystallization, as previously reported for the petrogenetic system of Elba Island.

As a final remark, the comparison of the abundances of selected elements (Fe, Mn, Ca, Cu and Mg), which occur in both the overgrowths and the core zones of the analyzed tourmaline grains, confirms a sudden increase in Fe level in the overgrowth of all samples. In few cases, the overgrowths are characterized by an enrichement in Ca and Mg content (Fig. 4.34). This is particularly evident for the MAV 6 (Ca) and the MAV 10 (Mg). The availability in the system of Ca can be ascribed to the chemical alteration of apatite, a Ca-rich mineral commonly present

in the amphibolitic host rock of the Alto Ligonha pegmatitic disctrict. Magnesium can be instead released by alteration of Mg-rich biotite and/or Mg-rich amphiboles.

Concerning Cu, the core zones are generally characterized by a higher content of this element compared to the overgrowths, and no samples show a Cu content in the overgrowth higher than the corresponding core zone. This behavior strongly suggests that this element was already available in the pegmatitic melt during the early-stages of the tourmalines crystallization. Little information is available for Cu source in the "Marina" pegmatite that was supposed to be the primary deposit from which the Mavuco detrital tourmalines were originated (Federico Pezzotta personal communication). However, it can be assumed that the "Marina" pegmatite derived from the melting of a Cu-bearing granite.

4.4.2 Identification of the gemological varieties characterizing the core zone of the Mavuco tourmaline grains

From a gemological view point, the core of the analyzed tourmaline grains belongs to different varieties according to the color displayed and the relative chemical composition.

The identified gemological varieties are:

- *Indicolite*, with a light to deep blue coloration. This variety is better represented in MAV 1 and MAV 2 samples. The blue color is mainly caused by a significant amount of Fe (FeO ranging from ~ 3 wt% to ~ 5 wt%). CuO content is very low (< 0.05 wt%).
- *Canary tourmaline*, with a yellow, ochre to yellow-green color. The core zone of MAV 11 and MAV 12 samples better represent this variety. Chemically, the content in Mn is quite high (5-7 wt%), which associated with Ti, gives rise to the yellowish coloration (Rossman and Mattson, 1986). At the same time, Fe content is very low (< 0.5 wt%). The presence of Cu (0.1–0.2 wt%) can modify the color displayed towards a green hue (as observable in the C3 and C4 zones of MAV 4 and MAV 7 samples, respectively).

- *Paraiba-type*, with a bright blue to blue-green color. The core zones of the samples in which this variety is clearly evident, are MAV 5 and MAV 14. These crystal zones are characterized by the absence of Fe (below detection limit) and a quite amount of Cu (0.4–0.6 wt%), the latter responsible for the typical blue "neon" color resembling the Brazilian Paraiba variety.
- *"Cu-bearing rubellite"*, with a pink-reddish color, as result of the presence of Mn and the relative absence or very low amount of Fe. Differently from the typical rubellite, this variety is characterized by the presence of Cu, which modify the color displayed towards a purplish hue. This variety is better evident in MAV 13, containing MnO ~1 wt%, undetectable amount of FeO and 0.1 wt% of CuO.

4.4.3 OAS analysis and determination of the cause of color

To provide additional information on the mechanisms underlying the color displayed by the core regions of the tourmaline grains from the secondary deposit of Mavuco, optical absorption spectroscopy analyses in the UV-Vis region were performed on selected samples with particular chromatic features. Among these samples, one is MAV 6, which is characterized by a marked polychromism ranging from dark-green, pink-red, blue-green, ochre to black. Additionally, the MAV 5 and MAV 10 samples, which show a similar blue coloration but a different Cu/Fe -ratio, were analyzed.

The optical absorption spectra of MAV 6 and MAV 10 samples were measured in **E⊥c-**polarization mode as the samples represent a crystal section cut mostly perpendicular to the **c**-axis (by the presence of a dark-colored prismatic overgrowth). Because MAV 5 sample represents a fragment of a tourmaline core region without any clear orientation, the spectra were recorded both in **E⊥c** and **E||c** polarization mode.

Colors in tourmaline are essentially related to transitions elements (Ti, V, Cr, Fe, Mn and Cu), acting as color-causing agents through several mechanisms at structural levels, with the most common ones being crystal field transitions (CFT),

intervalence charge transfer interactions (IVCT), and color centres (e.g., Fritsch and Rossman,1987; Pezzotta and Laurs, 2011; Rossman, 2014). Because chemical analyses of the MAV 6, MAV 10 and MAV 5 samples revealed contents of V_2O_3, and Cr_2O_3 below the detection limit (≤ 0.03 wt%), the main transition metals that could contribute to the color displayed by these tourmaline crystals are Fe, Mn, Cu and Ti.

Polarized spectra (**E⊥c**) were recorded on selected spots of MAV 6 sample displaying a different coloration (Fig. 4.35). Spectrum of the ochre zone (C2) shows a very strong absorption band in the near UV-region at ~30700 cm^{-1} and a sharp and very weak absorption band at ~27000 cm^{-1}, which can be assigned to Mn^{2+}-Ti^{4+} IVCT and Mn^{2+} spin-forbidden transitions, respectively (Fig. 4.35) (Rossman and Mattson, 1986; da Fonseca-Zang et al., 2008). This assignment is consistent with the enrichment in MnO and TiO_2 observed from chemical data (Table 4.17). On the other hand, the weak and broad absorption bands at ~14000 cm^{-1} and ~11000 cm^{-1} can be attributed to spin-allowed *d-d* transitions in Cu^{2+} (Rossman et al., 1991; Mashkovtsev et al., 2006). This is in accord with the presence of CuO, even in small amount, and a FeO level below detection limit (Table 4.17). Consequently, the yellowish coloration for C2 zone of MAV 6 sample is controlled by Mn, Ti and Cu. For this reason, this zone belongs to the *canary tourmaline* gemological variety (e.g. Laurs et al., 2007).

The spectrum recorded in the blue-green core zone (C1-inner part) reveals only the presence of a very weak broad band at ~14000 cm^{-1} and an intense broad band at ~11000 cm^{-1} in the near-infrared-range, both ascribed to Cu^{2+} spin-allowed *d-d* transitions (Fig. 4.35) (Rossman et al., 1991; Mashkovtsev et al., 2006). EMPA results confirmed the presence of Cu as only color-causing agent for the blue-green coloration of the C1 zone, given the enhanced Cu-contents (Table 4.17). Moreover, the enrichment in Cu in this part of the crystal is double of that in the ochre tourmaline zone. This compares well with the band intensity ratios of the bands in the blue and ochre zones. The low concentration in MnO (1.47 wt%) is likely not enough to contribute to the color displayed by this core zone through

Mn^{2+} spin-forbidden electronic transitions, as Mn^{2+} is a weak absorber (Rossman, 1997). Additionally, the lack of TiO_2, under detection limit, does not allow Mn-Ti interaction and consequently the occurrence of a stronger Mn^{2+}-Ti^{4+} IVCT absorption band. Based on overall results, the blue-green core zone (C1-inner part) can be classified as *Paraiba-type* tourmaline variety (e.g. Laurs et al., 2008).

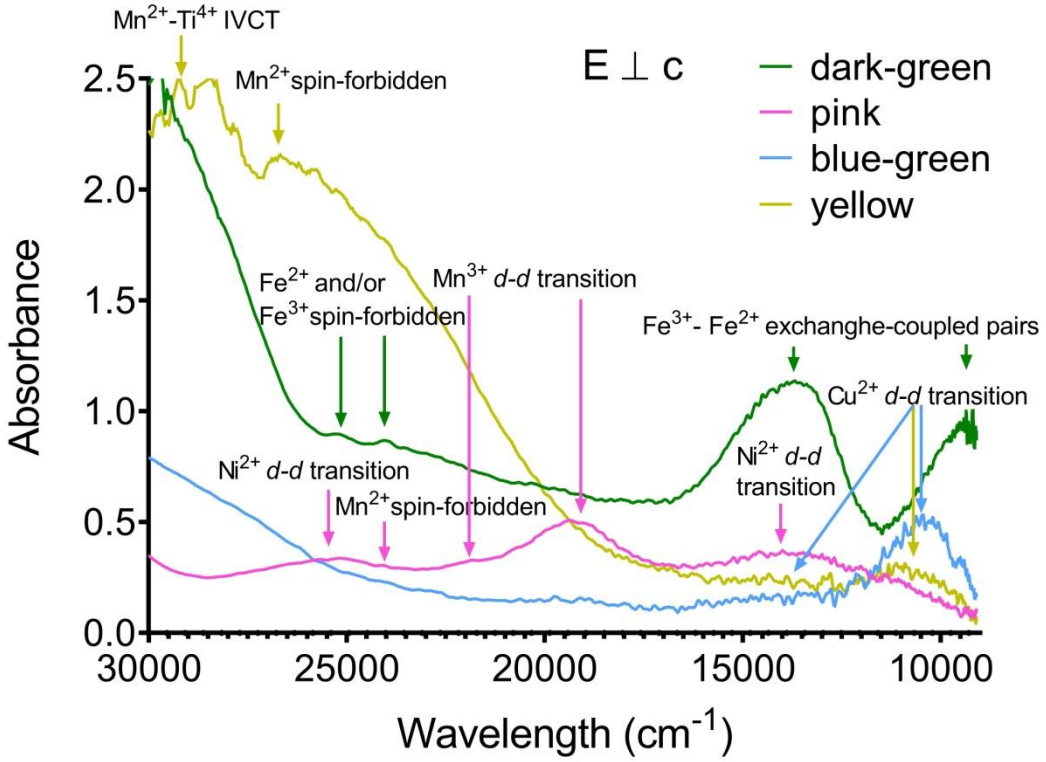

Figure 4.35. OAS spectra polarised perpendicular to the **c**-axis direction (E⊥c) of the different colored regions of the core zone and dark-green overgrowth of the MAV 6 samples. Sample thickness: ochre zone = 832 μm; blue-green zone = 838 μm; pink zone = 843 μm; dark-green zone = 424 μm.

The recorded optical absorption spectrum of the pink core zone (C1-outer part) is characterized by a weak and broad absorption band at ~22000 cm^{-1} and a stronger broad band at ~19000 cm^{-1} (Fig. 4.35). These assignments agree with the pink color displayed by this part of the crystal, which can be ascribed to the presence of Mn^{3+} as color-causing agent. (Reinitz and Rossman, 1988; Taran et al., 1993 ; Ertl et al., 2005; Bosi et al., 2021). Differently, the very weak and sharp absorption band at ~24100 cm^{-1} can be assigned to Mn^{2+} spin-forbidden transitions (Rossman, 1997). The origin of the broad and weak absorption bands at ~25200 cm^{-1} and ~14000 cm^{-1} is less obvious. The very low Fe- and Ti-content recorded by EMPA in this

zone, rules out Fe^{2+}-Ti^{4+} IVCT as well as spin-allowed Fe^{2+} origins of these bands (Table 4.17). Thus, the origin of these two absorption bands is to be found in other transition metals, such as Ni. Although the content of Ni in this sample has not been measured, the intensities data and peak positions of such absorption bands are comparable with those observed by Taran et al. (1993). Consequently, the weak and broad absorption bands at ~25200 cm^{-1} and ~14000 cm^{-1} can be tentatively assigned to spin-allowed Ni^{2+} transitions. On the basis of these results, the pink coloration of the C1 zone of MAV 6 sample is exclusively caused by the presence of Mn in the oxidized state +3. Hence, this zone is classifiable as *rubellite* tourmaline variety (Pezzotta and Laurs, 2011).

The spectrum of dark-green overgrowth displays two broad absorption bands centred at 13800 cm^{-1} and 9200 cm^{-1}, and a weak broad band at 24000 cm^{-1} (Fig. 4.35). The strong polarization of the bands at 13800 cm^{-1} and 9200 cm^{-1} is attributable to the presence of Fe^{3+} in this zone of the MAV 6 sample. Consequently, the these bands can be caused by electronic exchange interactions in an Fe^{2+}-Fe^{3+} pair at adjacent *Y* sites in the tourmaline structure. (Taran and Rossman, 2002). The set of weak and relatively sharp bands between ~25000–24000 cm^{-1} can be instead assigned to spin-forbidden Fe^{2+} and/or Fe^{3+} bands (Mattson and Rossman, 1987). In accord with these assignments, the dark-green coloration of the MAV 6 overgrowth is mainly controlled by Fe^{2+}-Fe^{3+} interactions. Consequently, this overgrowth belongs to the *verdelite* gemological variety (Pezzotta and Laurs, 2006).

OAS data demonstrate the presence of Fe and Mn in the oxidation state +3 in the overgrowth and the outer part of the C1 core zone characterized by a pink coloration. On the contrary, these elements are in the oxidation state +2 in the remaining part of the sample including the inner blackish zone (C3-C4), which likely represents the primitive part of the crystal. This OAS information suggests a change in the oxidation state of the geochemical environment that occurred just before the formation of the dark-green overgrowth. A change in the redox state, associated with the opening of the geochemical system, was already observed in

the petrogenetic system of Elba granitic pegmatites. This change was ascribed to an intense fracturing of the pocket, which propagates to the enclosing pegmatite (see the case study reported in the section 1.4 of this thesis). Therefore, it is possible to hypothesize that during the crystallization of the tourmaline crystal from which the MAV 6 sample derived, a pocket rupture occurred. In this particular case, the modification of the redox state within the cavity occurred before the sudden increase in both Fe and Mn in the dark-green overgrowth, in correspondence of the pink colored outer part of the C1 zone. The oxidizing environment within the cavity was probably promoted by a very limited opening of the pocket, which changed the oxygen fugacity. This occurred before the destabilizing event, which allowed the leaching and corrosion of the early-crystallized Fe/Mn-rich minerals. This oxidation allowed the formation of the pink core zone, characterized by a low Mn content in the redox state +3 (in accord with the presence of Mn^{3+} *d-d* transition absorption bands), compared to the nearby blue-green core zone, with a comparable or greater amount of Mn, but lacking any Mn^{3+} absorption bands in the OAS spectrum. The redox state of Mn is still +2 in the ochre zone (C2), because its OAS spectrum is dominated by Mn^{2+}-Ti^{4+} IVCT and Mn^{2+} spin-forbidden transitions.

Polarized spectra (**E⊥c** and **E||c**) recorded on a selected spot of MAV 5 sample light-blue core region, reveals very weak and broad absorption bands at ~26000 cm^{-1}, ~14000 cm^{-1} and ~11000 cm^{-1} (Fig. 4.36). Based on EMPA results (Table 4.18), the band at ~26000 cm^{-1} can be assigned to Mn^{3+} *d-d* transitions, whereas the absorption bands at ~14000 cm^{-1} and ~11000 cm^{-1} are caused by Cu^{2+} *d-d* transitions. The stronger intensity of this latter band compared to that at ~14000 cm^{-1}, and the total absence of any Fe^{2+} absorption bands in the OAS spectra, confirm that MAV 5 sample belongs to the *Paraiba-type* gemological variety (Mashkovtsev et al., 2006; Krzemnicki and Wang, 2022). The weakness of the absorption bands in the OAS spectra is essentially due to the unclear orientation of the sample, as it represents a fragment of a tourmaline core zone.

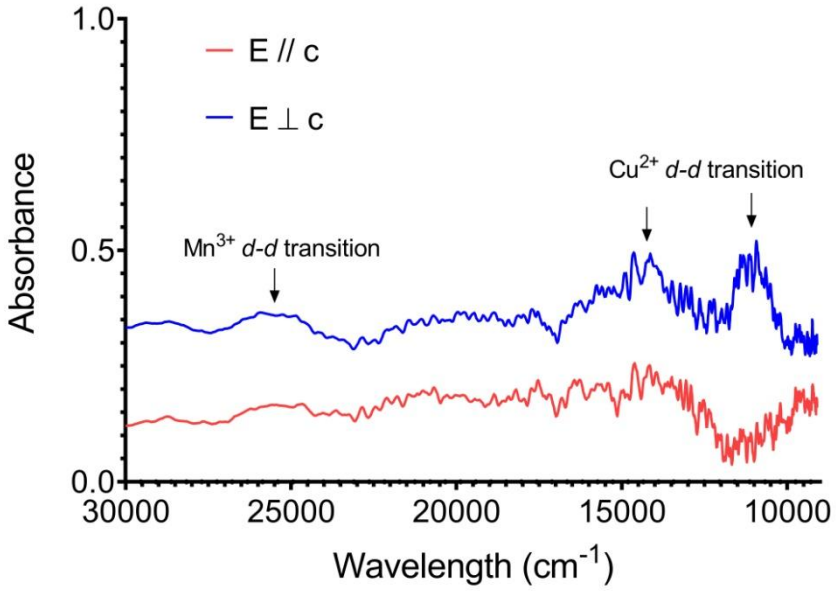

Figure 4.36. OAS spectra polarised perpendicular (E⊥c, blue line) and parallel (E||c, red line) to the **c**-axis direction of the light-blue core region of the MAV 5 sample. Sample thickness: 846 μm.

The **E⊥c**-spectrum of the greenish-blue core zone of the MAV 10 sample is dominated by two broad absorption bands at ~14000 cm^{-1} and ~11000 cm^{-1} in the near-infrared-range (Fig 4.37). The color of a *Paraiba-type* tourmaline, is primarily related to two broad Cu^{2+} absorption bands centred at around 14000 cm^{-1} and 11000 cm^{-1}, with this latter predominant respect to the band at ~14000 cm^{-1}(Mashkovtsev et al., 2006; Krzemnicki and Wang, 2022). Because the spectrum of the light-blue-green color of MAV 10 sample is characterized by absorption bands at ~14000 cm^{-1} and ~11000 cm^{-1} with nearly equal intensity, it can be deduced that its color is due to a combination of Cu and Fe. EMPA data agree with this result, as MAV 10 sample is characterized by the presence of both Cu (CuO ~0.7 wt%) and Fe (FeO ~1.2 wt%), with a Cu/Fe-ratio of 0.33 (Table 4.18). As previously observed for the blue-green zone (C1-inner part) of the MAV 6 sample, the low concentration in MnO (1.42 wt%) in the core region of MAV 10, is not enough to contribute to the color displayed by this core zone through Mn^{2+} spin-forbidden electronic transitions, as Mn^{2+} is a weaker absorber than Fe^{2+} and Cu^{2+} (Rossman, 1997). Although the greenish-blue color resembles that of most of *paraiba-type* tourmalines, its intermediate composition due to the presence of both Cu^{2+} and

Fe^{2+} does not allow to classify this sample neither as *indicolite* nor as *Paraiba-type*, but as Fe-Cu bearing tourmaline.

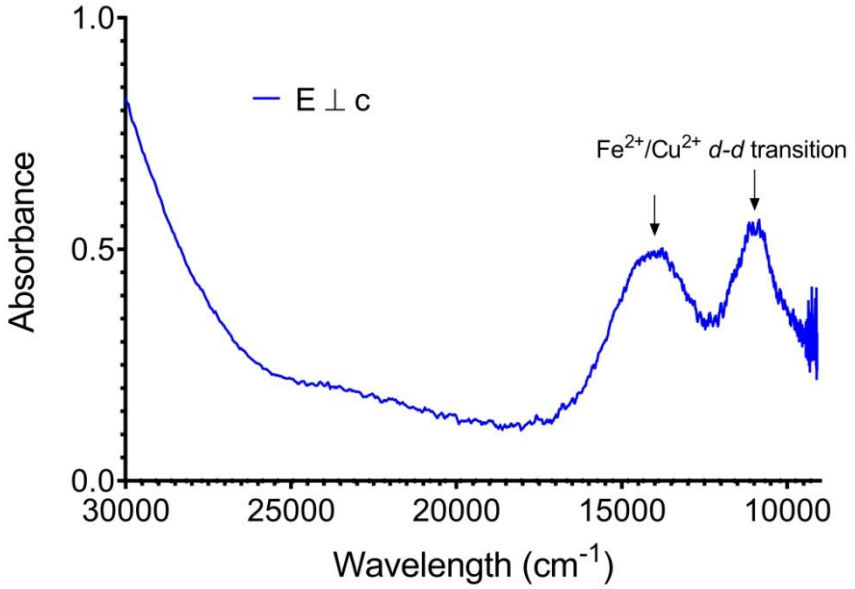

Figure 4.37. OAS spectra polarised perpendicular to the **c**-axis direction (E⊥c) of the greenish-blue core zone of the MAV 10 samples. Sample thickness: 815 μm.

Despite the similarity in the color displayed, the MAV 5 and MAV 10 samples belong to two different gemological varieties. Based on OAS data and chemical composition, the MAV 5 sample can be classified as Cu-dominant (*Paraiba-type)* tourmaline with a CuO concentration of ~0.40 wt% and the total absence of Fe, whereas the MAV 10 sample as Fe-Cu bearing tourmaline, for its intermediate composition between *indicolite* and *Paraiba-type* (FeO ~1.2 wt% and CuO ~0.7 wt%).

Table 4.18. Interpretation of OAS results for selected spots on the colored core zones of MAV 5 and MAV 10 samples (Mavuco, Mozambique), according to the concentrations of the main transition metals.

Samples	Color	FeO (wt%)	MnO (wt%)	TiO_2 (wt%)	CuO (wt%)	Absorption bands	Assignments
MAV 5	light-blue	-	0.45	0.01	0.40	~26000 cm^{-1}	Mn^{3+} *d-d* transitions
						~14000 cm^{-1}	Cu^{2+} *d-d* transitions
						~11000 cm^{-1}	Cu^{2+} *d-d* transitions
MAV 10	greenish-blue	1.23	1.42	-	0.68	~14000 cm^{-1}	Fe^{2+} and Cu^{2+} *d-d* transitions
						~11000 cm^{-1}	Fe^{2+} and Cu^{2+} *d-d* transitions

This is a typical issue in gemology, where the color appearance is the main classification method. However, a more rigorous classification should be made on the basis of chemical composition. In this context, it is very important to obtain

information on the relationships between chemical composition and color displayed. This could help to develop quick and cost-effective analytical methods, mainly based on specific spectroscopic signatures, which will reduce the change of fraudulence in the trading of gemological material.

4.4.4 The MAV 21 sample from the "Marina" pegmatite and the origin of the detrital tourmaline samples from the secondary deposit of Mavuco

The presence of Cu in the tourmaline grains from the secondary deposit of Mavuco, suggested that a primary deposit from which they originated, could have the same geochemical signature.

The recent discovery of the "Marina" granite pegmatite in the Pegmatitic District of the Alto Ligonha, raised the possibility that such detrital tourmalines could be originated from this primary deposit. Moreover, the "Marina" pegmatite is up to now the only primary deposit in the Pegmatitic District of the Alto Ligonha, close to the Mavuco deposit, with an LCT geochemical signature and thus prone to produce tourmalines. To confirm this hypothesis, a tourmaline crystal from the "Marina" pegmatite (MAV 21), was analyzed.

The MAV 21 sample is a multicolored tourmaline crystal of about 3 cm in length, and characterized by a dark-colored overgrowth at the analogous pole (Fig. 4.7). From the base to the termination, the the crystal shows a color zoning ranging from yellow, dark-green, pale pink, blue-green, pink-reddish to brownish in the direction of the analogous overgrowth. The narrow blue-green sector, in the upper part of the crystal, appears divided in two half along the crystal width, which are also shifted along the **c**-axis.

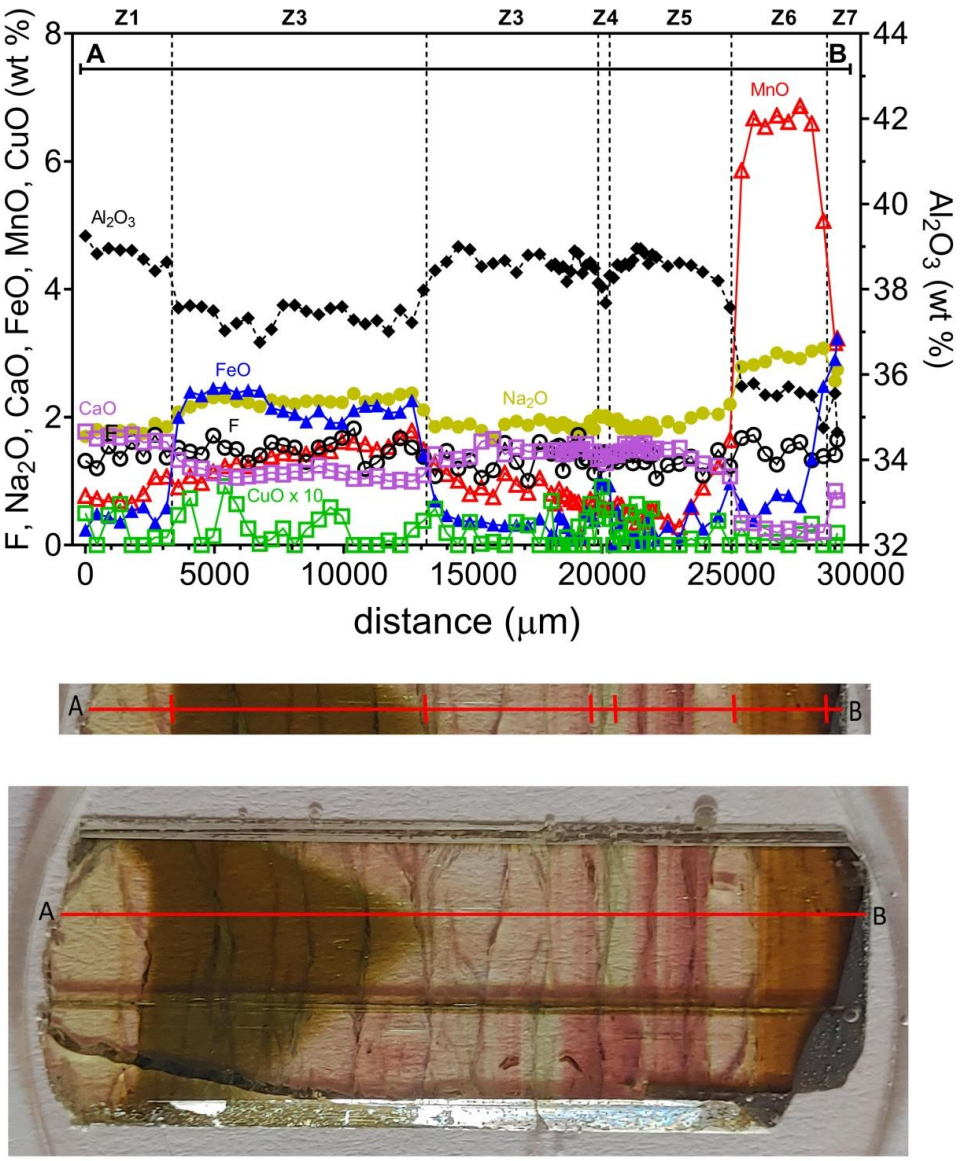

Figure 4.38. EMP analysis of the MAV 21 sample along a straight traverse parallel to the c-axis (only selected oxides are reported. See Table 4.19 for complete chemistry.

Table 4.19. Average chemical composition and atoms per formula unit (a.p.f.u) for each zone of the MAV 21 sample (Mavuco, Mozambique) with the relative empirical formula.

	Z1	**Z2**	**Z3**	**Z4**	**Z5**	**Z6**	**Z7**
	n = 8	*n* = 22	*n* = 22	*n* = 4	*n* = 18	*n* = 8	*n* = 2
SiO_2 (wt%)	38.07(31)	37.45(31)	38.22(31)	37.99(32)	38.20(25)	37.16(25)	36.82(26)
TiO_2	0.13(4)	0.33(5)	0.05(4)	0.05(1)	0.04(3)	0.45(20)	0.20(1)
B_2O_3[a]	10.86	10.72	10.86	10.8	10.85	10.61	10.45
Al_2O_3	38.83(25)	37.38(28)	38.61(20)	38.05	38.56(32)	35.51(33)	35.10(64)
FeO	0.45(13)	2.15(25)	0.33(15)	0.96(2)	0.28(25)	0.95(68)	3.07(23)
MnO	0.81(17)	1.39(23)	0.80(25)	0.59(3)	0.62(34)	6.37(60)	3.20(5)
MgO	0.02(2)	0.20(3)	0.02(1)	0.15(18)	0.02(2)	0.08(6)	0.06(1)
CuO	0.03(3)	0.03(3)	0.02(2)	0.06(2)	0.04(2)	0.02(1)	0.02(1)
CaO	1.68(6)	1.11(8)	1.48(8)	1.35(5)	1.44(13)	0.25(6)	0.77(10)
Na_2O	1.80(6)	2.25(7)	1.86(7)	2.00(3)	1.91(11)	2.93(10)	2.65(13)
Li_2O[b]	2.17	1.87	2.24	2.2	2.28	1.47	1.61
K_2O	0.02(2)	0.01(1)	0.01(1)	0.01(1)	0.01(1)	0.02(1)	0.03(0)
F	1.44(17)	1.50(15)	1.36(20)	1.38(9)	1.33(13)	1.50(17)	1.53(17)
H_2O[a]	2.80	2.75	2.93	2.95	2.95	2.76	2.65
$-O \equiv F$	−0.61	−0.63	−0.57	−0.58	−0.56	−0.63	−0.64
Total	98.50	98.55	98.26	97.98	97.99	99.47	97.54
Atoms normalized to 31 anions							
Si (a.p.f.u)	6.091	6.070	6.105	6.101	6.110	6.077	6.114
Ti^{4+}	0.016	0.040	0.006	0.006	0.005	0.056	0.025
B	3.000	3.000	3.000	3.000	3.000	3.000	3.000
Al	7.312	7.140	7.280	7.214	7.280	6.856	6.881
Fe^{2+}	0.060	0.291	0.044	0.129	0.037	0.131	0.427
Mn^{2+}	0.109	0.191	0.109	0.081	0.084	0.883	0.450
Mg	0.005	0.048	0.005	0.036	0.005	0.020	0.015
Cu	0.004	0.004	0.005	0.007	0.004	0.003	0.003
Ca	0.287	0.193	0.253	0.232	0.248	0.044	0.138
Na	0.557	0.706	0.576	0.625	0.593	0.931	0.856
Li	1.396	1.219	1.441	1.423	1.469	0.969	1.077
K	0.003	0.003	0.002	0.002	0.002	0.004	0.006
F	0.728	0.767	0.687	0.701	0.676	0.775	0.804
OH	2.985	2.977	3.131	3.164	3.157	3.017	2.942

[a] Calculated by stoichiometry (see text)

[b] Estimated with the procedure of Pesquera et al. (2016)

Errors for oxides and fluorine are standard deviations (in brackets)

Empirical chemical formulae

Z1
$$^{X}(Na_{0.56}\square_{0.15}Ca_{0.29})_{\Sigma 1.00}{}^{Y}(Al_{1.31}Li_{1.40}Fe^{2+}_{0.06}Mn^{2+}_{0.11}Mg_{0.01}Ti_{0.02})_{\Sigma 2.91}{}^{Z}Al_6(^{T}Si_{6.09}O_{18})(BO_3)_3\ {}^{V}(OH_{2.99}O_{0.01})_{\Sigma 3.00}{}^{W}(F_{0.73}O_{0.27})_{\Sigma 1.00}$$

Z2
$$^{X}(Na_{0.71}\square_{0.10}Ca_{0.19})_{\Sigma 1.00}{}^{Y}(Al_{1.14}Li_{1.22}Fe^{2+}_{0.29}Mn^{2+}_{0.19}Mg_{0.05}Ti_{0.04})_{\Sigma 2.93}{}^{Z}Al_6(^{T}Si_{6.07}O_{18})(BO_3)_3\ {}^{V}(OH_{2.98}O_{0.02})_{\Sigma 3.00}{}^{W}(F_{0.77}O_{0.23})_{\Sigma 1.00}$$

Z3
$$^{X}(Na_{0.58}\square_{0.17}Ca_{0.25})_{\Sigma 1.00}{}^{Y}(Al_{1.28}Li_{1.44}Fe^{2+}_{0.04}Mn^{2+}_{0.11}Mg_{0.01}Ti_{0.01})_{\Sigma 2.90}{}^{Z}Al_6(^{T}Si_{6.10}O_{18})(BO_3)_3\ {}^{V}(OH)_{3.00}{}^{W}(OH_{0.13}F_{0.69}O_{0.18})_{\Sigma 1.00}$$

Z4
$$^{X}(Na_{0.63}\square_{0.14}Ca_{0.23})_{\Sigma 1.00}{}^{Y}(Al_{1.21}Li_{1.42}Fe^{2+}_{0.13}Mn^{2+}_{0.08}Mg_{0.04}Cu_{0.01}Ti_{0.01})_{\Sigma 2.90}{}^{Z}Al_6(^{T}Si_{6.10}O_{18})(BO_3)_3\ {}^{V}(OH)_{3.00}{}^{W}(OH_{0.16}F_{0.70}O_{0.14})_{\Sigma 1.00}$$

Z5
$$^{X}(Na_{0.59}\square_{0.16}Ca_{0.25})_{\Sigma 1.00}{}^{Y}(Al_{1.28}Li_{1.47}Fe^{2+}_{0.04}Mn^{2+}_{0.08}Mg_{0.01}Ti_{0.01})_{\Sigma 2.89}{}^{Z}Al_6(^{T}Si_{6.11}O_{18})(BO_3)_3\ {}^{V}(OH)_{3.00}{}^{W}(OH_{0.16}F_{0.68}O_{0.16})_{\Sigma 1.00}$$

Z6
$$^{X}(Na_{0.93}\square_{0.02}Ca_{0.04})_{\Sigma 1.00}{}^{Y}(Al_{0.86}Li_{0.97}Fe^{2+}_{0.13}Mn^{2+}_{0.88}Mg_{0.02}Ti_{0.06})_{\Sigma 2.92}{}^{Z}Al_6(^{T}Si_{6.08}O_{18})(BO_3)_3\ {}^{V}(OH)_{3.00}{}^{W}(OH_{0.02}F_{0.78}O_{0.20})_{\Sigma 1.00}$$

Z7
$$^{X}(Na_{0.86}Ca_{0.14})_{\Sigma 1.00}{}^{Y}(Al_{0.88}Li_{1.08}Fe^{2+}_{0.43}Mn^{2+}_{0.45}Mg_{0.02}Ti_{0.03})_{\Sigma 2.89}{}^{Z}Al_6(^{T}Si_{6.11}O_{18})(BO_3)_3\ {}^{V}(OH_{2.94}O_{0.06})_{\Sigma 3.00}{}^{W}(F_{0.80}O_{0.20})_{\Sigma 1.00}$$

Figure 4.38 displays the pattern of selected elements (as wt% oxides) determined along the considered traverse parallel to **c**-axis. Table 4.19 summarizes the chemical composition in wt%, apfu for each chemically homogeneous zone in which the sample was divided, and the relative empirical formulae.

The yellow Z1 zone is characterized by a low content in FeO (< 0.5 wt%) and MnO (< 1 wt%), while CaO content is about 1.7 wt%. The presence of TiO_2 (0.13 wt%), suggests that the yellow coloration is due to the combined effect of Mn and Ti (IVCT Mn^{2+}–Ti^{4+}). The dark-green Z2 zone, shows a sharp increase in Fe with an average FeO content of about 2 wt%, followed by a slight increase in Mn (MnO up 1.4 wt%), and a decrease in Ca (CaO ~ 1 wt%). The presence of a moderate amount of Ti (TiO_2 ~ 0.3 wt%) is likely consistent with the involvement of this element as color-causing agent in combination with both Fe and Mn though Fe^{2+}-Ti and Mn^{2+}-Ti IVCT transitions, resulting in a dark-green coloration. The Z3 zone is characterized by an abruptly decrease in Fe content reaching the same average value of Z1. At the same time, a slow decrease in MnO content and an increase in CaO can be observed, reaching at the end of the zone the same content observed in Z1. Despite the similar composition to Z1, the different color displayed can be ascribed to the absence of TiO_2 in Z3. Thus, the pink coloration can be mainly ascribed to Mn. The narrow blue-green zone observable in the upper part of the crystal (Z4), is the result of a local and sharp increase in FeO, which reaches a value up to 1 wt%. The presence of ~ 0.1 wt% of CuO, may modifiy the blue color associated with Fe towards a greenish hue. The Z5 zone shows a similar average composition to Z3. Its reddish hue is probably the result of the slight increase in MnO content within the zone. In the brownish region of the analogous overgrowth (Z6) a huge increase in MnO can be observed, reaching value about 7 wt%, as well as TiO_2, with an average content of 0.45 wt%. This region of the analogous overgrowth is also characterized by a decrease in Ca (CaO < 0.2 wt%), while the FeO content does not change too much. The last blackish part of the crystal termination shows a sharp decrease in MnO content, as well as an increase in FeO and CaO. The color displayed by the analogous termination can be mainly

due to the contribution of Mn and Ti in the brownish part, and Fe alone or in combination with Ti, for the blackish one.

The content in Cu was evaluated in MAV 21 sample and most spot analyses reveal a detectable amount of CuO. Cu is mainly concentrated in some areas of the sample including the narrow blue zone (Z4) in which reaches a value up to 0.1 wt%. The content of CuO measured in several parts of MAV 21 sample is absolutely comparable with the range observed in the tourmaline fragments and grains of the residual deposit of Mavuco, thus confirming the hypothesis of "Marina" pegmatite as a primary deposit for the detrital tourmalines in the Mavuco area.

4.4.5 The MAV 22 sample from the "Marina" pegmatite (Alto Ligonha pegmatite district): a further confirmation on the origin of the detrital tourmaline samples from the secondary deposit of Mavuco

Chemical composition

The MAV 22 sample is a tourmaline crystal of about 7 cm in length characterized by a thick (up to 4 mm) black late-stage overgrowth developed all over the tourmaline surfaces, from the analogous to the antilogous pole, including the prism faces. The analogous and antilogous overgrowths show a different textural characteristic: acicular at the analogous pole, and more compact at the steep pyramidal faces of the antilogous pole (Figura 4.39). The prismatic overgrowth mainly shares the same textural features of the antilogous one.

Figure 4.39. MAV 22 sample from the "Marina" pegmatite, Alto Ligonha, Mavuco, Mozambique. Crystal 70 mm across.

Once cut as thin section along the growth direction (**c**-axis), the prismatic section of the sample reveals a brownish coloration, darker in the direction of the antilogous pole, surrounded by a thick black rim corresponding to the whole overgrowth.

On the basis of the variation in chemical homogeneity, the sample was divided in different zones. Initially, the sample was partitioned in three areas: two related to the analogous and antilogous overgrowths, respectively, and one to the prismatic section of the crystal. The area corresponding to the antilogous overgrowth was labeled "OG_{anti}", while that of the analogous overgrowth was labeled "OG_{ana}". The overgrowth and prismatic regions were further subdivided in chemically homogenous zones, labeled by adding a progressive numerical suffix in the direction of the analogous pole. This subdivision is mainly the result of the variation in the amount of FeO, MgO and MnO. The "OG_{anti}" region was divided in three zones, and the prismatic section of the crystal in four zones with the latter one representing a short transition towards the analogous overgrowth region. The "OG_{ana}" region was instead divided in ten zones.

Figure 4.40 displays the pattern of selected elements (as wt% oxides) determined along the considered traverse parallel to **c**-axis, from the analogous to the antilogous pole. To highlights the chemical variation, Figures 4.41 and 4.42 displays the patter of selected oxides relative to the "OG_{anti}", "OG_{ana}" and prismatic regions, respectively. Tables 4.20, 4.21A,B and 4.22 summarize the chemical composition in wt%, apfu and the relative empirical chemical formulae of each zone in which the antilogous, analogous and prismatic regions, respectively, were subdivided.

Considering the chemical pattern along the whole crystal (Fig. 4.40), it can be pointed out that, while the prismatic section is enriched in MnO, the overgrowths are characterized by an increased amount in FeO, MgO and TiO_2, which are much less abundant in the prismatic region. However, the two overgrowths show quite a difference in the relative amount of FeO and MgO. The "OG_{anti}" is characterized by a similar content in MgO and FeO (~ 8 wt%), while in the "OG_{ana}" FeO is much

higher than MgO, reaching values around 20 wt%. Additionally, the "OG_{ana}" contains a very low amount in F (< 0.4 wt%). On the contrary, the "OG_{anti}" contains the highest amount of F, reaching values up to 1.7 wt%.

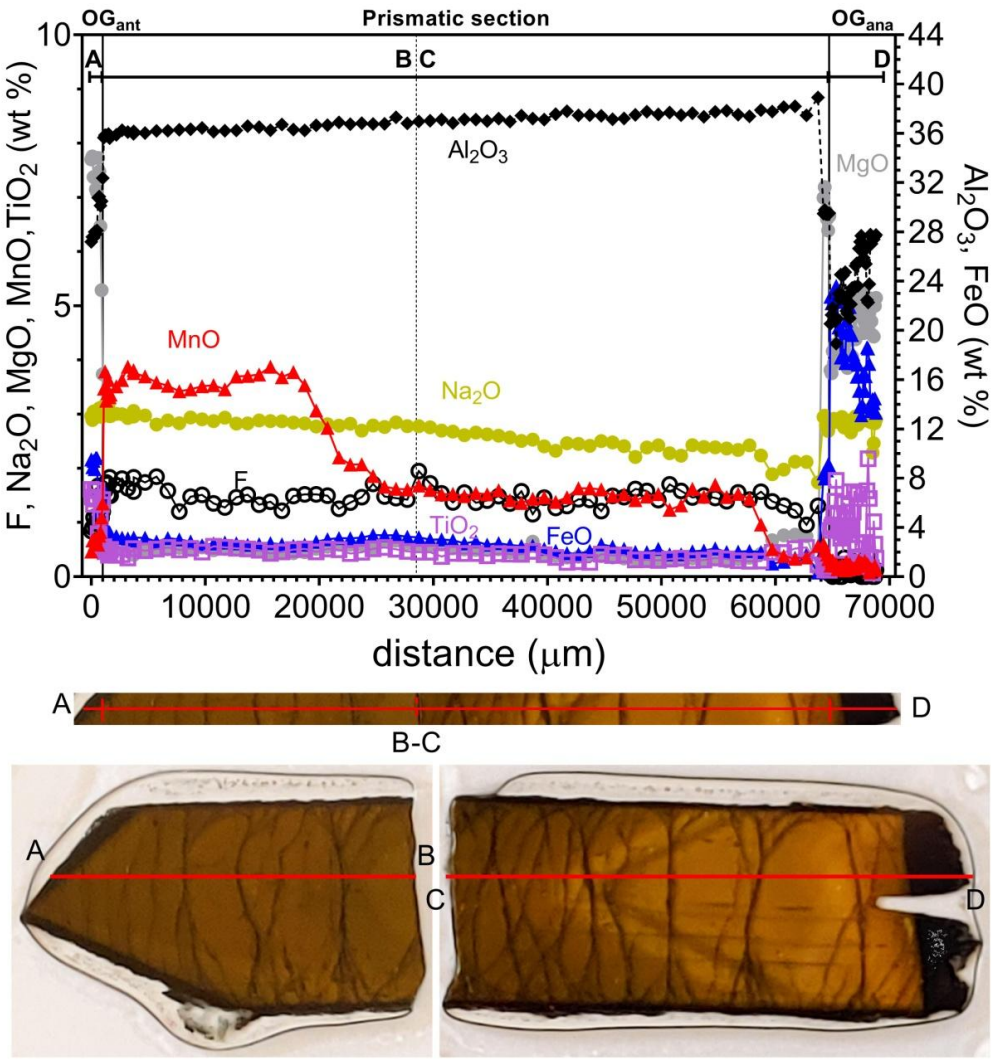

Figure 4.40. EMP analysis of the MAV 22 sample along a straight traverse parallel to the c-axis (only selected oxides are reported. See Tables 4.20-4.22 for complete chemistry.

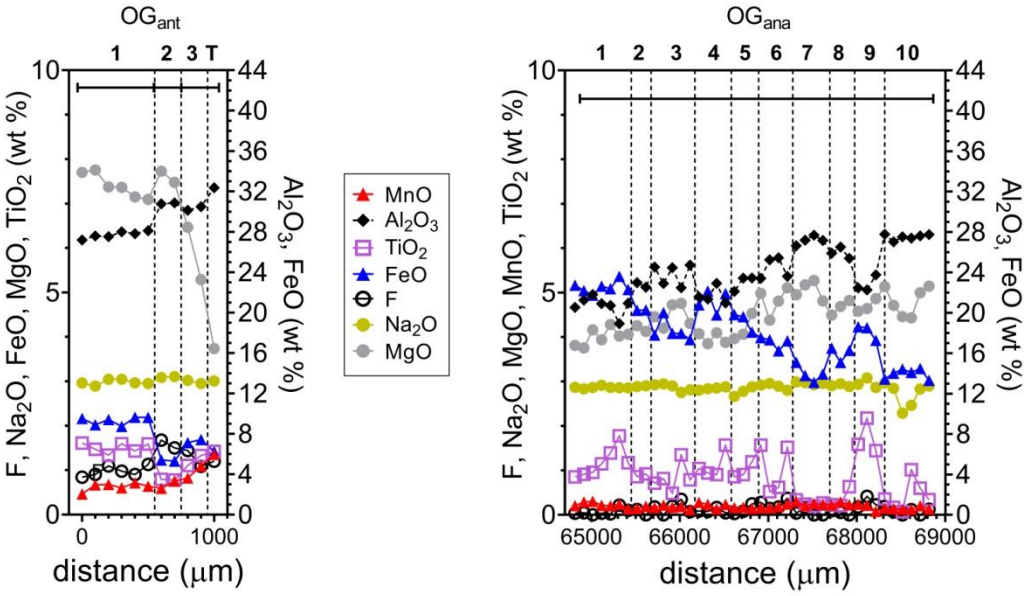

Figure 4.41. Close-up of the chemical composition of antilogous (OG$_{ant}$) and analogous (OG$_{ana}$) overgrowths in the MAV 22 sample (only selected oxides are reported). See Tables 4.20 and 4.21A,B for complete chemistry.

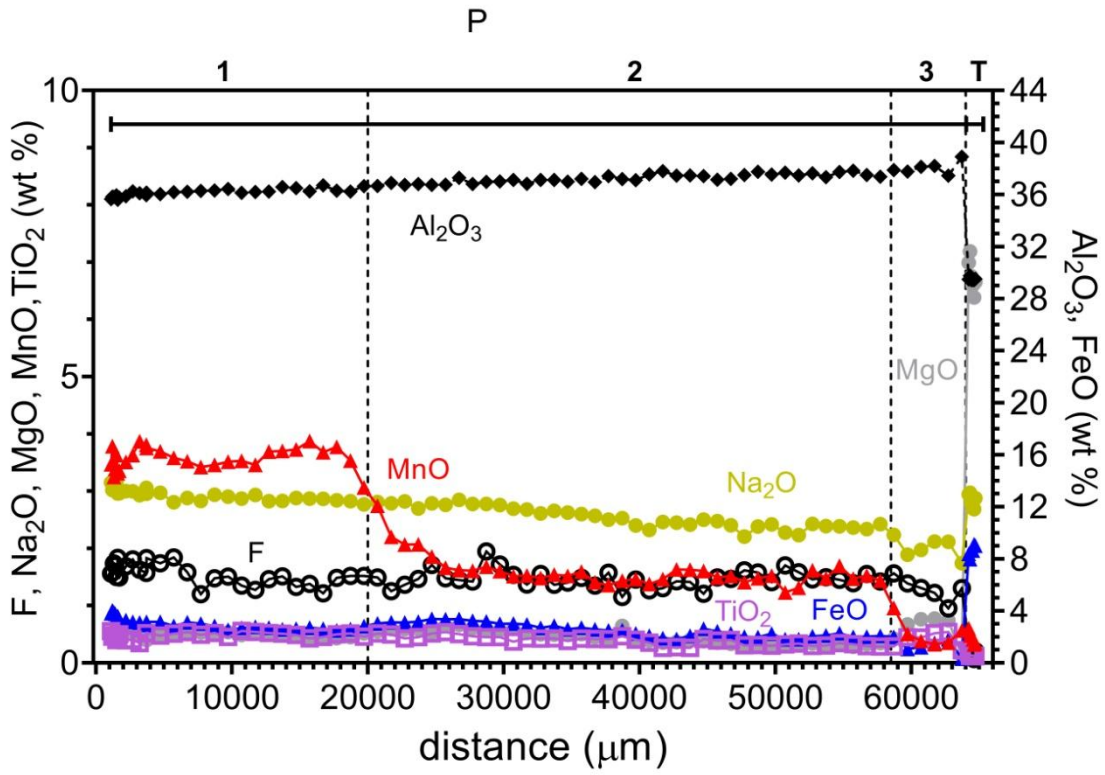

Figure 4.42. Close-up of the chemical composition of the prismatic section (P) in the MAV 22 sample (only selected oxides are reported). See Table 4.22 for complete chemistry.

Table 4.20. Average chemical composition and atoms per formula unit (a.p.f.u) for each zone of the antilogous overgrowth of the MAV 22 sample (Alto Ligonha pegmatite district, Mozambique) with the relative empirical formula.

	$OG_{anti}1$ $n = 6$	**$OG_{anti}2$** $n = 2$	**$OG_{anti}3$** $n = 2$	**$OG_{anti}T$** $n = 1$
SiO_2 (wt%)	36.96(9)	37.85(2)	37.36(8)	37.50
TiO_2	1.51(11)	0.79(1)	1.22(16)	1.42
B_2O_3[a]	10.44	10.56	10.39	10.60
Al_2O_3	27.7(34)	30.81(7)	30.31(26)	32.36
V_2O_3	0.07(2)	0.07(1)	0.09(0)	0.04
FeO_{tot}[b]	9.3(39)	5.35(7)	7.28(22)	6.24
MnO	0.63(9)	0.67(12)	0.96(19)	1.35
MgO	7.41(27)	7.60(18)	5.88(83)	3.74
CuO	0.01(3)	-	-	0.03
CaO	0.17(7)	0.08(1)	0.09(5)	0.09
Na_2O	2.98(6)	3.10(1)	2.98(5)	3.01
Li_2O[c]	-	-	-	-
K_2O	0.04(2)	0.02(0)	0.02(1)	0.03
F	0.98(12)	1.59(12)	1.27(25)	1.20
H_2O[a]	2.46	1.98	1.84	3.09
$-O \equiv F$	−0.411	−0.669	−0.533	−0.506
Fe_2O_3	4.48	2.58	3.51	-
FeO	5.27	3.03	4.13	6.24
Total	100.72	100.05	99.53	100.20
	Atoms normalized to 31 anions			
Si (a.p.f.u)	6.060	6.105	6.092	6.150
Ti^{4+}	0.186	0.095	0.149	0.175
B	3.000	3.000	3.000	3.000
Al	5.353	5.858	5.825	6.255
V^{3+}	0.009	0.009	0.012	0.005
Fe^{3+}	0.553	0.313	0.430	-
Fe^{2+}	0.723	0.409	0.563	0.856
Mn^{2+}	0.087	0.092	0.132	0.188
Mg	1.811	1.828	1.429	0.914
Cu	0.001	-	-	0.004
Ca	0.031	0.015	0.016	0.015
Na	0.946	0.968	0.944	0.956
Li	-	-	-	-
K	0.009	0.003	0.004	0.005
F	0.506	0.811	0.653	0.623
OH	3.494	3.189	3.347	3.377

[a] Calculated by stoichiometry (see text)
[b] From Mössbauer spectroscopy
[c] Estimated with the procedure of Pesquera et al. (2016)
Errors for oxides and fluorine are standard deviations (in brackets)

Empirical chemical formulae

$OG_{anti}1$
$$^{X}(Na_{0.95}K_{0.01}\square_{0.01}Ca_{0.03})_{\Sigma 1.00}\,^{Y}(Mn^{2+}_{0.09}Fe^{2+}_{0.63}Mg_{1.81}Ti_{0.17})_{\Sigma 2.70}$$
$$^{Z}(Al_{5.35}V_{0.01}Fe^{3+}_{0.55}Fe^{2+}_{0.09})_{\Sigma 6.00}(^{T}Si_{6.06}O_{18})(BO_3)_3\,^{V}(OH)_{3.00}\,^{W}(OH_{0.49}F_{0.51})_{\Sigma 1.00}$$

$OG_{anti}2$
$$^{X}(Na_{0.97}\square_{0.01}Ca_{0.02})_{\Sigma 1.00}\,^{Y}(Fe^{3+}_{0.18}Mn^{2+}_{0.09}Fe^{2+}_{0.41}Mg_{1.83}Ti_{0.10})_{\Sigma 2.61}$$
$$^{Z}(Al_{5.86}V_{0.01}Fe^{3+}_{0.13})_{\Sigma 6.00}(^{T}Si_{6.11}O_{18})(BO_3)_3\,^{V}(OH)_{3.00}\,^{W}(OH_{0.19}F_{0.81})_{\Sigma 1.00}$$

$OG_{anti}3$
$$^{X}(Na_{0.94}\square_{0.04}Ca_{0.02})_{\Sigma 1.00}\,^{Y}(Fe^{3+}_{0.26}Mn^{2+}_{0.13}Fe^{2+}_{0.56}Mg_{1.43}Ti_{0.15})_{\Sigma 2.53}$$
$$^{Z}(Al_{5.83}V_{0.01}Fe^{3+}_{0.17})_{\Sigma 6.00}(^{T}Si_{6.09}O_{18})(BO_3)_3\,^{V}(OH)_{3.00}\,^{W}(OH_{0.35}F_{0.65})_{\Sigma 1.00}$$

$OG_{anti}T$
$$^{X}(Na_{0.96}\square_{0.02}Ca_{0.02})_{\Sigma 1.00}\,^{Y}(Al_{0.26}V^{3+}_{0.01}Mn^{2+}_{0.19}Fe^{2+}_{0.86}Mg_{0.91}Ti_{0.18})_{\Sigma 2.41}$$
$$^{Z}Al_6(^{T}Si_{6.15}O_{18})(BO_3)_3\,^{V}(OH)_{3.00}\,^{W}(OH_{0.38}F_{0.62})_{\Sigma 1.00}$$

Table 4.21A. Average chemical composition and atoms per formula unit (a.p.f.u) for each zone of the analogous overgrowth of the MAV 22 sample (Alto Ligonha pegmatite district, Mozambique) and the relative empirical formulae

	$OG_{ana}1$	**$OG_{ana}2$**	**$OG_{ana}3$**	**$OG_{ana}4$**	**$OG_{ana}5$**
	n = 7	*n* = 2	*n* = 5	*n* = 4	*n* = 3
SiO_2 (wt%)	34.43(25)	34.91(25)	35.21(26)	35.01(10)	35.53(17)
TiO_2	1.17(32)	0.89(4)	0.83(32)	1.11(31)	0.99(18)
B_2O_3[a]	9.82	9.93	9.97	9.88	9.94
Al_2O_3	20.73(90)	22.76(31)	24.02(92)	21.65(74)	23.00(76)
V_2O_3	0.11(3)	0.08(2)	0.10(3)	0.12(2)	0.11(3)
FeO_{tot}[b]	22.52(58)	20.26(3)	18.02(61)	21.12(0.99)	19.18(94)
MnO	0.23(6)	0.17(3)	0.17(4)	0.22(6)	0.16(1)
MgO	4.01(19)	4.19(9)	4.49(25)	3.98(13)	4.19(30)
CuO	0.02(3)	0.01(2)	0.01(2)	-	-
CaO	0.03(2)	0.03(0)	0.03(2)	0.03(2)	0.05(3)
Na_2O	2.87(2)	2.90(1)	2.87(8)	2.84(3)	2.77(11)
Li_2O[c]	-	-	-	-	-
K_2O	0.08(2)	0.08(1)	0.07(2)	0.07(3)	0.07(1)
F	0.07(7)	0.06(8)	0.16(13)	0.09(5)	0.12(11)
H_2O[a]	2.87	2.82	2.69	2.73	2.73
$-O \equiv F$	−0.03	−0.03	−0.07	−0.04	−0.05
Fe_2O_3	12.59	11.33	10.07	11.86	9.83
FeO	11.19	10.07	8.96	10.54	10.33
Total	100.20	100.19	99.58	100.13	99.81
	Atoms normalized to 31 anions				
Si (a.p.f.u)	6.074	6.104	6.118	6.166	6.202
Ti^{4+}	0.156	0.117	0.109	0.148	0.130
B	3.000	3.000	3.000	3.000	3.000
Al	4.325	4.692	4.934	4.492	4.739
V^{3+}	0.016	0.011	0.014	0.017	0.015
Fe^{3+}	1.677	1.491	1.321	1.570	1.294
Fe^{2+}	1.657	1.474	1.306	1.552	1.510
Mn^{2+}	0.034	0.025	0.025	0.033	0.024
Mg	1.058	1.093	1.167	1.044	1.092
Cu	0.003	0.001	0.001	-	-
Ca	0.004	0.005	0.005	0.006	0.010
Na	0.984	0.982	0.970	0.971	0.941
Li	-	-	-	-	-
K	0.019	0.017	0.016	0.016	0.016
F	0.037	0.033	0.087	0.052	0.066
OH	3.391	3.288	3.124	3.209	3.180

[a] Calculated by stoichiometry (see text)
[b] From Mössbauer spectroscopy
[c] Estimated with the procedure of Pesquera et al. (2016)
Errors for oxides and fluorine are standard deviations (in brackets)

Empirical chemical formulae

$OG_{ana}1$

$$^{X}(Na_{0.98}K_{0.02})_{\Sigma 1.00}\,^{Y}(Fe^{3+}_{0.02}Mn^{2+}_{0.03}Fe^{2+}_{1.66}Mg_{1.06}Ti_{0.16})_{\Sigma 2.93}\,^{Z}(Al_{4.32}V_{0.02}Fe^{3+}_{1.66})_{\Sigma 6.00}(^{T}Si_{6.07}O_{18})(BO_3)_3\,^{V}(OH)_{3.00}\,^{W}(OH_{0.39}F_{0.02}O_{0.59})_{\Sigma 1.00}$$

$OG_{ana}2$

$$^{X}(Na_{0.98}K_{0.02})_{\Sigma 1.00}\,^{Y}(Fe^{3+}_{0.19}Mn^{2+}_{0.03}Fe^{2+}_{1.47}Mg_{1.09}Ti_{0.12})_{\Sigma 2.90}\,^{Z}(Al_{4.69}V_{0.01}Fe^{3+}_{1.30})_{\Sigma 6.00}(^{T}Si_{6.10}O_{18})(BO_3)_3\,^{V}(OH)_{3.00}\,^{W}(OH_{0.29}F_{0.03}O_{0.68})_{\Sigma 1.00}$$

$OG_{ana}3$

$$^{X}(Na_{0.97}K_{0.02})_{\Sigma 1.00}\,^{Y}(Fe^{3+}_{0.26}Mn^{2+}_{0.03}Fe^{2+}_{1.31}Mg_{1.17}Ti_{0.11})_{\Sigma 2.88}\,^{Z}(Al_{4.93}V_{0.01}Fe^{3+}_{1.06})_{\Sigma 6.00}(^{T}Si_{6.12}O_{18})(BO_3)_3\,^{V}(OH)_{3.00}\,^{W}(OH_{0.12}F_{0.09}O_{0.79})_{\Sigma 1.00}$$

$OG_{ana}4$

$$^{X}(Na_{0.97}K_{0.02})_{\Sigma 1.00}\,^{Y}(Fe^{3+}_{0.06}Mn^{2+}_{0.03}Fe^{2+}_{1.55}Mg_{1.04}Ti_{0.15})_{\Sigma 2.83}\,^{Z}(Al_{4.49}V_{0.02}Fe^{3+}_{1.49})_{\Sigma 6.00}(^{T}Si_{6.17}O_{18})(BO_3)_3\,^{V}(OH)_{3.00}\,^{W}(OH_{0.21}F_{0.05}O_{0.74})_{\Sigma 1.00}$$

$OG_{ana}5$

$$^{X}(Na_{0.94}K_{0.02}\square_{0.03}Ca_{0.01})_{\Sigma 1.00}\,^{Y}(Fe^{3+}_{0.05}Mn^{2+}_{0.02}Fe^{2+}_{1.51}Mg_{1.09}Ti_{0.13})_{\Sigma 2.80}\,^{Z}(Al_{4.74}V_{0.02}Fe^{3+}_{1.24})_{\Sigma 6.00}(^{T}Si_{6.20}O_{18})(BO_3)_3\,^{V}(OH)_{3.00}\,^{W}(OH_{0.18}F_{0.07}O_{0.75})_{\Sigma 1.00}$$

Table 4.21B. Average chemical composition and atoms per formula unit (a.p.f.u) for each zone of the analogous overgrowth of the MAV 22 sample (Alto Ligonha pegmatite district, Mozambique) with the relative empirical formula

	$OG_{ana}6$ $n = 4$	**$OG_{ana}7$** $n = 4$	**$OG_{ana}8$** $n = 3$	**$OG_{ana}9$** $n = 3$	**$OG_{ana}10$** $n =$
SiO_2 (wt%)	35.66(15)	36.36(23)	35.93(18)	35.24(38)	35.28(91)
TiO_2	1.06(56)	0.26(6)	0.36(24)	1.74(39)	0.42(34)
B_2O_3[a]	10.07	10.2	10.11	9.94	10.08
Al_2O_3	24.48(0.99)	27.17(42)	25.93(56)	22.83(81)	27.51(28)
V_2O_3	0.11(4)	0.04(2)	0.05(1)	0.14(1)	0.04(2)
FeO_{tot}[b]	17.08(58)	13.99(83)	15.96(77)	18.14(75)	13.97(49)
MnO	0.19(4)	0.25(4)	0.25(4)	0.18(9)	0.15(3)
MgO	4.82(32)	5.05(21)	4.67(16)	4.70(15)	4.81(33)
CuO	0.01(1)	0.02(2)	0.01(2)	0.01(2)	0.02(2)
CaO	0.03(2)	0.02(1)	0.02(1)	0.04(1)	0.11(13)
Na_2O	2.89(6)	2.96(3)	2,91(3)	2.96(11)	2.72(27)
Li_2O[c]	-	-	-	-	-
K_2O	0.04(1)	0.03(1)	0.03(1)	0.11(11)	0.03(2)
F	0.24(10)	0.05(8)	0.05(5)	0.27(13)	0.08(7)
H_2O[a]	2.72	2.73	2.80	2.60	2.81
$-O \equiv F$	−0.10	−0.02	−0.02	−0.12	−0.04
Fe_2O_3	8.76	7.17	8.18	9.30	6.73
FeO	9.20	7.53	8.60	9.77	7.91
Total	100.20	99.87	99.88	99.72	98.68
			Atoms normalized to 31 anions		
Si (a.p.f.u)	6.123	6.187	6.155	6.142	6.073
Ti^{4+}	0.137	0.033	0.046	0.228	0.055
B	3.000	3.000	3.000	3.000	3.000
Al	4.978	5.457	5.253	4.705	5.591
V^{3+}	0.015	0.005	0.007	0.020	0.006
Fe^{3+}	1.137	1.080	1.058	1.224	0.873
Fe^{2+}	1.328	0.914	1.235	1.429	1.140
Mn^{2+}	0.027	0.036	0.036	0.027	0.021
Mg	1.240	1.283	1.197	1.225	1.236
Cu	0.001	0.001	0.001	0.001	0.003
Ca	0.005	0.003	0.004	0.008	0.021
Na	0.968	0.979	0.971	1.004	0.908
Li	-	-	-	-	-
K	0.010	0.007	0.006	0.024	0.007
F	0.133	0.028	0.028	0.150	0.045
OH	3.129	2.948	3.205	3.028	3.229

[a] Calculated by stoichiometry (see text)
[b] From Mössbauer spectroscopy
[c] Estimated with the procedure of Pesquera et al. (2016)
Errors for oxides and fluorine are standard deviations (in brackets)

Empirical chemical formulae

$OG_{ana}6$

$$^{X}(Na_{0.97}K_{0.01}\square_{0.01}Ca_{0.01})_{\Sigma 1.00}\,^{Y}(Fe^{3+}_{0.14}Mn^{2+}_{0.03}Fe^{2+}_{1.33}Mg_{1.24}Ti_{0.14})_{\Sigma 2.88}$$
$$^{Z}(Al_{4.98}V_{0.02}Fe^{3+}_{1.00})_{\Sigma 6.00}(^{T}Si_{6.12}O_{18})(BO_3)_3\,^{V}(OH)_{3.00}\,^{W}(OH_{0.18}F_{0.07}O_{0.75})_{\Sigma 1.00}$$

$OGa_{na}7$

$$^{X}(Na_{0.98}K_{0.01}\square_{0.01})_{\Sigma 1.00}\,^{Y}(Fe^{3+}_{0.55}Mn^{2+}_{0.04}Fe^{2+}_{0.91}Mg_{1.28}Ti_{0.03})_{\Sigma 2.81}$$
$$^{Z}(Al_{5.46}V_{0.01}Fe^{3+}_{0.53})_{\Sigma 6.00}(^{T}Si_{6.19}O_{18})(BO_3)_3\,^{V}(OH_{2.95}O_{0.05})_{\Sigma 3.00}\,^{W}(F_{0.03}O_{0.93})_{\Sigma 1.00}$$

$OG_{ana}8$

$$^{X}(Na_{0.97}K_{0.01}\square_{0.02})_{\Sigma 1.00}\,^{Y}(Fe^{3+}_{0.32}Mn^{2+}_{0.04}Fe^{2+}_{1.24}Mg_{1.20}Ti_{0.05})_{\Sigma 2.85}$$
$$^{Z}(Al_{5.25}V_{0.01}Fe^{3+}_{0.74})_{\Sigma 6.00}(^{T}Si_{6.15}O_{18})(BO_3)_3\,^{V}(OH)_{3.00}\,^{W}(OH_{0.21}F_{0.03}O_{0.76})_{\Sigma 1.00}$$

$OG_{ana}9$

$$^{X}(Na)_{\Sigma 1.00}\,^{Y}(Mn^{2+}_{0.03}Fe^{2+}_{1.37}Mg_{1.23}Ti_{0.23})_{\Sigma 2.86}$$
$$^{Z}(Al_{4.70}V_{0.02}Fe^{3+}_{1.22}\,Fe^{2+}_{0.06})_{\Sigma 6.00}(^{T}Si_{6.14}O_{18})(BO_3)_3\,^{V}(OH)_{3.00}\,^{W}(OH_{0.03}F_{0.15}O_{0.82})_{\Sigma 1.00}$$

$OG_{ana}10$

$$^{X}(Na_{0.91}K_{0.01}\square_{0.06}Ca_{0.02})_{\Sigma 1.00}\,^{Y}(Fe^{3+}_{0.47}Mn^{2+}_{0.02}Fe^{2+}_{1.14}Mg_{1.24}Ti_{0.06})_{\Sigma 2.93}$$
$$^{Z}(Al_{5.59}V_{0.01}Fe^{3+}_{0.40})_{\Sigma 6.00}(^{T}Si_{6.07}O_{18})(BO_3)_3\,^{V}(OH)_{3.00}\,^{W}(OH_{0.23}F_{0.05}O_{0.72})_{\Sigma 1.00}$$

Table 4.22. Average chemical composition and atoms per formula unit (a.p.f.u) for each zone of the prismatic section of the MAV 22 sample (Alto Ligonha pegmatite district, Mozambique) with the relative empirical formula.

	P1	**P2**	**P3**	**PT**
	n = 31	*n* = 37	*n* = 5	*n* = 6
SiO_2 (wt%)	38.29(21)	38.29(21)	38.26(38)	37.19(13)
TiO_2	0.48(5)	0.38(8)	0.41(13)	0.14(3)
B_2O_3[a]	10.9	10.92	10.96	10.40
Al_2O_3	36.21(33)	37.29(33)	38.06(49)	29.51(13)
V_2O_3	0.02(2)	0.02(2)	0.02(2)	0.02(1)
FeO	3.06(44)	2.50(50)	1.33(60)	8.63(42)
MnO	3.51(34)	1.54(20)	0.52(24)	0.44(10)
MgO	0.48(5)	0.44(12)	0.58(26)	6.76(29)
CuO	0.01(2)	0.02(2)	0.02(1)	0.01(2)
CaO	0.22(10)	0.72(25)	1.42(22)	0.02(2)
Na_2O	2.93(11)	2.52(18)	2.01(18)	2.86(11)
Li_2O[b]	1.61	1.90	2.17	-
K_2O	0.02(1)	0.03(10)	0.02(1)	0.02(1)
F	1.53(19)	1.48(15)	1.29(20)	0.18(8)
H_2O[a]	2.94	2.96	3.09	3.29
$-O \equiv F$	−0.64	−0.62	−0.54	−0.07
Total	101.55	100.39	99.62	99.41
	Atoms normalized to 31 anions			
Si (a.p.f.u)	6.107	6.094	6.064	6.216
Ti^{4+}	0.058	0.046	0.049	0.017
B	3.000	3.000	3.000	3.000
Al	6.807	6.996	7.115	5.814
V^{3+}	0.003	0.003	0.003	0.003
Fe^{2+}	0.408	0.332	0.177	1.206
Mn^{2+}	0.474	0.208	0.070	0.063
Mg	0.114	0.104	0.137	1.684
Cu	0.001	0.002	0.002	0.001
Ca	0.037	0.123	0.241	0.004
Na	0.906	0.778	0.619	0.927
Li	1.033	1.217	1.384	-
K	0.004	0.007	0.003	0.005
F	0.771	0.744	0.648	0.093
OH	3.128	3.145	3.269	3.673

[a] Calculated by stoichiometry (see text)
[b] Estimated with the procedure of Pesquera et al. (2016)
Errors for oxides and fluorine are standard deviations (in brackets)

Empirical chemical formulae

P1
$$^{X}(Na_{0.91}\square_{0.05}Ca_{0.04})_{\Sigma 1.00}\,^{Y}(Al_{0.81}Li_{1.03}Fe^{2+}_{0.41}Mn^{2+}_{0.47}Mg_{0.11}Ti_{0.06})_{\Sigma 2.89}\,^{Z}Al_6(^{T}Si_{6.11}O_{18})(BO_3)_3\,^{V}(OH)_{3.00}\,^{W}[(OH)_{0.13}F_{0.77}O_{0.10})]_{\Sigma 1.00}$$

P2
$$^{X}(Na_{0.78}\square_{0.10}Ca_{0.12})_{\Sigma 1.00}\,^{Y}(Al_{1.00}Li_{1.22}Fe^{2+}_{0.33}Mn^{2+}_{0.21}Mg_{0.10}Ti_{0.05})_{\Sigma 2.91}\,^{Z}Al_6(^{T}Si_{6.09}O_{18})(BO_3)_3\,^{V}(OH)_{3.00}\,^{W}[(OH)_{0.15}F_{0.74}O_{0.11})]_{\Sigma 1.00}$$

P3
$$^{X}(Na_{0.62}\square_{0.14}Ca_{0.24})_{\Sigma 1.00}\,^{Y}(Al_{1.12}Li_{1.38}Fe^{2+}_{0.18}Mn^{2+}_{0.07}Mg_{0.14}Ti_{0.05})_{\Sigma 2.94}\,^{Z}Al_6(^{T}Si_{6.06}O_{18})(BO_3)_3\,^{V}(OH)_{3.00}\,^{W}[(OH)_{0.27}F_{0.65}O_{0.08})]_{\Sigma 1.00}$$

PT
$$^{X}(Na_{0.92}\square_{0.08})_{\Sigma 1.00}\,^{Y}(Fe^{2+}_{1.02}Mn^{2+}_{0.06}Mg_{1.68}Ti_{0.02})_{\Sigma 2.78}\,^{Z}(Al_{5.81}Fe^{2+}_{0.19})_{\Sigma 6.00}(^{T}Si_{6.22}O_{18})(BO_3)_3\,^{V}(OH)_{3.00}\,^{W}[(OH)_{0.67}F_{0.09}O_{0.24})]_{\Sigma 1.00}$$

The high content in FeO that characterize both the overgrowths required the evaluation of Fe oxidation state. To obtain this information, small amounts of material from the antilogous and the analogous overgrowths were subject to Mössbauer analysis using a conventional spectrometer system equipped with a 10 mCi point source and operated in constant acceleration mode. Results are shown in Fig. 4.43 and summarized in Table 4.23. The final fitting model of the obtained spectra indicate that the antilogous overgrowth is characterized by Fe^{3+}/FeO_{tot}-ratio of 0.48, while the analogous overgrowth is richer in Fe^{3+}, with a Fe^{3+}/FeO_{tot}-ratio ranging from 0.56 to 0.51.

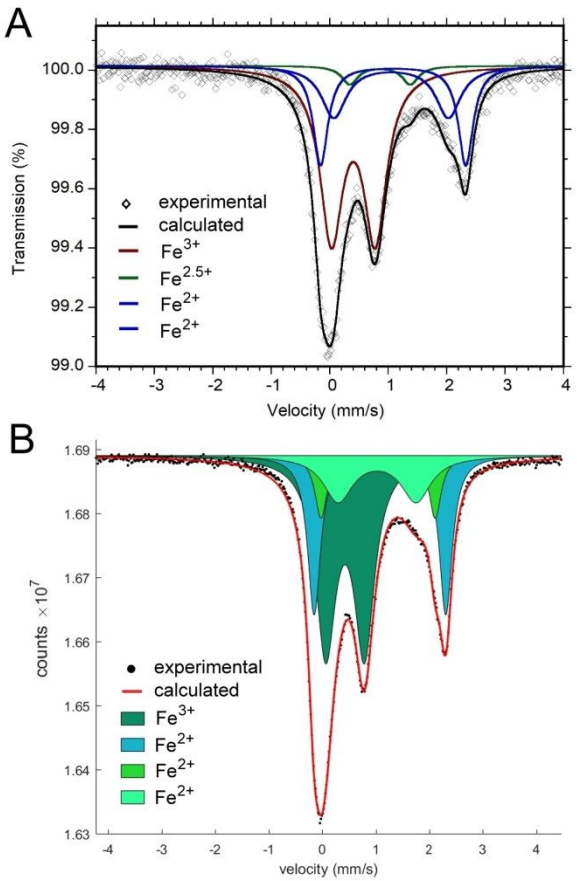

Figure 4.43. Room temperature ^{57}Fe Mössbauer spectra for the analogous (A) and antilogous (B) overgrowths of MAV 22 sample. For the analogous overgrowth (A), fitted absorption doublets assigned to Fe^{2+} are indicated in blue, Fe^{3+} in red, and $Fe^{2.5+}$ due to electron delocalization in green. Diamonds denote measured spectrum, and black curve represents summed fitted spectra. For the antilogous overgrowth (B), Lorentzian absorption doublets assigned to Fe^{2+} are represented by neon-green, light-green and light-blue colore areas. The dark-green colored area refers to the assignment of Fe^{3+}. Dots denote measured spectrum, and thick red curve represents calculated spectrum.

Table 4.23. Room temperature ^{57}Fe Mössbauer parameters for the analogous and antilogous overgrowths of MAV 22 sample (Alto Ligonha pegmatite district).

	δ mm/s	ΔE_Q mm/s	Γ mm/s	Assignment	%Area
Analogous	1.08	2.48	0.30	Fe^{2+}	21.3
	1.05	1.96	0.51	Fe^{2+}	18.5
	0.86	1.03	0.33	$Fe^{2.5+}$	4.3
	0.40	0.75	0.47	Fe^{3+}	55.9
Antilogous	1.07	2.46	0.29	Fe^{2+}	25.7
	1.04	2.13	0.27	Fe^{2+}	9.4
	1.02	1.46	0.67	Fe^{2+}	16.7
	0.42	0.72	0.46	Fe^{3+}	48.2

Centroid shift (δ) in mm/s relative to α-Fe foil; errors are estimated no less than ±0.02 mm/s for δ, quadrupole splitting (ΔE_Q), and peak width (Γ), and no less than ±3% for doublets areas.

A closer view of the "OG_{anti}" region is reported in Fig 4.39 left panel. This region was divided in three zones ("$OG_{anti}1$", "$OG_{anti}2$" and "$OG_{anti}3$"), and a very short transition area ("$OG_{anti}T$") connecting to the prismatic region. The "OG_{anti}" region is characterized by a low content in MnO, constantly below 1 wt%, which raises in correspondence of the transition to the prismatic section ("$OG_{anti}T$"). As above mentioned, FeO and MgO are abundant and quite similar in concentration. However, a sharp decrease in MgO content can be observed in the "$OG_{anti}3$" and "$OG_{anti}T$" zones.

Despite the variation in MgO content, the relative abundance of this element (> 3 wt%), coupled with a significant amount of F (> 0.9 wt%) and NaO (> 2.9 wt%) (Fig 4.41 left panel and Table 4.20), led to the antilogous overgrowth classified as fluor-dravite. The presence of high concentration in FeO (~ 8 wt%) and a significant amount of TiO_2, more than 1 wt%, are surely responsible for the blackish coloration of this overgrowth.

The prismatic region was divided in three zones ("P1", "P2" and "P3") and a short transition area connecting to the analogous overgrowth ("PT") (Fig. 4.42). The prismatic region of the crystal is characterized by a lower content in FeO, MgO and TiO_2 compared to the overgrowths, while MnO content is higher. However, MnO amount decreases along the prismatic section, allowing its subdivision in

three zones characterized by different MnO content: P1 zone with ~ 3.5 wt% MnO, P2 zone with ~1.5 wt% MnO and P3 with less than 0.5 wt% MnO. This decrease is responsible of the fading of the brownish coloration displayed by the prismatic region, in the direction of the analogous overgrowth. In the short transition area to the analogous overgrowth ("PT"), a rapid increase in Mg and Fe content can be observed, with MgO reaching values up to 7 wt% and FeO of 8 wt%. At the same time, a considerable decrease in the F content, from an average value of ~1.3 wt% to 0.2 wt%, can be observed. On the basis of the chemical composition, "P1", "P2" and "P3" zones can be classified as fluor-elbaite (Fig 4.42 and Table 4.22). On the other hand, the composition of the "PT" zone corresponds to a dravite.

In Figure 4.41 right panel is highlighted the chemical composition of the "OG_{ana}" region. As stated above, this part of the crystal is characterized by the highest content in FeO, which reaches values up to 24 wt%. The analogous overgrowth is also enriched in MgO, ranging from 4 w% to 5 wt%, and TiO_2 with values up to 2 wt%. On the contrary, the content in MnO and F are very low.

The analogous overgrowth is characterized by an uneven content in Fe, Ti and Mg: TiO_2 values range from 0.2 wt% to 2 wt%, while FeO content ranges from 12 wt% to 24 wt%, with a calculated Fe^{3+}/FeO_{tot}-ratio ranging from 0.55 to 0.51. A less extent in variability can be observed for MgO. Based on this peculiar behavior, the analogous overgrowth can be divided in at least ten different zones with a relative homogenous composition. In addition, a trend in the decrease in FeO characterizes the end of the crystal. A tentative to identify the tourmaline species to which the different zones belong, gave unpredictable results. In fact, most of the zones showed a composition that did not converge to any currently approved tourmaline species. The only zones, which composition agree with a previously described species are the Z1, Z4, Z5 and Z9. These zones show an high content in FeO, with an average value ranging from 18 wt% to 22 wt%, as well as the higher content in TiO_2 considering all the analogous region. Iron and Ti content, coupled with a significant amount of Na (NaO > 2.7 wt%) and a Fe^{3+}/FeO_{tot}-ratio > 0.50, led to classify these zones as dutrowite [ideally,$Na(Fe^{2+}_{2.5}Ti_{0.5})Al_6(Si_6O_{18})(BO_3)_3(OH)_3O$],

as the composition of these zones correspond to Fe-rich and Ti-rich oxy-tourmaline species (Fig 4.41 right panel and Tables 4.21A,B).

Differently, the Z2, Z3, Z6 and Z8 zones are still characterized by a high content in FeO, with an average value between 16 wt% to 20 wt% and a Fe^{3+}/FeO_{tot}-ratio > 0.50, but a slight lower content in Ti (TiO_2 < 1 wt%) (Fig 4.41 right panel and Tables 4.21A,B). The interesting aspect of these zones is that their chemical composition does not fit to any currently approved tourmaline species, and chemical, spectroscopic and crystal-structure refinement results lead to a new tourmaline species (ferro-bosiite), ideally $NaFe^{3+}_3(Al_4Fe^{2+}_2)(Si_6O_{18})(BO_3)_3(OH)_3O$, recently approved by the IMA-CNMNC (proposal n. 2022-069) (see Annex A).

The zones Z7 and Z10 show the lowest amount of FeO, with an average value of 13 wt% and a Fe^{3+}/FeO_{tot}-ratio > 0.50, a low content in Ti (TiO_2 < 1 wt%), and the highest amount of Mg (MgO ~ 5 wt%) (Fig 4.41 right panel and Tables 4.21A,B). On the basis of the chemical composition, these zones can be ascribed as tourmalines belonging to Fe- and Mg-rich oxy-species. As the above described zones (Z2, Z3, Z6 and Z8), the composition does not fit with any currently approved tourmaline species. However, further studies are required before a proposal for a new mineral species can be put forward.

As for the antilogous overgrowth, the high abundance in FeO and TiO_2, which characterized the analogous overgrowth, is surely responsible for its blackish coloration.

Minerogenersis and evolution of the black overgrowth in the MAV 22 sample from the “Marina” pegmatite (Alto Ligonha pegmatite district)

The MAV 22 sample was found in a giant collapse cavity (about 12 m in size) discovered in the “Marina” granitic pegmatite and hosted in meta-amphibolites. The cavity was discovered a few years ago during a downdip exploration of the pegmatite, which resulted in excavation of a large open-pit that continues into some tunnels. At the depth of about 25 m, such giant collapsed cavity was encountered. It appeared mostly filled with collapsed crystals and rocks partially

cemented by a late-stage thick crust of whitish chalcedony. The collapsed material is mostly composed by cleavelandite (in large "pillows"), large milky quartz crystals in aggregates up to over a ton in weight, and several hundreds of kilos of yellow to pink tourmaline crystals, from few cm up to about 20 cm, covered by a thick black tourmaline overgrowth. The tourmaline crystals found in the cavity, suffered damaging and broke off from the matrix during the pocket collapse. Among the other minerals found in the collapsed materials, it is noteworthy to mention the occurrence of several tens of kilos of native bismuth, purple fluorite in octahedral crystals up to 20 cm across, and apatite. After the partial removal of the collapsed materials, the cavity shows to be over 12 m long and up to 5-6 m wide. The vertical development of the original cavity is uncertain, as the collapse affected progressively the roof of the pocket, the intermediate and the border zones of the pegmatite, and finally the amphibolitic metamorphic hosting rock. The collapse structure is vertically developed for at least 10−12 m.

The main feature that distinguishes the MAV 22 sample is the presence of a thick black overgrowth occurring not only at the analogous termination but extending all over the prism faces covering also the steep pyramidal faces at the antilogous pole. The formation of such a developed overgrowth is surely related to a dramatic change in the chemical composition of the crystallization environment. Structural and paragenetic observations of the cavity in which this tourmaline crystal was collected, provide evidences that this change is related to an intense and widespread fracturing of the cavity, which culminated with the subsequent collapse of the pocket roof. During the early-stages of pocket rupture, the highly reactive cavity fluids penetrated the fractures propagating in the enclosing pegmatite and leached the primitive Fe/Mg-rich minerals hosted in the intermediate and the border zones of the pegmatite. Then, the subsequent propagation of the fracturing phenomenon, allowed the collapse of the amphibolitic metamorphic host rock, which reacted with the residual cavity fluids, thus releasing large amounts of Fe and Mg in the system. The great availability of Fe and Mg allowed the formation of a thick (up to 3-4 mm) late-stage black

overgrowth of MAV 22 sample, which developed all over the tourmaline surfaces, including the prism faces, the steep pyramidal faces at the antilogous pole and the broken surfaces.

In this case, the pocket collapse was associated to oxidizing conditions as supported by the high Fe^{3+}/Fe_{tot} ratio (> 0.50) observed at the analogous termination of MAV 22 sample. The analogous overgrowth is characterized by a very high content in Fe (FeO up to 24 wt%), which decreases at the end of the termination to values of ~12 wt%. This decrease is consistent with the reduced Fe availability in the system caused by the uptake of this element by the tourmaline crystallization. Additionally, the antilogous overgrowth is characterized by a lower Fe concentration (FeO ~ 8 wt%), supporting the further decrease in the availability of this element in the late-stage fluids. On the other hand, the MgO availability did not change too much during the entire overgrowth formation, as result of the abundance of Mg-rich minerals in the amphibolite rock that collapsed within the cavity. The very low content in Mn recorded in both the overgrowth compared to the prismatic section of the crystal (MnO up to 4 wt%), is linked to the leaching and corrosion of Mg-bearing apatite. When tourmaline and apatite co-crystallize in the early-stage of cavity evolution, Mn-enrichment in tourmaline reaches significant levels, as apatite is a fairly-competitive mineral for Mn. Consequently, the chemical alteration of Mn-bearing apatite during the late-stage of tourmaline crystallization is responsible for the release of low amount of Mn in the system.

The presence of a prismatic overgrowth in the MAV 22 sample, as well as the finding of further tourmaline crystals covered by a similar thick black overgrowth in the same cavity of MAV 22 sample, further strengthen the hypothesis that the "Marina" pegmatite is a primary source of the detrital tourmalines found in the Mavuco secondary deposit, which are mostly characterized by the presence of a prismatic dark-colored overgrowth. Additionally, the study of this very peculiar tourmaline, as well as the cavity in which it was formed, provide further information regarding the mechanism underlying the genesis of the dark-colored

overgrowths, not only at the termination of the tourmaline crystals, but also all over the crystal surfaces from the analogous to the antilogous pole, including the prism faces.

4.5 Conclusions

The in-depth study on several tourmaline samples from the secondary deposit of Mavuco, allowed a detailed characterization of their chemical composition, which was correlated to the color displayed. Chemical data indicate that all the studied samples are characterized by a CuO content that never exceeds 1 wt%. Despite the moderate concentration, Cu is able to contribute as color-causing agent especially in those zones where its value approaches 1 wt% (e.g. MAV 6 blue-green core zone and MAV 5). Furthermore, EMPA data revealed that most of the detrital tourmalines are of fluor-elbaite composition. This is the evidence that the tourmalines from the secondary deposit of Mavuco do not belong only to elbaite species, as had been assumed in previous studies (e.g., Laurs et al., 2008), but also to different species, including fluor-liddicoatite (OG of MAV 6 sample). A correlation study between chemical composition by EMP analysis and color displayed by the studied tourmaline samples, allowed identifying the gemological variety to which the core zone of these grains belong. Specifically, in the secondary deposit of Mavuco, tourmalines belonging to *indicolite*, *canary tourmaline*, *Paraiba-type* and "*Cu-bearing rubellite"* varieties were identified. In addition, for selected samples with particular chromatic features and different Cu/Fe-ratio (MAV 5, MAV 6 and MAV 10), it was possible to determine through OAS analyses the atomic mechanisms that regulate the tourmalines color appearance.

Chemical analysis on MAV 21 tourmaline sample from the "Marina" granitic pegmatite confirmed the presence of Cu in this crystal. Moreover, the amount of Cu detected in this sample is comparable with that of the detrital tourmalines. The presence of Cu supports the hypothesis that the "Marina" pegmatite represents a source from which the detrital tourmalines of the secondary deposit of Mavuco

were originated. Thus, the "Marina" pegmatite can be considered a primary deposit for Cu-bearing (*Paraiba-type*) tourmalines and its further exploration can be economically advantageous.

MAV 22 sample is characterized by the presence of a peculiar late-stage black overgrowth covering all over the crystal surfaces, including the prism faces and the antilogous pole, which chemical and morphological features are similar to those observed in most of the detrital tourmalines from the secondary deposit of Mavuco. The presence of such an extended overgrowth, further strengthen the hypothesis that "Marina" pegmatite is a primary source of the detrital tourmalines in the Mavuco area. Furthermore, chemical and spectroscopic characterization of the MAV 22 sample, along with structural and paragenetic observations of the miarolitic cavity in which the tourmaline crystal was collected, allowed extend the genetic model already proposed for Elba tourmaline crystals to the prismatic dark overgrowths, which characterize the tourmaline crystals from the Alto Ligonha pegmatitic district. In this latter case, structural and paragenetic observations of the giant cavity in which the MAV 22 tourmaline crystal was collected (about 12 m in size), provide evidences that the changes in the chemical composition of the crystallization environment are related to an intense and widespread fracturing of the cavity, which culminated with the subsequent collapse of the pocket roof. The great availability of Fe and Mg in the pocket environment allowed the formation of a thick (up to 3-4 mm) late-stage black overgrowth developed all over the tourmaline surfaces, covering the prism faces.

5. CONCLUDING REMARKS

The color anomalies are sharp transitions to dark color at the termination and, in some cases, along the prismatic faces of tourmaline crystals, which are associated with a sudden increase in Fe and/or Mn. The formation of such dark-colored overgrowths is related to a sudden physicochemical change in the geochemical system during the latest-stages of tourmaline crystallization. However, the detailed events that led to the availability of Fe and/or Mn in the pocket environment, resulting in the growth of late-stage tourmalines, were unclear. The goal of this Ph.D project is the definition of a model for the genesis of the dark-colored overgrowths in pegmatitic gem tourmaline crystals. Since tourmaline is an excellent petrogenetic indicator, the origin and the chemical composition of fluids involved in the tourmaline crystallization, responsible for such color anomalies, were also investigated.

Eleven tourmaline samples from different miarolitic Li-bearing pegmatites located in the eastern border of Monte Capanne monzogranite pluton, between the villages of San Piero and San't Ilario in Campo (Elba Island, Italy), were studied. All these tourmalines are characterized by a dark overgrowth at the termination ranging from blackish, brownish, purplish-red to bluish colors. Compositional data were collected with electron microprobe along a straight traverse parallel to the **c**-axis from the base to the termination of each crystal using an average step size of 300 μm, except at the overgrowths, where the step size was reduced to about 150 μm, to capture more fine-scale details. A total of 400 spot analyses were collected. Iron oxidation state was determined in selected Fe-rich overgrowths by Mössbauer spectroscopy. On the basis of the chemical data and color displayed, each sample was divided in different zones relatively homogeneous in composition. Then, for each zone, the mineral formula was assessed. It is interesting to point out that during this chemical characterization activity, a new mineral species of the tourmaline supergroup was discovered: celleriite, ideally $\square(Mn^{2+}_2Al)Al_6(Si_6O_{18})(BO_3)_3(OH)_3(OH)$. It was found in the Rosina pegmatite (San Piero in Campo, Elba Island, Italy) and occurs as chemically homogeneous,

millimetric to sub-millimetric zones within the analogous pole of a zoned tourmaline crystal. This new mineral species was approved by the Commission on New Minerals, Nomenclature and Classification (CNMNC) of the International Mineralogical Association (IMA), proposal n. 2019-089 (Bosi et al., 2022a).

In general, chemical analysis revealed that the termination of each crystal is characterized by a sharp increase in Fe and/or Mn that is responsible for the color variation at the analogous pole. However, in some tourmaline samples, the increase in Fe/Mn is quite significant (MnO > 5 wt% and FeO > 2 wt%) to determine not only a color change, but also the evolution from an initial elbaite/F-elbaite composition to celleriite, foitite or schorl at the crystal termination. Such increase in Fe/Mn suggests that a sudden chemical variation in the crystallization environment, with a new supply in Fe/Mn during the latest stages of tourmaline growth, occurred. The increase in Fe and Mn is consistent with the substitution of Li and Al at the *Y* site of the tourmaline structure. However, this substitution can occur in different ways according to whether Fe and Mn totally or partially replace Li and Al. In the crystals from Elba, a partial substitution occurred at *Y*, according to the simplified mechanism $(1.5Li^{+} + 0.5Al^{3+}) \leftrightarrow 2(Mn^{2+},Fe^{2+})$. As this substitution determines a total charge variation, it needs to be balanced by a cation vacancy (□) replacing Na at the X site: $Na^{+} + (1.5Li + 0.5Al)^{\Sigma 3+} \leftrightarrow \square + 2(Mn,Fe)^{\Sigma 4+}$.

Results obtained, along with structural and paragenetic observation of the cavities in which the tourmaline samples were collected, provide evidence that the formation of the observed dark-colored overgrowths is the result of a pocket rupture. This event is further supported by the crystal-chemical features of an elbaitic multicolored tourmaline crystal found in the cavity naturally broken in two fragments and characterized by dark-colored overgrowths, respectively purplish-red at the analogous pole, and yellow-orange at the antilogous pole. On the basis of results obtained, the pocket rupture was responsible for the breakage of this crystal, resulting in the formation of new growth surfaces in the direction of the analogous and the antilogous pole on which Mn-rich overgrowths were formed (Altieri et al., 2023). The crystal breakage strengthens the hypothesis that

the cavity has undergone a mechanical destabilization before overgrowths formation. Consequently, the studied tourmaline crystal fragments preserved important records not only in terms of compositional variations of the geochemical system represented by the dark overgrowths, but also in the mechanical events, i.e. the crystal breakage. In the same work, a comparison of the overgrowths at the analogous and antilogous poles provides evidence of a preferential incorporation of particular elements at the growth surfaces. Beside the preferential uptake of Ca, F and Ti at the antilogous pole, already described in literature, we report for the first time a further preference at level of the ionic charge of the same element (Altieri et al., 2023). In fact, OAS data show a selective uptake of Mn^{2+} at the antilogous pole in the presence of a substantial amount of Mn^{3+} ions, which preferred the analogous one.

On the basis of the overall data obtained, we clearly correlate structural information (i.e., fracturing of the pocket and breakage of tourmaline crystals) to the late-stage tourmaline growth, allowing us to define a genetic model for the dark-colored overgrowths in Elba tourmaline crystals. The event of pocket rupture, probably related to a rigid mechanical shock to which the cavity underwent, caused, for instance, by a thermal contraction during pegmatite cooling, led to mechanical brittle deformations of the enclosing pegmatite through the formation of late-stage fractures. This condition allowed the highly reactive late-stage cavity fluids to permeate the fractures surrounding the cavity, where the early-crystallized cavity-lining and cavity-coating Fe- and Mn-rich minerals were formed. Leaching and corrosion processes ascribed to the late-stage cavity fluids led to the hydrothermal alteration of such minerals, with the subsequent release of Fe and/or Mn in the system, causing a sudden change in the chemical composition of the pocket environment. Based on the size of the cavity, the extent of the fracturing phenomena and the consequent leaching processes, as well as the relative abundance of different primitive minerals in the enclosing pegmatite (such as biotite and spessartine, which are typical paragenetic minerals in Elba pegmatites), the chemical composition of the residual cavity fluids underwent a

variation in concentration in Fe and Mn. This can result in a simple color change up to a chemical evolution from an initial elbaite/F-elbaite composition to foitite, celleriite or schorl at the termination of the tourmaline crystals. For instance, in the case of the "blue-cap" tourmalines, found in small cavities within the San Silvestro and Fucili veins, compositional analyses revealed that the blue coloration of these crystals is related to a slight enrichment in Fe^{2+} (Altieri et al., 2022). In addition, the presence of Fe only in the divalent state suggests persisting reducing conditions in the pocket environment. This interpretation is consistent with a partial opening of the cavity system associated to minor fracturing phenomena (Altieri et al., 2022). On the contrary, in the cavities where the "dark cap" crystals were formed, more extensive fracturing phenomena associated with the presence of abundant Fe/Mn-rich primitive minerals in the enclosing pegmatite, allowed the release of high amounts of Fe/Mn to the residual cavity fluids. In these conditions, a chemical evolution at the analogous termination of the tourmaline crystal occurred. Depending on the prevalence of Fe or Mn, the overgrowth can result in celleriite (Rosina and San Silvestro pegmatites), foitite (Pastori pegmatite) or schorl (Federico pegmatite) compositions. A similar scenario occurred in a cavity of the Rosina pegmatite where a tourmaline crystal, found naturally broken in two fragments and characterized by late-stage Mn-rich dark-colored overgrowths, respectively purplish-red at the analogous pole (Mn^{3+} dependent), and yellow–orange at the antilogous one (Mn^{2+} dependent), was collected (Altieri et al., 2023). In this case the partial collapse of the cavity allowed not only an intense leaching and corrosion of the primitive Mn-rich in the enclosing pegmatite, but also the breakage of the crystal with the formation of two new growth surfaces. However, the extent of Mn in the residual cavity fluid was not sufficient to determine a chemical evolution at the crystal termination. Thus, the mineralogical species remain elbaite/F-elbaite. The presence of Mn of both in the redox state +3 and +2 suggests that corrosion and alteration phenomena occurred in a relatively oxidizing environment.

Sixteen tourmaline grains collected from the secondary deposit of Mavuco in the

Alto Ligonha pegmatite district were studied. The samples collected were found as waterworn grains with a sub-angular to sub-rounded shape. Most of them show a dark-colored prismatic overgrowth that surrounds completely, or in part, a multicolored core ranging from blue, green, yellow to purple-red, even within the same crystal. Compositional data were collected with electron microprobe along a straight traverse perpendicular to the **c**-axis with an average step size of 300 μm for a total of 501 spot analyses. The traverse analyzed in each sample included, when occurring, all the dark-colored overgrowths. In addition, to gain information on the mechanisms underlying the color displayed by the core regions of the tourmaline grains, optical absorption spectroscopy analyses in the UV-Vis region were performed on selected samples with particular chromatic features. The in-depth study on these tourmaline grains, allowed a detailed characterization of their chemical composition, which was correlated to the color displayed. Chemical data indicate that all the studied samples are characterized by a CuO content that never exceeds 1 wt%. Despite the moderate concentration, Cu is able to contribute as color-causing agent especially in those zones where its value approaches 1 wt%. Furthermore, EMPA data revealed that most of the detrital tourmalines are of F-elbaite composition. This is the evidence that the tourmalines from the secondary deposit of Mavuco do not belong only to elbaite species, as assumed in previous studies, but also to different species, including fluor-liddicoatite. A correlation study between chemical composition by EMP analysis and color displayed by the studied tourmaline samples, allowed identifying the gemological variety to which the core zone of these grains belong. Specifically, in the secondary deposit of Mavuco, tourmalines belonging to *indicolite*, *canary tourmaline*, *Paraiba-type* and "*Cu-bearing rubellite*" varieties were identified.

Compositional analysis was extended to two tourmaline crystals from the "Marina" granitic pegmatite (MAV 21 and MAV 22). The presence of Cu in MAV 21 sample, which amount is comparable with that of the detrital tourmalines, supports the hypothesis that the "Marina" pegmatite represents a source from which the tourmaline grains of the secondary deposit of Mavuco were originated.

Thus, the "Marina" pegmatite can be considered a primary deposit for Cu-bearing (*Paraiba-type*) tourmalines and its further exploration can be economically advantageous. The MAV 22 sample is characterized by the presence of a peculiar late-stage black overgrowth covering all over the crystal surfaces, including the prism faces and the antilogous pole, which chemical and morphological features are similar to those observed in most of the detrital tourmalines from the secondary deposit of Mavuco. The presence of such an extended overgrowth, further strengthen the hypothesis that "Marina" pegmatite is a primary source of the detrital tourmalines in the Mavuco area. Furthermore, chemical and spectroscopic investigations on the MAV 22 sample, along with structural and paragenetic observations of the miarolitic cavity in which the tourmaline crystal was collected, allowed extend the genetic model already proposed for Elba tourmaline crystals to the prismatic dark overgrowths characterizing the tourmaline crystals from the Alto Ligonha pegmatitic district.

In this latter case, structural and paragenetic observations of the giant cavity in which the tourmaline crystal was collected (about 12 m in size), provide evidences that the change in the chemical composition of the crystallization environment is related to an intense and widespread fracturing of the cavity, which culminated with the subsequent collapse of the pocket roof. In this scenario, the collapsed amphibolitic host rock, reacting with the residual cavity fluids, allowed the release of large amounts of Fe but also Mg in the system (FeO up to 24 wt% and MgO up to 8 wt%). This condition, associated with a long lasting late-stage tourmaline crystallization ensured by B, which must be still present in the residual fluids of the cavity, allowed for the development of a thick (up to 3-4 mm) late-stage black overgrowth covering all over the tourmaline surfaces that characterize the MAV 22 sample. In this case, the pocket collapse was associated to oxidizing conditions as supported by the high Fe^{3+}/Fetot ratio (> 0.50) observed at the analogous termination of MAV 22 sample. Moreover, the chemical composition of the analogous overgrowth does not fit to any currently approved tourmaline species, and chemical, spectroscopic and crystal-structure refinement results lead to a new

tourmaline species, ferro-bosiite, ideally $NaFe^{3+}_3(Al_4Fe^{2+}_2)(Si_6O_{18})(BO_3)_3(OH)_3O$, recently approved by the IMA-CNMNC (proposal n. 2022-069).

In this study, the cavity-lining and cavity-coating minerals responsible for the Fe/Mg and Mn supply in the residual cavity fluids were identified. While biotite is the main Fe/Mg-source in Elba aplite-pegmatite dikes, both biotite and ferromagnesian amphiboles are accounted for Fe/Mg supply in the petrogenetic systems of the Mavuco area.

Also regarding Mn-supply, more than one Mn-source can be recognized. In the petrogenetic system of Elba pegmatites, spessartine garnet is responsible for both Mn depletion and release in the chemical environment, being the main regulator of Mn levels during the evolution of the pegmatite system. This is consistent with the low content in Mn in the early-stage of tourmaline crystallization, because of the high degree of Mn incorporation in spessartine garmet. On the other hand, spessartine etching results in high availability of Mn ions in the chemical environment, with the consequent formation of unusual Mn-rich dark-colored overgrowths. Differently, the petrogenetic system of the Mavuco area is characterized by the presence of two Mn-bearing minerals, spessartine garnet and apatite, which behave as highly- to fairly-competitive minerals for Mn, respectively. Thus, the initial content of Mn in tourmaline is directly dependent on the abundance of Mn in the pegmatitc melt and the crystallization of spessatine garnet or apatite. The degree of Mn availability in response to the cavity opening is also related to the presence of spessartine or Mn-bearing apatite crystals.

The results obtained in this PhD research improved the knowledge on the opening of geochemical systems in which tourmaline crystallized, and allowed the definition of a model for the genesis of the dark-colored overgrowths in pegmatitic tourmaline crystals. This model can likely be exported to explain the late-stage color and composition anomalies in gem tourmaline crystals of many other gem-pegmatite deposits in the world.

6. REFERENCES

Akizuki M., Kuribayashi T., Nagase T., and Kitakaze A. (2001) Triclinic liddicoatite and elbaite in growth sectors of tourmaline from Madagascar. American Mineralogist, 86, 364–369.

Altieri A., Pezzotta F., Skogby H., Hålenius, U. and Bosi, F. (2022) Blue-growth zones caused by Fe^{2+} in tourmaline crystals from the San Piero in Campo gem-bearing pegmatites, Elba Island, Italy. Mineralogical Magazine, 86, 910–919.

Altieri A., Pezzotta F., Skogby H., Hålenius, U. and Bosi, F. (2023) Dark-coloured Mn-rich overgrowths in an elbaitic tourmaline crystal from the Rosina pegmatite, San Piero in Campo, Elba Island, Italy: witness of late-stage opening of the geochemical system. Mineralogical Magazine, https://doi.org/10.1180/mgm.2022.125

Andreozzi G.B., Bosi F. and Longo M. (2008) Linking Mossbauer and structural parameters in elbaite-schorl-dravite tourmalines. American Mineralogist, 93, 658–666.

Aurisicchio, C., Ottolini, L. and Pezzotta, F. (1999): Electron- and ion-microprobe analyses, and genetic inferences of tourmalines of the foitite–schorl solid solution, Elba Island (Italy). European Journal of Mineralogy, 11, 217–225.

Bartole R. (1995) The North Tyrrhenian-Northern Apennines postcollisional system: constraints for geodynamic model Terra Nova 7, 7–30.

Barton P. Jr (1969) Refinement of the crystal structure of buergerite and the absolute orientation of tourmalines. Acta Crystallographica, 25, 1524–1533.

Berryman E.J., Wunder B., Ertl A., Koch-Müller M., Rhede D., Scheidl K., Giester G. and Heinrich W. (2016) Influence of the X-site composition on tourmaline's crystal structure: Investigation of synthetic K-dravite, dravite, oxy-uvite, and magnesio-foitite using SREF and Raman spectroscopy. Physics and Chemistry of Minerals, 43, 83–102.

Bettencourt Dias M. and Wilson W.E. (2000) Famous mineral localities: The Alto Ligonha pegmatites, Mozambique. Mineralogical Record, 31, 459–497.

Bortolotti V., Pandeli E. and Principi G. (2001) - The geology of Elba Island: an historical introduction. Ofioliti, 26, 79–96.

Bosi F. (2010) Octahedrally coordinated vacancies in tourmaline: A theoretical approach. Mineralogical Magazine 74, 1037–1044.

Bosi F. (2018) Tourmaline crystal chemistry. American Mineralogist, 103, 298–306.

Bosi F., Skogby H., Agrosì G. and Scandale E. (2012) Tsilaisite, $NaMn_3Al_6(Si_6O_{18})(BO_3)_3(OH)_3OH$, a new mineral species of the tourmaline supergroup from Grotta d'Oggi, San Piero in Campo, island of Elba, Italy. American Mineralogist, 97, 989–994.

Bosi F., Skogby H., Lazor P. and Reznitskii L. (2015) Atomic arrangements around the O3 site in Al- and Cr-rich oxy-tourmalines: a combined EMP, SREF, FTIR and Raman study. Physics and Chemistry of Minerals, 42, 441−453.

Bosi F., Skogby H. and Balić-Žunić T. (2016) Thermal stability of extended clusters in dravite: a combined EMP, SREF and FTIR study. Physics and Chemistry of Minerals, 43, 395–407.

Bosi F., Biagioni C. and Oberti R. (2019) On the chemical identification and classification of minerals. Minerals, 9, 591–602.

Bosi F., Altieri A., Cámara F. and Ciriotti M.E. (2020) Chromium-rich vanadio-oxy-dravite from the Tzarevskoye uranium–vanadium deposit, Karelia, Russia: a second world-occurrence of Al–Cr–V–oxy-tourmaline. Mineralogical Magazine, 84, 797–804.

Bosi F., Celata B., Skogby H., Hålenius U., Tempesta G., Ciriotti M.E., Bittarello E., Marengo A. (2021) Mn-bearing purplish-red tourmaline from the Anjanabonoina pegmatite, Madagascar. Mineralogical Magazine, 85, 242–253.

Bosi F., Pezzotta F., Altieri A., Andreozzi G.B., Ballirano P., Tempesta G., Cempírek J., Škoda R., Filip J., Čopjacová R., Novák M., Kampf,A.R., Scribner E.D., Groat L.A. and Evans, R.J. (2022a) Celleriite, $\square(Mn^{2+}_2Al)Al_6(Si_6O_{18})(BO_3)_3(OH)_3(OH)$, a new mineral species of the tourmaline supergroup. American Mineralogist, 107, 31–42.

Bosi, F., Pezzotta, F., Skogby, H., Altieri, A., Hålenius, U., Tempesta, G. and Cempírek, J. (2022b) Princivalleite, $Na(Mn_2Al)Al_6(Si_6O_{18})(BO_3)_3(OH)_3O$, a new mineral species of the tourmaline supergroup from Veddasca Valley, Varese, Italy. Mineralogical Magazine, 86, 78–86.

Bosi F., Skogby H., Hålenius U., Ciriotti M.E, and Mills S.J. (2022c) Lowering R3m symmetry in Mg-Fe-tourmalines: The crystal structures of triclinic schorl and oxy-dravite, and the mineral luinaite-(OH) discredited. Minerals, 12, 430.

Breeding C.M., Rockwell K. and Laurs B.M. (2007) Gem News International: New

Cu-bearing tourmaline from Nigeria. Gems & Gemology, 43, 384–385.

Buŕival Z. and Novák M. (2015) Hydrothermal replacement of garnet by tourmaline in elbaite subtype LCT pegmatites. 7th International Symposium on Granitic Pegmatites, PEG 2015 Książ, Poland.

Carmignani L. and Kligfield R. (1990) Crustal extension in the northern Apennines: the transition from compression to extension in the Alpi Apuane core complex. Tectonics, 9, 1275–1303.

Černý P. (1991) Rare-element granite pegmatites. I. Anatomy and internal evolution of pegmatite deposits. Geosci. Can. 18, 49–67.

Černý P. (2000) Constitution, petrology, affiliations and categories of miarolitic pegmatites. Memorie della Società Italiana di Scienze Naturali e del Museo Civico di Storia Naturale di Milano, 30, 5–12.

Cronwright M.S. (2005) A Review of the Rare-element Pegmatites of the Alto Ligonha Pegmatite Province, Northern Mozambique and Exploration Guidelines. MSc thesis (unpublished), Rhodes University, Grahamstown, South Africa.

da Fonseca-Zang W.A, Zang J.W. and Hofmeister W. (2008) The Ti-Influence on the Tourmaline Color. Journal of the Brazilian Chemical Society, 19, 1186–1192.

D'Achiardi G. (1894) Le tormaline del granito elbano. Parte I. Atti della Società Toscana di Scienze Naturali. Memorie, XIII, 229–322.

D'Achiardi G. (1897) Le tormaline del granito elbano. Parte II. Atti della Società Toscana di Scienze Naturali. Memorie, XV, 3–75.

De Vito C., Aurisicchio C., Ferrini V. and Pezzotta F. (2002) Nb-Ta oxides from Anjanabonoina pegmatite. International Mineralogical Association 18th General Meeting (Edinburgh), Program Abstract, 275

Dietrich R.V. (1985) The Tourmaline Group, 1st edition. Van Nostrand Reinhold, New York, 300 pp.

Dini A., Innocenti F., Rocchi S., Tonarini S. and Westerman D.S. (2002) Magmatic evolution of the laccolith-pluton-dyke complex of Elba Island, Italy. Geological Magazine, 139, 257–279.

Dirlam D.M., Laurs B.M., Pezzotta F. and Simmons W.B. (2002) Liddicoatite tormaline from Anjanabonoina, Madagascar. Gems & Gemology, 38, 28–53.

Dutrow B.L. and Henry D.J. (2000) Complexly zoned fibrous tourmaline, Cruzeiro mine, Minas Gerais, Brazil: a record of evolving magmatic and hydrothermal fluids. Canadian Mineralogist, 38, 131–143.

Dutrow B.L. and Henry D.J. (2011) Tourmaline: A geologic DVD. Elements, 7, 301–306.

Dutrow B.L. and Henry D.J. (2016) Fibrous tourmaline: a sensitive probe of fluid compositions and petrologic environments. The Canadian Mineralogist, 54, 311–335.

Dutrow B.L. and Henry D.J. (2018) Tourmaline compositions and textures: reflections of the fluid phase. Journal of Geosciences, 63, 99–110.

Ertl A., Rossman G.R., Hughes J.M., Prowatke S. and Ludwig T. (2005) Mn-bearing "oxy-rossmanite" with tetrahedrally coordinated Al and B from Austria: Structure, chemistry and infrared and optical spectroscopic study. American Mineralogist, 90, 481–487.

Farina F., Dini A., Innocenti F., Rocchi S. and Westerman D.S. (2010) Rapid incremental assembly of the Monte Capanne pluton (Elba Island, Tuscany) by downward stacking of magma sheets. GSA Bulletin, 120, 1463–1479.

Felch. M., Falster A.U., and Simmons W.B. (2016) Iron-bearing pollucite and tourmaline replacement of garnet in the garnet line in the Mt. Mica and Havey pegmatites, Western Maine. The Canadian Mineralogist, 54, 1071–1086.

Ferrara G. and Tonarini S. (1993) - L'Isola d'Elba: un laboratorio di geocronologia. Memorie della Società Geologica Italiana, 49, 227–232.

Foord E.E. (1976): Mineralogy and Petrogenesis of Layered Pegmatite–Aplite Dikes in the Mesa Grande District, San Diego County, California. Ph.D. thesis, Stanford Univ., Stanford, California.

Fritsch E. and Rossman G.R. (1987) An update on color in gems. Part I. Introduction and colors caused by dispersed metal ions. Gems and Gemology, 23, 126–139.

Fritsch E., Shigley J.E., Rossman G.R., Mercer M.E., Muhlmeister S.M. and Moon M. (1990) Gem-quality cuprian-elbaite tourmalines from São José da Batalha, Paraíba, Brazil. Gems & Gemology, 26, 189–205

Furuya M. and Furuya M. (2007) Paraíba Tourmaline—Electric Blue Brilliance Burnt into Our Minds. Japan Germany Gemmological Laboratory, Kofu, Japan,

24 pp.

Garfagnoli F., Menna F., Pandeli E. & Principi G. (2005) The Porto Azzurro unit (Monte Calamita promontori, southeastern Elba Island, Tuscany): stratigraphic, tectonic and metamorphic evolution. Bollettino della Società Geologica Italiana.Volume Speciale n.3, 119–138.

Gebert W. and Zemann J. (1965) Messung des Ultrarot-Pleochroismus von Mineralen II. Der Pleochroismus der OH-Streckfrequenz in Turmalin. Neues Jahrbuch für Mineralogie, Monatshefte, 8, 232–235.

Goldschmidt V.M. (1922) Atlas der Kristallformen. Carl Winters Universitäts Buchhandlung, Heidelberg, Germany IX, 193 pp

Gonzalez-Carreño T., Fernandez M. and Sanz J. (1988) Infrared and electron microprobe analysis in tourmalines. Physics and Chemistry of Minerals, 15, 452–460.

Grew E.S., Krivovichev S.V., Hazen R.M., and Hystad G. (2016) Evolution of structural complexity in boron minerals. Canadian Mineralogist, 54, 125–143.

Haralampiev A.G. and Grover J. (1993) Synthesis experiments in the binary system tsilaisite–dravite, $Na(Mn_xMg_{1-x})_3Al_6(BO_3)_3Si_6O_{18}(OH)_4$, at T = 375-700° and P = 2000 bars; does garnet control the occurrence of tourmaline? Geological Society of America Abstracts with Program, 25, 94–55.

Hawthorne F.C. (1996) Structural mechanisms for light-element variations in tourmaline. Canadian Mineralogist, 34, 123–132.

Hawthorne F.C. and Dirlam D.M. (2011) Tourmaline the indicator mineral: From atomic arrangement to Viking navigation. Elements, 7, 307–312.

Henry D.J. and Dutrow B.L. (1992) Tourmaline in a low grade clastic metasedimentary rocks: an example of the petrogenetic potential of tourmaline. Contribution to Mineralogy and Petrology, 112, 203–218.

Henry D.J. and Dutrow B.L. (1996) Metamorphic tourmaline and its petrologic applications. In: Grew ES, Anovitz LM (eds) Boron: Mineralogy, Petrology and Geochemistry. Reviews in Mineralogy, 33, 503–557.

Henry D.J. and Dutrow B.L. (2011) The incorporation of fluorine in tourmaline: Internal crystallographic controls or external environmental influences? Canadian Mineralogist, 49, 41–56.

Henry D.J. and Dutrow B.L. (2012) Tourmaline at diagenetic to low-grade metamorphic conditions: its petrologic applicability. Lithos 154, 16–32

Henry D.J. and Dutrow B.L. (2018) Tourmaline studies through time: contributions to scientific advancements. Journal of Geosciences, 63, 77–98.

Henry D.J., Novák M., Hawthorne F.C., Ertl A., Dutrow B., Uher P. and Pezzotta F. (2011) Nomenclature of the tourmaline supergroup minerals. American Mineralogist, 96, 895–913.

Hernández-Filiberto L., Roda-Robles E., Simmons W.B. and Webber K.L. (2021) Garnet as Indicator of Pegmatite Evolution: The Case Study of Pegmatites from the Oxford Pegmatite Field (Maine, USA). Minerals, 11, 802. https://doi.org/10.3390/min11080802

Hughes J.M., Rakovan J., Ertl A., Rossman G.R., Bakshee, I., and Bernhardt H.J. (2011) Dissymmetrization in tourmaline: the atomic arrangement of sectorally zoned triclinic Ni-bearing dravite. Canadian Mineralogist, 49, 29–40.

Koivula J.I. and Kammerling R.C., Eds. (1989) Gem News: Unusual tourmalines from Brazil. Gems & Gemology, 25, 181–182.

Krzemnicki M.S. and Wang H.A.O. (2022) Paraíba or Not? Cu-bearing Tourmaline with a Distinct Fe Concentration. The Journal of Gemology, 38, 20–22.

Krivovichev S.V. (2013) Structural complexity of minerals: Information storage and processing in the mineral world. Mineralogical Magazine, 77, 275–326.

Lächelt S. (2004) The Geology and Mineral Resources of Mozambique. National Directorate of Geology, Maputo, Mozambique, 515 pp.

Lagarec K. and Rancourt D. G. (1998) RECOIL, Mössbauer spectral analysis software for windows (version 1.0). Department of Physics, University of Ottawa, Canada.

Laurs B.M., Simmons W.B., Rossman G.R., Fritz E.A, Koivula J.I., Anckar B. and Falster A.U. (2007) Yellow Mn-rich tourmaline from the Canary Mining Area, Zambia. Gems & Gemology, 43, 314–331.

Laurs B.M., Zwaan J.C.,. Breeding C.M., Simmons W.B., Beaton D., Rijsdijk K.F., Befi R. and Falster A.U. (2008) Copper-bearing (Paraiba-type) tourmaline from Mozambique. Gems & Gemology, 44, 4–30.

London, D. (2006). Spessartine from Navegador, Minas Gerais, Brazil: etch or

growth features.
http://www.minsocam.org/msa/special/pig/pig_articles/etched_spssrtn.pdf.

Lussier A.J. and Hawthorne F.C. (2011) Oscillatory zoned liddicoatite from Anjanabonoina, central Madagascar. II. Compositional variation and mechanisms of substitution. The Canadian Mineralogist, 49, 89–104.

Lussier A.J., Aguiar P.M., Michaelis V.K., Kroeker S., Herwig S., Abdu Y. and Hawthorne F.C. (2008) Mushroom elbaite from the Kat Chay mine, Momeik, near Mogok, Myanmar: I. Crystal chemistry by SREF, EMPA, MAS NMR and Mössbauer spectroscopy. Mineralogical Magazine, 72, 747–761.

Lussier A., Ball N.A., Hawthorne F.C., Henry D.J., Shimizu R., Ogasawara Y., and Ota T. (2016) Maruyamaite, $K(MgAl_2)(Al_5Mg)Si_6O_{18}(BO_3)_3(OH)_3O$, a potassium-dominant tourmaline from the ultrahigh-pressure Kokchetav massif, northern Kazakhstan: description and crystal structure. American Mineralogist, 101, 355–361.

Marinelli G. (1959) Le intrusioni terziarie dell'Isola d'Elba. Atti Società Toscana, Scienze Naturali 66, 50–253.

Mashkovtsev R.I., Smirnov S.Z. and Shigley J.E. (2006) The features of the Cu^{2+}-entry into the structure of tourmaline. Journal of Structural Chemistry, 42, 252–257.

Marschall H.R., Korsakov A.V., Luvizotto G.L., Nasdala L., and Ludwig T. (2009) On the occurrence and boron isotopic composition of tourmaline in (ultra)highpressure metamorphic rocks. Journal of the Geological Society, 166, 811–823.

Mattson S.M. and Rossman G.R. (1987) Fe^{2+}-Fe^{3+} interactions in tourmaline. Physics and Chemistry of Minerals, 14, 163–171.

Melcher F., Graupner T., Gäbler H., Sitnikova M., Henjes-Kunst F., Oberthür T., Gerdes A. and Dewaele S. (2015) Tantalum–(niobium–tin) mineralisation in African pegmatites and rare metal granites: Constraints from Ta–Nb oxide mineralogy, geochemistry and U–Pb geochronology. Ore Geology Reviews, 64, 667–719.

Novák M. and Taylor M.C. (2000) Foitite: formation during late stages of evolution of complex granitic pegmatites at Dobrá Voda, Czech Republic, and Pala,

California, U.S.A. The Canadian Mineralogist, 38, 1399–1408.

Novák M., Selway J.B. Černý P., Chapman R.C. and Masau M. (2000) Correlation between Mn content in tourmaline and garnet abundance in two elbaite-subtype pegmatites: Dolní Rožínka and Pikárec, Czech Republic. Geological Association of Canada - Mineralogical Association of Canada, Joint Annual Meeting, abstract #584.

Orlandi P. and Pezzotta F. (1996) Minerali dell'Isola d'Elba, i minerali dei giacimenti metalliferi dell'Elba orientale e delle pegmatiti del M.te Capanne. Ed. Novecento Grafico, Bergamo. 248 pp.

Pandeli E. and Puxeddu M. (1990) Palaeozoic age for the Tuscan upper metamorphic sequences of Elba and its implications for the geology of the Northern Apennines (Italy). Eclogae Geologicae Helvetiae, 83, 123–142.

Pandeli E., Principi G., Bortolotti V., Benvenuti M., Fazzuoli M., Dini A., Fanucci A., Menna F and Nirta G. (2013) The Elba Island: an intriguig geological puzzle in the Northern Tyrrhenian Sea. Periodico semestrale del Servizio Geologico d'Italia - ISPRA e della Società Geologica Italiana Geological Field Trips, 5,.2.1 (DOI 10.3301/GFT.2013.03).

Pesquera A., Gil-Crespo P.P., Torres-Ruiz F., Torres-Ruiz J. and Roda-Robles E. (2016) A multiple regression method for estimating Li in tourmaline from electron microprobe analyses. Mineralogical Magazine, 80, 1129–1133.

Pezzotta F. (2000) Internal structures, parageneses and classification of the miarolitic Li-bearing complex pegmatites of Elba Island (Italy). Mineralogy and petrology of shallow depth pegmatites. Papers from the First International Workshop. Memorie della Società Italiana di Scienze Naturali e del Museo Civico di Storia Naturale di Milano, 30, 29–43.

Pezzotta F. (2021) A history of tourmaline from the Island of Elba. The Mineralogical Record, 52, 669–720.

Pezzotta F. and Laurs B.M. (2011) Tourmaline: The kaleidoscopic gemstone. Elements, 7, 331–336.

Pinna P., Jourde G., Calvez J.Y., Mroz J.P. and Marques J.M. (1993) The Mozambique Belt in northern Mozambique: Neo-proterozoic (1100–850 Ma) crustal growth and tectogenesis, and superimposed Pan-African (800–550 Ma) tectonism. Precambrian Research, 62, 1–59.

Pouchou J.L. and Pichoir F. (1991) Quantitative analysis of homogeneous or stratified microvolumes applying the model "PAP". Pp. 31–75 in: Electron Probe Quantitation (K.F.J. Heinrich and D.E. Newbury, editors). Plenum, New York.

Prescher C., McCammon C. and Dubrowinsky L. (2012) MossA: a program for analyzing energy-domain Mössbauer spectra from conventional and synchrotron sources. Journal of Applied Crystallography, 45, 329–331.

Puxeddu M., Saupé F., Dechomets R., Gianelli G. and Moine B. (1984) Geochemistry and stratigraphic correlations. Application to the investigation of geothermal and mineral resources of Tuscany, Italy (contribution to the knowledge of the ore deposits of Tuscany, II). Chemical Geology, 43, 77–113.

Reinitz I. and Rossman G.R. (1988) Role of natural radiation in tourmaline coloration. American Mineralogist, 73, 822–825.

Rossman G.R. (1997) Color in tourmaline. Tourmaline 1997., Int. Symp. On Tourmaline (Nové Město na Moravě), Abstr. Vol.

Rossman G.R. (2014) Optical spectroscopy. In: Henderson G.S., Neuville D.R., Downs R.T. (eds) Spectroscopy Methods in Mineralogy and Materials Sciences. Reviews in Mineralogy and Geochemistry, 78, 371–398.

Rossman G.R. and Mattson S.M. (1986) Yellow, Mn-rich elbaite with Mn-Ti intervalence charge transfer. American Mineralogist, 71, 599–602.

Rossman G.R., Fritsch E. and Shigley J.E. (1991) Origin of color in cuprian elbaite from São José de Batalha, Paraíba, Brazil. American Mineralogist, 76, 1479–1484

Selway J.B. (1999): Compositional Evolution of Tourmaline in Granitic Pegmatites. Ph.D. thesis, Univ. Manitoba, Winnipeg, Manitoba.

Selway J.B., Novák M., Černý P. and Hawthorne F.C. (1999) Compositional evolution of tourmaline in lepidolite-subtype pegmatites. European Journal of Mineralogy, 11, 569–584.

Shigley J.E., Cook B.C., Laurs B.M., Bernardes de Oliveira M. (2001) An update on "Paraíba" tourmaline from Brazil. Gems & Gemology, 37, 260–276.

Shtukenberg A., Rozhdestvenskaya I., Frank-Kamenetskaya O., Bronzova J., Euler H., Kirfel A., Bannova I., and Zolotarev A. (2007) Symmetry and crystal structure of biaxial elbaite-liddicoatite tourmaline from the Transbaikalia region, Russia. American Mineralogist, 92, 675–686.

Skogby H., Bosi F., and Lazor P. (2012) Short-range order in tourmaline: a vibrational spectroscopic approach to elbaite. Physics and Chemistry of Minerals, 39, 811–816.

Slater M. (2006) Globetrotter Travel Map – Mozambique, 3rd ed. New Holland (Publishers) Ltd., London, UK.

Smith G. (1978) A reassessment of the role of iron in the 5000–30,000 cm−1 region of the electronic absorption spectra of tourmaline. Physics and Chemistry of Minerals, 3, 343–373.

Smith C.P., Bosshart G. and Schwarz D. (2001) Gem News International: Nigeria as a new source of copper-manganese-bearing tourmaline. Gems & Gemology, 37, 239–240.

Taran M.N., Lebedev, A.S. and Platonov A.N. (1993) Optical absorption apectroscopy of synthetic tourmalines. Physics and Chemistry of Minerals, 20, 209–220.

Taran M.N and Rossman G.R. (2002) High-temperature, high-pressure optical spectroscopic study of ferric-iron-bearing tourmaline. American Mineralogist, 87, 1148–1153.

Trevisan L. (1951) La 55a Riunione Estiva della Società Geologica Italiana. Isola d'Elba, Settembre 1951, 70 (1953), 435–472. van Hinsberg V.J., Henry D.J. and Dutrow B.L. (2011a) Tourmaline as a petrologic forensic mineral: A unique recorder of its geologic past. Elements, 7, 327–332.

van Hinsberg V.J., Schumacher J.C., Kearns, S., Mason P.R.D. and Franz G. (2006) Hourglass sector zoning in metamorphic tourmaline and resultant major and trace-element fractionation. American Mineralogist, 91, 717–728.

van Hinsberg V.J., Henry D.J. and Dutrow B.L. (2011a) Tourmaline as a petrologic forensic mineral: A unique recorder of its geologic past. Elements, 7, 327–332.

van Hinsberg V.J., Henry D.J. and Marschall H.R. (2011b) Tourmaline: an ideal indicator of its host environment. Canadian Mineralogist, 49, 1–16.

Watenphul A., Burgdorf M., Schlüter J., Horn I., Malcherek T. and Mihailova B. (2016) Exploring the potential of Raman spectroscopy for crystallochemical analyses of complex hydrous silicates: II. Tourmalines. American Mineralogist, 101, 970–985.

Wentzell C.Y. (2004) Lab Notes: Copper-bearing color-change tourmaline from

Mozambique. Gems & Gemology, 40, 250–251.

Westerman D.S., Dini A., Innocenti F. and Rocchi S. (2004) Rise and fall of a nested Christmas-tree laccolith complex, Elba Island, Italy. In: Breitkreu, C, Petford N (eds). Physical geology of high-level magmatic systems. Geological Society of London, Spec Pub 234, London, 195–213.

Zang J and da Fonseca-Zang W (2002) Is there really black tourmaline? extraLapis English, 3, 30–33.

7. ANNEXES

7.1 Annex A

During my PhD research activity, I had the opportunity to identify three new mineral species of the tourmaline supergroup. For each of them, a proposal for introducing the possible new mineral was submitted for approval to the IMA-CNMNC (International Mineralogical Association-Commission on New Minerals, Nomenclature and Classification).

The new tourmaline species identified are:

- **2019-089 Celleriite**

  Ideal chemical formula: $\square(Mn^{2+}_2Al)Al_6(Si_6O_{18})(BO_3)_3(OH)_3(OH)$

  It was discovered in a wide miarolitic cavity of the Rosina pegmatite, San Piero in Campo, Elba Island (Tyrrhenian Sea, Italy), and occurs as a millimetric brownish overgrowth at the analogous pole of an elbaite–fluor-elbaite–rossmanite crystal. In the Rosina pegmatite, celleriite grew during the latest-stage of the pegmatite cavity evolution, after an event of pocket rupture.

  This new mineral species was approved by the Commission on New Minerals, Nomenclature and Classification (CNMNC) of the International Mineralogical Association (IMA), proposal n. 2019-089.

  After the approval, a manuscript on this new tourmaline species was drafted and consequently published in a peer-reviewed international journal (see Annex B).

- **2020-056 Princivalleite**

  Ideal chemical formula: $Na(Mn^{2+}_2Al)Al_6(Si_6O_{18})(BO_3)_3(OH)_3O$

  It was discovered in the Veddasca Valley, Luino area, Varese (Lombardy, Italy), at the centre of a small vertical pegmatitic vein (2–3 cm wide and few metres long) crosscutting a lens of flaser gneiss, and occurs as aggregates of azure crystals up to 1 cm long. Princivalleite from Veddasca Valley is a geochemical anomaly, originated in a B-rich and peraluminous anatectic pegmatitic melt formed in situ, poor in Fe and characterized by reducing

conditions in the late-stage metamorphic fluids derived by the flaser gneiss. The Mn-enrichment in this new tourmaline is due to absence of other minerals competing for Mn such as spessartine garnet.

This new mineral species was approved by the Commission on New Minerals, Nomenclature and Classification (CNMNC) of the International Mineralogical Association (IMA), proposal n. 2020-056.

After the approval, a manuscript on this new tourmaline species was drafted and consequently published in a peer-reviewed international journal (see Annex C).

- **2022-069 Ferro-bosiite**

  Ideal chemical formula: $NaFe^{3+}_3(Al_4Fe^{2+}_2)(Si_6O_{18})(BO_3)_3(OH)_3O$

  It was discovered in a giant collapsed cavity of about 12 m in size, in the "Marina" granitic pegmatite, at the Mavuco locality (Alto Ligonha, Mozambique), and occurs as a thick (up to 4 mm) and chemically inhomogeneous black acicular late-stage overgrowth at the analogous pole of a fluor-elbaite crystal. The genesis of Ferro-bosiite in the "Marina" pegmatite is related to an event of pocket collapse within a giant miarolitic cavity. Such dramatic event led the collapsed material, composed among other accessory minerals by biotite crystals, to react with the cavity fluids within the pocket. This led to a massive release of Fe into the fluids, in a new crystallization environment characterized by oxidizing conditions.

  This new mineral species was approved by the Commission on New Minerals, Nomenclature and Classification (CNMNC) of the International Mineralogical Association (IMA), proposal n. 2022-069.

  After the approval, a manuscript on this new tourmaline species has been planned to draft.

The front pages of the announcement of the discovered new minerals, published in the *European Journal of Mineralogy* under the heading of a CNMNC Newsletter, are collected in this section.

Known synthetic analogue
Monoclinic: $P2_1/n$; structure determined
$a = 7.3830(3)$, $b = 10.7545(5)$, $c = 9.3517(7)$ Å, $\beta = 111.500(8)°$
6.744(47), 3.454(80), 3.301(100), 3.114(42), 3.048(73), 2.803(41), 2.745(44), 1.752(45)
Type material is deposited in the mineralogical collections of the Natural History Museum of Los Angeles County, 900 Exposition Boulevard, Los Angeles, California 90007, USA, catalogue number 67505 (holotype), and the RRUFF Project, University of Arizona, USA, deposition number R190033 (cotype)
How to cite: Kampf, A. R., Housley, R. M., Rossman, G. R., Yang, H., and Downs, R. T.: Adanite, IMA 2019-088, in: CNMNC Newsletter 53, Eur. J. Mineral., 32, https://doi.org/10.5194/ejm-32-209-2020, 2020.

IMA No. 2019-089

Celleriite
$\square(Mn_2^{2+}Al)Al_6(Si_6O_{18})(BO_3)_3(OH)_3(OH)$
Rosina pegmatite, San Piero in Campo, Campo nell'Elba (LI), Elba, Tuscany, Italy
Ferdinando Bosi*, Federico Pezzotta, Alessandra Altieri, Giovanni B. Andreozzi, Paolo Ballirano, and Gioacchino Tempesta
*E-mail: ferdinando.bosi@uniroma1.it
Tourmaline supergroup
Trigonal: $R3m$; structure determined
$a = 15.9518(4)$, $c = 7.1579(2)$ Å
6.345(45), 4.210(60), 3.983(88), 3.453(55), 2.942(55), 2.573(100), 2.036(38), 1.913(26)
Type material is deposited in the mineralogical collections of the Museo Universitario di Scienze della Terra, Sapienza Università di Roma, P.le Aldo Moro, 5, 00185 Rome, Italy, catalogue number 33287/403 (holotype), and the Museo Civico di Storia Naturale, Corso Venezia 55, 20121 Milan, Italy, catalogue number M38847 (cotype)
How to cite: Bosi, F., Pezzotta, F., Altieri, A., Andreozzi, G. B., Ballirano, P., and Tempesta, G.: Celleriite, IMA 2019-089, in: CNMNC Newsletter 53, Eur. J. Mineral., 32, https://doi.org/10.5194/ejm-32-209-2020, 2020.

IMA No. 2019-090

Grammatikopoulosite
NiVP
Agios Stefanos mine, ca. 10 km S of the Domokos village, Othrys ophiolite, Greece (39°04′59″ N, 22°25′59″ E)
Luca Bindi*, Federica Zaccarini, Elena Ifandi, Basilios Tsikouras, Chris J. Stanley, Giorgio Garuti, and Daniela Mauro
*E-mail: luca.bindi@unifi.it
Structurally related to florenskyite
Orthorhombic: *Pnma*; structure determined
$a = 5.8893(8)$, $b = 3.5723(4)$, $c = 6.8146(9)$ Å
2.950(20), 2.785(25), 2.273(60), 2.157(100), 2.118(25), 1.915(15), 1.824(15), 1.784(20)
Type material is deposited in the mineralogical collections of the Museo di Storia Naturale, Università di Pisa, Via Roma 79, Calci (PI), Italy, catalogue number 19911
How to cite: Bindi, L., Zaccarini, F., Ifandi, E., Tsikouras, B., Stanley, C. J., Garuti, G., and Mauro, D.: Grammatikopoulosite, IMA 2019-090, in: CNMNC Newsletter 53, Eur. J. Mineral., 32, https://doi.org/10.5194/ejm-32-209-2020, 2020.

IMA No. 2019-091

Ellinaite
$CaCr_2O_4$
In paralavas in the Halamish and Zohar wadi, southern part of the Hatrurim Basin, Israel (31°09′47″ N, 35°17′57″ E – holotype); as mineral phase of an inclusion within diamond, collected from gravel of Sorriso creek, a tributary of Aripuanã River, Mato Grosso, Brazil (11°20′ S, 59°11′ W – cotype).
Victor V. Sharygin*, Sergey N. Britvin, Felix V. Kaminsky, Richard Wirth, Elena N. Nigmatulina, Grigory A. Yakovlev, Konstantin A. Novoselov, and Mikhail N. Murashko
*E-mail: sharygin@igm.nsc.ru
The Cr analogue of harmunite
Orthorhombic: *Pnma*; structure determined
$a = 8.868(9)$, $b = 2.885(3)$, $c = 10.355(11)$ Å
4.434(23), 2.589(54), 2.567(100), 2.424(69), 2.418(62), 2.148(34), 1.767(35), 1.758(22)
Type material is deposited in the collections of the Fersman Mineralogical Museum, Russian Academy of Sciences, Leninskiy Prospekt 18-2, Moscow 119071, Russia, registration number 5439/1 (holotype), the Central Siberian Geological Museum, V.S. Sobolev Institute of Geology and Mineralogy, Siberian Branch of the RAS, prospekt Akademika Koptyuga 3, Novosibirsk 630090, Russia, catalogue number VII-102/1 (holotype), and the Vernadsky Institute of Geochemistry and Analytical Chemistry, Kosygin St. 19, Moscow 119334, Russia, F.V. Kaminsky collection, catalogue number 8/108 (cotype)
How to cite: Sharygin, V. V., Britvin, S. N., Kaminsky, F. V., Wirth, R., Nigmatulina, E. N., Yakovlev, G. A., Novoselov, K. A., and Murashko, M. N.: Ellinaite, IMA 2019-091, in: CNMNC Newsletter 53, Eur. J. Mineral., 32, https://doi.org/10.5194/ejm-32-209-2020, 2020.

IMA No. 2019-029a

Michitoshiite-(Cu)
$Rh(Cu_{1-x}Ge_x)\quad 0 < x \leq 0.5$
Haraigawa, Misato machi, Kumamoto Prefecture, Kyushu, Japan

Poudrette (Demix) quarry, Mont Saint-Hilaire, Quebec, Canada (45°33′46″ N, 73°08′30″ W)

Inna Lykova*, Ralph Rowe, Glenn Poirier, Henrik Friis, and Kate Helwig

*E-mail: ilykova@nature.ca

Mckelveyite group

Triclinic: $P1$; structure determined

$a = 8.9950(4)$, $b = 9.0096(3)$, $c = 6.7676(4)$ Å, $\alpha = 102.745(4)$, $\beta = 116.324(5)$, $\gamma = 60.011(5)°$

6.07(31), 4.372(100), 4.037(25), 3.201(25), 2.831(67), 2.601(39), 2.236(24), 1.974(24)

Type material is deposited in the mineralogical collections of the Canadian Museum of Nature, 240 McLeod Street, Ottawa, Ontario, Canada, catalogue number CMNMC 53660

How to cite: Lykova, I., Rowe, R., Poirier, G., Friis, H., and Helwig, K.: Alicewilsonite-(YCe), IMA 2020-055, in: CNMNC Newsletter 58, Eur. J. Mineral., 32, https://doi.org/10.5194/ejm-32-645-2020, 2020.

IMA no. 2020-056

Princivalleite

$Na(Mn_2Al)Al_6(Si_6O_{18})(BO_3)_3(OH)_3O$

Along the cut of a small road on the eastern side of the Curiglia Village, Veddasca Valley, Luino (Varese), Lombardy, Italy (46°03′30.74″ N, 8°48′24.47″ E)

Ferdinando Bosi*, Federico Pezzotta, Henrik Skobgy, Alessandra Altieri, Ulf Hålenius, Gioacchino Tempesta, and Jan Cempírek

*E-mail: ferdinando.bosi@uniroma1.it

Tourmaline supergroup

Trigonal: $R3m$; structure determined

$a = 15.9155(2)$, $c = 7.1166(1)$ Å

4.198(43), 3.974(50), 3.441(67), 2.934(78), 2.567(100), 2.028(51), 1.908(41), 1.647(34)

Type material is deposited in the mineralogical collections of the Museo Civico di Storia Naturale, Corso Venezia 55, 20121 Milan, Italy, catalogue number M38850

How to cite: Bosi, F., Pezzotta, F., Skobgy, H., Altieri, A., Hålenius, U., Tempesta, G., and Cempírek, J.: Princivalleite, IMA 2020-056, in: CNMNC Newsletter 58, Eur. J. Mineral., 32, https://doi.org/10.5194/ejm-32-645-2020, 2020.

IMA no. 2020-057

Ferriprehnite

$Ca_2Fe^{3+}(AlSi_3)O_{10}(OH)_2$

Kouragahana, Kitaura, Mihonoseki-cho, Matsue City, Shimane Peninsula, Shimane Prefecture, Japan

Mariko Nagashima*, Daisuke Nishio-Hamane, Shuichi Ito, and Takahiro Tanaka

*E-mail: nagashim@yamaguchi-u.ac.jp

The Fe^{3+} analogue of prehnite

Orthorhombic: $Pma2$; structure determined

$a = 18.615(1)$, $b = 5.4882(3)$, $c = 4.6735(3)$ Å

4.674(32), 3.558(32), 3.495(54), 3.324(45), 3.298(43), 3.087(100), 2.572(77), 1.779(45)

Type material is deposited in the mineralogical collections of the National Museum of Nature and Science, 4-1-1 Amakubo, Tsukuba 305-0005, Japan, specimen number NSM-M47662

How to cite: Nagashima, M., Nishio-Hamane, D., Ito, S., and Tanaka, T.: Ferriprehnite, IMA 2020-057, in: CNMNC Newsletter 58, Eur. J. Mineral., 32, https://doi.org/10.5194/ejm-32-645-2020, 2020.

IMA no. 2020-058

Ferro-fluoro-edenite

$NaCa_2Fe_5^{2+}(Si_7AlO_{22})F_2$

La Fossa crater, Vulcano Island, Messina province, Sicily, Italy (38°23′59″ N, 14°57′36″ E)

Italo Campostrini*, Francesco Demartin, Pietro Vignola, and Federico Pezzotta

*E-mail: italo.campostrini@unimi.it

Amphibole supergroup

Monoclinic: $C2/m$; structure determined

$a = 9.913(2)$, $b = 18.174(4)$, $c = 5.294(1)$ Å, $\beta = 104.85(3)°$

8.54(100), 4.506(16), 3.154(16), 2.833(43), 2.057(14), 1.910(12), 1.662(15), 1.517(11)

Type material is deposited in the mineralogical collections of the Museo Civico di Storia Naturale, Corso Venezia 55, 20121 Milan, Italy, catalogue number M38849

How to cite: Campostrini, I., Demartin, F., Vignola, P., and Pezzotta, F.: Ferro-fluoro-edenite, IMA 2020-058, in: CNMNC Newsletter 58, Eur. J. Mineral., 32, https://doi.org/10.5194/ejm-32-645-2020, 2020.

IMA no. 2020-059

Nakkaalaaqite

$K_2[Na_3Ca]LiCa_2Ti_2Be_4Si_{12}O_{38}$

Mount Nakkaalaaq, Ilímaussaq Alkaline Complex, Greenland (60°58′56″ N, 45°54′58″ W)

Henrik Friis*, Glenn Poirier, Tom Andersen, and Robert A. Gault

*E-mail: geofriis@yahoo.com

The Li analogue of odintsovite

Orthorhombic: $Fddd$; structure determined

$a = 13.1029(2)$, $b = 14.2468(2)$, $c = 33.6099(5)$ Å

9.249(100), 4.424(39), 4.159(40), 3.278(84), 3.162(41), 3.046(41), 2.928(32), 2.412(34)

Type material is deposited in the mineralogical collections of the Natural History Museum of Denmark, University of Copenhagen, Øster Voldgade 5–7, 1350 Copenhagen K, Denmark, catalogue number 2000.280 (optical study), the

Type material is deposited in the collections of the Geological Museum of China, No. 16, Yangrou Hutong, Xisi, Beijing 100031, People's Republic of China, catalogue number M16138

How to cite: Meng, Y., and Gu, X.: Ruizhongite, IMA 2022-066, in: CNMNC Newsletter 70, Eur. J. Mineral., 34, https://doi.org/10.5194/ejm-34-591-2022, 2022.

IMA no. 2022-067

Novikovite

$(NH_4)_4(Mo_2^{6+}Mo_2^{5+})_4O_8(SO_4)_5$

Nvi

Near Ravat Kishlak (village), about 100 km north of Dushanbe, Kuhi-Malik area, Fan-Jagnob lignite basin, Tajikistan (39°11′02″ N, 68°35′11″ E)

Leonid A. Pautov, Mirak A. Mirakov, Oleg I. Siidra*, Nikita V. Chukanov, Artem S. Borisov, Vladimir Y. Karpenko, Pavel Y. Plechov, and Saimudasir Makhmadsharif

* E-mail: o.siidra@spbu.ru

New structure type

Monoclinic: $P2_1/n$; structure determined

$a = 8.936(2)$, $b = 13.210(3)$, $c = 22.555(5)$ Å, $\beta = 94.484(4)°$

11.39(51), 8.54(40), 8.46(100), 6.49(20), 6.34(40), 5.70(41), 4.28(23), 3.468(20)

Type material is deposited in the collections of the Fersman Mineralogical Museum, Russian Academy of Sciences, Leninskiy Prospekt 18-2, Moscow 119071, Russia, registration number 5886/1

How to cite: Pautov, L. A., Mirakov, M. A., Siidra, O. I., Chukanov, N. V., Borisov, A. S., Karpenko, V. Y., Plechov, P. Y., and Makhmadsharif, S.: Novikovite, IMA 2022-067, in: CNMNC Newsletter 70, Eur. J. Mineral., 34, https://doi.org/10.5194/ejm-34-591-2022, 2022.

IMA no. 2022-068

Pengite

$(Pb_8Sb_3^{3+})_{\Sigma 11}Sb_9^{5+}O_{35}$

Peg

Wuxu ore field, Nandan-Hechi metallogenic belt, Guangxi, China (23° N, 108° E)

Guowu Li*, Ningyue Sun, Qi Lu, Yuan Xue, Zhesheng Ma, Nicheng Shi, Jinhua Hao, and Junjia Fan

* E-mail: liguowu@cugb.edu.cn

Structurally related to pyrochlore supergroup minerals

Trigonal: $R\bar{3}m$; structure determined

$a = 7.3651(3)$, $c = 48.346(2)$ Å

3.236(43), 3.039(100), 2.669(55), 1.932(18), 1.846(21), 1.604(13), 1.578(11), 1.518(12)

Type material is deposited in the collections of the Geological Museum of China, Yangrou Hutong No. 15, Xisi, Xicheng District, Beijing 100031, People's Republic of China, catalogue number M16137 (holotype), and the Crystal Structure Laboratory, China University of Geosciences, Beijing 100083, People's Republic of China, catalogue number Hc-1 (cotype)

How to cite: Li, G., Sun, N., Lu, Q., Xue, Y., Ma, Z., Shi, N., Hao, J., and Fan, J.: Pengite, IMA 2022-068, in: CNMNC Newsletter 70, Eur. J. Mineral., 34, https://doi.org/10.5194/ejm-34-591-2022, 2022.

IMA no. 2022-069

Ferro-bosiite

$NaFe_3^{3+}(Al_4Fe_2^{2+})(Si_6O_{18})(BO_3)_3(OH)_3O$

Fbos

"Marina" granitic pegmatite, Mavuco, Alto Ligoña, Nampula Province, Mozambique (15°54′16″ S, 39°02′56″ E)

Ferdinando Bosi*, Alessandra Altieri, Henrik Skobgy, Federico Pezzotta, Ulf Hålenius, Gioacchino Tempesta, Paolo Ballirano, Tomáš Flégr, and Jan Cempírek

* E-mail: ferdinando.bosi@uniroma1.it

Tourmaline supergroup

Trigonal: $R3m$; structure determined

$a = 16.0499(5)$, $c = 7.2977(2)$ Å

6.461(51), 4.264(48), 4.012(62), 3.529(46), 2.997(59), 2.598(100), 2.060(41), 1.937(23)

Type material is deposited in the collections of the Museo Universitario di Scienze della Terra, Dipartimento di Scienze della Terra, Sapienza Università di Roma, Piazzale Aldo Moro 5, I-00185 Rome, Italy, catalogue number 33308/405

How to cite: Bosi, F., Altieri, A., Skobgy, H., Pezzotta, F., Hålenius, U., Tempesta, G., Ballirano, P., Flégr, T., and Cempírek, J.: Ferro-bosiite, IMA 2022-069, in: CNMNC Newsletter 70, Eur. J. Mineral., 34, https://doi.org/10.5194/ejm-34-591-2022, 2022.

IMA no. 2022-070

Zincorietveldite

$Zn(UO_2)(SO_4)_2(H_2O)_5$

Zrvd

Blue Lizard mine, Red Canyon, White Canyon district, San Juan Co., Utah, USA (37°33′26″ N, 110°17′44″ W)

Anthony R. Kampf*, Travis A. Olds, Jakub Plášil, and Joe Marty

* E-mail: akampf@nhm.org

The Zn analogue of rietveldite

Orthorhombic: $Pmn2_1$; structure determined

$a = 12.8712(9)$, $b = 8.3148(4)$, $c = 11.2959(4)$ Å

8.35(37), 6.42(62), 5.09(58), 4.67(100), 4.23(38), 3.916(46), 3.429(47), 3.340(39)

Cotype material is deposited in the collections of the Natural History Museum of Los Angeles County, 900 Exposition

7.2 Annex B

Here are collected the publications related to my PhD project.

The first paper provides a detailed crystal-chemical characterization of celleriite, a new tourmaline species from the Rosina pegmatite, San Piero in Campo, Elba Island (Tyrrhenian Sea, Italy). Insights on its minerogesis are also supplied.
This paper was published in *American Mineralogist* (Bosi et al., 2022a).

The second paper reports the first detailed chemical and spectroscopic study on tourmaline crystals with blue-growth zones at the analogous pole from the San Piero in Campo pegmatites, Elba Island (Tyrrhenian Sea, Italy). Furthermore, it contributes to the understanding on the origin and chemical composition of fluids involved in tourmaline crystallization, which are responsible for the color changes at the analogous termination observed in Elba tourmaline crystals.
This paper was published in *Mineralogical Magazine* (Altieri et al., 2022), and represents the topic of the case study 1 (section 3.3) in this PhD thesis.

The third paper is focused on the crystal-chemical characterization of a tourmaline crystal, found naturally broken into two fragments in a wide miarolitic cavity of the Rosina pegmatite (San Piero in Campo, Elba Island, Italy), and characterized by dark-colored overgrowths at both analogous and antilogous poles. This study clearly correlates structural evidences (i.e., fracturing of the pocket and breakage of tourmaline crystals) to the late-stage tourmaline generation. On the basis of structural and paragenetic observations of the cavity in which the tourmaline crystal was collected as well as chemical and spectroscopic analyses, we propose a genetic model for the dark-coloured overgrowths in Elba tourmaline crystals. Furthermore, a comparison of the dark overgrowths formed at the

analogous and the antilogous poles provides additional information on tourmaline crystallization process at the two different poles. This paper was published in *Mineralogical Magazine* (Altieri et al., 2023), and represents the topic of the case study 2 (section 3.4) in this PhD thesis.

The front pages of these publications are attached to this section.

American Mineralogist, Volume 107, pages 31–42, 2022

Celleriite, □(Mn$_2^{2+}$Al)Al$_6$(Si$_6$O$_{18}$)(BO$_3$)$_3$(OH)$_3$(OH), a new mineral species of the tourmaline supergroup

Ferdinando Bosi[1,*,||], Federico Pezzotta[2], Alessandra Altieri[1], Giovanni B. Andreozzi[1], Paolo Ballirano[1,†], Gioacchino Tempesta[3], Jan Cempírek[4,*,‡], Radek Škoda[4], Jan Filip[5], Renata Čopjaková[4], Milan Novák[4], Anthony R. Kampf[6,§], Emily D. Scribner[7], Lee A. Groat[8], and R. James Evans[8]

[1]Department of Earth Sciences, Sapienza University of Rome, Piazzale Aldo Moro, 5, 00185 Rome, Italy
[2]Natural History Museum, Corso Venezia 55, 20121 Milan, Italy
[3]Department of Earth and Geoenvironmental Sciences, University of Bari "Aldo Moro", via Orabona 4, 70125 Bari, Italy
[4]Department of Geological Sciences, Faculty of Science, Masaryk University, 659 37 Brno, Czech Republic
[5]Regional Centre of Advanced Technologies and Materials, Czech Advanced Technology and Research Institute (CATRIN), Palacký University, Šlechtitelů 27, 783 71 Olomouc, Czech Republic
[6]Mineral Sciences Department, Natural History Museum of Los Angeles County, 900 Exposition Boulevard, Los Angeles, California 90007, U.S.A.
[7]Environmental Engineering and Earth Sciences, Clemson University, 445 Brackett Hall, 321 Calhoun Drive, Clemson, South Carolina 29634, U.S.A.
[8]Department of Earth, Ocean and Atmospheric Sciences, University of British Columbia, Vancouver, British Columbia V6T 1Z4, Canada

Abstract

Celleriite, □(Mn$_2^{2+}$Al)Al$_6$(Si$_6$O$_{18}$)(BO$_3$)$_3$(OH)$_3$(OH), is a new mineral of the tourmaline supergroup. It was discovered in the Rosina pegmatite, San Piero in Campo, Elba Island, Italy (holotype specimen), and in the Pikárec pegmatite, western Moravia, Czech Republic (co-type specimen). Celleriite in hand specimen is violet to gray-blue (holotype) and dark brownish-green (co-type) with a vitreous luster, conchoidal fracture, and white streak. Celleriite has a Mohs hardness of ~7 and a calculated density of 3.13 and 3.14 g/cm^3 for holotype and its co-type, respectively. In plane-polarized light in thin section, celleriite is pleochroic (O = pale violet and E = light gray-blue in holotype; O = pale green and E = colorless in co-type) and uniaxial negative. Celleriite has trigonal symmetry: space group *R*3*m*, *Z* = 3, *a* = 15.9518(4) and 15.9332(3) Å, *c* = 7.1579(2) and 7.13086(15) Å, *V* = 1577.38(9) and 1567.76(6) Å^3 for holotype and co-type, respectively (data from single-crystal X-ray diffraction). The crystal structure of the holotype specimen was refined to *R*1 = 2.89% using 1696 unique reflections collected with Mo*K*α X-ray intensity data. Structural, chemical, and spectroscopic analyses resulted in the formulas:

$^{X}(\square_{0.58}Na_{0.42})_{\Sigma 1.00}{}^{Y}(Mn^{2+}_{1.39}Fe^{2+}_{0.16}Mg_{0.01}Al_{1.14}Fe^{3+}_{0.01}Li_{0.28}Ti_{0.01})_{\Sigma 3.00}{}^{Z}Al_6[^{T}(Si_{5.99}Al_{0.01})_{\Sigma 6.00}O_{18}](BO_3)_3(OH)_3{}^{W}[(OH)_{0.65}F_{0.03}O_{0.32}]_{\Sigma 1.00}$ (for holotype)

and

$^{X}(\square_{0.51}Na_{0.49})_{\Sigma 1.00}{}^{Y}(Mn^{2+}_{0.90}Fe^{2+}_{0.50}Al_{1.36}Fe^{3+}_{0.04}Li_{0.17}Zn_{0.04})_{\Sigma 3.00}{}^{Z}Al_6[^{T}(Si_{5.75}B_{0.25})_{\Sigma 6.00}O_{18}](BO_3)_3(OH)_3{}^{W}[(OH)_{0.35}F_{0.17}O_{0.48}]_{\Sigma 1.00}$ (for co-type)

Celleriite is a hydroxy species belonging to the *X*-site vacant group of the tourmaline supergroup. The new mineral was approved by the Commission on New Minerals, Nomenclature and Classification of the International Mineralogical Association, proposal no. 2019-089.

In the Rosina pegmatite, celleriite formed an overgrowth at the analogous pole of elbaite–fluor-elbaite–rossmanite crystals during the latest stage of evolution of pegmatite cavities after an event of a pocket rupture. In the Pikárec pegmatite, celleriite occurs as an intermediate growth sector of elbaite, princivalleite, and fluor-elbaite.

Keywords: Celleriite, tourmaline, crystal-structure refinement, electron microprobe, Mössbauer spectroscopy, laser-induced breakdown spectroscopy, laser-ablation inductively coupled plasma mass-spectroscopy, Raman spectroscopy; Lithium, Beryllium, and Boron: Quintessentially Crustal

Introduction

Tourmaline minerals are reported to be the first boron minerals to have formed in Earth's crust and now are the most widespread of minerals for which boron is an essential constituent (Grew et al. 2016; Dutrow and Henry 2018). It is no surprise that this supergroup receives an ever-increasing interest from the geoscience community. Tourmaline minerals are complex borosilicates that have been extensively studied in terms of their crystal structure and crystal chemistry (e.g., Foit 1989; Grice and Ercit 1993; Ertl et al. 2002, 2018; Novák et al. 2004, 2011; Bosi and Lucchesi 2007; Bosi 2013, 2018; Henry and Dutrow 2011; Henry et al. 2011; Filip

* E-mail: ferdinando.bosi@uniroma1.it, jan.cempirek@gmail.com
† Orcid 0000-0001-9116-5393
‡ Orcid 0000-0003-3180-9534
§ Orcid 0000-0001-8084-2563
|| Special collection papers can be found online at http://www.minsocam.org/MSA/AmMin/special-collections.html.

0003-004X/22/0001–031$05.00/DOI: https://doi.org/10.2138/am-2021-7818

Mineralogical Magazine (2022), 1–10
doi:10.1180/mgm.2022.101

CAMBRIDGE UNIVERSITY PRESS

Article

Blue growth zones caused by Fe^{2+} in tourmaline crystals from the San Piero in Campo gem-bearing pegmatites, Elba Island, Italy

Alessandra Altieri[1]*, Federico Pezzotta[2], Henrik Skogby[3], Ulf Hålenius[3] and Ferdinando Bosi[1]

[1]Department of Earth Sciences, Sapienza University of Rome, Piazzale Aldo Moro 5, I-00185 Rome, Italy; [2]Natural History Museum, Corso Venezia 55, 20121 Milan, Italy; and [3]Department of Geosciences, Swedish Museum of Natural History, Box 50007, SE-10405 Stockholm, Sweden

Abstract

Two tourmaline crystals with a blue growth zone at the analogous pole, respectively from the San Silvestro and the Fucili pegmatites, located in the San Piero in Campo village, Elba Island (Tyrrhenian Sea, Italy), have been described for the first time using compositional and spectroscopic data to define their crystal-chemical aspects and the causes of the colour. Compositional data obtained by electron microprobe analysis indicate that both tourmalines belong to the elbaite–fluor-elbaite series. The upper part of each crystal is characterised by an increased amount of Fe (FeO up to ~1 wt.%) and a Ti content below the detection limit. Optical absorption spectra recorded on the blue zone of both samples show absorption bands caused by spin-allowed *d-d* transitions in [6]-coordinated Fe^{2+}, and no intervalence charge transfer Fe^{2+}-Ti interactions, indicating that Fe^{2+} is the only chromophore. Mössbauer analysis of the blue zone of the Fucili sample confirmed the Fe^{2+} oxidation state, implying that the redox conditions in the crystallisation environment were relatively reducing. The presence of colour changes at the analogous termination during tourmaline crystal growth suggests a change in the composition of the crystallisation environment, probably associated with a partial opening of the system.

Keywords: tourmaline, electron microprobe, optical absorption spectroscopy, infrared spectroscopy, petrogenetic indicator, growth history, miarolitic cavities, Elba Island

(Received 28 May 2022; accepted 15 August 2022; Accepted Manuscript published online: 22 August 2022; Associate Editor: Anthony R Kampf)

Introduction

Tourmaline is the dominant host for boron (B) in most rocks of the Earth's crust, occurring in granites and granitic pegmatites, though also in sedimentary and in low-grade to ultrahigh-pressure metamorphic rocks (van Hinsberg *et al.*, 2011a, 2011b; Dutrow and Henry, 2018; Henry and Dutrow, 2018). Tourmaline minerals are complex borosilicates with a significant compositional variability containing both light and heavy elements, from H to Pb, and across multiple valence states. This variability results in a wide range of distinct mineral species. In accordance with Henry *et al.* (2011), the general formula of tourmaline can be written as $XY_3Z_6T_6O_{18}(BO_3)_3V_3W$, where X = Na^+, K^+, Ca^{2+}, Pb^{2+}, □ (□ = vacancy); Y = Mg^{2+}, Fe^{2+}, Mn^{2+}, Li^+, Al^{3+}, Fe^{3+}, Cr^{3+}, V^{3+}, Ti^{4+}; Z = Al^{3+}, Fe^{3+}, Cr^{3+}, V^{3+}, Mg^{2+}, Fe^{2+}, Ti^{4+}; T = Si^{4+}, Al^{3+}, B^{3+}; B = B^{3+}; V = OH^{1-}, O^{2-} and W = OH^{1-}, F^{1-}, O^{2-}. The non-italicised letters X, Y, Z, T and B represent groups of cations accommodated at the $^{[9]}X$, $^{[6]}Y$, $^{[6]}Z$, $^{[4]}T$ and $^{[3]}B$ crystallographic sites (italicised letters). The letters V and W represent groups of anions accommodated at the $^{[3]}$O3 and $^{[3]}$O1 crystallographic sites, respectively. The H atoms occupy the H3 and H1 sites, which are related to O3 and O1, respectively.

According to the dominance of specific ions at one or more sites of the crystal structure, the tourmaline-supergroup minerals can be classified in three primary groups based on the *X*-site occupancy: *X*-site vacant, alkali and calcic (e.g. Henry *et al.*, 2011). A further level of classification into subgroups is based on charge arrangements at the *Y* and *Z* sites. Tourmalines are also distinguished by the dominant anion at the W position of the general formula into hydroxy-, fluor- and oxy-species (Henry *et al.*, 2011). In particular, partitioning of the *X* and *Y*-site occupancy has been calibrated and is useful to reconstruct the chemical history of the fluids involved in tourmaline crystallisation (van Hinsberg *et al.*, 2011a, 2011b; Dutrow and Henry, 2018; Bosi *et al.*, 2022a).

Gem-quality tourmalines from Elba Island are easily recognisable and distinguishable from those of all other world localities for the delicate pastel colours and the perfection of their crystal shape, even in small sizes. Specifically, the main features which make them unique are the pastel colours of the crystal prismatic section and an unusual dark coloured termination at the analogous pole (the so-called 'Moor's head' textural type), which is commonly black (Pezzotta, 2021). However, in some cases, the terminations of the tourmaline crystals are not black, but are composed of multiple thin growth zones of greenish, brownish, purplish or even bluish colours (Pezzotta, 2021). The blue hues

*Author for correspondence: Alessandra Altieri, Email: alessandra.altieri@uniroma1.it
Cite this article: Altieri A., Pezzotta F., Skogby H., Hålenius U. and Bosi F. (2022) Blue growth zones caused by Fe^{2+} in tourmaline crystals from the San Piero in Campo gem-bearing pegmatites, Elba Island, Italy. *Mineralogical Magazine* 1–10. https://doi.org/10.1180/mgm.2022.101

https://doi.org/10.1180/mgm.2022.101 Published online by Cambridge University Press

Mineralogical Magazine (2023), 1–13
doi:10.1180/mgm.2022.125

CAMBRIDGE UNIVERSITY PRESS

Article

Dark-coloured Mn-rich overgrowths in an elbaitic tourmaline crystal from the Rosina pegmatite, San Piero in Campo, Elba Island, Italy: witness of late-stage opening of the geochemical system

Alessandra Altieri[1]*, Federico Pezzotta[2], Henrik Skogby[3], Ulf Hålenius[3] and Ferdinando Bosi[1]

[1]Department of Earth Sciences, Sapienza University of Rome, Piazzale Aldo Moro 5, I-00185 Rome, Italy; [2]Natural History Museum, Corso Venezia 55, 20121 Milan, Italy; and [3]Department of Geosciences, Swedish Museum of Natural History, Box 50007, SE-10405 Stockholm, Sweden

Abstract

Multicoloured tourmalines from Elba Island, commonly display dark-coloured terminations due to incorporation of Fe, and also occasionally Mn. The mechanisms which led to the availability of these elements in the late-stage residual fluids are not yet completely understood. For this purpose, we investigated a representative tourmaline crystal found naturally in two fragments within a wide miarolitic cavity in the Rosina pegmatite (San Piero in Campo, Elba Island, Italy), and characterised by late-stage dark-coloured overgrowths. Microstructural and paragenetic observations, together with compositional and spectroscopic data (electron microprobe and optical absorption spectroscopy), provide evidence which shows that the formation of the dark-coloured Mn-rich overgrowths are the result of a pocket rupture. This event caused alteration of the cavity-coating spessartine garnet by highly-reactive late-stage cavity fluids by leaching processes, with the subsequent release of Mn to the residual fluids. We argue that the two fragments were originally a single crystal, which underwent natural breakage followed by the simultaneous growth of Mn-rich dark terminations at both breakage surfaces. This conclusion supports the evidence for a pocket rupture event, responsible for both the shattering of the tourmaline crystal and the compositional variation of the cavity-fluids related to the availability of Mn, which was incorporated by the tourmaline crystals. Additionally, a comparison of the dark overgrowths formed at the analogous and the antilogous poles, provides information on tourmaline crystallisation at the two different poles. The antilogous pole is characterised by a higher affinity for Ca, F and Ti, and a selective uptake of Mn^{2+}, even in the presence of a considerable amount of Mn^{3+} in the system. This uneven uptake of Mn ions resulted in the yellow–orange colouration of the antilogous overgrowth (Mn^{2+} dependent) rather than the purple-reddish colour of the analogous overgrowths (Mn^{3+} dependent).

Keywords: tourmaline, electron microprobe, optical absorption spectroscopy, granitic pegmatites, miarolitic cavities, Elba Island

(Received 18 August 2022; accepted 6 November 2022; Accepted Manuscript published online: 28 November 2022; Associate Editor: František Laufek)

Introduction

Tourmaline is the most widespread borosilicate mineral in the Earth's crust, typically occurring in granites and granite pegmatites as well as in sedimentary and metamorphic rocks (van Hinsberg *et al.*, 2011a, 2011b; Dutrow and Henry, 2018; Henry and Dutrow, 2018). The compositional complexity of this mineral arises from its general formula, which can be written as $XY_3Z_6T_6O_{18}(BO_3)_3V_3W$, where X = Na^+, K^+, Ca^{2+}, □ (= vacancy); Y = Mg^{2+}, Fe^{2+}, Mn^{2+}, Li^+, Al^{3+}, Fe^{3+}, Cr^{3+}, V^{3+}, Ti^{4+}; Z = Al^{3+}, Fe^{3+}, Cr^{3+}, V^{3+}, Mg^{2+}, Fe^{2+}; T = Si^{4+}, Al^{3+}, B^{3+}; B = B^{3+}; V = $(OH)^-$, O^{2-}; and W = $(OH)^-$, F^-, O^{2-}.

Due to the occurrence of an extensive short-range order, which can impose extremely slow diffusion rates of the constituents in the structure, tourmalines can, once formed, retain their original composition (e.g. Hawthorne and Dirlam, 2011; van Hinsberg *et al.*, 2011a, 2011b; Bosi, 2018). Thus, they are able to preserve the chemical-physical variation of the crystallisation environment during crystal growth (e.g. Agrosì *et al.*, 2006). Moreover, the extensive *P*–*T* stability range of tourmalines make them an efficient geological tool for investigating *P*–*T*–*X* conditions in all crustal settings within the Earth (van Hinsberg *et al.*, 2011a, 2011b). As a result, tourmaline is an excellent petrogenetic indicator that can provide information about the formation and evolution of complex crystals over time, acting as a 'geologic DVD' (Dutrow and Henry, 2011).

Multicoloured tourmalines of pastel or light colours with dark crystal terminations at the analogous pole (the **c**$^-$ side of the crystal) are characteristics of Elba Island pegmatites, Italy. These terminations are usually black, though can appear in different colours such as brown, green, red–violet, and blue. Such more-or-less dark-coloured terminations may occur as narrow overgrowths, but can also compose a significant zone of the

*Author for correspondence: Alessandra Altieri, Email: alessandra.altieri@uniroma1.it
Cite this article: Altieri A., Pezzotta F., Skogby H., Hålenius U. and Bosi F. (2023) Dark-coloured Mn-rich overgrowths in an elbaitic tourmaline crystal from the Rosina pegmatite, San Piero in Campo, Elba Island, Italy: witness of late-stage opening of the geochemical system. *Mineralogical Magazine* 1–13. https://doi.org/10.1180/mgm.2022.125

https://doi.org/10.1180/mgm.2022.125 Published online by Cambridge University Press

7.3 Annex C

Besides the studies on tourmaline crystals from Elba Island and Mozambique, I was involved in research works external to my PhD project.

The first research work in which I collaborated, concerns the crystal-chemical characterization of a rare tourmaline crystal from the Tzarevskoye uranium-vanadium deposit (Karelia, Russia), which represents the second world-occurrence of a Cr-rich vanadio-oxy-dravite. In this study, my contribution was to provide a compositional overview of Al-V-Cr-Fe^{3+}-oxy-tourmalines based on the chemical data obtained from the analyzed sample, along with those from 102 oxy-tourmaline samples from the literature, by developing a new $^{[6]}$Al-Cr-V-Fe^{3+} diagram for the classification of oxy-tourmalines. The development of this new diagram resulted in simplify the oxy-tourmaline nomenclature as it merges the chemical information over the octahedrally-coordinated sites (*Y* and *Z*) by removing the issues of uncertainty associated with cation order–disorder across *Y* and *Z*. The innovativeness of this new classification diagram relies in the direct identification of oxy-tourmalines by using the chemical data alone.
The results obtained from this study were published in *Mineralogical Magazine* (Bosi et al., 2020).

The second research work to which I contributed, is focused on an azure tourmaline crystal from the Curiglia Village (Veddasca Valley, Varese, Lombardy, Italy). The blue coloration is one of the most scientifically interesting colors in tourmaline crystals, as it can be produced by different color-causing agents, such as Fe^{2+} and/or Cu^{2+}. To investigate on this, and determine the cause of azure coloration, I started a chemical and spectroscopic study on this particular tourmaline sample. In addition, the crystal-chemical characterization of this sample resulted in the identification of princivalleite.

The results obtained from this study were published in *Mineralogical Magazine* (Bosi et al., 2022b), in which the crystal-chemical characteristics and the minerogenesis of princivalleite were detailed described.

The front pages of these publications are attached to this section.

Mineralogical Magazine (2020), 1–8
doi:10.1180/mgm.2020.77

CAMBRIDGE UNIVERSITY PRESS

Article

Chromium-rich vanadio-oxy-dravite from the Tzarevskoye uranium–vanadium deposit, Karelia, Russia: a second world-occurrence of Al–Cr–V–oxy-tourmaline

Ferdinando Bosi[1]*, Alessandra Altieri[1], Fernando Cámara[2,3] and Marco E. Ciriotti[4,5]

[1]Department of Earth Sciences, Sapienza University of Rome, Piazzale Aldo Moro 5, I-00185 Rome, Italy; [2]Department of Earth Sciences "Ardito Desio", University of Milan, via Luigi Mangiagalli 34, 20133 Milan, Italy; [3]CrisDi, Interdepartmental Centre for the Research and Development of Crystallography, via Pietro Giuria 5, I-10125, Turin, Italy; [4]Associazione Micromineralogica Italiana, via San Pietro 55, I-10073 Devesi-Cirié, Italy; and [5]Dipartimento di Scienze della Terra, Università di Torino, via Tommaso Valperga Caluso 35, I-10125 Torino, Italy

Abstract

A green tourmaline sample from the Tzarevskoye uranium–vanadium deposit, close to the Srednyaya Padma deposit, Lake Onega, Karelia Republic, Russia, has been found to be the second world-occurrence of Cr-rich vanadio-oxy-dravite in addition to the Pereval marble quarry, Sludyanka crystalline complex, Lake Baikal, Russia, type-locality. From the crystal-structure refinement and chemical analysis, the following empirical formula is proposed: $^{X}(Na_{0.96}K_{0.02}\square_{0.02})_{\Sigma 1.00}$ $^{Y}(V_{1.34}Al_{0.68}Mg_{0.93}Cu^{2+}_{0.02}Zn_{0.01}Ti_{0.01})_{\Sigma 3.00}$ $^{Z}(Al_{3.19}Cr_{1.36}V_{0.03}Mg_{1.42})_{\Sigma 6.00}(^{T}Si_6O_{18})(^{B}BO_3)_3{}^{V}(OH)_3{}^{W}[O_{0.60}(OH)_{0.23}F_{0.17}]_{\Sigma 1.00}$. Together with the data from the literature, a compositional overview of Al–V–Cr–Fe^{3+}-tourmalines is provided by using $^{[6]}$Al–V–Cr–Fe^{3+} diagrams for tourmaline classification. These diagrams further simplify the tourmaline nomenclature as they merge the chemical information over the octahedrally-coordinated sites (*Y* and *Z*) by removing the issues of uncertainty associated with cation order–disorder across *Y* and *Z*. Results show the direct identification of tourmalines by using the chemical data alone.

Keywords: tourmaline, crystal-structure refinement, electron microprobe, nomenclature

(Received 6 August 2020; accepted 1 October 2020; Accepted Manuscript published online: 23 October 2020; Associate Editor: Ian T. Graham)

Introduction

The tourmaline-supergroup minerals are chemically complex borosilicates. They are widespread in the Earth's crust, occurring in sedimentary rocks, granites and granitic pegmatites and in low-grade to ultrahigh-pressure metamorphic rocks (e.g. Dutrow and Henry, 2011). In accordance with Henry *et al.* (2011), the general formula of tourmaline can be written as $XY_3Z_6T_6O_{18}(BO_3)_3V_3W$, where $X = Na^+$, K^+, Ca^{2+} and $\square$ ($\square$ = vacancy); $Y = Al^{3+}$, Fe^{3+}, Cr^{3+}, V^{3+}, Mg^{2+}, Fe^{2+}, Mn^{2+} and Li^+; $Z = Al^{3+}$, Fe^{3+}, Cr^{3+}, V^{3+}, Mg^{2+} and Fe^{2+}; $T = Si^{4+}$, Al^{3+} and B^{3+}; $B = B^{3+}$, $V = OH^{1-}$ and O^{2-} and $W = OH^{1-}$, F^{1-} and O^{2-}. The (non-italicised) letters X, Y, Z, T and B represent groups of cations accommodated at the $^{[9]}X$, $^{[6]}Y$, $^{[6]}Z$, $^{[4]}T$ and $^{[3]}B$ crystallographic sites (identified with *italicised* letters); the letters V and W represent groups of anions accommodated at the $^{[3]}$O(3) and $^{[3]}$O(1) crystallographic sites, respectively. The H atoms occupy the *H*(3) and *H*(1) sites, which are related to O(3) and O(1), respectively (e.g. Bosi, 2013; Gatta *et al.*, 2014).

Due to their highly variable chemical composition and refractory behaviour, tourmaline is considered a very useful indicator of geological processes in igneous, hydrothermal and metamorphosed systems (Dutrow and Henry, 2011; van Hinsberg *et al.*, 2011; Ahmadi *et al.*, 2019; Sipahi, 2019) and able to record and preserve the chemical composition of their host rocks.

Vanadium and Cr-bearing hydroxyl- and oxy-tourmaline species have been described widely in the literature (Cossa and Arzruni, 1883; Badalov, 1951; Bassett, 1953; Snetsinger, 1966; Peltola *et al.*, 1968; Jan *et al.*, 1972; Dunn, 1977; Nuber and Schmetzer, 1979; Foit and Rosenberg, 1979; Rumyantseva, 1983; Gorskaya *et al.*, 1984, 1987; Reznitskii *et al.*, 1988; Hammarstrom, 1989; Kazachenko *et al.*, 1993; Reznitskii and Sklyarov, 1996; Ertl *et al.*, 2008; Arif *et al.*, 2010; Lupulescu and Rowe, 2011; Rozhdestvenskaya *et al.*, 2011; Cempírek *et al.*, 2013; Vereshchagin *et al.*, 2014). Currently, they are known from several localities: Sludyanka (Slyudyanka) crystalline complex, Lake Baikal, Russia; Onega region, Central Karelia, Russia; Primorye, Far eastern Russia; Balmat, St. Lawrence County, New York, USA; Silver Knob deposit, Mariposa County, California, USA; Nausahi deposit, Orissa, India; Outokumpu deposit, Finnish North Karelia, Finland; Mingora and Gujar Kili mines, Swat, Pakistan; Alpurai, Pakistan; Shabrovskoe ore deposit, Middle Urals, Russia; Syssertox Dach, Ural Mountains, Russia; Umba Valley, Tanga Province, Tanzania; Kwal District, Kenya;

*Author for correspondence: Ferdinando Bosi, Email: ferdinando.bosi@uniroma1.it
Cite this article: Bosi F., Altieri A., Cámara F. and Ciriotti M.E. (2020) Chromium-rich vanadio-oxy-dravite from the Tzarevskoye uranium–vanadium deposit, Karelia, Russia: a second world-occurrence of Al–Cr–V–oxy-tourmaline. *Mineralogical Magazine* 1–8. https://doi.org/10.1180/mgm.2020.77

Mineralogical Magazine (2022), **86**, 78–86
doi:10.1180/mgm.2022.3

CAMBRIDGE UNIVERSITY PRESS

Article

Princivalleite, $Na(Mn_2Al)Al_6(Si_6O_{18})(BO_3)_3(OH)_3O$, a new mineral species of the tourmaline supergroup from Veddasca Valley, Varese, Italy

Ferdinando Bosi[1]*, Federico Pezzotta[2], Henrik Skogby[3], Alessandra Altieri[1], Ulf Hålenius[3], Gioacchino Tempesta[4] and Jan Cempírek[5]

[1]Department of Earth Sciences, Sapienza University of Rome, Piazzale A. Moro, 5, I-00185 Rome, Italy; [2]Natural History Museum, Corso Venezia 55, 20121 Milan, Italy; [3]Department of Geosciences, Swedish Museum of Natural History, Box 50007, SE-10405 Stockholm, Sweden; [4]Dipartimento di Scienze della Terra e Geoambientali, Università degli Studi di Bari Aldo Moro, Bari, Italy; and [5]Department of Geological Sciences, Faculty of Science, Masaryk University, Kotlářská 2, 611 37, Brno, Czech Republic

Abstract

Princivalleite, $Na(Mn_2Al)Al_6(Si_6O_{18})(BO_3)_3(OH)_3O$, is a new mineral (IMA2020-056) of the tourmaline supergroup. It occurs in the Veddasca Valley, Luino area, Varese, Lombardy, Italy (46°03'30.74"N, 8°48'24.47"E) at the centre of a narrow (2–3 cm wide) vertical pegmatitic vein, a few metres long, crosscutting a lens of flaser gneiss. Crystals are subhedral (up to 10 mm in size), azure with a vitreous lustre, conchoidal fracture and white streak. Princivalleite has a Mohs hardness of ~7, a calculated density of 3.168 g/cm^3 and is uniaxial (–). Princivalleite has trigonal symmetry, space group $R3m$, $a = 15.9155(2)$ Å, $c = 7.11660(10)$ Å, $V = 1561.15(4)$ Å^3 and $Z = 3$. The crystal structure was refined to $R_1 = 1.36\%$ using 1758 unique reflections collected with Mo$K\alpha$ X-ray intensity data. Crystal-chemical analysis resulted in the empirical crystal-chemical formula

$^{X}(Na_{0.54}Ca_{0.11}\square_{0.35})_{\Sigma 1.00}{}^{Y}(Al_{1.82}Mn^{2+}_{0.84}Fe^{2+}_{0.19}Zn_{0.07}Li_{0.08})_{\Sigma 3.00}{}^{Z}(Al_{5.85}Fe^{2+}_{0.13}Mg_{0.02})_{\Sigma 6.00}[{}^{T}(Si_{5.60}Al_{0.40})_{\Sigma 6.00}O_{18}](BO_3)_3{}^{O(3)}[(OH)_{2.71}O_{0.29}]_{\Sigma 3.00}{}^{O(1)}[O_{0.66}F_{0.22}(OH)_{0.12}]_{\Sigma 1.00}$ which recast in its ordered form for classification purposes is:

$^{X}(Na_{0.54}Ca_{0.11}\square_{0.35})_{\Sigma 1.00}{}^{Y}(Al_{1.67}Mn^{2+}_{0.84}Fe^{2+}_{0.32}Zn_{0.07}Mg_{0.02}Li_{0.08})_{\Sigma 3.00}{}^{Z}Al_{6.00}[{}^{T}(Si_{5.60}Al_{0.40})_{\Sigma 6.00}O_{18}](BO_3)_3{}^{V}[(OH)_{2.71}O_{0.29}]_{\Sigma 3.00}{}^{W}[O_{0.66}F_{0.22}(OH)_{0.12}]_{\Sigma 1.00}$.

Princivalleite is an oxy-species belonging to the alkali group of the tourmaline supergroup. The closest end-member compositions of valid tourmaline species are those of oxy-schorl and darrellhenryite, to which princivalleite is related by the substitutions $Mn^{2+} \leftrightarrow Fe^{2+}$ and $Mn^{2+} \leftrightarrow 0.5Al^{3+} + 0.5Li^{+}$, respectively. Princivalleite from Veddasca Valley is a geochemical anomaly, originated in a B-rich and peraluminous anatectic pegmatitic melt formed *in situ*, poor in Fe and characterised by reducing conditions in the late-stage metamorphic fluids derived by the flaser gneiss. The Mn-enrichment in this new tourmaline is due to absence of other minerals competing for Mn such as garnet.

Keywords: princivalleite, new mineral species, crystal-structure refinement, electron microprobe, Mössbauer spectroscopy, infrared spectroscopy, optical absorption spectroscopy, micro-laser induced breakdown spectroscopy

(Received 30 November 2021; accepted 4 January 2022; Accepted Manuscript published online: 14 January 2022; Associate Editor: Oleg I Siidra)

Introduction

Tourmalines are complex borosilicates that have been studied extensively in terms of their crystal structure and crystal chemistry (e.g. Foit, 1989; Hawthorne, 1996; Hawthorne and Henry, 1999; Ertl *et al.*, 2002; Novák *et al.*, 2004; Bosi and Lucchesi, 2007; Bosi, 2013, 2018; Henry and Dutrow, 2011; Cempírek *et al.*, 2013; Bačík and Fridrichová, 2020). In accordance with Henry *et al.* (2011), the general chemical formula of tourmaline is written as: $XY_3Z_6T_6O_{18}(BO_3)_3V_3W$, where X = Na^+, K^+, Ca^{2+}, $\square$ (= vacancy); Y = Al^{3+}, Fe^{3+}, Cr^{3+}, V^{3+}, Mg^{2+}, Fe^{2+}, Mn^{2+}, Li^+; Z = Al^{3+}, Fe^{3+}, Cr^{3+}, V^{3+}, Mg^{2+}, Fe^{2+}; T = Si^{4+}, Al^{3+}, B^{3+}; B = B^{3+}; V = $(OH)^-$, O^{2-}; and W = $(OH)^-$, F^-, O^{2-}. Note that the non-italicised letters X, Y, Z and B represent groups of cations hosted in the $^{[9]}X$, $^{[6]}Y$, $^{[6]}Z$, $^{[4]}T$ and $^{[3]}B$ crystallographic sites (letters italicised). As for the letters V and W, they represent groups of anions accommodated at the [3]-coordinated O3 and O1 crystallographic sites, respectively. The dominance of specific ions at one or more sites of the structure gives rise to a range of distinct mineral species.

A formal description of the new tourmaline species princivalleite is presented here. The mineral is named after Francesco

*Author for correspondence: Ferdinando Bosi, Email: ferdinando.bosi@uniroma1.it
Cite this article: Bosi F., Pezzotta F., Skogby H., Altieri A., Hålenius U., Tempesta G. and Cempírek J. (2022) Princivalleite, $Na(Mn_2Al)Al_6(Si_6O_{18})(BO_3)_3(OH)_3O$, a new mineral species of the tourmaline supergroup from Veddasca Valley, Varese, Italy. *Mineralogical Magazine* **86**, 78–86. https://doi.org/10.1180/mgm.2022.3

https://doi.org/10.1180/mgm.2022.3 Published online by Cambridge University Press